UNIVERSITY OF SOUTHAMPTON

FACULTY OF ENGINEERING AND PHYSICAL SCIENCES
School Electronics and Computer Science

Optical-OFDM-Aided Wireless Communications

by

Xiaoyu Zhang
BEng, MSc (Hons)

ORCID ID 0000-0002-0793-889X

Thesis for the degree of Doctor of Philosophy

Supervisors: Professor Lajos Hanzo,
Professor Sheng Chen, and
Dr Rong Zhang

March 2020

UNIVERSITY OF SOUTHAMPTON

ABSTRACT

FACULTY OF ENGINEERING AND PHYSICAL SCIENCES
School Electronics and Computer Science

Thesis for the degree of Doctor of Philosophy

OPTICAL-OFDM-AIDED WIRELESS COMMUNICATIONS

by Xiaoyu Zhang

Orthogonal Frequency-Division Multiplexing (OFDM) has compelling benefit in Optical Wireless Communications (OWC). Hence, we analyse the Layered Asymmetrically Clipped Optical OFDM (LACO-OFDM), which is one of the most advanced Optical OFDM (O-OFDM) schemes, and improve its overall system performance.

We commence in Chapter 1 with a review of the development of OWC and O-OFDM, discussing its Spectral Efficiency (SE) and Power Efficiency (PE). Then, LACO-OFDM introduced for striking a trade-off between the attainable SE and PE. This is followed by a literature review of its recent development. A more detailed tutorial on LACO-OFDM is then given in Chapter 2, relying on detailed examples.

To further study the properties of LACO-OFDM, Chapter 3 analyses its 1) Probability Density Function (PDF) and its statistical moments; 2) Bit Error Ratio (BER); and 3) Peak-to-Average Power Ratio (PAPR). As a further advance, we propose a tone-injection aided PAPR reduction design for LACO-OFDM, which in turn improves the BER performance. Simulations are provided for verifying both the analytical BER performance and the PAPR distribution of LACO-OFDM. The results show that the expressions derived match well with the simulations. Furthermore, the PAPR reduction method proposed attains a 5 dB PAPR reduction at the 10^{-3} probability-point of the complementary cumulative distribution function, as well as a better BER performance than the original LACO-OFDM scheme.

For the sake of improving the BER performance, multi-class channel coded LACO-OFDM is proposed in Chapter 4, where the channel capacity of the system is derived based on our mutual information analysis. We conceive a multi-class channel encoding scheme integrated with the layered transmitter. At the receiver, both the coded and uncoded likelihood ratios (LLRs) are extracted for inter-layer interference cancellation and symbol detection, respectively. Simulations are conducted and the results show that our design approaches the achievable rate within 1.1 dB for 16QAM 4-layer LACO-OFDM with the aid of a half-rate 8-iteration turbo code at BER $= 10^{-3}$, outperforming its conventional counterpart by about 3.6 dB.

In Chapter 5, we propose algorithms for optimising the Discrete-input Continuous-output Memoryless Channel (DCMC) capacity of LACO-OFDM. Then, an algorithm is proposed for maximising the capacity for twin-layer LACO-OFDM by optimising the power sharing between the layers. This is followed by the conception of a more general algorithm applicable to LACO-OFDM having an arbitrary number of layers. Numerical results are provided for quantifying the capacity improvement attained by the proposed algorithm. Moreover, an adaptive layer-activation scheme is proposed for adjusting the number of layers to be used for maximising the capacity at different SNRs.

Contents

Nomenclature

Global Symbols

Statistical Distributions

$\mathcal{B}(n, p)$	Binomial distribution with n trails and success probability p
$\mathcal{B}(1, p)$	Bernoulli distribution with success probability p
$\mathcal{CN}$	Complex Gaussian distribution
$\mathcal{N}(\mu, \sigma^2)$	(Real-valued) Gaussian distribution with mean μ (0 if absent) and variance σ^2 (1 if absent)

Functions and Operations

$(\cdot)^*$	The complex conjugate of number $(\cdot)$
$\otimes$	The signal convolution operation
$\|\cdot\|_1$	The ℓ_1-norm operation
$\|\cdot\|_2$	The ℓ_2-norm operation
$\mathbb{D}\{\cdot\}$	The statistical variance of signal $(\cdot)$'s amplitude
$\mathbb{E}\{\cdot\}$	The statistical expectation of signal $(\cdot)$'s amplitude
$\exp[\cdot]$	The exponential function
$F_{\boldsymbol{s}}(z)$	The CDF of signal $\boldsymbol{s}$'s amplitude evaluated at z
$f_{\boldsymbol{s}}(z)$	The PDF of signal $\boldsymbol{s}$'s amplitude evaluated at z
$\mathcal{F}\{\cdot\}$	The Discrete Fourier Transform / Fast Fourier Transform operation
$\mathcal{F}^{-1}\{\cdot\}$	The Inverse Discrete Fourier Transform (IDFT) / Inverse Fast Fourier Transform (IFFT) operation
$\mathcal{F}_K^{-1}\{\cdot\}$	The IDFT/IFFT with number of points K specified
$\mathsf{H}(\cdot)$	The information entropy function
$I(\cdot\ ,\ \cdot)$	The mutual information function
$\Im\{\cdot\}$	The imaginary part of $(\cdot)$
$\mathcal{L}_\mathrm{a}(\cdot)$	The *a priori* logarithm likelihood ratio
$\mathcal{L}_\mathrm{p}(\cdot)$	The *a posteriori* logarithm likelihood ratio
$\Pr(\cdot)$	The probability of event $(\cdot)$
$\mathsf{u}(\cdot)$	The Heaviside step function

$\mathrm{mod}(a,\ b)$	The modulo-b operation for a
$\mathrm{Mod}(\cdot,\ \cdot)$	The modulo operation for complex numbers
$\Re\{\cdot\}$	The real part of $(\cdot)$
$\mathrm{sgn}(\cdot)$	The sign function
W_K	The Kth root of unity $e^{j\frac{2\pi}{K}}$
$\delta(\cdot)$	The Dirac delta function
$\Phi(\cdot)$	The CDF of the standard Gaussian distribution
$\phi(z;\ \sigma^2)$	The PDF of Gaussian distribution with zero mean and σ^2 variance

Sets

$\mathbb{N}$	The set of natural numbers
$\mathbb{R}$	The set of real numbers
$\mathbb{Z}$	The set of integers

Chapter 2

General Symbols

B	The total number of bits transmitted
$\boldsymbol{b}$	The input bit stream
$\hat{\boldsymbol{b}}$	The bit stream detected by the receiver
K	The total number of subcarriers available
M	The number of points in the mapping constellation pattern
$\boldsymbol{r}$	The received TD sample stream
T_{IFFT}	The time consumption for one IFFT stage

ACO-OFDM-Related

$\mathcal{S}$	The constellation set used for modulation
$\boldsymbol{S}$, $S[u]$	The mapped transmitting FD symbol stream and its uth symbol
$\overline{\boldsymbol{S}}$, $\overline{S}[k]$	The FD symbol stream loaded under ACO-OFDM rule and its kth symbol
$\overline{\boldsymbol{s}}$, $\overline{s}[n]$	The TD samples of ACO-OFDM before clipping at zero and its nth sample
$\boldsymbol{s}$, $s[n]$	The TD samples of ACO-OFDM after clipping at zero and its nth sample

LACO-OFDM-Related

B_l	The number of bits transmitted on layer l
$\boldsymbol{b}_l$	The input bit stream for layer l
$\hat{\boldsymbol{b}}_l$	layer l's bit stream detected by the receiver
K_l	The number of subcarriers controlled by layer l, $K_l = K/2^{l-1}$
P_l	The (electric) power of the clipped layer l TD signal $\boldsymbol{s}_l$
$\boldsymbol{r}_l$	The received TD signal with the clipping distortion of layers $1 \sim (l-1)$ removed
$\mathcal{S}_l$	The constellation set used for modulation on layer l

$\boldsymbol{S}_l$, $S_l[u]$	The mapped transmitting FD symbol stream for layer l and its uth symbol
$\boldsymbol{s}_l$, $s_l[n]$	The length-K clipped TD signal of layer l and its nth sample
$\overline{\boldsymbol{S}}_l$, $\overline{S}_l[k]$	The length-K loaded FD signal of layer l using TX model 1 and its kth symbol
$\overline{\boldsymbol{s}}_l$, $\overline{s}_l[n]$	The length-K unclipped TD signal of layer l and its nth sample
$\overline{\overline{\boldsymbol{S}}}_l$, $\overline{\overline{S}}[k]$	The length-K_l loaded FD signal of layer l using TX model 2 and its kth symbol, where $0 \leq k \leq (K_l - 1)$
$\overline{\overline{\boldsymbol{s}}}_l$, $\overline{\overline{s}}_l[n]$	The length-K_l unclipped TD signal of layer l and its nth sample, where $0 \leq n \leq (K_l - 1)$
$\boldsymbol{x}$, $x[k]$	The TD superimposed LACO-OFDM signal and its kth sample

Chapter 3

Signals

$\boldsymbol{n}_\mathrm{c}$	The UB clipping noise in the UB clipping model
$\hat{\boldsymbol{S}}_l$, $\hat{S}[u]$	The detected transmitting FD signal at receiver, and its uth symbol
$\boldsymbol{T}_l$, $T_l[u]$	The injecting signal for layer l and its uth symbol
$\lceil\boldsymbol{x}\rceil$, $\lceil x\rceil[k]$	The LACO-OFDM TD signal with UB clipping and its kth sample
$\overset{\leftarrow}{\boldsymbol{x}}$, $\overset{\leftarrow}{x}[k]$	The TD superimposed injected LACO-OFDM signal and its kth sample
$\lceil\overset{\leftarrow}{\boldsymbol{x}}\rceil$, $\lceil\overset{\leftarrow}{\boldsymbol{x}}\rceil\,[k]$	The UB clipped counterpart of $\overset{\leftarrow}{\boldsymbol{x}}$ and $\overset{\leftarrow}{x}[k]$
$\boldsymbol{Y}_l$, $Y_l[u]$	The injected signal for layer l and its uth symbol
$\overline{\boldsymbol{Y}}_l$, $\overline{Y}_l[k]$	The length-K loaded FD symbol stream for the injected lth layer and its kth symbol
$\overline{\boldsymbol{y}}_l$, $\overline{y}[k]$	The TD counterpart of $\overline{\boldsymbol{Y}}_l$ and $\overline{Y}_l[k]$
$\boldsymbol{y}_l$, $y_l[k]$	The LB clipped counterpart of $\overline{\boldsymbol{y}}_l$ and $\overline{y}[k]$

Statistical Characteristics

B_u	The upper clipping boundary of the LACO-OFDM signal
$\mathcal{D}$	The coefficient of the impulse representing UB clipping in PDF
d_min, $d_{\mathrm{min},l}$	The nearest constellation pattern distance overall, and for layer l
$\underline{\boldsymbol{I}}_l$, $\underline{I}_l[k]$	The clipping distortion created by layer l, and its kth symbol
N_0	The AWGN noise power
$\mathbb{P}_\mathrm{b}$, $\mathbb{P}_{\mathrm{b},\,l}$	The BER of the overall signal, and for layer l
$\mathbb{P}_{\mathrm{s},}$	The SER for layer l
$\mathrm{PAPR}\{\boldsymbol{x}\}$	The PAPR of signal $\boldsymbol{x}$
P_LACO	The power of an LACO-OFDM signal
$\Gamma_{\mathrm{s},\,l}$	The signal-to-noise-and-interference-plus-distortion ratio of layer l
γ_b, $\gamma_{\mathrm{b},\,l}$	The energy-per-bit-to-noise-power-spectral-density of the overall signal, and for layer l
$\mathcal{G}_l$	The ILI power generated by layer l

κ	The attenuation of signal in the UB clipping model
σ_{c}^2	The variance of the UB clipping noise in the UB clipping model
σ_l^2	The variance of the unclipped base layer LACO-OFDM TD signal $\overline{\boldsymbol{s}}_l$
τ	The UB clipping ratio

Tone Injection

$\boldsymbol{A}$	The matrix containing the real and imaginary contributions of any mapped symbol to any time slot on any layer
$c_{l,n,u}$, $g_{l,n,u}$	The real and imaginary part's contribution of the uth FD mapped symbol to the nth TD slot on layer l
$\boldsymbol{c}_{l,n}$, $\boldsymbol{g}_{l,n}$	The collection vector of $c_{l,n,u}$ and $g_{l,n,u}$ for all mapped symbols on layer l to the nth time slot
$\boldsymbol{C}_l$, $\boldsymbol{G}_l$	The collection matrix of $\boldsymbol{c}_{l,n}$ and $\boldsymbol{g}_{l,n}$ for all time slots on layer l
$\mathbb{D}$	The amount of shifting per branch for tone injection
h_w	The wth element from a random index sequence
$n^\star$	The time slot having the maximum power in LACO-OFDM TD signal
$\boldsymbol{p}$, $\boldsymbol{p}_l$, $p_{l,u}$	The Boolean indicating whether or not the real part will be shifted for all mapped symbols, the symbols on layer l, and its uth symbol
$\boldsymbol{q}$, $\boldsymbol{q}_l$, $q_{l,u}$	The Boolean indicating whether or not the imaginary part will be shifted for all mapped symbols, the symbols on layer l, and its uth symbol
t	The nominal optimisation target for the original PAPR reduction algorithm
t'	The nominal optimisation target for the simplified PAPR reduction algorithm
$\boldsymbol{v}$, v_u	The length-$(KL/2)$ vector containing all shifting Booleans $\boldsymbol{p}$ and $\boldsymbol{q}$ for the LACO-OFDM signal, and its uth element
$\boldsymbol{v}^*$	The solution vector using the simplified PAPR reduction algorithm, containing floating point numbers
$\boldsymbol{\mathcal{W}}$	The matrix restricting vector $\boldsymbol{v}$ in the simplified PAPR reduction algorithm
Z	The number of candidate vectors for PAPR reduction method
$(\cdot)^{(z)}$	A signal/sequence related to the zth candidate in the simplified PAPR reduction algorithm
z^*	The index of the solution candidate with optimum PAPR reduction performance
ρ	The scaling factor for injecting signal
$\boldsymbol{\varsigma}$	The long vector collecting the elements in the sum of the first L' layers' unclpped signals, for all possible L'

Chapter 4

Channel Capacity

$\mathsf{C}_{\text{RF}}^{\text{CCMC}}$	CCMC capacity of an RF system
$\mathsf{C}_{\text{ACO}}^{\text{CCMC}}$	CCMC Capacity of an ACO-OFDM system
$\mathsf{C}_{\text{ACO},k}^{\text{CCMC}}$	CCMC capacity of an ACO-OFDM system's kth subcarrier
$\mathsf{C}_{\text{LACO}}^{\text{CCMC}}$	CCMC Capacity of a LACO-OFDM system
$\mathsf{C}_{\text{LACO},k}^{\text{CCMC}}$	CCMC Capacity of a LACO-OFDM system's kth subcarrier
$\mathsf{C}_{\text{ACO}}^{M\text{QAM}}$	DCMC capacity of an ACO-OFDM system with MQAM constellation
$\mathsf{C}_{\text{LACO}}^{\text{DCMC}}$	DCMC capacity of a LACO-OFDM system
$\mathsf{C}_{\text{LACO}}^{\{Ml\}\text{QAM}}$	DCMC capacity of a LACO-OFDM system with $\{Ml\}$QAM constellation on each layer
$d_{l,k,m}$	The Euclidean distance between the kth received symbols on the lth layer and the mth symbol of the QAM constellation set
$E_{\text{s},k}/N_{0,k}$	The effective SNR of the kth subcarrier in the system
R, R_l	The information sink and its lth layer
$\mathsf{R}_{L\text{LACO}}^{M\text{QAM}}\Big\rvert_r$	The overall throughput (or rate) of an L-layer LACO-OFDM with MQAM constellation and FEC coding rate r
S, S_l	The information source and its lth layer
$\mathcal{S}^{\langle m\rangle}$	The mth symbol of the QAM constellation set $\mathcal{S}$
$\mathbb{W}$, $\mathbb{W}_k$	The bandwidth of the system and its kth subcarrier
$\sigma_n^2/2$	The effective AWGN power

Channel Coding

$\tilde{\boldsymbol{b}}$, $\tilde{\boldsymbol{b}}_l$	The coded bit stream and its sub-stream for layer l
$\hat{\tilde{\boldsymbol{b}}}$, $\hat{\tilde{\boldsymbol{b}}}_l$	The detected coded bit stream and its sub-stream for layer l
$\mathcal{M}$	The memory length in convolutional code
$\mathcal{I}$	The number of maximum detection iterations in turbo code

Chapter 5

C_{RF}	The DCMC capacity of an RF system
C_{ACO}	The DCMC capacity of an ACO system, an abbreviation of $\mathsf{C}_{\text{ACO}}^{M\text{QAM}}$
C_l	The DCMC capacity of the lth of a LACO-OFDM system
p_l, q_l	The left and right boundaries of the searching algorithm for optimising α_l, updated in every iteration
$\boldsymbol{s}_l^{\text{c}}$	The length-K unclipped TD signal of layer l and its nth sample before power control
$\boldsymbol{s}_l$	The length-K unclipped TD signal of layer l and its nth sample after power control
α_l, $\boldsymbol{\alpha}$	The power ratio between the first and the $(l+1)$th layer, and a vector containing all $(L-1)$ ratios
α_l^*	The optimum value of α_l

$\overline{\alpha}_l$	A temporary variable used when binary-searching α_l^*
Γ_l	The effective signal-to-noise power ratio on the lth layer
ϵ	The accuracy requirement for the searching algorithm

Declaration of Authorship

I, Xiaoyu Zhang, declare that the thesis entitled *Optical-OFDM-Aided Wireless Communications* and the work presented in the thesis are both my own, and have been generated by me as the result of my own original research. I confirm that:

- this work was done wholly or mainly while in candidature for a research degree at this University;
- where any part of this thesis has previously been submitted for a degree or any other qualification at this University or any other institution, this has been clearly stated;
- where I have consulted the published work of others, this is always clearly attributed;
- where I have quoted from the work of others, the source is always given. With the exception of such quotations, this thesis is entirely my own work;
- I have acknowledged all main sources of help;
- where the thesis is based on work done by myself jointly with others, I have made clear exactly what was done by others and what I have contributed myself;
- parts of this work have been published as: [1–3]

Signed:..

Date:...

List of Publications

1. **X. Zhang**, Q. Wang, R. Zhang, S. Chen, and L. Hanzo, “ Performance analysis of layered ACO-OFDM,” *IEEE Access*, vol. 5, pp. 18366-18381, 2017.
2. **X. Zhang**, Z. Babar, S. Chen, and L. Hanzo, “Multi-class coded layered asymmetrically clipped optical OFDM,” *IEEE Trans. Commun.*, vol. 67, no. 1, pp. 579-589, Jan. 2019.
3. Z. Babar, **X. Zhang**, P. Botsinis, D. Alanis, D. Chandra, S. X. Ng, and L. Hanzo, “Near-capacity multilayered code design for LACO-OFDM-aided optical wireless systems,” *IEEE Trans. Veh. Technol.*, vol. 68, no. 4, pp. 4051-4054, Apr. 2019.
4. **X. Zhang**, S. Chen, and L. Hanzo, “On the capacity of layered ACO-OFDM,” *J. Lightw. Technol.*, submitted.
5. C. Lacava, Z. Babar, **X. Zhang**, I. Demirtzioglou, P. Petropoulos, and L. Hanzo, “High-speed multi-layer coded adaptive LACO-OFDM and its experimental verification,” *IEEE Access*, submitted.

Acknowledgements

I would like to express my sincere appreciation and gratitude to my supervisor, Professor Lajos Hanzo, for offering me this opportunity and providing invaluable supervision, guidance and support throughout my MSc and PhD programmes. I would also like to thank my co-supervisors Professor Sheng Chen and Dr Rong Zhang, who introduced me to visible light communications and provided insightful support during my research.

Special thanks go to Dr Qi Wang and Dr Zunaira Babar, for their inspirations, collaborations and discussions. I would also like to thank Dr Cosimo Lacava and Prof Periklis Petropoulos from the Optoelectronics Research Centre, for the enjoyable collaboration memory.

I would also like to thank the people at the Next Generation Wireless (NGW) research group, notably Prof Lie-Liang Yang, Prof Robert Maunder, Dr Soon Xin Ng and Dr Mohammed El-Hajjar, for their academic support. Thanks also go to Dr Chaowen Liu, Dr Fasong Wang, Dr Peng Pan, Dr Xuan Li, Dr Tong Bai, Dr Simeng Feng, Haochen Liu, Yanqing Zhang, Shuai Shao, Yusha Liu, Luping Xiang, Dr Jiankang Zhang, Dr Chao Xu, and the rest of students, academics and secretaries in NGW, who have made it such an interesting place to work for the past four years. I would like to express my special gratitude to Dr Siyao Lu, Dr Zhenzhou Wang and their family member Nemo, for being my best friends and having my back.

I wish to thank the Engineering and Physical Sciences Research Council (EPSRC) for supporting me by the means of Internal Doctoral Scholars (IDS) grant and under grant numbers EP/M508147/1, EP/L505067/1 and EP/M50662X/1. I am also thankful for the research facilities and support provided by the staffs of the School of Electronics and Computer Science (ECS) throughout my time at Southampton, including Andreas, David and Mark from the electronics laboratory, as well as Fern, Olivia and Rob from professional services.

This thesis is dedicated to my parents for always being there for me, without whom none of this would have been possible.

Chapter 1

Introduction

1.1 Motivation

The ever-growing urban population density, the proliferation of portable devices and the demanding multimedia streaming requirements result in increased tele-traffic [4]. As a potential remedy of the spectrum-shortage, the unregulated visible light band is gaining statistical research attention as an alternative. Hence, Optical Wireless Communication (OWC) is expected to play a role as a potential component of next generation wireless systems [5–7], given that the substantial unlicensed visible light band spanning roughly between 400 and 800 THz band can be readily exploited by low-cost off-the-shelf transmitters, such as Light-Emitting Diodes (LEDs) [8]. Therefore, extensive investigations have been dedicated to the physical layer of OWC [9–16].

As an attractive modulation technique originally conceived in 1966 [17], Orthogonal Frequency Division Multiplexing (OFDM) has been widely researched and developed for Radio Frequency (RF) applications [18–21]. As an off-shoot of RF-OFDM, Optical OFDM (O-OFDM) has been proposed for the Visible Light Communications (VLC) downlink, as a benefit of its ability to mitigate the multipath-induced inter-symbol interference [22]. However, O-OFDM has had a shorter history than RF-OFDM [7, 22–24]. There are significant differences between the physical layer of the O-OFDM and RF-OFDM systems, which are summarised in Tab. 1.1.

This treatise is dedicated to the further development of O-OFDM systems. The rest of this chapter is organised as follows. In Sec. 1.2, we review the development of O-OFDM, while in Sec. 1.3, we continue by surveying the evolution of Layered Asymmetrically Clipped O-OFDM (LACO-OFDM), which is the main topic of this thesis. Finally, our novel contributions and an outline of this thesis are presented in Sec 1.4.

Table 1.1: Comparison of typical system characteristics in RF-OFDM and OWC

Topic	RF-OFDM	OWC
TX Signal	bipolar and complex-valued	unipolar
Media	RF electromagnetic waves	lightwave
Detection	(majorly) coherent	direct detection

1.2 Development of O-OFDM

1.2.1 A Problem of Unipolarity

In [25], Kahn and Barry characterised the physical behaviour of infrared channels using Intensity Modulation with Direct Detection (IM/DD). In IM/DD systems, the signal to be transmitted modulates the optical power of the emitted lightwave. At the receiver, a Photo Detector (PD) is used for converting the optical signal into electronic current for representing the received signal. The resultant IM/DD systems have been widely employed both in optical wireless [4, 8] and in fibre-optic communications [26].

However, the optical signals must be real- and positive-valued, whereas conventional baseband OFDM signals relying on Fast Fourier Transform (FFT)-based modulation are typically bipolar- and complex-valued. As shown in Appendix A, upon satisfying the constraint of Hermitian symmetry in the Frequency Domain (FD), the Time Domain (TD) counterpart of the OFDM signal after Inverse FFT (IFFT) is guaranteed to be real-valued, but we still have to eliminate the negative samples.

To circumvent this problem, DC-Biased Optical OFDM (DCO-OFDM) [27, 28] and Asymmetrically Clipped OFDM (ACO-OFDM) [29, 30] have been proposed, which are introduced here.

1.2.2 DCO-OFDM vs ACO-OFDM

Carruthers and Kahn [27] have proposed to positively bias the bipolar real-valued signal generated after satisfying the Hermitian symmetry with the aid of a DC component, so that the signal became positive, hence the terminology of DCO-OFDM. Since the magnitude of the signal is randomly distributed, some small residual negative samples may persist after adding the DC offset. Therefore, the DC offset to be used must be carefully decided, so that the damage to the integrity of the information conveyed remains negligible after clipping the negative residual samples. As a common practice [30], the DC offset of DCO-OFDM is typically in excess of 10 dB. Various experiments have been conducted using DCO-OFDM in different scenarios, such as Free-Space Optical (FSO) wireless [31–33] and optical fibre [34, 35].

In order to avoid the above-mentioned substantial power-loss imposed by the DC-bias, Armstrong and Lowery [29] proposed the ACO-OFDM concept, where the bipolar modulated signal is directly clipped at zero after IFFT. Explicitly, this is achieved by arranging for the FD OFDM signals that only their odd-indexed subcarriers are non-zero, hence creating an opportunity for all the distortions generated by clipping the negative samples to fall solely on the even-indexed ones. This specific measure allows ACO-OFDM to retain information integrity, despite the drastic clipping process. Armstrong *et al.* [36] as well as Armstrong and Schmidt [30] carried out the Bit Error Ratio (BER) performance analysis of ACO-OFDM and DCO-OFDM, respectively, and compared their optical efficiency to that of on-off keying (OOK). In [37], the clipping distortions encountered both by DCO-OFDM and ACO-OFDM were also taken into consideration by Dimitrov *et al.*, and the clipping effects together with the associated BER expression for transmission both over Additive White Gaussian Noise (AWGN) and over fading channels were also provided. Experiments have also been conducted for evaluating the performance of ACO-OFDM and for comparing it against that of DCO-OFDM [38–40].

Moreover, we would also like to mention that similar characteristic features are exhibited by the Pulse-Amplitude-Modulated Discrete MultiTone (PAM-DMT) scheme, where the imaginary part of all subcarriers is actively modulated, while the real part is left blank [41]. The performance of PAM-DMT was compared to that of ACO-OFDM and other optical schemes in [42], where PAM-DMT and ACO-OFDM have been found to perform similarly. Other diverse schemes have also been advocated for avoiding the DC energy wastage, such as Flip-OFDM/U-OFDM [43, 44], which transmit the positive and inverted negative parts of the real-valued symbols separately in the TD .

1.2.3 Power- vs Spectrum-Efficiency

Again, DCO-OFDM meets the unipolar requirement by dissipating a large amount of DC power for offsetting the negative TD samples, which is clearly inefficient. Hence, ACO-OFDM was proposed as an alternative solution requiring a reduced power, which is achieved by halving its effective throughput.

Table 1.2 summarises the pros and cons of DCO-OFDM and ACO-OFDM. More explicitly, Fig. 1.1 portrays the Spectral Efficiency (SE) and Power Efficiency (PE) of the two schemes under same bandwidth and modulation constellation (64QAM). Observe from Fig. 1.1 that huge gaps exist between DCO-OFDM and ACO-OFDM.

Table 1.2: Pros and Cons of DCO- and ACO-OFDM Schemes

Scheme	Power Domain	Spectrum Domain
DCO-OFDM	Less efficient due to DC offset	Half of the subcarriers are information-bearing
ACO-OFDM	Efficient thanks to the absence of DC offset	A quarter of the subcarriers are information-bearing

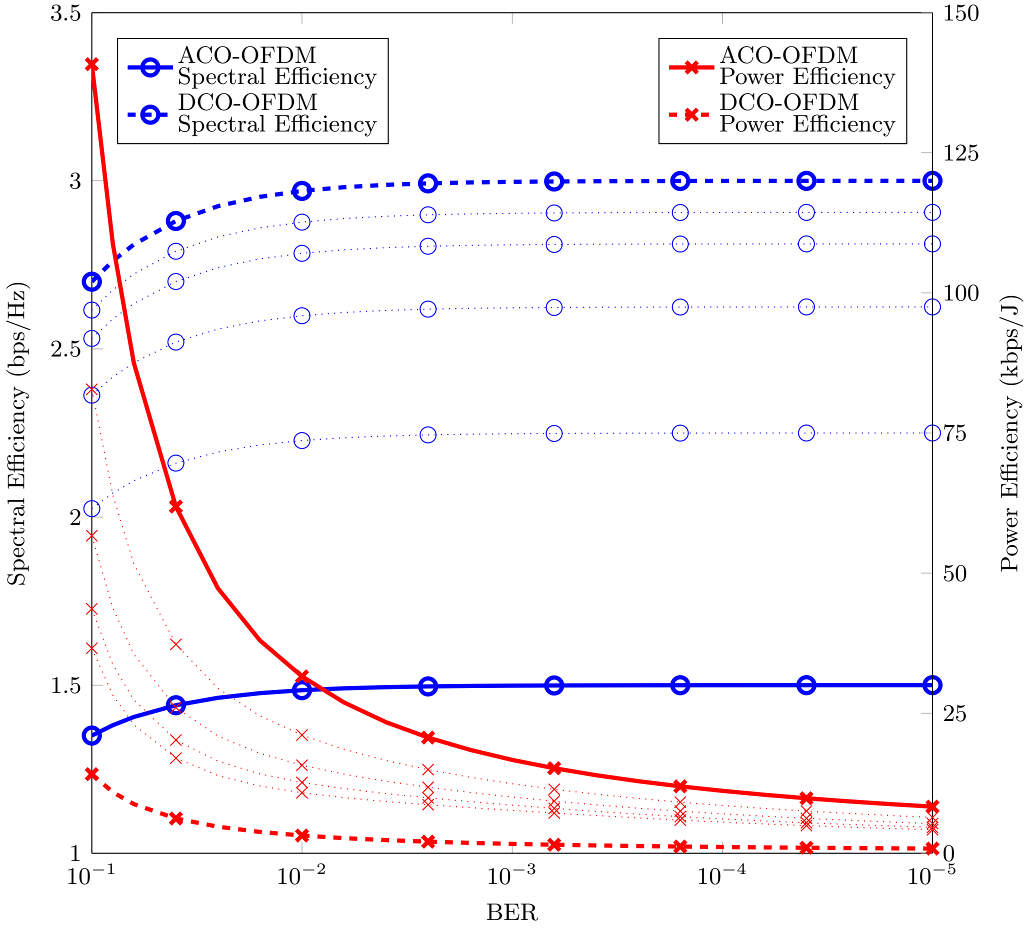

Figure 1.1: Comparison of spectrum and power efficiency for ACO-OFDM (solid lines) and DCO-OFDM (dashed lines). Blue lines marked by circles and scaled on the left axis represent the spectral efficiency, while those in red, marked by crosses and scaled on the right axis represent power efficiency. In addition, some dotted lines are depicted to indicate possible trade-offs. The data are obtained for 64QAM modulation and the DC offset for DCO-OFDM is 13 dB based on [30].

1.2.4 A Hybrid Solution

Naturally, the power saved by using blank subcarriers may be invested into the active subcarriers, either for reducing their BER or for enhancing their throughput, which is a common practice in improving the performance in the literature [45, 46]. As a compromise, a small amount of the power conserved by ACO-OFDM can be assigned to transmit additional information on the idle subcarriers, in order to increase the spectral efficiency, at the cost of degrading the power efficiency. In Fig. 1.1, the compromise solutions are marked by dotted lines between ACO-OFDM and DCO-OFDM.

In terms of practical implementation, a great variety of designs can be found in the literature. They are commonly termed as hybrid schemes, since they tend to have multiple basic unipolar OFDM schemes (*e.g.* ACO-OFDM, DCO-OFDM, PAM-DMT, *etc.*) in their structures. The Asymmetrically Clipped DC Biased Optical OFDM (ADO-OFDM) scheme was proposed by Dissanayake *et al.* [47], which utilises both ACO- and DCO- OFDM by multiplexing the two schemes in the FD. In [48], ADO-OFDM was analysed and its performance was compared to that of ACO-OFDM and DCO-OFDM. Relying on a similar multiplexing philosophy, Ranjha and Kavehrad [49] proposed the Hybrid Asymmetrically Clipped Optical OFDM (HACO-OFDM) scheme, combining ACO-OFDM and PAM-DMT. In [50], a more advanced hybrid system combining ACO-OFDM and PAM-DMT was proposed, under the terminology of Asymmetrical Hybrid Optical OFDM (AHO-OFDM). In contrast to HACO-OFDM, one of the two constituent signals in AHO-OFDM must be inverted, yielding a bipolar signal, which requires additional DC bias for eliminating the negative samples. AHO-OFDM is considered to be more flexible and more spectral-efficient than HACO-OFDM, which is a benefit of both its ability to adjust the power ratio between the constituent ACO-OFDM and PAM-DMT schemes, as well as owing to the full utilisation of all the subcarriers with the aid of its DC offset. Moreover, Asymmetrically and Symmetrically Clipped Optical OFDM (ASCO-OFDM) was proposed by Wu and Bar-Ness [51], which relies on an idea equivalent to multiplexing ACO-OFDM and Flip-OFDM in the FD. In [52], a pair of hybrid schemes, namely the Absolute Value Optical OFDM (AVO-OFDM) and Asymmetrically Clipped Absolute Value Optical OFDM (AAO-OFDM) were proposed. The AVO-OFDM scheme transmits the absolute value of the bipolar Hermitian-symmetry-constrained signal and uses additional resources to transmit their sign information. On the other hand, AAO-OFDM amalgamates AVO-OFDM and ACO-OFDM for attaining an improved performance.

Before we proceed, Tab 1.3 summaries all the O-OFDM schemes[1] that have been mentioned up to this stage. The last column of Tab 1.3 shows the corresponding typical spectral efficiency, when compared to its RF counterpart having the same bandwidth. Observe from Tab 1.3 that

---

[1] PAM-DMT is classified here as an O-OFDM for the sake of comparison.

Table 1.3: List of Basic and Hybrid O-OFDM Schemes Introduced

Nature	Time	Ref.	Name	Design	SE
Basic	Apr. 1996	[27]	DCO-OFDM	DC offset	$\frac{1}{2}$
	Mar. 2006	[29]	ACO-OFDM	Clipping at zero, idle subcarrier for distortion	$\frac{1}{4}$
	Dec. 2009	[41]	PAM-DMT	Clipping at zero, only imaginary part in FD	$\frac{1}{4}$
	May. 2012	[44]	U-OFDM	Transmit positive and negative parts separately	$\frac{1}{4}$
	Dec. 2012	[43]	Flip-OFDM	Transmit positive and negative parts separately	$\frac{1}{4}$
	Sep. 2017	[52]	AVO-OFDM	Transmit magnitude and sign parts separately	$< \frac{1}{2}$
Hybrid	Dec. 2011	[47]	ADO-OFDM	ACO-OFDM + DCO-OFDM	$\frac{1}{2}$
	Apr. 2014	[49]	HACO-OFDM	ACO-OFDM + PAM-DMT	$\frac{3}{8}$
	Jan. 2015	[51]	ASCO-OFDM	ACO-OFDM + Flip-OFDM	$\frac{3}{8}$
	May 2015	[50]	AHO-OFDM	ACO-OFDM + PAM-DMT + DC	$\frac{1}{2}$
	Sep. 2017	[52]	AAO-OFDM	ACO-OFDM + AVO-OFDM	$< \frac{1}{2}$

- Only DCO-OFDM as well as the hybrid schemes relying on it, and AHO-OFDM can achieve the SE of $\frac{1}{2}$, but unfortunately all of them require DC offset;
- The hybrid schemes have fixed SE values, which is dependent on the specific choice of its constituent schemes.

A further design option is contributed by the recently proposed Layered ACO-OFDM (LACO-OFDM) [53], which populates the idle subcarriers of ACO-OFDM by creating an additional layer and mapping an extra set of symbols to the originally un-populated positions of the ACO-OFDM scheme. To elaborate further, in the next section, we survey the evolution of LACO-OFDM.

1.3 Survey of Layered ACO-OFDM

In this section, we review the propositions and recent developments of LACO-OFDM, which are summarised below in Tab. 1.4, where the dates of publications and their main contributions are listed.

Table 1.4: Research Timeline

May 2015	[53]	The proposition of LACO-OFDM
Jun. 2015	[54]	Independent proposition of SEE-OFDM
Dec. 2015	[55]	Independent proposition of eACO-OFDM
Feb. 2016	[56]	Improved clipping distortion cancellation at RX
Mar. 2016	[57]	Independent proposition of EACO-OFDM
Jun. 2017	[58]	RX with diversity combining and SIC
	[59]	RX with diversity combining and clipping distortion recovery
	[60]	Performance analysis and comparison
Aug. 2017	[1]	Performance analysis and PAPR reduction
Sep. 2017	[61]	Channel coding and experiment
Dec. 2017	[62]	Capacity analysis and adaptive modulation
Jan. 2018	[63]	SCFDM and reduced PAPR
Apr. 2018	[64]	Capacity analysis
Jun. 2018	[65]	Improved RX with SIC
Oct. 2018	[66]	Performance analysis
Jan. 2019	[67]	Improved RX on clipping noise mitigation
	[2]	Capacity analysis, channel coding
Mar. 2019	[68]	NOMA and network scheduling
	[69]	NOMA and HPD-LACO-OFDM
Apr. 2019	[3]	Channel coding

1.3.1 Philosophy

The LACO-OFDM architecture is constructed from ACO-OFDM, which was proposed by Armstrong [29]. In the FD, the second half of the subcarriers of an ACO-OFDM signal are the conjugate complex counterpart of the first half, which satisfies the Hermitian symmetry and results in a real-valued TD signal. The negative-valued samples in the TD signal are clipped at a lower boundary (LB clipping), so that the signal becomes suitable for IM/DD transmission. Moreover, only the subcarriers having odd-valued indices are modulated, while the even-indexed ones are left blank for accommodating the clipping distortion generated by the previous clipping process, which would otherwise contaminate the subcarrier. Therefore, at the receiver, the first half of the even-indexed subcarriers can be straightforwardly extracted after FFT.

In LACO-OFDM, the transmitter loads an additional signal on the even-indexed subcarriers of an ACO-OFDM signal, using the same ACO-OFDM principle mentioned above, but with only half the length, which makes up a second layer. This justifies the terminology of layered ACO-OFDM. On the second layer, these signals occupy every other even-indexed subcarrier and have only half the length of the signals on the first layer. In order to improve the SE of the OFDM signal, this process can continue with further layers added to the LACO-OFDM structure, with each layer occupying half the number of subcarriers of the preceding one. In this manner, the signals and their clipping distortion can be removed from the structure layer-by-layer at the receiver and the signal can be detected. However, due to external influences, such as thermal noise, the detection may not be perfect. This would lead to an unclear clipping distortion cancellation, defined as the Inter-Layer Interference (ILI), which in turn further degrades the performance of the higher layers.

The LACO-OFDM signal is subject to clipping at an upper boundary (UB clipping), due to the linearity limitation of the optical devices. This process causes further distortion, which may be reduced when the signal has a lower Peak-to-Average Power Ratio (PAPR).

1.3.2 Developments

The original concept of LACO-OFDM was published by Wang *et al.* [53] in May 2015. They quantified the spectral efficiency improvement attained by LACO-OFDM, which eventually converges to that of the DCO-OFDM scheme, as the number of layers is increased. The BER performance for transmission over AWGN channels under limited electric and optical powers was also quantified.

Interestingly, during the same time period, three other independently proposed schemes utilising a similar philosophy were reported in the literature.

- Elgala and Little [54] quantified both the throughput and PAPR of their scheme, which was termed as spectral- and energy-efficient OFDM (SEE-OFDM).
- As a further development, in [55] the idea of superimposing multiple streams was proposed by Islim *et al.*, which was then applied to ACO-OFDM. The authors studied the spectral efficiency of the superimposed signal, where the length of the OFDM Cyclic Prefix (CP) was also considered. It was demonstrated that the SE approached that of the DCO-OFDM. Therefore, they referred to this scheme as enhanced ACO-OFDM (eACO-OFDM). The BER performance of eACO-OFDM

was also studied and it was contrasted to that of DCO-OFDM and ePAM-DMT [70].

- Finally, Lowery [57] metaphorised the symbol-to-subcarrier loading process as the arrangement of notes into chords of different octaves in music. On a particular octave, only specific harmonics could be loaded with notes, which resembled the ACO-OFDM philosophy. The SE improvement attained was calculated and compared to that of ACO-OFDM, leading to the terminology of Enhanced ACO-OFDM (EACO-OFDM). The performance of EACO-OFDM was characterised by the Error Vector Magnitude (EVM) metric through simulations and it was contrasted to both PAM-DMT and ADO-OFDM.

1.3.3 Improvements

Several research studies have been carried out since 2017 in order to improve the performance of LACO-OFDM, which are surveyed below.

1.3.3.1 LB Clipping Distortion and ILI

Wang *et al.* [56] provided an improved LACO-OFDM receiver by further exploring the characteristics of the TD LACO-OFDM signals. The original receiver of [53] detects the signal from layer 1 upwards to layer L, successively cancelling out the distortion generated by each layer after detecting and re-modulating it. By contrast, the receiver proposed in [56] conducts an additional round of interference cancellation for improving the attainable BER at the cost of an increased complexity.

When cancelling out the clipping distortion imposed on each layer, the original receiver of [53] relied on hard decisions. In doing so, the receiver re-maps the detected bits of each layer back to QAM symbols for reproducing the clipping distortion. By contrast, in [58], Wang *et al.* used soft-decision-based Successive Interference Cancellation (SIC) at the receiver. The soft-value of each bit is used for reproducing the clipping distortion, rather than the bits after hard-decisions. Simulations were performed for characterising the scheme advocated, demonstrating that this scheme mitigated the error propagation imposed by hard-decisions. This scheme was even further improved by Wang *et al.* [58], resulting in reduced residual interference and an improved BER. As a further development, Mohammed *et al.* [59] proposed to use diversity combining for improving the performance. Simulations were conducted for transmission over both flat and frequency selective channels to verify the improved BER performance.

In [69], Li *et al.* improved the transmitter signal processing of the LACO-OFDM signal. Explicitly, in their TX design, the higher layer signals were pre-distorted by subtracting the clipping distortions of the previous layers from the signal before LB clipping. Therefore, the signals became free from clipping distortion contamination at the receiver side and all layers were directly detected. This new scheme was referred to as Hierarchical Pre-Distorted LACO-OFDM (HPD-LACO-OFDM). Their solution prevented the error propagation from the transmitter side and resulted in outstanding BER performance, despite its complexity reduction at the RX.

1.3.3.2 UB Clipping Distortion and PAPR

Sun *et al.* [60] analysed the Probability Density Function (PDF), PAPR as well as the BER performance of LACO-OFDM, and compared its performance to both ADO-OFDM [47] and HACO-OFDM [49].

Zhang *et al.* [1] studied the performance of LACO-OFDM and provided the mathematical expressions of the BER and PAPR, where UB clipping was considered. A novel PAPR reduction method was also proposed for improving the performance attained. Simulations were conducted for verifying the accuracy of the formulae derived.

In [63], Zhou *et al.* designed a layered scheme similar to LACO-OFDM. Instead of using QAM based ACO-OFDM on each layer as in the original LACO-OFDM [53], the scheme of [63] applied Discrete Hartley Transform (DHT)-based OFDM for PAM symbols on each layer, resulting in Single-Carrier Frequency Domain Multiplexed (SCFDM) layered signals. These signals were then clipped and superimposed in the TX. At the receiver, they were detected in the same way as in the original LACO-OFDM of [53]. Finally, its performance analysis was carried out for demonstrating its reduced computational complexity and PAPR, while the simulations provided revealed its higher immunity to both transmitter nonlinearity and to the multi-path fading.

In [67], Wang *et al.* studied the UB clipping distortion in LACO-OFDM by modelling the distortions imposed on each layer using Bussgang's theorem, which led to an accurate mathematical expression of the distortion. Using the results derived, an improved LACO-OFDM receiver was proposed, which is capable of identifying the peaks that are UB-clipped and therefore it makes improved decisions. Their simulations demonstrated the improved BER performance under clipping.

1.3.3.3 Multi-User system

In [68], a multi-user LACO-OFDM scheme was proposed by Feng *et al.* based on the Non-Orthogonal Multiple Access (NOMA) concept, where the signal of the users superimposed at different powers was separated in the power domain on each layer. At the receiver, the detector employed a pair of nested loops, where the inner loop processed the signal of the different users as in conventional RF-NOMA, while the outer loop mitigated the clipping distortion and ILI, as in single-user LACO-OFDM. The problems of power sharing and user-scheduling were also solved and the simulation results verified the accuracy of the theory.

In [69], Li *et al*. applied NOMA to their proposed HPD-LACO-OFDM (mentioned in Sec. 1.3.3.1) in the same manner as in [68], but succeeded in mitigating the source of ILI, which is a benefit brought about by the pre-distortion invoked at the TX. Hence, they improved the BER performance in their conventional NOMA LACO-OFDM benchmark system.

1.3.3.4 Capacity and Coding

Song *et al*. [61] considered an optical fibre system using LACO-OFDM. Convincing hardware experiments were conducted for demonstrating an improved BER performance both on a layer basis and overall. Yang *et al*. [62] analysed the channel capacity of LACO-OFDM for different numbers of layers and provided numerical results. An adaptive modulation scheme was also proposed by varying the number of layers modulated in LACO-OFDM for maximising the capacity of the system.

Zhou and Zhang [64] compared the performance in the face of Gaussian optical intensity channel for a variety of unipolar OFDM schemes, ranging from single-component ones like ACO- and DCO-OFDM, to the multiplexing-based ones like ADO- and LACO-OFDM. Closed-form expressions were derived for their information rates and comprehensive simulations were provided for comparing their behaviour for different parameter sets.

Sun *et al*. [66] quantified both the spectral- and energy-efficiency of different O-OFDM schemes, including PAM-DMT [41], ACO- [29], DCO- [27], ADO- [47], HACO- [49] and LACO-OFDM [53]. The performance of each scheme was then compared to one another under an AWGN channel using both theoretical analysis and simulations, while the DC gain and other hardware-related parameters were also considered.

Zhang *et al*. [2] derived the achievable rate of LACO-OFDM for the modulation schemes considered. A multi-class coding architecture was then conceived for LACO-OFDM, where the Forward Error Correction (FEC) components were embeded into the layered system and the attainable performance was quantified. A sophisticated multilayered channel coding was conceived for LACO-OFDM by Babar *et al*. [3], where the protection was established not only within each separate layer, but also across different layers. Hence, a near-capacity performance was attained.

1.4 Thesis Outline and Novel Contributions

1.4.1 Outline of the Thesis

Figure 1.2 portrays the outline of this thesis, which includes the following highlights:

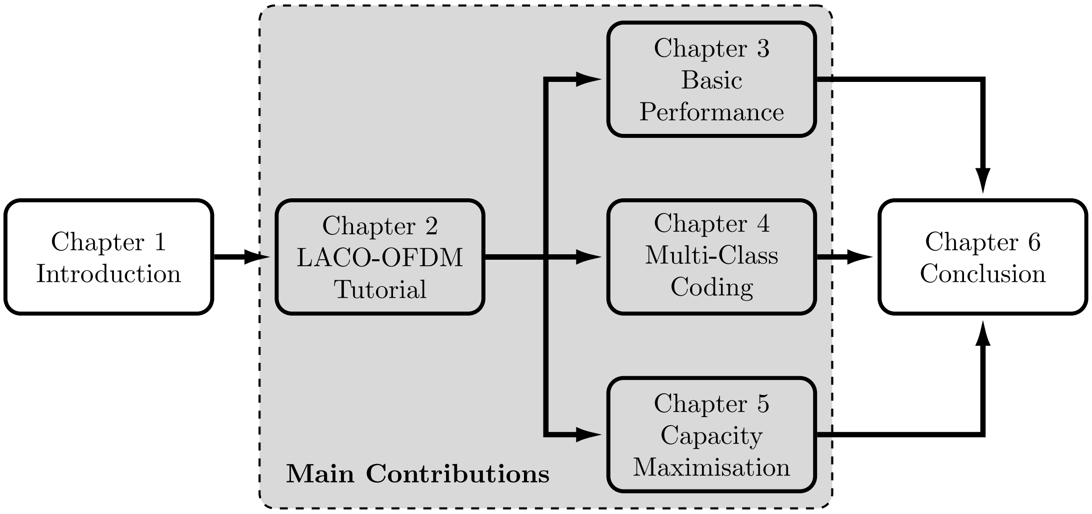

Figure 1.2: Organisation of the thesis.

- **Chapter 2:** A Tutorial on LACO-OFDM
  In this chapter, we present a detailed tutorial introduction to ACO-OFDM and LACO-OFDM. Explicitly, we present the spectral-domain and time-domain characteristics of both the constituent layers and the of superimposed signal, accompanied by detailed mathematical proofs and examples. We also briefly introduce the power allocation strategy that is conventionally adopted generally.

- **Chapter 3:** Basic Performance Analysis and Improvements of LACO-OFDM
  In this chapter, we provide a comprehensive performance analysis of the LACO-OFDM system presented in Chapter 2, including its BER and PAPR performance. Meanwhile, a method to reduce the PAPR of LACO-OFDM is also proposed and verified by simulation.

- **Chapter 4:** Multi-Class Coded LACO-OFDM
  With the uncoded BER performance detailed in Chapter 3, we now focus our attention on designing a dedicated channel coding scheme for LACO-OFDM. We commence with the channel capacity analysis of LACO-OFDM. First, a conceptually straightforward but naïve single-class coding system is proposed and evaluated, followed by a discussion of its impediments. Then, a more sophisticated multi-class coding scheme is proposed for enhancing the attainable performance, which lends itself to harmonised integration with the layered structure of LACO-OFDM in both of its TX and RX design. A log-likelihood-based layer detection

and distortion cancellation method is also proposed for improving the performance attained. Finally, the performance of the proposed system is contrasted to that of its single-class counterpart, as well as to the uncoded system.

- **Chapter 5:** Optimum Power Allocation in LACO-OFDM
  In Chapter 5, we improve the capacity by quantifying the relationship between the LACO-OFDM DCMC capacity and its layer-power allocation strategy. The maximum attainable capacity is quantified for different number of layers. Moreover, we propose an adaptive scheme for deciding on how many layers to use for LACO-OFDM under certain channel conditions, in order to maximise the overall capacity.

Finally, Chapter 6 summaries the findings of the thesis, and offers a range of future research ideas.

1.4.2 Novel Contributions of the Thesis

The novel contributions of this theses are listed as follows.

1. A survey of the short but rapidly-evolving history of LACO-OFDM is provided.
2. The BER performance of LACO-OFDM is analysed in the face of thermal noise, ILI and clipping distortion [1]. The bit rate difference between layers is also quantified and its BER expression is provided, which suggests that the clipping distortion becomes a major performance-limiting factor in the high-SNR region.
3. A novel PAPR reduction method based on tone-injection is also proposed for improving the performance of LACO-OFDM, which relies on formulating an optimisation problem that may be solved by off-the-shelf tools, regardless of the number of layers [1].
4. We quantify the achievable rate of LACO-OFDM systems relying on different modulation schemes and different number of layers, which is based both on the theoretical mutual information and on our simulations [2].
5. We conceive a novel FEC coded LACO-OFDM system, which intrinsically amalgamates the classic FEC codes with our LACO-OFDM system [2]. Our results demonstrate that the proposed coded LACO-OFDM system significantly outperforms the benchmark system consisting of a separate FEC and LACO-OFDM scheme in terms of its BER performance.
6. We further analyse the layered BER of the proposed coded system [2]. It is demonstrated that the proposed coded LACO-OFDM system is capable of drastically reducing the ILI. Quantitatively, the coded LACO-OFDM system relying on 4-layer

16QAM LACO-OFDM and turbo coding (8-iteration) completely eliminates the ILI at $E_b/N_0 = 10$ dB, which is 9 dB lower than that of the uncoded system.

7. We derive the DCMC capacity of LACO-OFDM as a function of the Signal to Noise Ratio (SNR) and the number of layers in the system, as well as the power sharing amongst the layers.

8. We provide an algorithm for determining the optimum power allocation strategy for twin-layer LACO-OFDM at a given SNR, followed by our generalised algorithm suitable for an arbitrary number of layers.

9. Finally, we compare the optimised capacities of LACO-OFDM systems relying on different number of layers, which leads to an adaptive scheme using the optimum number of layers maximising the capacity at a given SNR.

Chapter 2

A Tutorial on LACO-OFDM

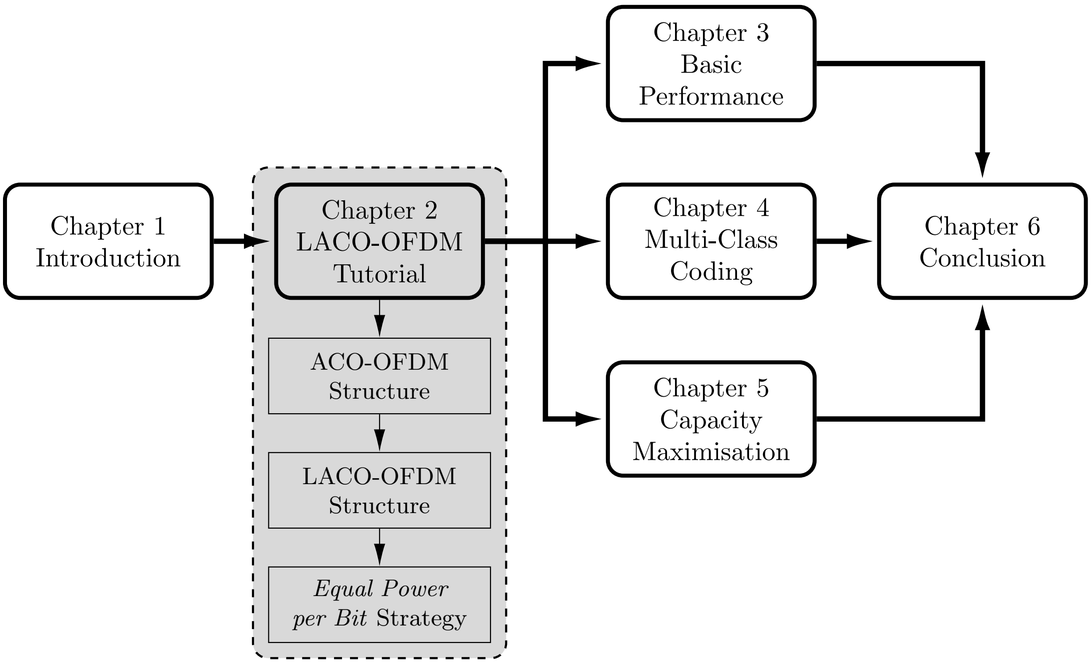

Figure 2.1: Linkage of Chapter 2 with the thesis structure.

2.1 Introduction

Before commencing our detailed performance analysis, this chapter presents a tutorial on the basic LACO-OFDM transceiver design, followed by the introduction of the basic concepts and notations to be used throughout this thesis.

In Sec. 2.2, the transmitter and receiver structures are presented, complemented by a detailed example of its operation. The ACO-OFDM architecture constitutes the root of the LACO-OFDM scheme introduced in Sec. 2.3, where the associated transmitters and receivers are introduced and compared. These discussions are followed by detailed step-by-step examples of the LACO-OFDM operations. Then, Sec. 2.4 describes the most commonly adopted power allocation strategy of LACO-OFDM. Finally, Sec. 2.5 summarises in this chapter.

2.2 The ACO-OFDM Scheme

2.2.1 ACO-OFDM Transmitter

Figure 2.2 shows the general schematic of the ACO-OFDM transmitter, relying on M-ary quadrature amplitude modulation (MQAM). The input bit stream $\boldsymbol{b}$ of length B is mapped onto the complex FD symbols $\boldsymbol{S}$ based on a given MQAM constellation $\mathcal{S}$. This provides a total of $B/\log_2 M$ complex symbols, which, together with their $B/\log_2 M$ conjugate counterparts and with the additional $2B/\log_2 M$ null placeholder symbols, are then mapped onto $K = 4B/\log_2 M$ subcarriers $\overline{\boldsymbol{S}}$ as follows:

$$\begin{gathered}\overline{S}[k] = \begin{cases} S[u], & k = 2u+1, \\ S^*[u], & k = K-(2u+1), \\ 0, & \text{otherwise}, \end{cases} \\ 0 \leq u \leq \tfrac{K}{4} \qquad \text{and} \qquad 0 \leq k \leq K-1, \end{gathered} \tag{2.1}$$

where * denotes the conjugate of a complex number.

Since the FD symbols $\overline{\boldsymbol{S}}$ obey Hermitian symmetry, the TD signal $\overline{\boldsymbol{s}}$ obtained after IFFT becomes real-valued and anti-symmetric, *i.e.* we have:

$$-\,\overline{s}\,[n] = \overline{s}\left[\frac{K}{2} + n\right], \qquad 0 \leq k < \frac{K}{2}. \tag{2.2}$$

Detailed mathematical proof of this property is provided in Appendix A.1. Therefore, all negative samples of $\overline{\boldsymbol{s}}$ can be dropped without losing information. The resultant non-negative electric signal $\boldsymbol{s}$ is converted into optical signal and emitted through an LED.

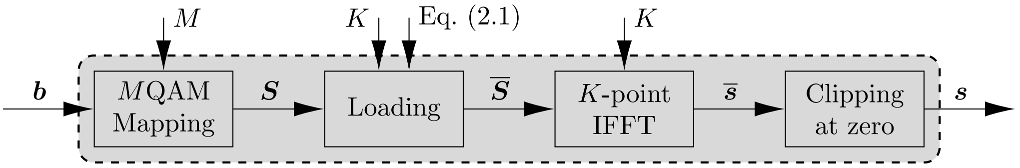

Figure 2.2: An ACO-OFDM transmitter block (ACO TX).

2.2.2 ACO-OFDM Signals

In Fig. 2.3, an example is provided for further illustrating the signal processing operations of an ACO-OFDM transmitter. In the example given, the system has a total of 16 subcarriers, hence capable of conveying 4 symbols per OFDM block.

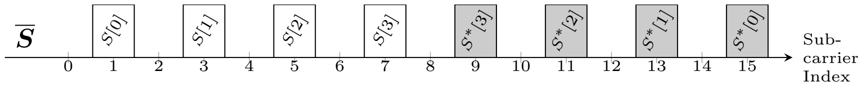

(a) Loaded FD Signal

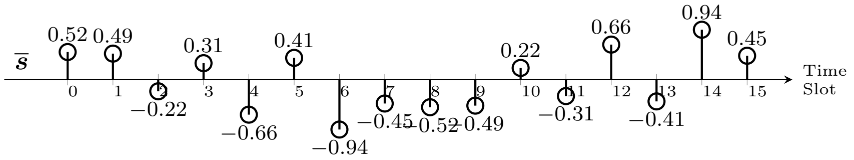

(b) Loaded TD Signal

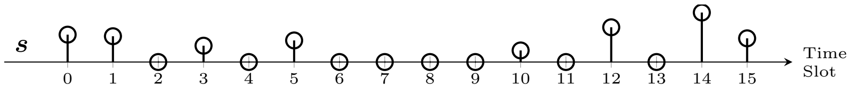

(c) Clipped TD Signal

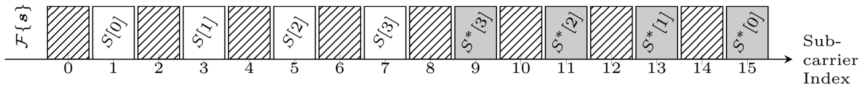

(d) Clipped FD Signal, where the hatched boxes represent clipping distortion

Figure 2.3: Example of ACO-OFDM TX process signal flow.

Figure 2.3(a) shows the FD representation of the signal $\overline{\boldsymbol{S}}$. It becomes clear in Fig. 2.3(a) that the requirements of Hermitian symmetry and blank subcarrier between every pair of subcarriers specified by Eq. (2.1) are strictly followed. As a result, the TD counterpart $\overline{\boldsymbol{s}}$ of the FD signal $\overline{\boldsymbol{S}}$ behaves exactly as portrayed Eq. (2.2). In Fig. 2.3(b), example data samples are provided to verify this property at a glance. Bear in mind that all TD samples in Fig. 2.3(b) are real-valued. The TD and FD views of the clipped signal $\boldsymbol{s}$ are provided in Figs. 2.3(c) and 2.3(d), respectively. It can be seen from Fig. 2.3(d) that all clipping distortions fall on the subcarriers having even indices, as elaborated on in Appendix A.1.

2.2.3 ACO-OFDM Receiver

Figure 2.4 shows the schematic of the ACO-OFDM receiver.

The received signal $\boldsymbol{r}$ seen in Fig. 2.4 is firstly passed through the FFT to obtain the corresponding FD signal $\overline{\boldsymbol{R}}$. Since the negative clipping distortion only falls on the even-indexed blank subcarriers ($k = 2u$), the desired information can be extracted from the

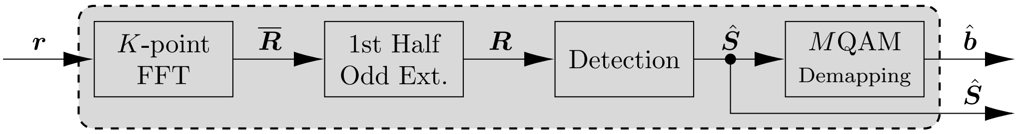

Figure 2.4: An ACO-OFDM receiver block (ACO RX).

first half odd-indexed subcarriers, *i.e.*

$$R[u] = \overline{R}[2u+1], \qquad 0 \leq u \leq \left(\frac{K}{4} - 1\right). \tag{2.3}$$

The information symbols $\hat{\boldsymbol{S}}$ of Fig. 2.4 are then detected from the symbols $\boldsymbol{R}$ based on the constellation $\mathcal{S}$, which is formulated as

$$\hat{S}[u] = \arg\min_{X \in \mathcal{S}} \left|X - 2\overline{R}[u]\right|, \qquad 0 \leq u \leq \left(\frac{K}{4} - 1\right), \tag{2.4}$$

where the multiplicative factor of 2 for $\overline{\boldsymbol{R}}$ compensates the signal power halving during in the clipping process. Finally, the bit stream $\hat{\boldsymbol{b}}$ is obtained at the receiver by mapping the symbols $\hat{\boldsymbol{S}}$ back to bits, as seen in Fig. 2.4.

It is worth noting that the ACO RX block of Fig. 2.4 has both $\hat{\boldsymbol{b}}$ and $\hat{\boldsymbol{S}}$ as its output, where the latter will be used in due course.

2.3 The LACO-OFDM Scheme

In this section, we introduce the architecture of LACO-OFDM transceivers, which is based on the ACO-OFDM structures described in Sec. 2.2. We will present two different designs for the LACO-OFDM transmitters and receivers, respectively, and discuss their difference, followed by our detailed examples.

2.3.1 LACO-OFDM Transmitter

The LACO-OFDM framework utilises the blank even-indexed subcarriers ($k = 2u$) of the classic ACO-OFDM frame for transmitting additional layers of ACO-OFDM symbols, since clipping distortion only exists at the even indices, which can be removed at the receiver. Explicitly, the classic ACO-OFDM relying on K_1-point IFFT/FFT constitutes the first layer ($l = 1$, hereinafter refers to as 'layer 1'). The $K_2 = K_1/2$ blank subcarriers of layer 1 are then filled by the *second* layer ($l = 2$, hereinafter refers to as 'layer 2') ACO-OFDM symbol, relying on K_2-point IFFT/FFT. Similarly, additional ACO-OFDM layers can be added, so that the number of subcarriers occupied by layer l is

$$K_l = \frac{K_1}{2^{l-1}}. \tag{2.5}$$

Below we present a pair of LACO-OFDM transmitters found in the literature, before discussing their pros and cons. The detailed mathematical proof that these two models are equivalent and produce exactly the same LACO-OFDM signal can be found in Appendix A.2.

2.3.1.1 Transmitter Model 1

Figure 2.5 shows the block diagram of a LACO-OFDM transmitter consisting of L ACO-OFDM blocks as its basic units. The serial input bit stream is firstly split into L parallel streams, corresponding to the L layers, each of which is independently fed to an ACO-OFDM TX unit.

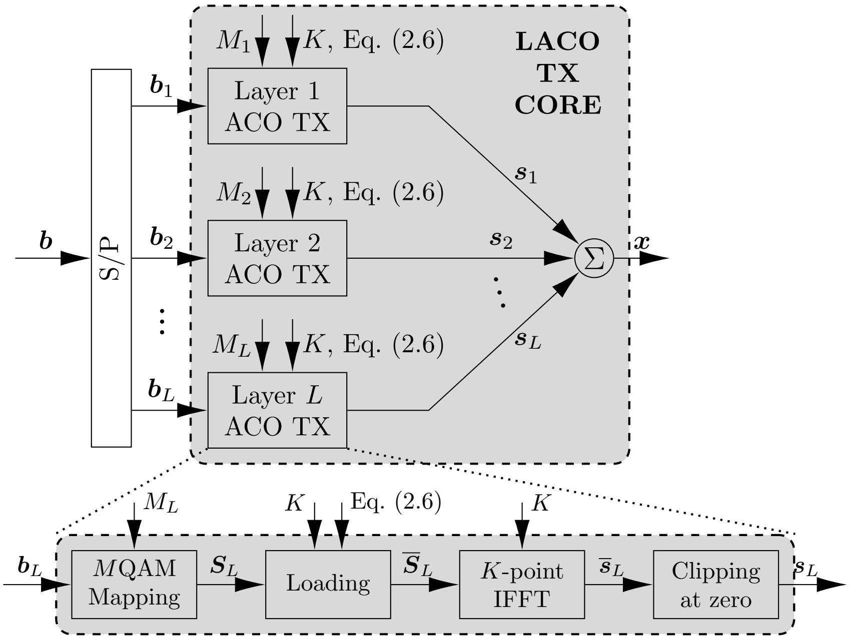

Figure 2.5: LACO-OFDM transmitter system model 1, where the zoom-in structure of ACO TX similar to Fig. 2.2 is provided.

The bit-to-symbol mapping and symbol-to-subcarrier loading strategies of layer 1 is the same as that of ACO-OFDM in Eq. (2.1), while for higher layers this should be modified. Since layer 2 occupies all the even-indexed subcarriers, *i.e.* $k = 2, 4, 6, 8, \ldots$, to obey the rule of ACO-OFDM by leaving every other subcarrier blank, the symbols of layer 2 can only be loaded onto those subcarriers whose indices are multiples of 4, *i.e.* $k = 4, 8, 16, \ldots$, leaving the rest blank. Similarly, layer 3 occupies subcarriers $k = 2, 6, 10, 14, \ldots$ and only load symbols on $k = 6, 14, 22, \ldots$ This strategy is summarised in Eq. (2.6), where for layer l the symbols are loaded onto subcarriers having indices, which are multiples of 2^l shifted by an additional 2^{l-1} positions, and the conjugated symbols are followed in a descending order

$$\overline{S}_l[k] = \begin{cases} S_l[u], & k = 2^l u + 2^{l-1}, \\ S_l^*[u], & k = K - (2^l u + 2^{l-1}), \\ 0, & \text{otherwise}, \end{cases}$$
$$1 \le l \le L,\ 0 \le u \le \tfrac{K}{2^{l+1}} \text{ for layer } l,\ 0 \le k \le K-1, \tag{2.6}$$

It is pertinent to mention that several factors, such as the throughput demand and Quality of Service (QoS) requirement, dictate both the number of bits B_l (length of $\boldsymbol{b}_l$) assigned to each layer and the modulation order (M_l) of each layer. However, the combination of B_l and M_l must ensure that the lth layer outputs exactly $K_1/2^{l+1}$ symbols.

Each of these loaded FD symbol streams $\overline{\boldsymbol{S}}_l$ of Fig. 2.5 is independently converted into a TD signal $\overline{\boldsymbol{s}}_l$ formulated as:

$$\overline{\boldsymbol{s}}_l = \mathcal{F}^{-1}\{\overline{\boldsymbol{S}}_l\}\,, \tag{2.7}$$

while have their negative samples clipped as follows:

$$\boldsymbol{s}_l = \lfloor \overline{\boldsymbol{s}}_l \rfloor\,. \tag{2.8}$$

The resultant unipolar signals $\boldsymbol{s}_l$ are finally superimposed to form the LACO-OFDM signal $\boldsymbol{x}$ of Fig. 2.5, which will be forwarded to the D/A process.

2.3.1.2 Transmitter Model 2

Figure 2.6 provides another portrayal of the LACO-OFDM transmitter, where signal repetition is required for the higher layers, in exchange for having a reduced number of IFFT stages. In the design shown in Fig. 2.6, the symbols on all layers are loaded onto subcarriers in the same manner as in ACO-OFDM, leaving only one blank subcarrier between each active pair. Since the number of subcarrier symbols conveyed by each layer is different, the lengths of the loaded signals $\overline{\overline{\boldsymbol{S}}}_l$ of Fig. 2.6 also vary. Explicitly, we have:

$$\overline{\overline{S}}_l[k] = \begin{cases} S_l[u], & k = 2u + 1, \\ S_l^*[u], & k = K_l - (2u+1), \\ 0, & \text{otherwise}, \end{cases}$$
$$1 \le l \le L,\ 0 \le u \le \tfrac{K}{2^{l+1}} \text{ for layer } l,\ 0 \le k \le K_l - 1. \tag{2.9}$$

This in turn implies that the TD signal must repeat itself several times for $l > 1$ for the sake of aligning the TD signals of all the L layers. Meanwhile, an attenuation factor of $\sqrt{K_k/K}$ is added after repetition for energy conservation proposes, yielding:

$$s_l[n] = \sqrt{\frac{K_l}{K}}\,\lfloor \overline{\overline{s}} \rfloor\,[\mathrm{mod}(n,\ K_l)]. \tag{2.10}$$

Finally, the resultant LACO-OFDM signal $\boldsymbol{x}$ of Fig. 2.6 is now ready for electric/optical conversion.

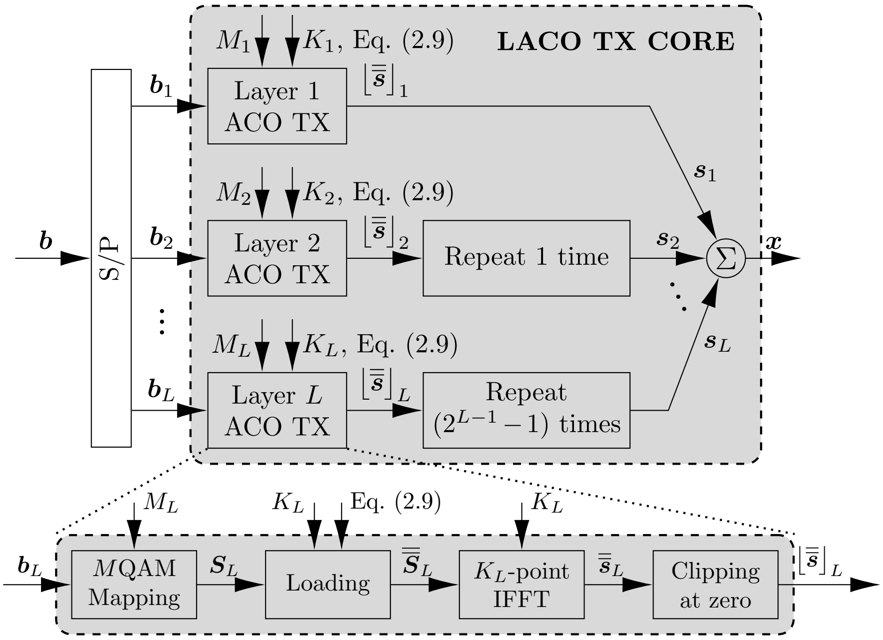

Figure 2.6: LACO-OFDM transmitter system model 2, where the zoom-in structure of ACO TX similar to Fig. 2.2 is provided.

2.3.1.3 Transmitter Design

Despite the fact that the two TX models produce exactly the same LACO-OFDM signals, in practice, more detailed issues have to be discussed in terms of their implementation.

Model 1 represents a balanced design, where the data processing of all layers follow the same structure. Therefore, the same layer processing module can be reused for all layers, hence potentially reducing the complexity. For a standard length-K IFFT operation, where K is a power of 2, the number of Complex Multiplications and Additions (CMA) equals $K \log_2 K$. Therefore, a LACO-OFDM system having L layers requires a total of $2LK \log_2 K$ CMAs using Model 1. Since the data processing of each layer can be operated independently, a parallel structure can be employed for potentially increasing the bit rate at a given processing power. If the time delay of a single IFFT stage is T_{IFFT}, the total time required for Model 1 will be proportional to $T_{\text{IFFT}} \log_2 K$.

On the other hand, TX Model 2 reduces the IFFT complexity by inserting fewer zeros at the symbol-to-subcarrier loading stage, resulting in shorter $\bar{\bar{\boldsymbol{S}}}_l$ sequences. The number of IFFT points for layer l is $K_l = K/2^{l-1}$ according to Eq. (2.5), yielding a total of $\frac{2K}{2^{l-1}} \log_2 \frac{K}{2^{l-1}}$ CMAs. Therefore, the total number of CMAs for a LACO-OFDM system having L layers using TX Model 2 will be

$$\begin{aligned}\sum_{l=1}^{L}\left(\frac{2K}{2^{l-1}}\log_2\frac{K}{2^{l-1}}\right) &= 2K\log_2 K\sum_{l=1}^{L}\frac{1}{2^{l-1}} - 2K\sum_{l=1}^{L}\frac{l-1}{2^{l-1}} \\ &= 4\left(1-\frac{1}{2^L}\right)K\log_2 K - \frac{2K}{2^{L-1}}\left(2^L - L - 1\right) \\ &< 2K\log_2 K,\ \forall\, l > 1.\end{aligned} \tag{2.11}$$

The reduced IFFT complexity comes at the cost of repeating higher layer TD signals multiple times for aligning them with the length-K layer 1. However, the repetition operation can be carried out while waiting for the lower layers' IFFT processes to be completed, which are more time consuming due to having more stages included. Therefore, the total time delay of the Model 2 IFFT is dominated by its layer 1 process, which is the same as in model 1, *i.e.* $T_{\text{IFFT}}\log_2 K$.

The discussions above are summarised below in Tab. 2.1. Note that the number of CMAs is estimated based on the classic RF-OFDM system. Since only a fraction of subcarriers are loaded with complex-valued symbols in O-OFDM, this number can be reduced by carefully optimising the IFFT structures. Nevertheless, the IFFT complexity of Model 1 will always be higher than that of Model 2.

Table 2.1: Comparison of the two transmitter designs in LACO-OFDM

Model	CMA	Delay	Comment
Model 1	$2K\log_2 K$	$T_{\text{IFFT}}\log_2 K$	Balanced design
Model 2	$4\left(1-\frac{1}{2^L}\right)K\log_2 K$ $-\frac{2K}{2^{L-1}}\left(2^L-L-1\right)$	$T_{\text{IFFT}}\log_2 K$	Less IFFT complexity

It is clear that Model 2 should be employed in practical design, as a benefit of its lower complexity. However, for the sake of analysing the LACO-OFDM system, both models are used in this thesis, but different notations are assigned to distinguish them.

2.3.2 LACO-OFDM Receiver

Recall from Fig. 2.3 that layer 1 is free from ILI, while all the subsequent layers are contaminated by the clipping distortion of the previous layers, *i.e.* layer l is contaminated by the clipping distortion of layers 1 to $(l-1)$. Therefore, the received LACO-OFDM signal is detected in a layer-by-layer manner, invoking SIC for removing the clipping distortion of the previous layers.

Figure 2.7 shows the block diagram of a LACO-OFDM receiver. The received signal $\boldsymbol{r}$ is firstly fed to the 'layer 1 ACO RX', since layer 1 is not contaminated by any clipping

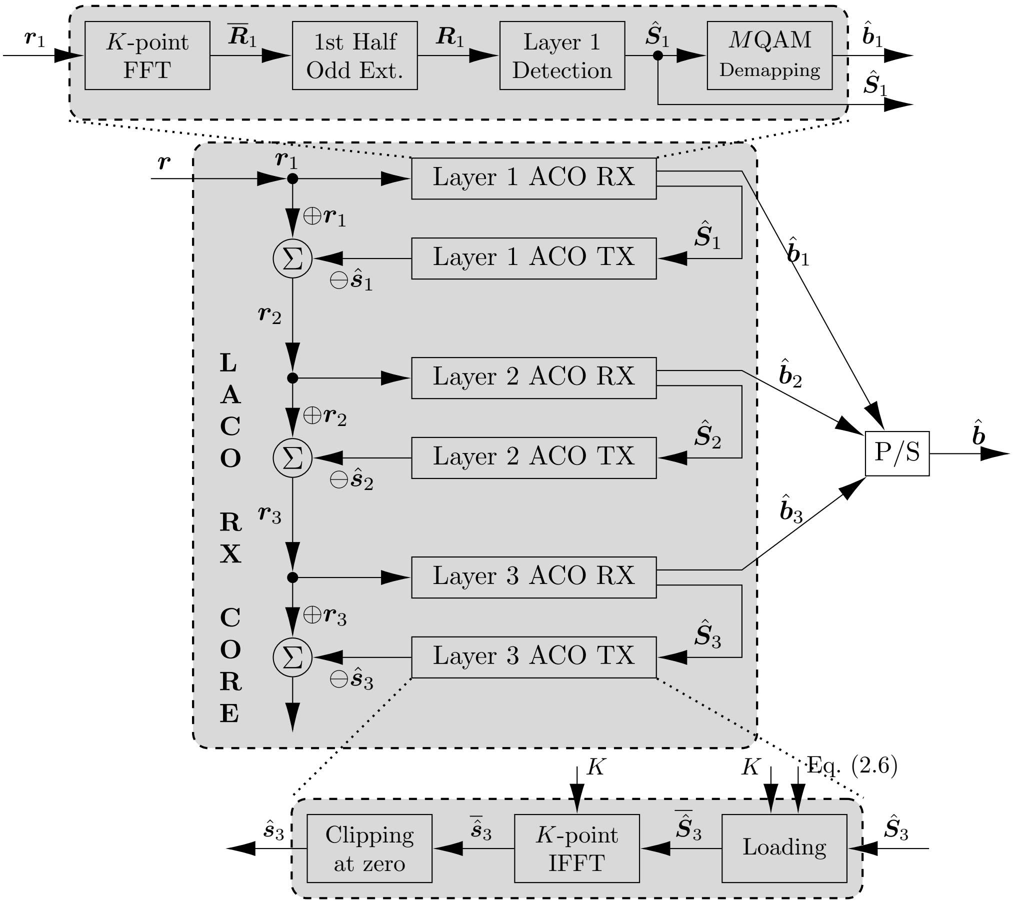

Figure 2.7: LACO-OFDM receiver system, where ACO TX and ACO RX represent the blocks seen in Figs. 2.2 and 2.4, respectively, and ⓢ subtracts the signal marked with $\ominus$ from the signal marked with $\oplus$.

distortion. The detected symbols $\hat{\boldsymbol{S}}_1$ are then fed to the 'layer 1 ACO TX' for the sake of locally regenerating the clipped signal $\boldsymbol{s}_1$ at the receiver as $\hat{\boldsymbol{s}}_1$.

Next, $\hat{\boldsymbol{s}}_1$ is subtracted from the received signal $\boldsymbol{r} = \boldsymbol{r}_1$, hence resulting in the signal $\boldsymbol{r}_2$, which is not contaminated by the clipping distortion of layer 1, provided that the layer bits have been perfectly detected, *i.e.* we have $\hat{\boldsymbol{b}}_1 = \boldsymbol{b}_1$. This SIC process is repeated for all the subsequent layers, so that the signal $\boldsymbol{r}_L$ fed to the 'ACO RX' unit of layer L becomes free from the clipping distortion of all the previous layers.

Unfortunately, the SIC is not perfect, because any residual errors in the detected bits $\hat{\boldsymbol{b}}_l$ may corrupt the regenerated signal $\hat{\boldsymbol{s}}_l$. Consequently, the clipping distortion is not completely eliminated and the residual ones of the successive layers accumulates, as we move to higher layers. This in turn implies that the higher layers exhibit a higher BER than the lower ones.

2.3.3 LACO-OFDM Signals

Figure 2.8 shows the basic schematic of a LACO-OFDM communications system, which has K OFDM subcarriers, and the final composite signal is composed of L layers. Circled numbers are used in Fig. 2.8 to mark the different data processing stages, where ①~④ belong to the TX, and the rest are carried out at the RX.

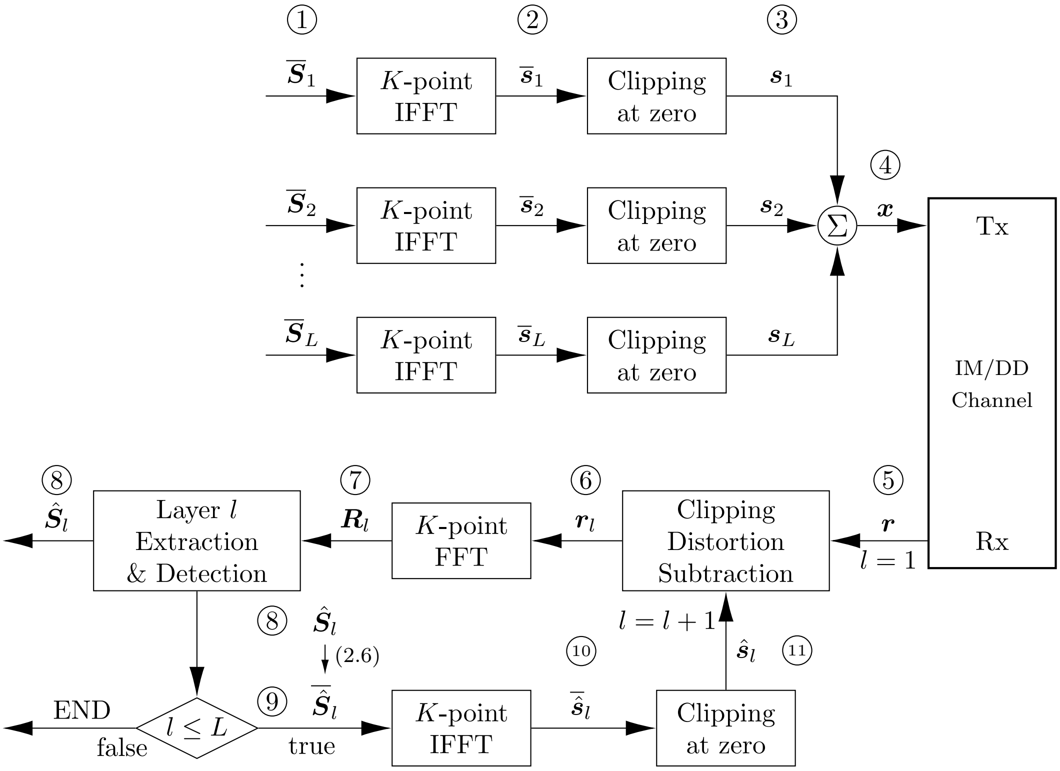

Figure 2.8: LACO-OFDM in IM/DD optical communication systems.

More specifically, in Figs. 2.9 and 2.10, we present side-by-side FD and TD views of the respective TX and RX processes for a LACO-OFDM signal that is composed of 3 layers and uses 16-point FFT. The legends for all the items appearing Figs. 2.9 and 2.10 are summarised in Tab. 2.2. The remainder of this part introduces each of the steps numbered in both figures.

2.3.3.1 Transmitter Signal Flow

① At the TX side, the serially modulated FD symbol stream generated from the symbol set $\mathcal{S}$ is firstly converted into parallel streams mapped to the layers. ACO-OFDM having K subcarriers is applied to layer 1, which is capable of accommodating $K/4$ symbols. This will leave $K/2$ empty subcarriers according to ACO-OFDM, which can be filled by the ACO-OFDM scheme on layer 2. In this way, the number of symbols loaded onto each of the higher layers is halved with respect to the former, *i.e.* layer l only has $K_l = K/2^{l-1}$ subcarriers for $K_l/4$ symbols.

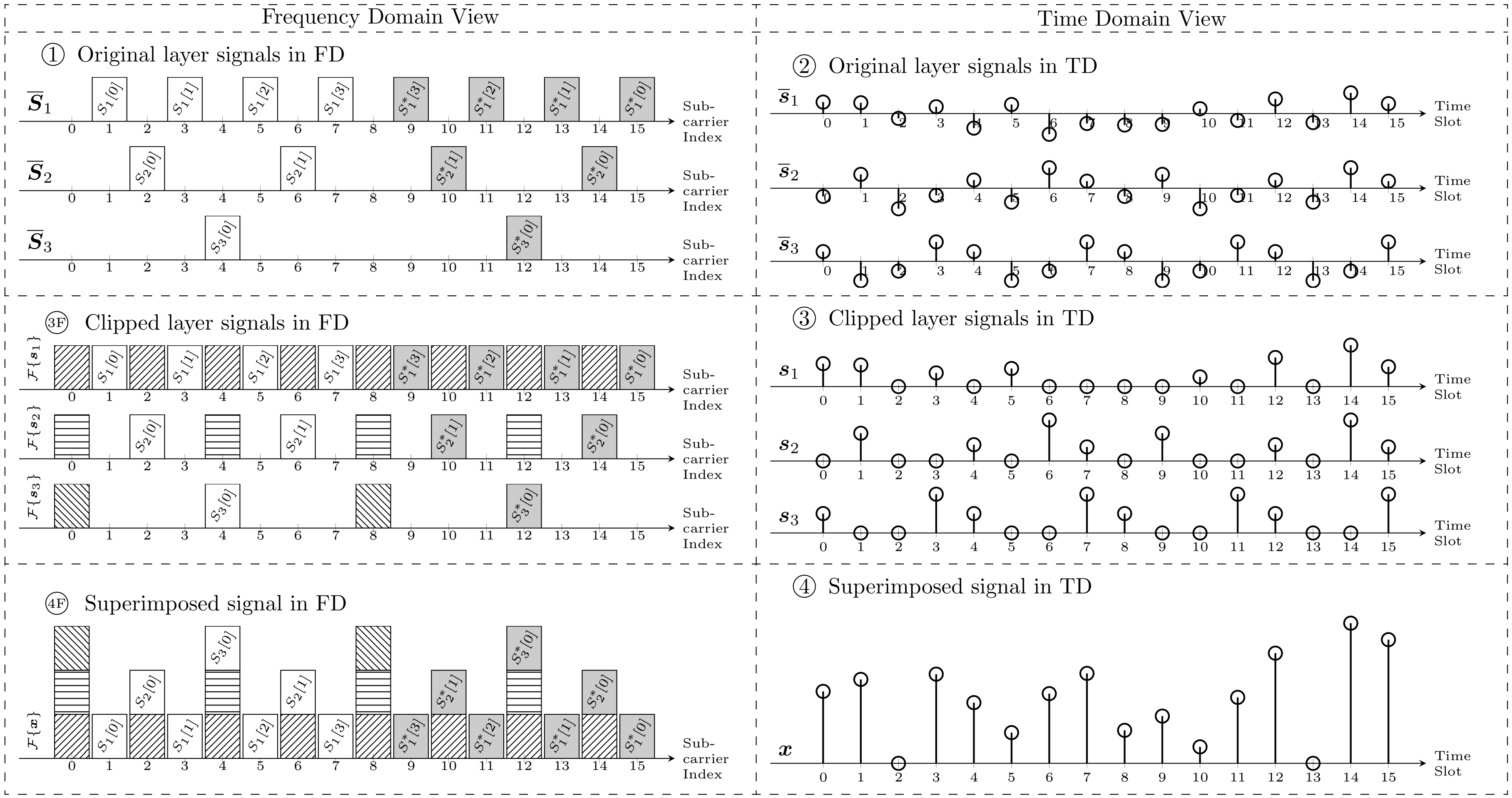

Figure 2.9: Frequency and time domain views of the TX process of a 3LACO-OFDM signal with 16-point FFT. The circled numbers and the symbol notations follow those defined in Fig. 2.8. All other items are defined in Tab. 2.2.

Table 2.2: Legend for Figs. 2.3, 2.9, 2.10 and 3.3

Item	Description	Representation
□	Empty box with $S_l[k]$ in the middle	The original kth symbol on layer l
▒	Light grey shaded box with $S_l^*[k]$ in the middle	The conjugate of symbol $S_l[k]$
▨	Box with north east hatching pattern	The clipping distortion of layer 1
▥	Box with vertical hatching pattern	The clipping distortion of layer 2
▧	Box with north west hatching pattern	The clipping distortion of layer 3
■	Dark grey shaded box without any pattern or text	Thermal noise
▨	Grey shaded box with north west hatching pattern	The ILI generated by layer 1
▥	Grey shaded box with vertical hatching pattern	The ILI generated by layer 2
▩	Grey shaded box with crosshatching pattern	The distortion generated by upper bound clipping
⫯	Circular marker stem	TD samples of signals processed at TX
↑	Triangular marker stem	TD samples of signals received or processed at RX

On each layer, the symbols themselves ($\boldsymbol{S}_l$), together with their conjugates ($\boldsymbol{S}_l^*$, shown as shaded bricks in Fig. 2.9 ①) generated for satisfying the Hermitian symmetry are aligned with their corresponding FD subcarriers, while the unused FD positions are left zero.

② For each layer, the signal $\overline{\boldsymbol{S}}_l$ is transformed by a K-point IFFT to generate the layered TD signals $\overline{\boldsymbol{s}}_l$. The resultant layered signals exhibit the half-wave symmetry of ACO-OFDM, which is also shown in Fig. 2.9 ②. Furthermore, the higher-layer signals tend to repeat themselves several times. As shown in Fig. 2.9 ②, the first half of $\overline{\boldsymbol{s}}_2$ repeats itself, and the first quarter of $\overline{\boldsymbol{s}}_3$ repeats itself three times.

③ These TD signals are then clipped at the lower boundary (LB) to zero. The resultant non-negative signals are denoted as $\boldsymbol{s}_l$. Naturally, this clipping imposes distortions on each of these signals, which appear in the FD at the specific subcarriers that were originally left blank by the current layer, like those shown in Fig. 2.9 (3F) using the diagonal and vertical patterns. Explicitly, the clipping distortions of layer 1 fall at all even-indexed subcarriers, layer 2 at subcarriers 0, 4, 8 and 12, and layer 3 at subcarriers 0 and 8. A more detailed explanation of why they fall on those particular subcarriers can be found in Appendix A.3.

④ Next, all non-negative layer signals are superimposed on each other to form the signal $\boldsymbol{x}$. In the FD, the original information symbols and the distortions located at the same subcarrier index are also superimposed on each other. In this way, the distortions generated by one layer will contaminate the symbols on higher layers, while layer 1 always remains free from this contamination. As shown in Fig. 2.9 (4F), all the symbols of layer 1 occupy their own subcarriers, while those of layer 2 must share their subcarrier with the clipping distortions of layer 1. Moreover, the two subcarriers accommodating layer 3 symbols, *i.e.* subcarriers 4 and 12, also host the clipping distortions of layers 1 and 2.

2.3.3.2 Receiver Signal Flow (layer 1)

⑤ $\boldsymbol{x}$ is then transmitted over the optical IM/DD channel, and received by the RX of Fig. 2.8 with the aid of a PD. The received signal $\boldsymbol{r}$ may differ from $\boldsymbol{x}$ due to the thermal noise imposed. In Fig. 2.10 ⑤, the received signal is shown in triangular stems, while the original sent signal $\boldsymbol{x}$ is also provided in circular stems for comparison.

⑥ Meanwhile, layer 1 is free from any clipping distortions based on our previous analysis. Therefore, at this stage ($l = 1$) the clipping distortion subtraction operation does not affect the signal, and $\boldsymbol{r}$ passes as $\boldsymbol{r}_1$ to the next step, yielding $\boldsymbol{r} = \boldsymbol{r}_1$.

⑦ The received TD signal is firstly transformed by a K-point FFT into the FD signal $\boldsymbol{R}_l$ at the RX of Fig. 2.8. The symbols of all layers and their corresponding clipping distortions, together with the thermal noise, all co-exist at the moment, as shown in Fig. 2.10 ⑥. It is worth mentioning that as the thermal noise is the AWGN, it spreads evenly across the full frequency spectrum, which is reflected in Fig. 2.10 ⑥ as the tiny dark grey bricks on top of all the subcarriers.

⑧ At the RX of Fig. 2.8, the detection has to be carried out on a layer-by-layer basis, commencing from layer 1. Since layer 1 has suffered from no clipping distortion, the symbols located at those subcarrier positions can be directly extracted from $\overline{\boldsymbol{R}}_1$ as $\boldsymbol{R}_1$, which is formulated as

$$R_1[u] = \overline{R}_1[2u + 1]. \tag{2.12}$$

This is the inverse operation of Eq. (2.6) for $l = 1$. Based on the M_1QAM mapping constellation $\mathcal{S}_1$, the estimated transmitted symbols $\hat{\boldsymbol{S}}_1$ on layer 1 of Fig. 2.8 can be detected as

$$\hat{S}_1[u] = \arg \min_{X \in \mathcal{S}_1} |X - 2R_1[u]| , \qquad 0 \leq u \leq \left(\frac{K_1}{4} - 1 \right). \tag{2.13}$$

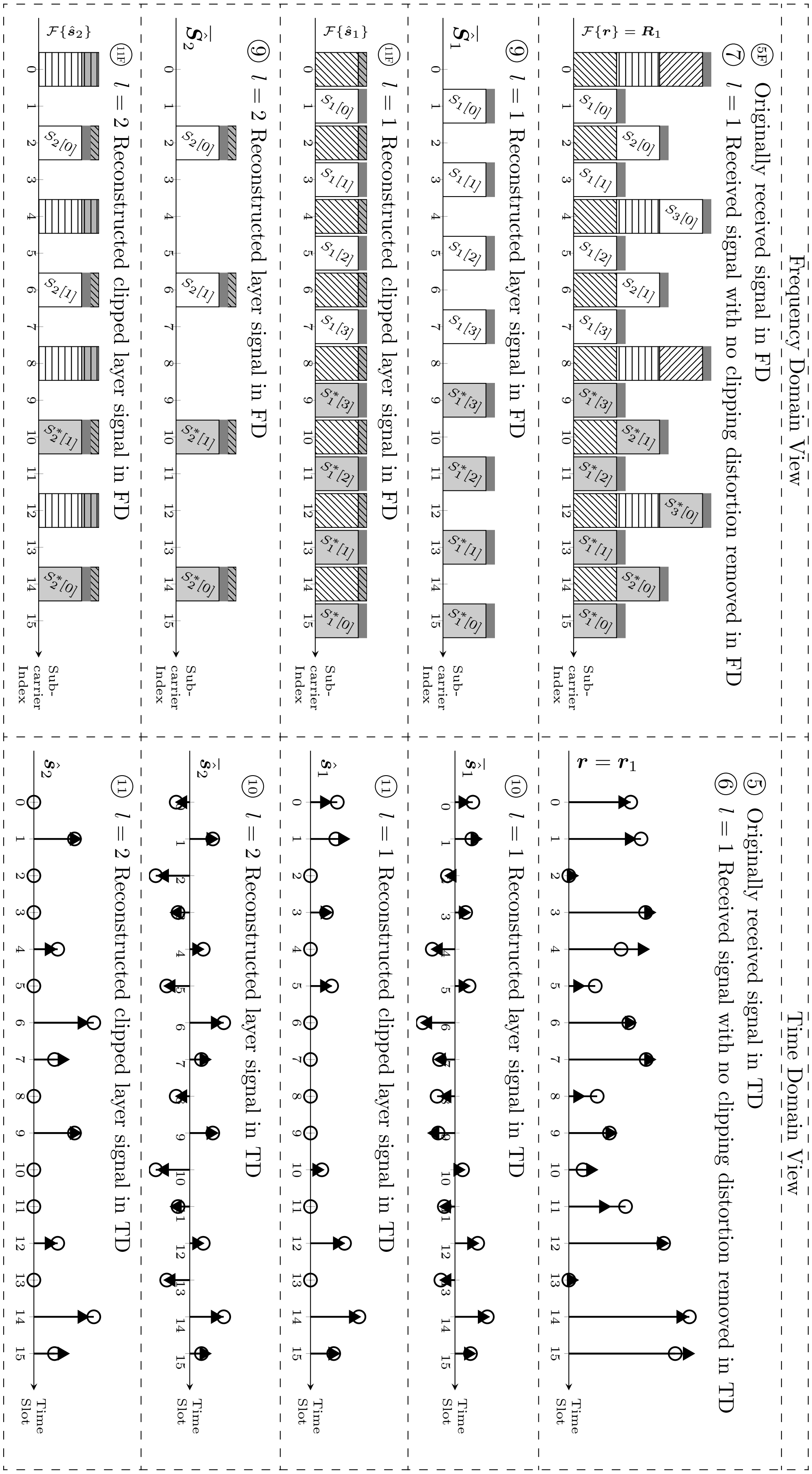

Figure 2.10: Frequency and time domain views of the RX process of a 3LACO-OFDM signal with 16-point FFT. The circled numbers and the symbol notations follow those defined in Fig. 2.8. All other items are defined in Tab. 2.2.

⑨ Then, $\hat{\boldsymbol{S}}_1$ is assembled into the length-K signal $\overline{\hat{\boldsymbol{S}}}_1$ as in Eq. (2.6), as shown in Fig. 2.10 ⑦ ($l = 1$). Comparing ⑦ ($l = 1$) to ①, it is clear that the receiver's copy of layer 1 signal is contaminated by the AWGN.

⑩ $\overline{\hat{\boldsymbol{S}}}_1$ is then transformed by the IFFT into the corresponding TD signal $\overline{\hat{\boldsymbol{s}}}_1$. Due to the unavoidable thermal noise encountered, $\overline{\hat{\boldsymbol{s}}}_1$ would be slightly different from $\overline{\boldsymbol{s}}_1$, as seen in Fig. 2.10 ⑧ ($l = 1$), where the circles represent the original signal $\overline{\boldsymbol{s}}_1$, while the triangle markers represent the locally generated $\overline{\hat{\boldsymbol{s}}}_1$.

⑪ Then, $\overline{\hat{\boldsymbol{s}}}_1$ is clipped again at zero for forming the non-negative signal $\hat{\boldsymbol{s}}_1$. The clipping distortion of layer 1 may now be generated at the RX of Fig. 2.8 as part of $\hat{\boldsymbol{s}}_1$. Viewing in the FD, owing to the noise, the clipping distortion generated locally at the RX of Fig. 2.8 will be slightly different from the actual distortion, as shown in Fig. 2.10 (9F), where this difference is represented by the small light grey bricks at the top of the clipping distortion bricks constituted by the even-index bars marked by the North East hatching pattern. Since we are going to cancel the clipping distortion from the received signal, in order to detect the layer 2's signal, the additional light grey bricks will interfere with the detection process and degrade the performance. Since this interference arises from layer 1 and affects the performance of layer 2, we refer to it as the ILI imposed by layer 1.

2.3.3.3 Receiver Signal Flow (layer 2)

⑥ ($l = 2$) At this stage, the iterative receiver now turns to decontaminating layer 2. Hence, locally generated clipping distortion of layer 1 constituted by the even-index bars marked by the North East hatching pattern is subtracted from $\boldsymbol{r}_1$ of stage ⑤, so that in the resultant $\boldsymbol{r}_2$ the symbols of layer 2 can be detected without the clipping distortion from layer 1.

⑦ ($l = 2$) Likewise, $\boldsymbol{r}_2$ is transformed by a K-point FFT to form $\boldsymbol{R}_2$ of Fig. 2.8.

⑧ ($l = 2$) The symbols of layer 2 can then be extracted from $\overline{\boldsymbol{R}}_2$ as $\boldsymbol{R}_2$, yielding:

$$R_2[u] = \overline{R}_2[4u+2] = \overline{R}_1[4u+2] - \mathcal{F}\{\hat{\boldsymbol{s}}_1\}[4u+2], \tag{2.14}$$

where the '$4u + 2$' indexing comes from the relationship of '$k = 2^l u + 2^{l-1}$' in Eq. (2.6).

⑨ ($l = 2$) Then, $\hat{\boldsymbol{S}}_2$ of Fig. 2.8 is assembled into the length-K signal $\overline{\hat{\boldsymbol{S}}}_2$ as in Eq. (2.6), as shown in Fig. 2.10 ⑨ ($l = 2$). Upon comparing ⑨ ($l = 2$) to ⑨ ($l = 1$) and ②, it becomes clear that the receiver's copy of the layer 2 signal is contaminated not only by the noise, but also by the ILI of layer 1.

⑩ ($l = 2$) Now, the layer 2 symbols may be invoked for regenerating its clipping distortion for supporting the detection of layer 3, using the procedure mentioned above.

The RX of Fig. 2.8 keeps on activating the iteration loop ⑥∼⑪ until all layers become detected.

2.4 The ***Equal Power per Bit*** Power Allocation Strategy

In this section, we introduce the *Equal Power per Bit* strategy for determining the power relationship between each layer, in other words, how the total power should be shared among all the layers[1]. The *Equal Power per Bit* strategy has been commonly adopted in the literature: to allocate the same power to every bit transmitted. Therefore, we have to use a fair power allocation scheme, where the power assigned is commensurate with the number of subcarriers occupied by each layer.

The M_lQAM mapper of layer l maps every $\log_2 M_l$ bits to one symbol, while there are a total of $\frac{K_l}{4} = \frac{K}{2^{l+1}}$ subcarriers to accommodate these symbols. To simplify the problem, we assume that the same modulation scheme is applied to all layers, thus we have $M_l \equiv M \ \forall l$. The total number of bits on layer l will be

$$B_l = \log_2 M_l \cdot \frac{K_l}{4} = \frac{K \log_2 M_l}{2^{l+1}} \propto \frac{1}{2^l}. \tag{2.15}$$

Hence the average symbol power P_l of layer l should be half that of layer $(l-1)$, yielding:

$$P_l = \frac{1}{2} P_{l-1} = \cdots = \frac{1}{2^l} P_1. \tag{2.16}$$

The transmitter designs of Sec. 2.3.1 automatically meet the *Equal Power per Bit* strategy. Explicitly, the length of QAM symbol stream $\boldsymbol{S}_l$ of layer l is

$$\frac{K_l}{4} = \frac{K}{2^{l+1}} = \frac{K_1}{4} \cdot \frac{1}{2^l}, \tag{2.17}$$

which is by a factor of $\frac{1}{2^l}$ lower than that of of layer 1. Therefore, the energy of $\boldsymbol{S}_l$ would be $\frac{1}{2^l}$ of $\boldsymbol{S}_1$. The loading and IFFT processes using TX model 1 conserve energy, while the clipping process halves the energy for all signals, without affecting their ratio. Therefore, the final TD layer signal $\boldsymbol{s}_l$ would also have a factor $\frac{1}{2^l}$ lower energy than that of $\boldsymbol{s}_1$. Since they are now of the same length, their power ratio is also $\frac{1}{2^l}$, which satisfies Eq. (2.16).

---

[1] Unless otherwise specified, electrical power/energy is considered here and hereinafter in this thesis, instead of the optical power/energy.

2.5 Chapter Summary

Figure 2.11 provides a detailed schematic diagram of the relationships between each of the sections in this chapter.

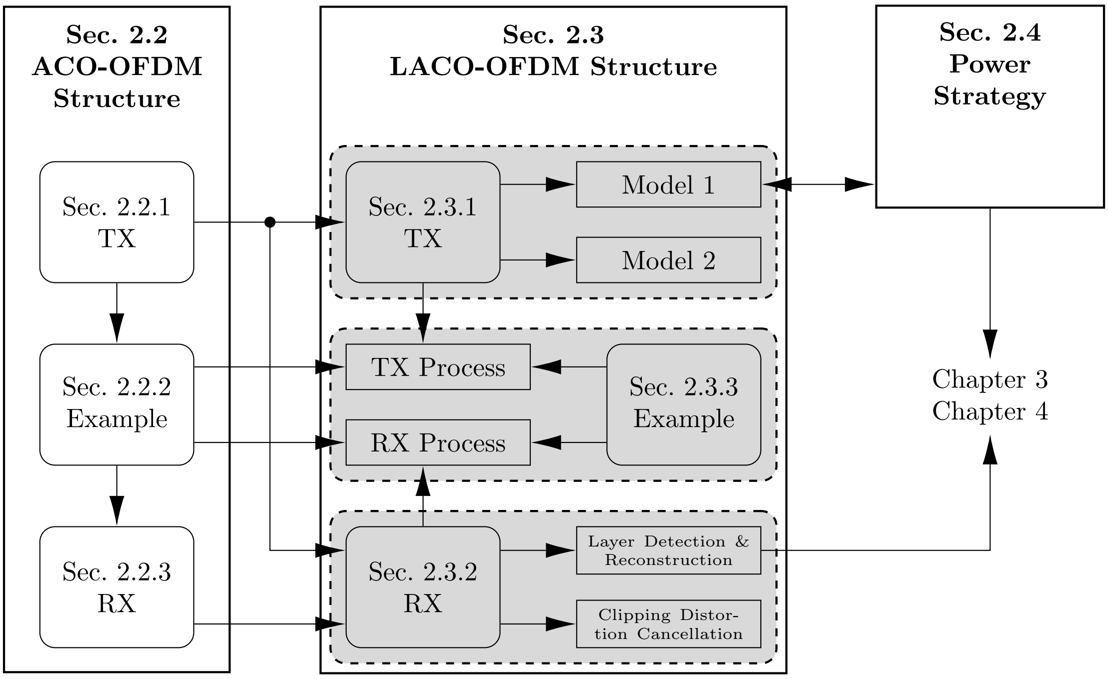

Figure 2.11: Summary of Chapter 2.

In Sec. 2.2, we presented the structure of the ACO-OFDM scheme. We started from its transmitter design in Sec. 2.2.1, which is based on a symbol-to-subcarrier loading system obeying the Hermitian symmetry and having gaps between every pair of subcarriers. Following this, an example depicting the loading and clipping operation of the ACO-OFDM TX of Fig. 2.2 both in the TD and FD is provided for demonstrating the process in Sec. 2.2.2. Inspired by the frequency spectrum of the clipped signal, the ACO-OFDM RX design is discussed in Sec. 2.2.3.

The LACO-OFDM scheme is then introduced in Sec. 2.3, which is an evolved version of the ACO-OFDM structure in Sec. 2.2.

- In Sec. 2.2.1, the motivation of conceiving a layered transmission system is provided by reusing the blank subcarriers of ACO-OFDM as an additional layer, but all the other layers rely on a slightly different loading strategy. In Secs. 2.3.1.1 and 2.3.1.2 we conceived a pair of TX models for orthogonally aligning the symbols of different layers in the FD. Comparisons of the two models indicate that while Model 2 has a lower IFFT complexity, both models produce exactly the same LACO-OFDM signal.

- In Sec. 2.3.2, the layer-by-layer detection-reconstruction-cancellation method of LACO-OFDM receiver design is discussed, where the detection of every layer relies on the ACO-OFDM RX of Sec. 2.2.3 and its reconstruction uses the ACO-OFDM TX architecture of Sec. 2.2.1.
- A detailed example of the LACO-OFDM processing is provided in Sec. 2.3.3, which provided the FD and TD view of each key stage of the LACO-OFDM TX and RX.

In Sec. 2.4, the *Equal Power per Bit* power allocation strategy is introduced, which is automatically satisfied by the LACO-OFDM TX design models of Sec. 2.3.1. The power relationship between layers is a key factor in the performance analysis of LACO-OFDM provided in Chapter 3. Finally, in Chapter 5, a more refined strategy will be proposed and analysed.

Chapter 3

Basic Performance Analysis and Improvements of LACO-OFDM

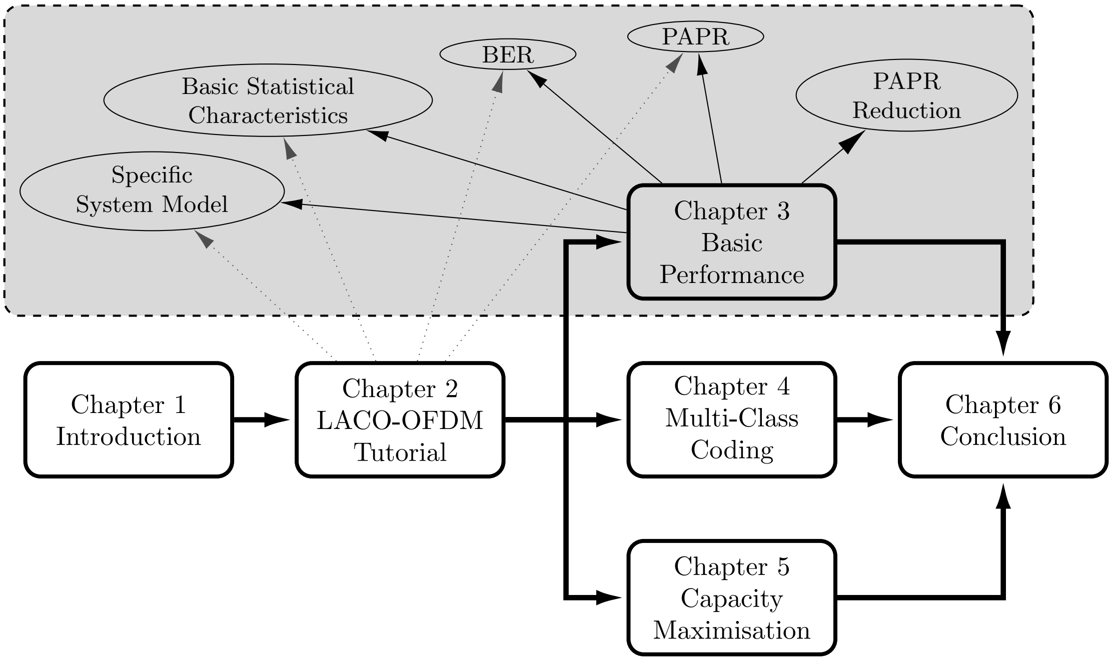

Figure 3.1: Linkage of Chapter 3 into the thesis structure.

3.1 Introduction

In Chapter 2, we have provided a comprehensive review of the LACO-OFDM system, with an emphasis on the signal flow of the TX and RX structure. In this chapter, we will take a closer look into the associated signal's characteristics. We commence with the statistical analysis of the LACO-OFDM TD signal, investigating its behaviour, such as its mean and distribution, as a function of its power, number of layers, number of subcarriers, *etc*. We then turn our attention to its BER performance.

Naturally, O-OFDM also has its impediments, such as its high PAPR, which is defined as the quotient of the maximum to the average power of the TD symbols [71]. Conventional RF-OFDM systems have a high PAPR, which is further increased as the number of subcarriers increases. Hence, the TX power amplifiers have to rely on a backoff and therefore the RX analogue-to-digital converters suffer from an increased granular noise [71]. For this reason, plenty of literature can be found on the PAPR reduction of OFDM in RF systems [72–74]. The situation in IM/DD systems is even worse, because the lifespan of LED emitters and the overall indoor lighting functionality would be affected by the high PAPR. However, the PAPR analysis of RF OFDM signals cannot be applied to the IM/DD optical scenario, due to its unipolar nature [4, 72]. A study by Wang *et al.* [75] has characterised the PAPR performance of several typical O-OFDM schemes, such as DCO-/ACO-/Flip-OFDM and PAM-DMT, where the Complementary Cumulative Distribution Function (CCDF) expressions have been derived and verified by simulations.

Naturally, the layered nature of the LACO-OFDM signal composition also leads to a significantly different statistical characteristics with respect to the Gaussian or truncated Gaussian distributions of the aforementioned schemes. This makes the reduction of PAPR in LACO-OFDM more difficult, since most of the methods proposed for O-OFDM only perform well for the Gaussian distribution, which is not the case for the multiple layers of LACO-OFDM and for the solution conceived in [76] for HACO-OFDM, which is composed of two base layers of equal weight.

Against this background, the BER performance of LACO-OFDM is analysed in the face of thermal noise, ILI and clipping distortion. The bit rate difference between layers is also quantified. Its BER expression is also provided, which suggests that the clipping becomes a major performance-limiting factor in the high SNR region. Since the clipping distortion is closely related to the PAPR of the signal, the PDF of the PAPR is studied. A novel PAPR reduction method based on tone-injection is also proposed for improving the performance of LACO-OFDM, which formulates an optimisation problem that may be solved by off-the-shelf tools, regardless of the number of layers. Monte-Carlo simulations are conducted to verify the analyses of PAPR and BER.

The contributions of this chapter is listed as follows.

1. The statistical behaviour of the LACO-OFDM signal is characterised versus its power, versus the number of subcarriers as well as the number of layers. The expressions of its statistical mean, various, total power and PAPR are formulated.
2. The BER performance of LACO-OFDM is analysed in the face of thermal noise, ILI and clipping distortion. The bit rate difference between layers is also quantified

and its BER expression is provided, which suggests that the clipping distortion becomes a major performance-limiting factor in the high-SNR region.

3. A novel PAPR reduction method based on tone-injection is also proposed for improving the performance of LACO-OFDM, which formulates an optimisation problem that may be solved by off-the-shelf tools, regardless of the number of layers.

Monte-Carlo simulations are conducted to verify the PAPR and BER analysis.

The structure of this chapter is as follows. In Sec. 3.2, a slightly modified LACO-OFDM system aligned with the main topics of this chapter is presented. The basic statistical characteristics of the LACO-OFDM TD signal is studied in Sec. 3.3, while the analyses of the LACO-OFDM BER and PAPR distribution are given in Sec. 3.4 and 3.5, respectively. A novel PAPR reduction method is proposed in Sec. 3.6 for improving the system performance. Finally, our summary and conclusions are offered in Sec. 3.7 and 3.8, respectively.

3.2 System Models

In this section, we introduce the LACO-OFDM transmitters that are slightly modified from Fig. 2.8. Explicitly, the transmitter model of this chapter includes two additional modules: Tone-Injection (TI) and Upper Bound (UB) clipping. The structure and signal processing of these two modules are described in this section, while the reasons for including them, as well as their mathematical characterisations are also provided in this chapter.

3.2.1 LACO-OFDM TX with UB Clipping

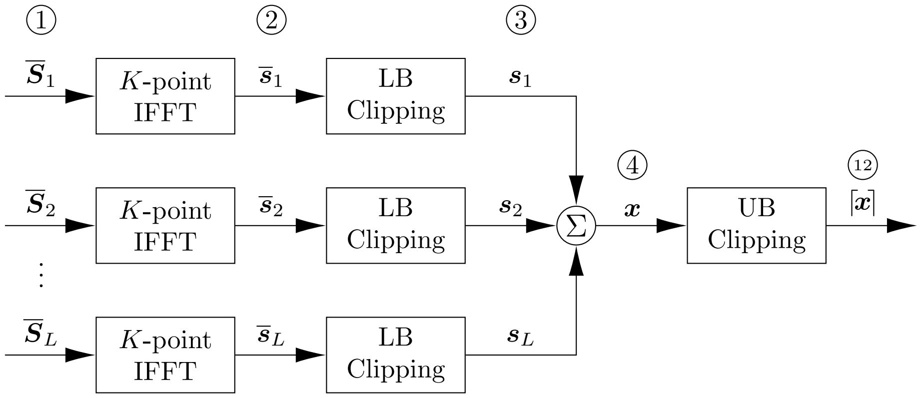

Figure 3.2: LACO-OFDM transmitter with upper bound clipping included.

Figure 3.2 shows the schematic of the LACO-OFDM transmitter when UB clipping is considered. Recall from Fig. 2.8 that the transmitter of LACO-OFDM generates superimposed signal $\boldsymbol{x}$ at Stage ④. However, the IM/DD transmission process is subject to the maximum power emitted by the LED and to the limited linear range of other components. Hence, $\boldsymbol{x}$ will be further clipped at a specific upper bound, resulting in the upper-bounded signal $\lceil \boldsymbol{x} \rceil$, shown at Stage ⑫ in Fig. 3.2.

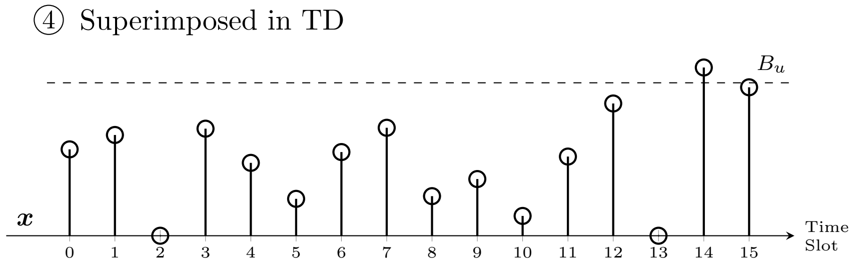

(a) Superimposed TD Signal

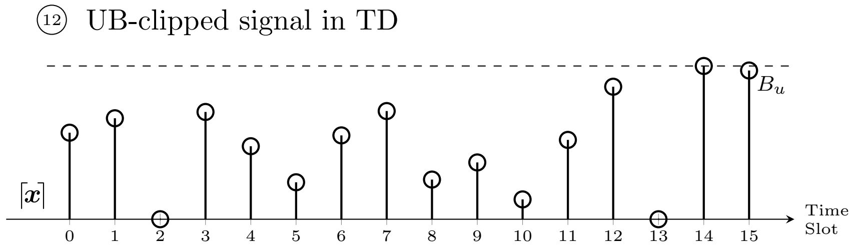

(b) UB-clipped TD Signal

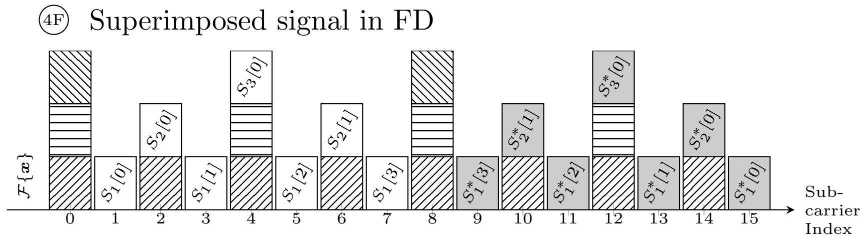

(c) Superimposed FD Signal

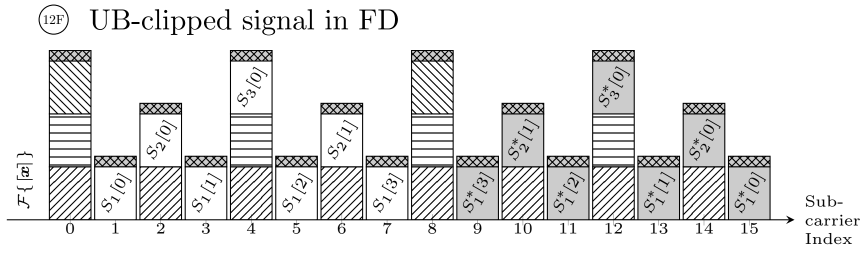

(d) UB-clipped FD Signal, where the grey boxes with crosshatches represent UB clipping distortion

Figure 3.3: Example of LACO-OFDM TX UB clipping process signal flow, as a supplementary to Fig. 2.9 and also follows the legend in Tab. 2.2.

As a supplementary to Fig. 2.9, in Fig. 3.3 we present an example of the same TX signal going through UB clipping. In Fig. 3.3 ④, B_u is used as the UB clipping threshold and the TD symbol at the 14th sample is clipped to B_u, *i.e.*

$$\lceil x \rceil [k] = x[k] \cdot \mathsf{u}(B_{\mathrm{u}} - x[k]) = \begin{cases} B_{\mathrm{u}}, & x[k] \geq B_{\mathrm{u}}, \\ x[k]\,, & \text{otherwise.} \end{cases} \tag{3.1}$$

In the FD, the UB clipping distortion will spread across the entire spectrum and will contaminate all subcarriers, as seen in Fig. 3.3 (12F), where the dark grey crosshatched bricks on the top represent the UB clipping distortion.

3.2.2 LACO-OFDM TX with Tone-Injection

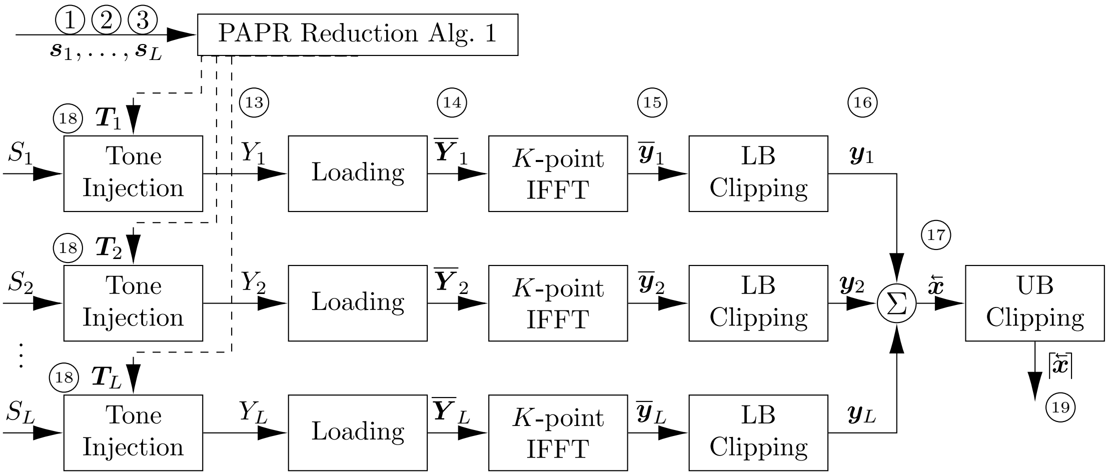

Figure 3.4: LACO-OFDM transmitter with tone-injection and upper bound clipping included.

Figure 3.4 shows the schematic of the LACO-OFDM transmitter relying on tone-injection, where the TX processes the data in the same way as without tone injection (Stage ⑬), and obtains the unclipped signal $\boldsymbol{s}_l$. In other words, the TX repeats Stages ① to ③ of Fig. 2.8. The signals obtained are then forwarded to the PAPR reduction processor of Fig. 3.4, which takes the information and generates a group of signals $\boldsymbol{T}_l$ to be injected into the FD of the signal in a beneficial way for reducing its PAPR. More detailed information about this process will be provided in Sec. 3.6.

Next, a tone-injection block is placed at the very front of each layer's symbol processing, directly processing the QAM symbols $\boldsymbol{S}_l$ as its input. Upon injecting, the tone-injector block generates $\boldsymbol{Y}_l$ from $\boldsymbol{S}_l$ and the injecting signals $\boldsymbol{T}_l$, as shown in Fig. 3.4 ⑬. These injected signals are processed the in same way as for the normal LACO-OFDM layer signals, which were subjected to symbol-to-subcarrier loading (⑭), IFFT (⑮), LB clipping (⑯) and superposition (⑰). The resultant LACO-OFDM TD signal is denoted as $\overleftarrow{\boldsymbol{x}}$ in Fig. 3.4. This signal is finally clipped by the UB clipping block of Fig. 3.4, yielding $\lceil \overleftarrow{\boldsymbol{x}} \rceil$, which is similarly to that of Eq. (3.1).

The receiver design of the tone-injected LACO-OFDM system is similar to that of the original ones shown at the bottom of Fig. 2.8, apart from using a more sophisticated layer symbol detector at stage ⑧ of Fig. 2.8, which will be further detailed in Sec. 3.6.

3.2.3 Simulation Parameters

All the simulations in this chapter rely on the *Equal Power per Bit* power allocation strategy of Sec. 2.4, with the overall signal power transmitted set to

$$P_{\text{LACO}} = 1 \text{ W}. \tag{3.2}$$

Table 3.1 summaries the parameters to be used in the numerical simulations throughout this chapter, if not been specified otherwise.

Table 3.1: Parameters Used for Simulation Results in Chapter 3

Symbol	**Definition**	**Value**	**Applicable Figures**
M	Size of the constellation pattern	16	3.6, 3.7, 3.8, 3.9, 3.10, 3.11, 3.12, 3.13, 3.14, 3.15, 3.16, 3.17, 3.18, 3.19
L	Number of layers composing the LACO-OFDM signal	2	3.11, 3.13, 3.16
		3	3.19
		4	3.11, 3.17
K	Number of FFT/IFFT points for scenarios without UB clipping[a]	64	3.17, 3.18
		1024	3.6, 3.7, 3.8, 3.9, 3.10, 3.11, 3.12, 3.14, 3.15, 3.16, 3.19
τ	UB clipping ratio	9 dB	3.12
ρ	Scaling factor for injecting signal	1.2	3.17, 3.17, 3.19
Z	Number of candidate vectors for PAPR reduction optimisation	200	3.17, 3.19
t'	Optimisation target for the simplified PAPR reduction algorithm	0.7	3.17, 3.19
N/A	Channel	AWGN	3.11, 3.12, 3.19

---

[a] For scenarios with UB clippings, longer FFT length is required.

3.3 Basic Statistical Characteristics

In this section, we discuss the basic statistical characteristics of the time domain LACO-OFDM signals. To begin with, we derive the PDF of the individual layers as well as that of the superimposed signal. Typical statistical moments, including the mean and variance, followed by the electric power are covered in this section.

3.3.1 PDF of Base Layers

Recall from the schematic diagram of the LACO-OFDM transmitter of Fig. 2.8 that for each of the layers, the IFFT process converts the FD signal $\overline{\boldsymbol{S}}_l$ into its TD counterpart $\overline{\boldsymbol{s}}_l$. With the help of the Central Limit Theorem (CLT), the amplitude of the real-valued signal $\overline{\boldsymbol{s}}_l$ can be considered to be Gaussian-distributed, when the number of subcarriers is reasonably high (typically $K > 64$). Explicitly, the PDF of $\overline{\boldsymbol{s}}_l$ with variance σ_l^2 can be written as

$$f_{\overline{\boldsymbol{s}}_l}(z) = \phi(z;\ \sigma_l^2) = \frac{1}{\sqrt{2\pi}}\exp\left[-\frac{z^2}{\sigma_l^2}\right], \tag{3.3}$$

where $\phi(z;\ \sigma_l^2)$ is the PDF of the standard Gaussian distribution with zero mean and variance of σ_l^2, while $z \in \mathbb{R}$ is used as the independent variable of the PDF. The clipping process following the IFFT in Fig. 3.2 removes all negative samples in $\overline{\boldsymbol{s}}_l$ to provide $\boldsymbol{s}_l$. Consequently, the distribution of *positive* samples in $\boldsymbol{s}_l$ remains the same as in $\overline{\boldsymbol{s}}_l$. On the other hand, all negative elements are condensed as a single impulse at $z = 0$, because the clipping process replaces those samples with 0. Therefore, the PDF of $\boldsymbol{s}_l$ evaluated at z should be

$$f_{\boldsymbol{s}_l}(z) = \frac{1}{2}\delta(z) + \phi(z;\ \sigma_l^2)\mathsf{u}(z)\,, \tag{3.4}$$

where $\delta(\cdot)$ is the Dirac delta function

$$\delta(z) = \begin{cases} +\infty, & z = 0, \\ 0, & \text{otherwise}, \end{cases} \qquad \text{and} \qquad \int_{-\infty}^{+\infty} \delta(z)\ \mathrm{d}z = 1, \tag{3.5}$$

with $\mathsf{u}(\cdot)$ being the Heaviside step function

$$\mathsf{u}(z) = \begin{cases} 1, & z > 0, \\ 0, & \text{otherwise}. \end{cases} \tag{3.6}$$

Figure 3.5 plots the PDFs of a LACO-OFDM layer signal before and after the clipping process, assuming that its variance before clipping is $\sigma_l^2 = 1$.

Moreover, by relying on the *Equal Power per Bit* strategy of Sec. 2.4 in the power control part, all the variances σ_l^2 for $l \geq 2$ can be replaced by σ_1^2. Under these circumstances, the PDF of the layer signals $\boldsymbol{s}_l$ is given by:

$$f_{\boldsymbol{s}_l}(z) = \frac{1}{2}\delta(z) + \phi\left(z;\ \frac{\sigma_1^2}{2^{l-1}}\right)\mathsf{u}(z)\,. \tag{3.7}$$

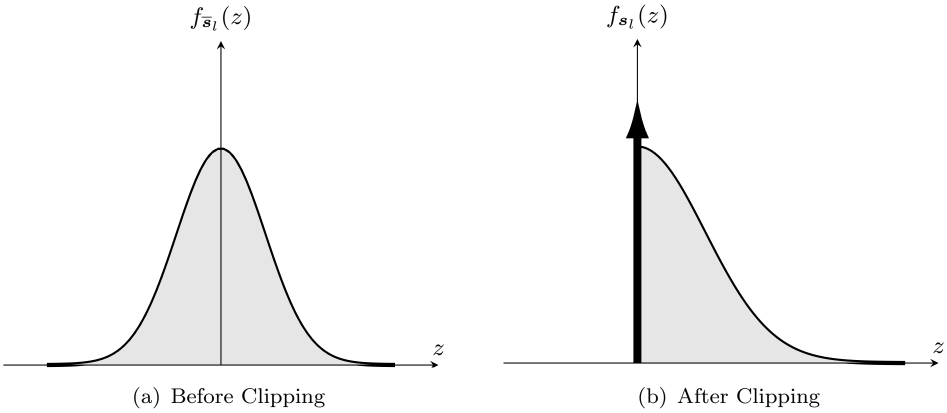

(a) Before Clipping (b) After Clipping

Figure 3.5: PDF plots of an example LACO-OFDM base layer signal (a) before and (b) after the clipping at zero.

3.3.2 Moments of the Layers

With the help of the PDF formula of Eq. (3.7), the statistical moments of the base layers can be derived.

The mean of the signal is the first order moment, expressed as

$$\begin{aligned}
\mathbb{E}\{\boldsymbol{s}_l\} &= \int_{-\infty}^{+\infty} z \cdot f_{\boldsymbol{s}_l}(z)\,\mathrm{d}z \\
&= \int_{-\infty}^{+\infty} z \cdot \left[\frac{1}{2}\delta(z) + \phi\left(z;\ \frac{\sigma_1^2}{2^{l-1}}\right)\mathsf{u}(z)\right]\mathrm{d}z \\
&= 0 \times \frac{1}{2} + \int_0^{+\infty} \frac{z}{\sqrt{2\pi}}\exp\left[-\frac{z^2}{2^{-(l-1)}\sigma_1^2}\right]\mathrm{d}z \\
&= \frac{2^{-(l-1)/2}\sigma_1}{\sqrt{2\pi}} \int_0^{+\infty} \exp\left[-\left(\frac{z}{2^{-(l-1)/2}\sigma_1}\right)^2\right]\mathrm{d}\left(\frac{z}{2^{-(l-1)/2}\sigma_1}\right) \\
&= \frac{\sigma_1}{2^{l/2}\sqrt{\pi}}.
\end{aligned} \tag{3.8}$$

The electric power of the signal is the mean of its squared samples, *i.e.* its second order moment, given as

$$\mathbb{E}\{\boldsymbol{s}_l^2\} = \int_{-\infty}^{+\infty} z^2 \cdot f_{\boldsymbol{s}_l}(z)\,\mathrm{d}z = \int_{-\infty}^{+\infty} z^2 \cdot \left[\frac{1}{2}\delta(z) + \phi\left(z;\ \frac{\sigma_1^2}{2^{l-1}}\right)\mathsf{u}(z)\right]\mathrm{d}z. \tag{3.9}$$

Alternatively, the *Equal Power per Bit* strategy of Eq. (2.16) simply implies that

$$\mathbb{E}\{\boldsymbol{s}_l^2\} = P_l = \frac{1}{2^{l-1}}P_1 = \frac{1}{2^l}\sigma_1^2. \tag{3.10}$$

The variance of the signal can be calculated as

$$\mathbb{D}\{\boldsymbol{s}_l\} = \mathbb{E}\{\boldsymbol{s}_l^2\} - (\mathbb{E}\{\boldsymbol{s}_l\})^2 = \frac{\sigma_1^2}{2^l} - \left(\frac{\sigma_1}{2^{l/2}\sqrt{\pi}}\right)^2 = \frac{1}{2^l}\left(1 - \frac{1}{\pi}\right)\sigma_1^2. \tag{3.11}$$

3.3.3 Moments of the Superimposed Signal

Since the signals of different layers are independent of each other before their superposition, the co-variance between any two of them is zero. Hence, the mean and variance of the combined signal $\boldsymbol{x}$, where we have:

$$\boldsymbol{x} = \boldsymbol{s}_1 + \boldsymbol{s}_2 + \cdots + \boldsymbol{s}_L = \sum_{l=1}^{L} \boldsymbol{s}_l, \tag{3.12}$$

becomes:

$$\begin{aligned}\mathbb{E}\{\boldsymbol{x}\} &= \mathbb{E}\left\{\sum_{l=1}^{L} \boldsymbol{s}_l\right\} = \sum_{l=1}^{L} \mathbb{E}\{\boldsymbol{s}_l\} \\ &= \sum_{l=1}^{L} \frac{\sigma_l}{\sqrt{2\pi}} = \frac{\sigma_1}{\sqrt{\pi}} \sum_{l=1}^{L} \frac{1}{\sqrt{2}^l} = \frac{(1 - 2^{-L/2})\sigma_1}{(\sqrt{2} - 1)\sqrt{\pi}},\end{aligned} \tag{3.13}$$

and

$$\begin{aligned}\mathbb{D}\{\boldsymbol{x}\} &= \mathbb{D}\left\{\sum_{l=1}^{L} \boldsymbol{s}_l\right\} = \sum_{l=1}^{L} \mathbb{D}\{\boldsymbol{s}_l\} \\ &= \sum_{l=1}^{L} \frac{\pi - 1}{2^l \pi}\sigma_1^2 = \frac{\sigma_1^2(\pi - 1)}{\pi} \sum_{l=1}^{L} \frac{1}{2^l} = \frac{\sigma_1^2(\pi - 1)}{\pi}\left(1 - \frac{1}{2^L}\right).\end{aligned} \tag{3.14}$$

Thus, the power of an L-layer LACO-OFDM signal $\boldsymbol{x}$ can be expressed as

$$P_{\text{LACO}} = \mathbb{E}\{\boldsymbol{x}^2\} = \mathbb{D}\{\boldsymbol{x}\} + (\mathbb{E}\{\boldsymbol{x}\})^2 \tag{3.15}$$

$$= \frac{\sigma_1^2}{\pi}\left[\frac{\left(1 - 2^{-L/2}\right)^2}{3 - 2\sqrt{2}} + (\pi - 1)\left(1 - \frac{1}{2^L}\right)\right]. \tag{3.16}$$

It is worth noting that

1. Eq. (3.16) only holds under the *Equal Power per Bit* strategy, and
2. it is a function of the total number of layers L, and thus can be written as $P_{\text{LACO}}(L)$.

3.3.4 PDF and CDF of the Superimposed Signal

Based on Eq. (3.7), the PDF of an L-layer LACO-OFDM signal's amplitude $\boldsymbol{x}$, denoted as $f_{\boldsymbol{x}}(z)$, can be obtained by successively convolving ($\otimes$) the PDFs of all L of its constituent layers $\boldsymbol{s}_l$ (please see Appendix B.1 for detailed proof), yielding:

$$\begin{aligned} f_{\boldsymbol{x}}(z) &= f_{\boldsymbol{s}_1}(z) \otimes f_{\boldsymbol{s}_2}(z) \otimes \cdots \otimes f_{\boldsymbol{s}_L}(z) \\ &= \int_{z_{L-1}=-\infty}^{z_{L-1}=\infty} \int_{z_{L-2}=-\infty}^{z_{L-2}=\infty} \cdots \int_{z_1=-\infty}^{z_1=\infty} \\ &\quad f_{\boldsymbol{s}_L}(z - z_{L-1})\, f_{\boldsymbol{s}_{L-1}}(z_{L-1} - z_{L-2}) \cdots f_{\boldsymbol{s}_2}(z_2 - z_1)\, f_{\boldsymbol{s}_1}(z_1)\, \mathrm{d}z_{L-1} \cdots \mathrm{d}z_1. \end{aligned} \tag{3.17}$$

In this way, the PDF of a 2-layer LACO-OFDM signal, namely that of $\boldsymbol{x}_2$ can be expressed as

$$\begin{aligned} f_{\boldsymbol{x}_2}(z) = \frac{\delta(z)}{4} &+ \frac{1}{2}\phi(z;\sigma_1^2)\,\mathsf{u}(z) + \frac{1}{2}\phi\left(z;\frac{\sigma_1^2}{2}\right)\mathsf{u}(z) + \\ &\phi\left(z;\frac{3\sigma_1^2}{2}\right)\left[\Phi\left(\frac{z}{\sqrt{3}\sigma_1}\right) + \Phi\left(\frac{z}{\sqrt{3}\sigma_1/2}\right) - 1\right]\mathsf{u}(z)\,, \end{aligned} \tag{3.18}$$

where $\Phi(\cdot)$ is the CDF of the standard Gaussian distribution given in Eq. (B.11). The detailed derivation of $f_{\boldsymbol{x}_2}(z)$ can be found in Appendix B.2.

However, due to the involvement of the term

$$\int \left(\phi(z) \int \phi(z')\mathrm{d}z'\right)\mathrm{d}z \longrightarrow \int \phi(z)\Phi(z')\mathrm{d}z, \tag{3.19}$$

it has been shown in [77] that no closed form expression can be obtained for $L > 3$ layers. Therefore, we have to resort to numerical computation of the PDF solution, which is extremely time-consuming. Fortunately, the complexity of this calculation can be slightly reduced by combining pairs of convolutions, yielding:

$$f_{\boldsymbol{x}}(z) = [f_{\boldsymbol{s}_1}(z) \otimes f_{\boldsymbol{s}_2}(z)] \otimes [f_{\boldsymbol{s}_3}(z) \otimes f_{\boldsymbol{s}_4}(z)] \otimes \cdots \tag{3.20}$$

since the double-layer PDFs of $f_{\boldsymbol{s}_1}(z)$ and $f_{\boldsymbol{s}_2}(z)$ have been derived in closed-forms.

When UB clipping is applied to the combined signal $\boldsymbol{x}$ with the clipping voltage set to B_u Volts ($B_\mathrm{u} > 0$), the PDF of $z < B_\mathrm{u}$ remains the same, while the $z \geq B_\mathrm{u}$ part is truncated and replaced with a pulse $\delta(z - B_\mathrm{u})\mathcal{D}$, where $\mathcal{D}$ is given by

$$\mathcal{D} = \int_{B_\mathrm{u}}^{+\infty} f_{\boldsymbol{x}}(z)\,\mathrm{d}z = 1 - \int_{0^-}^{B_\mathrm{u}} f_{\boldsymbol{x}}(z)\,\mathrm{d}z. \tag{3.21}$$

This leads to the following expression for the PDF of the final transmitted signal $\lceil \boldsymbol{x} \rceil$:

$$f_{\lceil \boldsymbol{x} \rceil}(z) = f_{\boldsymbol{x}}(z)\,\mathsf{u}(-z + B_\mathrm{u}) + \delta(z - B_\mathrm{u})\mathcal{D}. \tag{3.22}$$

Finally, the Cumulative Distribution Function (CDF) of signal $\boldsymbol{x}$ can be expressed as

$$F_{\boldsymbol{x}}(z) = \int_{-\infty}^{z} f_{\boldsymbol{x}}(z)\,\mathrm{d}z = \int_{0^-}^{z} f_{\boldsymbol{x}}(z)\,\mathrm{d}z, \tag{3.23}$$

while for $\lceil \boldsymbol{x} \rceil$, its CDF would have $f_{\boldsymbol{x}}(\cdot)$ substituted by $f_{\lceil \boldsymbol{x} \rceil}(\cdot)$.

Remark 3.1. Given Eq. (3.12), where the signal of interest $\boldsymbol{x}$ is the sum of L independent signals, one would intuitively consider the PDF of $\boldsymbol{x}$ being Gaussian (or at least close to Gaussian), based on the CLT. However, the CLT can only be applied when a sufficiently high number of signals having arbitrary PDFs are superimposed. Therefore, a LACO-OFDM signal can only be considered to be Gaussian distributed, when more than 30 layers are superimposed, *i.e.* $L \geq 12$ [78]. Since the highest layer (layer L) requires at least 4 subcarriers to operate ACO-OFDM (the symbol, its conjugate and two nulls), the corresponding minimum total subcarrier number per OFDM block is

$$K_{\min} \geq 2^{L+1} \geq 2^{13} = 8192. \tag{3.24}$$

Bear in mind that this is the minimum requirement and it is highly inefficient to utilise all 12 available layers when having $K_{\min}$ subcarriers, since layer 12 can only convey a single symbol. Therefore, the assumption of a Gaussian distribution shall never be *unconditionally* made for LACO-OFDM.

3.3.5 Numerical PDF Results

In this subsection, the LACO-OFDM signals' PDF is further explored with the aid of numerical simulations.

Figure 3.6 shows the PDF of LACO-OFDM signals utilising different total number of layers L, ranging from 1 up to 6, while the remaining simulation parameters are set according to Tab. 3.1 on page 38. The impulses at $z = 0$ are not depicted. When the *Equal Power per Bit* strategy is employed, the total power of all LACO-OFDM signals has to be 1 W for a fair comparison.

While the PDF of single-layer LACO-OFDM is a truncated one-sided Gaussian distribution, the peaks gradually move rightwards as more layers are added. The mean is increased and the variance is reduced, as total number of layers L is increased.

More quantitatively, in Fig. 3.7, the mean and variance of the LACO-OFDM signal are plotted against the total number of layers L. Observe in Fig. 3.7 that both the mean and variance tend to converge to a certain value for a sufficiently high number of layers, as stated in Remark 3.1.

To elaborate a little further, in Fig. 3.8 we provide a plot of the same PDF as in Fig. 3.6 on a logarithmic vertical axis to explore the characteristics of LACO-OFDM signals at high amplitudes. It can been seen from Fig. 3.8 that the signals having more layers statistically speaking tend to have lower amplitude, which determines their respective PAPR. This issue will be further elaborated on in Sec. 3.5.

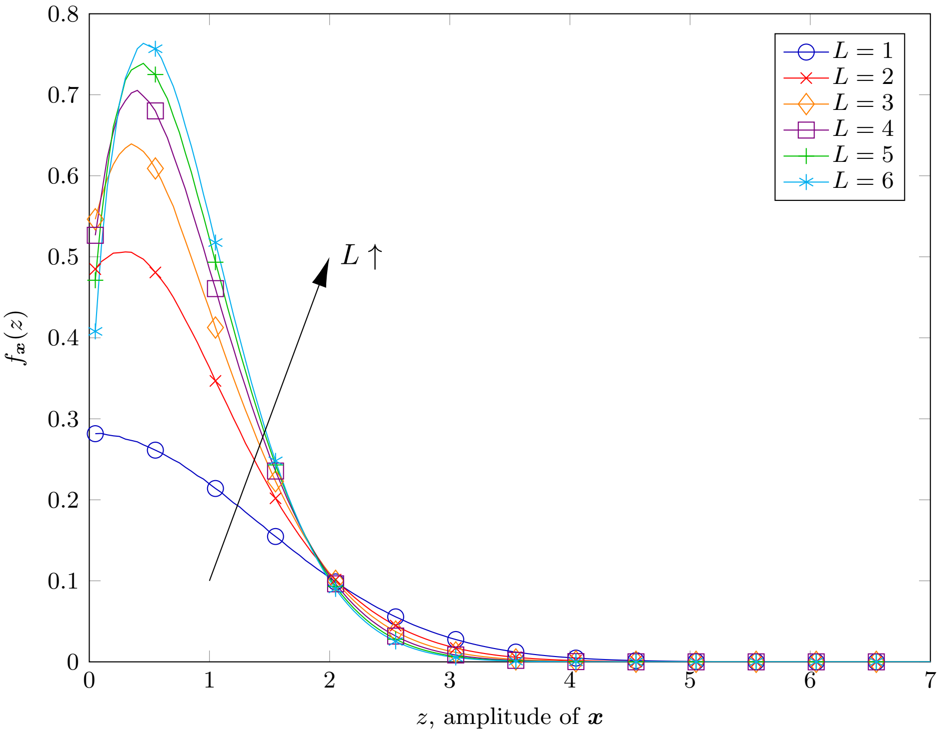

Figure 3.6: PDF of LACO-OFDM signal $\boldsymbol{x}$'s amplitude for different number of layers L and 64QAM modulation.

To expound further, in Fig. 3.9, we provide a 3-D view of the UB-clipped signal $\lceil \boldsymbol{x} \rceil$'s PDF, with the UB set at $z = B_{\mathrm{u}} = 2.818$ V. The impulses representing the LB and UB clipping are also shown in Fig. 3.9, noting that the impulses representing the UB clipping at $z = B_{\mathrm{u}}$ are amplified by a factor of 20 for a better view of their relationships. Observe that the single-layer LACO-OFDM, *i.e.* ACO-OFDM system, has the highest UB clipping distortion, as indicated by its highest impulse $\mathcal{D}$ at $z = B_{\mathrm{u}}$.

3.4 Bit Error Ratio

Compared to conventional RF communications, four major differences appear in the IM/DD LACO-OFDM scheme.

- Despite the fact that the signal suffers from complex-valued noise during communication, the optical signal modulated according to IM/DD scheme only processes the real-valued parts. Therefore, the imaginary part of the TD noise does not affect the communications quality, which halves the degradation imposed by AWGN.

- The diodes at the TX have limited dynamic ranges, hence they require clipping of the signal amplitude at the UB. Due to the non-Gaussian PDF of the LACO-OFDM signal, the clipping effects require particular attention.

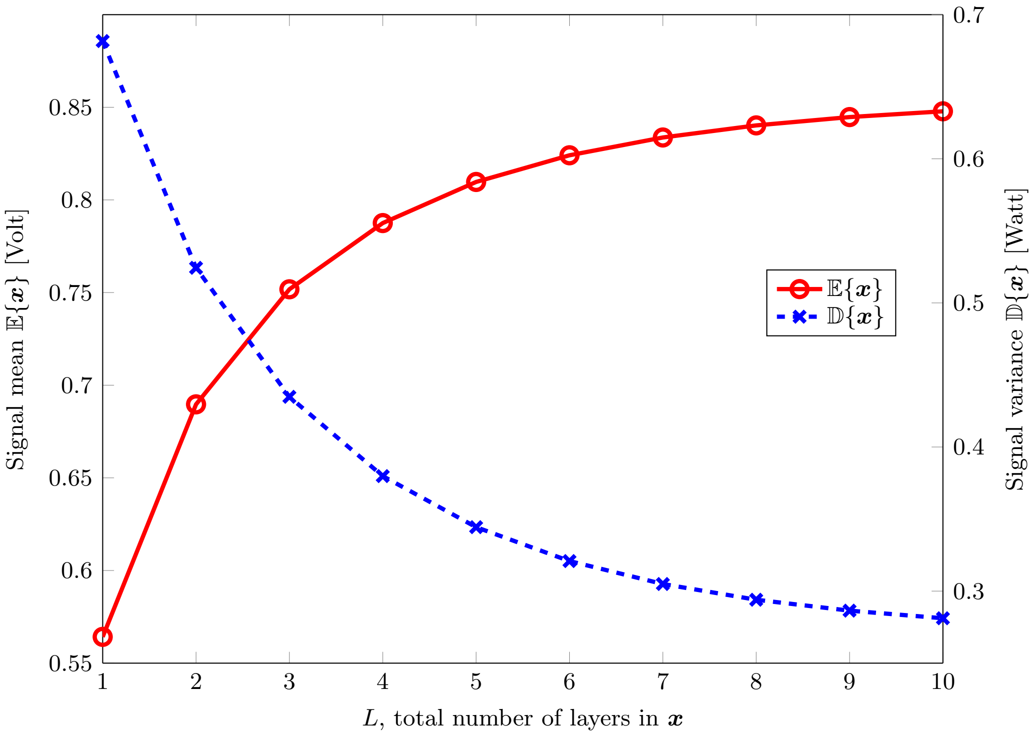

Figure 3.7: Mean and variance of the LACO-OFDM signal $\boldsymbol{x}$'s amplitude for different number of layers L, under a normalised signal power of $P_{\text{LACO}} = 1$ W.

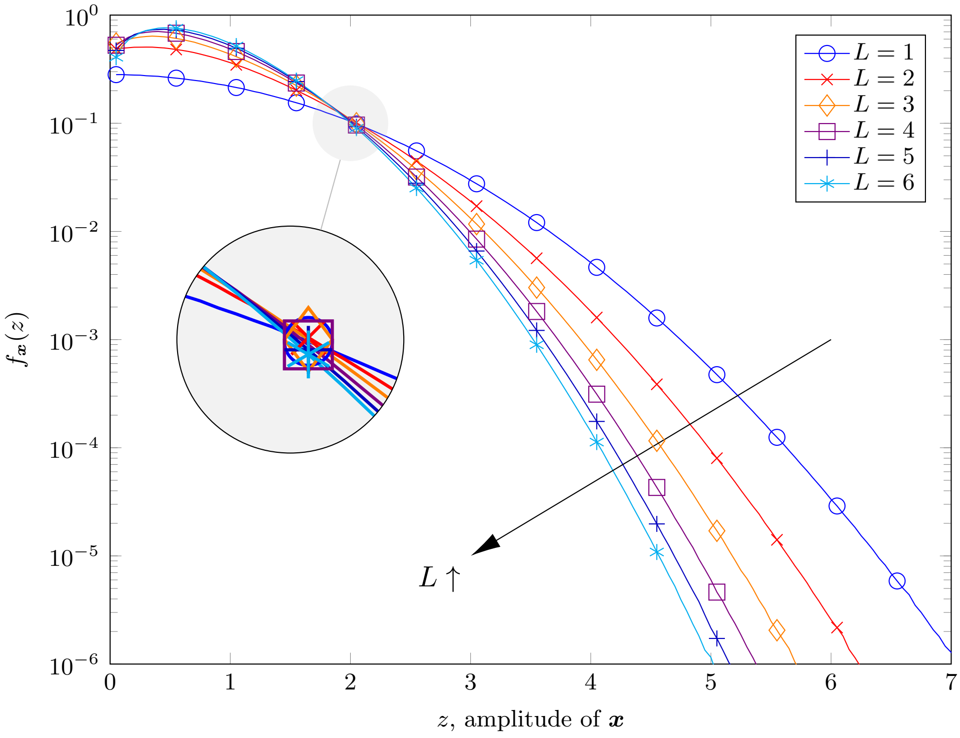

Figure 3.8: Fig. 3.6 plotted on a logarithmic y-axis.

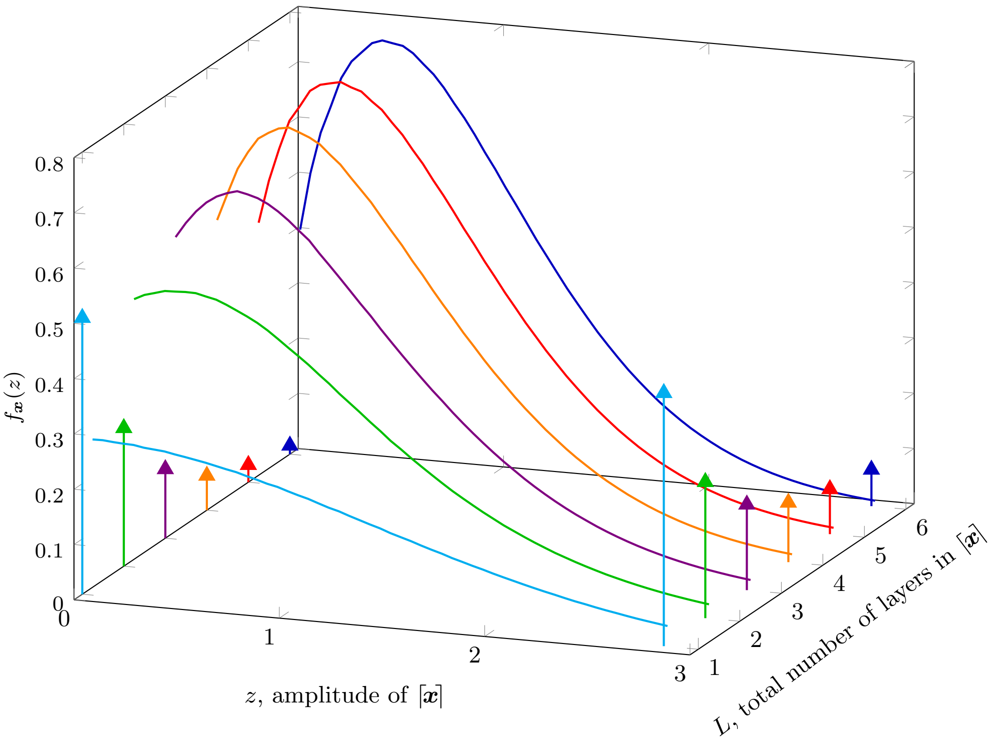

Figure 3.9: PDF of UB-clipped LACO-OFDM signal $\lfloor \boldsymbol{x} \rceil$ at an upper boundary $B_\mathrm{u} = 2.818$ V. The impulses at $z = B_\mathrm{u}$ have been amplified 20 times for a better legibility.

- For LACO-OFDM, the decision errors of a specific layer degrade the following layers. Furthermore, the RX also imposes clipping distortion.
- Due to the multi-layer nature of LACO-OFDM, both the number of layers and the modulation scheme utilised on each layer would affect the overall bit rate, which in turn affects the energy per bit, E_b.

The following parts of this section discuss the influence of the last three points on the BER.

3.4.1 Clipping

According to Sec. 3.2.1, LACO-OFDM experiences both LB and UB clipping. Their effects will be discussed separately.

For each of the layer signals $\boldsymbol{s}_l$ that is clipped at the LB, the power is halved, but no information loss is observed, due to the symmetric nature of ACO-OFDM. The clipping distorts the signal and reduces its power, which may be amplified to compensate for the clipping-induced power-reduction. More details about the LB clipping capable of avoiding information-loss can be found in Appendix A.3.

However, the UB clipping of the combined signal $\boldsymbol{x}$ has a more severe effect. Specifically, the UB clipping reduces the signal energy of $\boldsymbol{x}$, which again may be modelled by a simple attenuation factor κ that is related to the clipping threshold B_u (with the unit being Volt), which corresponds to a clipping ratio of

$$\tau = 20\log_{10}\left(\frac{B_\mathrm{u}}{\sqrt{P_\mathrm{LACO}}}\right)\ \mathrm{dB}, \tag{3.25}$$

where P_LACO is the power of $\boldsymbol{x}$ given in Eq. (3.16).

This UB clipping can be compensated in the same way as for LB clipping, while the estimation of the value κ can be performed at the RX with the aid of a training sequence. On the other hand, the non-linear process also introduces upper harmonics that may spread across all subcarriers. A simplified model of clipping distortion based on [79] is given below, where the power of the clipped part quantifies the clipping distortion of

$$\sigma_\mathrm{c}^2 = \int_{B_\mathrm{u}}^{+\infty} (z - B_\mathrm{u})^2 f_{\boldsymbol{x}}(z)\,\mathrm{d}z \tag{3.26}$$

Therefore, the clipping process affects the equivalent communication SNR by reducing the power of the signal and by increasing the noise power, which undoubtedly degrades the BER performance, as shown below:

$$\lceil \boldsymbol{x} \rceil = \kappa\boldsymbol{x} + \boldsymbol{n}_\mathrm{c}, \tag{3.27}$$

where $\boldsymbol{n}_\mathrm{c}$ is the UB clipping noise with variance σ_c^2 defined in Eq. (3.26).

Remark 3.2. Similar to Remark 3.1, Bussgang's theorem cannot be applied to the clipping analysis of LACO-OFDM associated with $L \geq 2$, because the amplitude of the signal is no longer Gaussian distributed. Therefore, despite $\boldsymbol{n}_\mathrm{c}$ being statistically uncorrelated with $\boldsymbol{x}$ in theory, it is not necessarily Gaussian distributed.

Example 3.1. *To further illustrate this, an example of UB clipping for a 2-layer LACO-OFDM signal has been provided in Fig. 3.10.*

To elaborate, in Fig. 3.10(a), a LACO-OFDM signal having a total of 2 layers is presented, whose average signal power has been normalised to 1 W. The signal is then subjected to an UB clipping having a clipping ratio of $\tau = 9$ *dB, corresponding to a clipping boundary of* $B_\mathrm{u} = 2.818$ *V, according to Eq.* (3.25).

The clipped signal $\lceil \boldsymbol{x} \rceil$ *is shown in Fig. 3.10(b), together with the attenuated signal* $\kappa\boldsymbol{x}$*, based on the model of Eq.* (3.27)*. We then obtain the clipping noise* $\boldsymbol{n}_\mathrm{c}$ *in Fig. 3.10(c). While the majority of the samples in* $\boldsymbol{n}_\mathrm{c}$ *is positive, there is a pair of negative values, corresponding to the two clipped samples in* $\boldsymbol{x}$*. Finally, we analyse the distribution of* $\boldsymbol{n}_\mathrm{c}$ *and provide its PDF in Fig. 3.10(d), which is clearly non-Gaussian.*

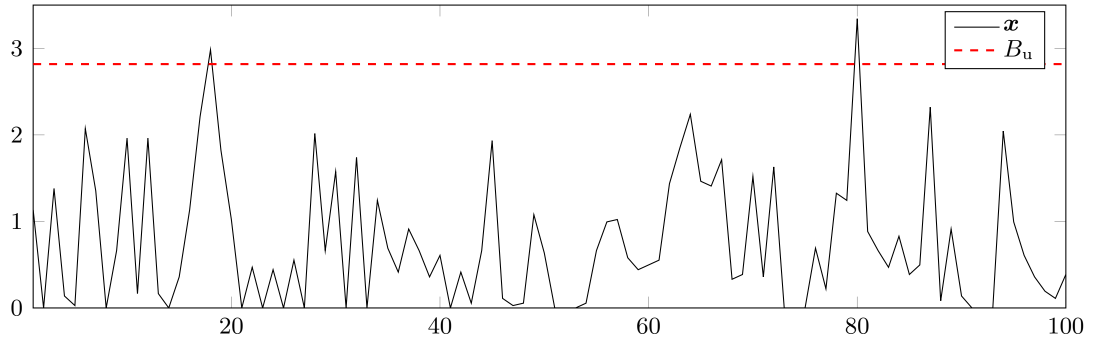

(a) Original signal

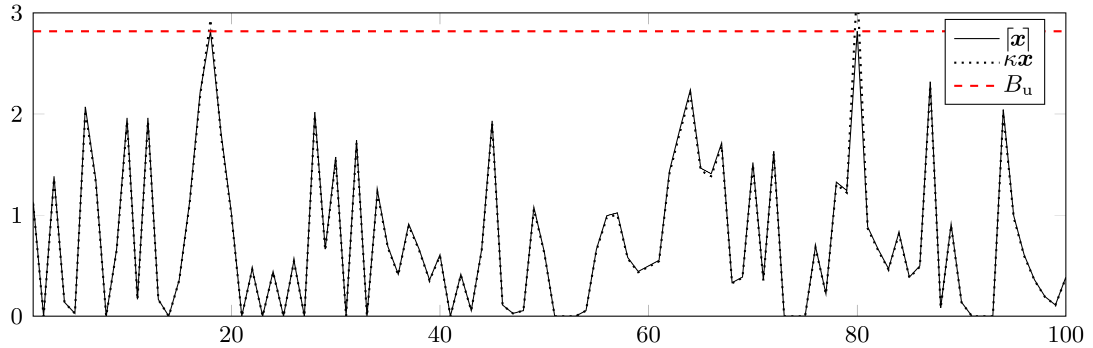

(b) UB-clipped Signal

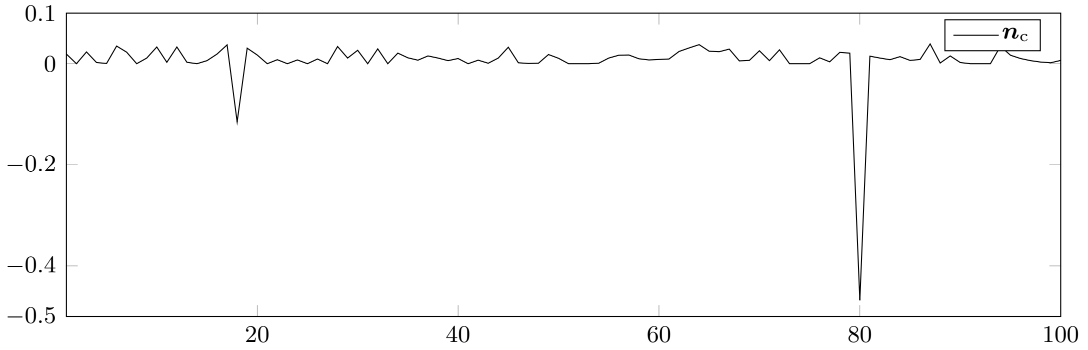

(c) UB clipping noise (positive side only)

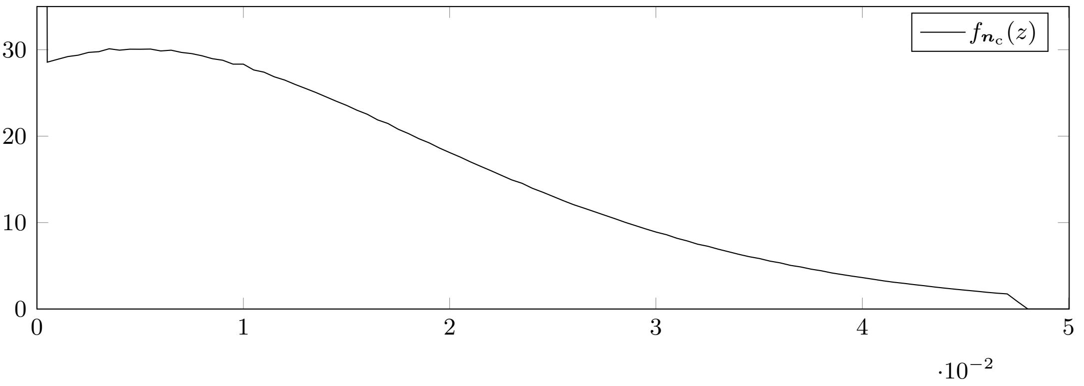

(d) PDF of the UB clipping noise (positive side only)

Figure 3.10: Example of a 3-layer LACO-OFDM signal's UB clipping process at $\tau = 9$ dB.

3.4.2 Inter-Layer Interference

Each base layer of LACO-OFDM generates its own ILI and influences that of its higher layers.

At the RX, layer 1's signal (represented as $\hat{\boldsymbol{S}}_1$ in FD) is immune to ILI and can be detected directly, as it has been shown in Eq. (2.13). More generally, the detection process for layer l of the LACO-OFDM signal after the removal of the previous layers' clipping distortion is given by:

$$\hat{S}_l[u] = \arg\min_{X \in \mathcal{S}_l} |X - 2R_l[u]|\,, \qquad 0 \leq u \leq \left(\frac{K_l}{4} - 1\right), \tag{3.28}$$

where $\hat{\boldsymbol{S}}_l$ is a length-$K_l/4$ stream of symbols from the modulated symbol set $\mathcal{S}_l$ for layer l, while $\boldsymbol{R}_l$ is the FD signal of layer l obtained at the RX by subtracting all the distortions generated by the former layers from the originally received signal $\boldsymbol{r}$, yielding:

$$\begin{aligned} R_l[u] &= \overline{R}_l[2^l u + 2^{l-1}] = \overline{R}_{l-1}[2^l u + 2^{l-1}] - \underline{\boldsymbol{I}}_{l-1}[2^l u + 2^{l-1}] \\ &= \cdots = \overline{R}_1[2^l u + 2^{l-1}] - \sum_{i=1}^{l-1} \underline{\boldsymbol{I}}_i[2^l u + 2^{l-1}]. \end{aligned} \tag{3.29}$$

Here, $\underline{\boldsymbol{I}}_l$ represents the clipping distortion created by layer l at the receiver, which, based on Fig. 2.8, is generated by

$$\underline{\boldsymbol{I}}_l \overset{⑪}{=\!=} \mathcal{F}\{\hat{\boldsymbol{s}}_l\} \overset{⑩}{=\!=} \mathcal{F}\{\lfloor \overline{\hat{\boldsymbol{s}}}_l \rfloor\} \overset{⑨}{=\!=} \mathcal{F}\Big\{\Big\lfloor \mathcal{F}^{-1}\Big\{\overline{\hat{\boldsymbol{S}}}_l\Big\}\Big\rfloor\Big\}, \tag{3.30}$$

where $\mathcal{F}\{\cdot\}$ and $\mathcal{F}^{-1}\{\cdot\}$ denote respectively the Fourier transform and inverse Fourier transform, while $\lfloor\cdot\rfloor$ indicates the clipping of a signal at its lower boundary (LB) $z = 0$.

Therefore, if an error is made when making a decision for layer l, so that $\hat{S}_l[u] \neq S_l[u]$, it will not only affect the BER behaviour of the current layer, but also spread across all of its following layers (layers $(l+1) \sim L$).

More specifically, as we have assumed previously, only single symbol detection errors are considered, which is equivalent a Hamming distance of 1. In this way, the interference generated by a single decision error can be quantified as the nearest constellation pattern distance $d_{\min,l}$ from the symbol set $\mathcal{S}_l$. Tab. 3.2 summarises the respective $d_{\min}$ values for some of the popular modulation schemes, under the assumption of the average symbol power being unitary.

After the re-generation process including the IFFT, asymmetric clipping and FFT, this error propagation process will contaminate all the $K/2^{l-1}$ subcarriers, just like its clipping noise does. Hence, when considering the BER of a specific layer, in addition to the AWGN noise inflicted by the channel, the interference imposed by all its previous layers should also be taken into account.

Table 3.2: Minimum Distance $d_{\min}$ for Different Modulation Constellations

Scheme	$d_{\min}$	Scheme	$d_{\min}$
BPSK/2PAM	2	4QAM	$\sqrt{2}$
4PAM	$\frac{2\sqrt{5}}{5}$	16QAM	$\frac{\sqrt{10}}{5}$
8PAM	$\frac{2\sqrt{21}}{21}$	64QAM	$\frac{\sqrt{42}}{21}$

The ILI $\mathcal{G}_i$ generated by the layer i can be calculated from the Symbol Error Rate (SER) $\mathbb{P}_{\mathrm{s},\,i}$ of layer i (to be derived later) and its corresponding quantified interference $d_{\min,i}$ for each single symbol error, yielding:

$$\mathcal{G}_i = \mathbb{P}_{\mathrm{s},\,i} \cdot d^2_{\min,i}. \tag{3.31}$$

Thus, for layer l, the cumulative sum of all its previous layers' interference, namely $\sum_{i=1}^{l-1} \mathcal{G}_i$, should be included when calculating the energy-per-bit-to-noise-power-spectral-density ratio $\gamma_{\mathrm{b},\,l}$ of layer l.

3.4.3 LACO-OFDM Bit Rate

Based on the previous discussions in Sec. 2.4, assuming that layer l uses a constellation size of M_l, the corresponding number of information bits transmitted by this layer becomes:

$$B_l = \frac{K}{2^{l+1}} \log_2 M_l. \tag{3.32}$$

Then, the total amount of information transmitted by an L-layer LACO-OFDM signal would be

$$\sum_{l=1}^{L} B_l = K \cdot \sum_{l=1}^{L} 2^{-l-1} \log_2 M_l. \tag{3.33}$$

Hence, for LACO-OFDM, the overall energy-per-bit-to-noise-power-spectral-density ratio $\gamma_{\mathrm{b},\,l}$ and the symbol-energy-to-noise ratio E_s/N_0 have the following relationship

$$\frac{E_s}{N_0} = \gamma_{\mathrm{b},\,l} \cdot \sum_{l=1}^{L} 2^{-l-1} \log_2 M_l. \tag{3.34}$$

Moreover, when using the *Equal Power per Bit* strategy and the common assumption of employing the same modulation scheme for all layers, we could simplify the variables as follows:

$$\gamma_{\mathrm{b},\,l} \equiv \gamma_{\mathrm{b}}, \qquad \forall l. \tag{3.35}$$

3.4.4 Overall BER Performance

The BER and SER performance under an AWGN channel for layer l of the LACO-OFDM, which relies on an M_l-QAM modulation scheme, will be dependent both on the clipping distortion as well as on the BER performance of all its previous layers, which can be expressed as [71]

$$\mathbb{P}_{\mathrm{b},\,l} \approx \frac{4(\sqrt{M_l}-1)}{\sqrt{M_l}\cdot\log_2\sqrt{M_l}}\cdot Q\left(\sqrt{\frac{3\Gamma_{\mathrm{s},\,l}\log_2 M_l}{M_l-1}}\right), \tag{3.36}$$

$$\mathbb{P}_{\mathrm{s},\,l} \approx \frac{4(\sqrt{M_l}-1)}{\sqrt{M_l}}\cdot Q\left(\sqrt{\frac{3\Gamma_{\mathrm{s},\,l}\log_2 M_l}{M_l-1}}\right), \tag{3.37}$$

where $Q(\cdot)$ is the tail probability of the standard normal distribution given by

$$Q(x) = \frac{1}{\sqrt{2\pi}}\int_x^{\infty}\exp\left(-\frac{z^2}{2}\right)\,\mathrm{d}z, \tag{3.38}$$

and $\Gamma_{\mathrm{s},\,l}$ is the signal-to-noise-and-interference-plus-distortion ratio of layer l.

For $l > 1$, $\Gamma_{\mathrm{s},\,l}$ can be expressed as

$$\Gamma_{\mathrm{s},\,l} = \frac{\kappa^2 E_s}{N_0 + \sum_{i=1}^{l-1}\mathcal{G}i + \sigma_{\mathrm{c}}^2} = \frac{\overbrace{\kappa^2}^{(\mathrm{a}_1)}\ \overbrace{\gamma_{\mathrm{b}}N_0}^{(\mathrm{b})}\overbrace{\sum_{l=1}^{L}(2^{-l-1}\log_2 M_l)}^{(\mathrm{c})}}{\underbrace{N_0}_{(\mathrm{d})}+\underbrace{\sum_{i=1}^{l-1}\mathcal{G}_i}_{(\mathrm{e})}+\ \underbrace{\sigma_{\mathrm{c}}^2}_{(\mathrm{a}_2)}}, \tag{3.39}$$

where the interpretation of the components in Eq. (3.39) is given below in Tab. 3.3.

Table 3.3: Interpretation of the Components in Eq. 3.39

Label	Component	Meaning	Definition
a	(a$_1$) κ^2	UB clipping attenuation	Sec. 3.4.1
	(a$_2$) σ_{c}^2	UB clipping noise power	
b	$\gamma_{\mathrm{b}}N_0$	Signal power per bit	
c	$\sum_{l=1}^{L}(2^{-l-1}\log_2 M_l)$	Overall bit rate	Sec. 3.4.3
d	N_0	AWGN power	
e	$\sum_{i=1}^{l-1}\mathcal{G}_i$	ILI	Sec. 3.4.2

For layer 1, the cumulative sum in the middle of the denominator (part e) can be neglected. Furthermore, if no UB clipping is considered, both κ and σ_c^2 (part a) can be omitted.

Finally, the overall BER performance of the LACO-OFDM system is given by the weighed average of each layer:

$$\mathbb{P}_{\mathrm{b}} = \frac{1}{\sum_{l=1}^{L} 2^{-l} \log_2 M_l} \sum_{l=1}^{L} 2^{-l} \mathbb{P}_{\mathrm{b},\,l} \log_2 M_l. \tag{3.40}$$

It is worth noting that for $l \geq 2$, the BER of the layer signal $\mathbb{P}_{\mathrm{b},\,l}$ always depends on the BER of its previous layers $(\mathbb{P}_{\mathrm{b},\,1}, \ldots, \mathbb{P}_{\mathrm{b},\,l-1})$, due to the cascading ILI term $\sum_i \mathcal{G}_i$. Therefore, in line with its receiver signal processing, the theoretical BER calculation of LACO-OFDM should also be carried out in a layer-by-layer manner, commencing from layer 1, where $\sum_i \mathcal{G}_i = 0$.

3.4.5 Numerical Results

Figure 3.11 shows the BER versus γ_{b} performance of each layer in a 4-layer LACO-OFDM (4LACO-OFDM) system without any UB clipping. The simulated BER results of each of the four layers are represented by the markers, while their analytical curves are marked by solid lines in all figures. The overall average BER performance of all four layers is also provided.

According to Fig. 3.11, the four layers exhibit different BER behaviours at low SNRs. Naturally, the first layer has the best BER, since no interference is imposed by the higher layers. By contrast, observed from Eq. (3.39) that all higher layers suffer from the ILI inflicted by the previous layers. As the SNR increases, the four BER curves tend to converge to the 16QAM BER curve. More explicitly, Eqs. (3.31) and (3.37) show that as the SNR increases, the SER of the lower layers is reduced. Hence, the interference imposed to the higher layers is also reduced, which in turn decreases the SER of the higher layers. Gradually all the interferences turned to zero and in this way all layers start to behave the same way as the first layers, since no more ILI exists.

Figure 3.12 shows the BER of LACO-OFDM both with and without a $\tau = 9\,\mathrm{dB}$ UB clipping operation.

The derivation of Eqs. (3.39), (3.40) is verified here by the simulations. As expected, the lower-throughput LACO-OFDM composed of less layers exhibit a better BER performance. On the other hand, since the PAPR of more layers is lower, they have better immunity against distortion, when clipped at the UB. Therefore, the BER curves of unclipped and clipped situations are closer to each other for signals composed of more layers. Furthermore, the BER curves of clipped signals tend to converge at a certain

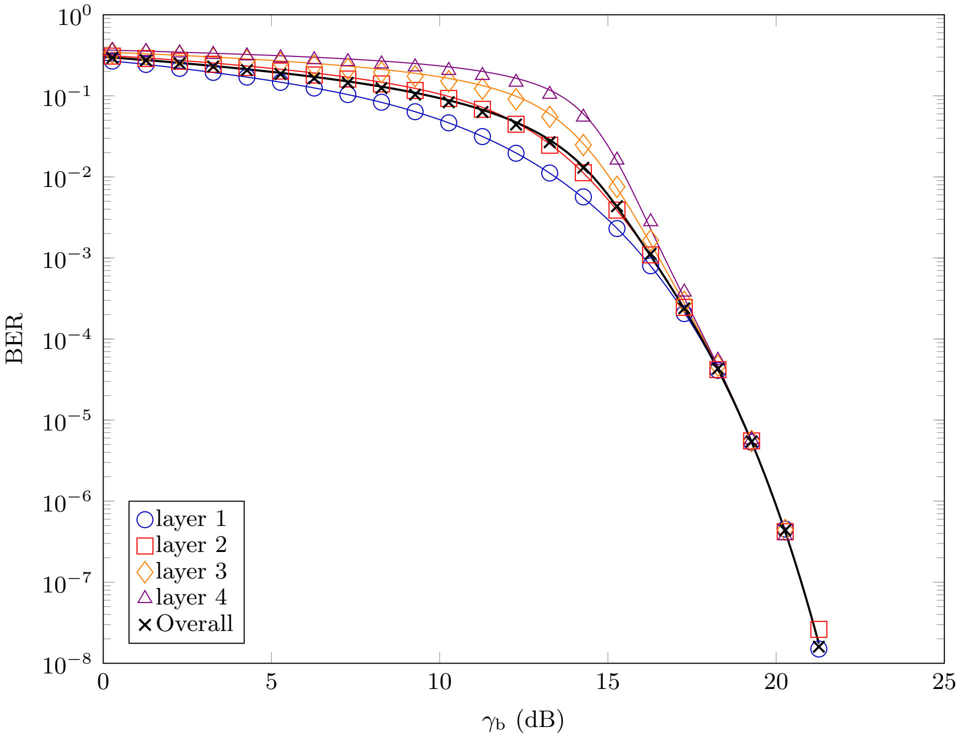

Figure 3.11: BER of all layers of 4LACO-OFDM signals for 16QAM modulation. Lines represent the theoretical values of Eqs. (3.36), (3.40) and markers the simulation results. All parameters are summarised in Table 3.1.

level, when the UB clipping distortion dominates the performance. Thanks to their lower PAPR, the schemes having more layers suffer from less distortion at the same clipping ratio, which leads to their lower BER.

According to Eq. (3.39), the clipping distortion is the major BER contributor when γ_b is high. Meanwhile, Eq. (3.26) shows that the clipping distortion is closely related to the upper tail of the signal's PDF, in other words to the signal's PAPR. Therefore, the next section will analyse the PAPR distribution of the LACO-OFDM signal in order to reveal the major factors influencing the clipping distortion.

3.5 Peak to Average Power Ratio

In this spirit, we embark on analysing the LACO-OFDM PAPR with the goal of avoiding the typically high BER performance degradation imposed by the clipping distortion. This section studies the LACO-OFDM PAPR as a function of the number of its layers L and in the next section develops a PAPR reduction method.

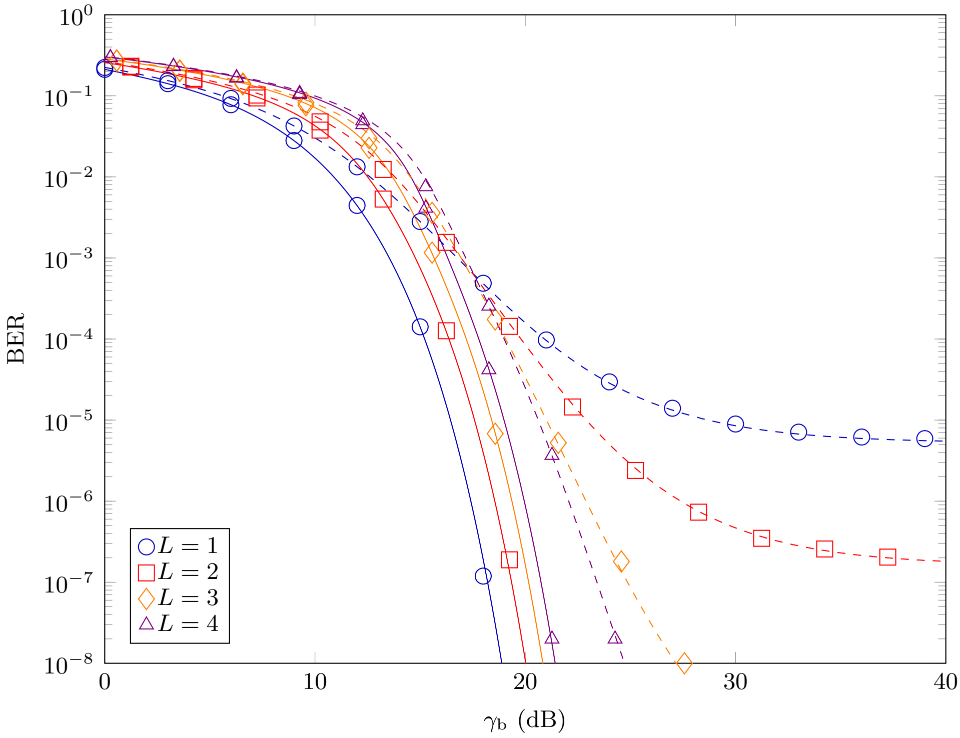

Figure 3.12: Overall BER performance of LACO-OFDM signals with different number of total layers L for 16QAM modulation. Lines represent the theoretical values of Eqs. (3.36), (3.40) and markers the simulation results. Dashed lines represent simulations with UB clipping $\tau = 9$ dB considered, while solid lines the absence of it. All parameters are summarised in Table 3.1.

3.5.1 Derivation of the LACO-OFDM PAPR

We commence with the mathematical definition of the PAPR.

Definition 3.3 (PAPR)**.** For a signal $\boldsymbol{x}$ having K elements $\{x[0], x[1], \dots, x[K-1]\}$, its PAPR is defined as the power ratio of the element with the maximum power over the signal's average power, yielding:

$$\text{PAPR}\{\boldsymbol{x}\} = \frac{\max\limits_{0 \le k \le K-1} |x[k]|^2}{\frac{1}{K} \sum\limits_{k=0}^{K-1} |x[k]|^2}. \tag{3.41}$$

For a length-K LACO-OFDM signal $\boldsymbol{x}$ composed of L layers, the CDF of its PAPR can be formulated as

$$\Pr(\text{PAPR}\{\boldsymbol{x}\} \le z) = \Pr\left(\frac{\max\limits_{0 \le k \le K-1} x^2[k]}{P_{\text{LACO}}} \le z \right), \tag{3.42}$$

where P_{LACO} is the average signal energy of the L-layer LACO-OFDM signal $\boldsymbol{x}$ expressed in Eq. (3.15). This can be further simplified as

$$\begin{aligned}\Pr(\text{PAPR}\{\boldsymbol{x}\} \le z) &= \Pr\Big(\max_{0\le k\le K-1} x[k] \le \sqrt{P_{\text{LACO}} z}\Big) \\ &= \Pr\Big(x[k] \le \sqrt{P_{\text{LACO}} z},\, \forall k = 0, \dots, K-1\Big).\end{aligned} \tag{3.43}$$

Since $\boldsymbol{x}$ can be expanded as the sum of its L unipolar layer signals, for the kth symbol within the signal, we have:

$$x[k] = s_1[k] + s_2[k] + \cdots + s_L[k]. \tag{3.44}$$

Recall that the energy of the symbols on each layer $\boldsymbol{s}_l$ decreases exponentially as the layer index l increases. Hence, the statistical characteristics of the signal $\boldsymbol{x}$ are dominated by *layer 1's* signal $\boldsymbol{s}_1$.

Due to the Hermitian symmetry and asymmetrical clipping, the relationship between the symbol pairs $s_l[k]$ and $s_l\left[k + \frac{K}{2}\right]$ (assuming $0 \le k < \frac{K}{2}$) becomes as follows:

- If the symbol obeys $s_1[k] > 0$, indicating that it was not clipped during the LB clipping process, the corresponding symbol $s_l\left[k + \frac{K}{2}\right]$ will then become 0, because the unclipped $\overline{s}_1[k] = -\overline{s}_1\left[n + \frac{N}{2}\right]$ and the symbol on the right hand side is clipped;
- Conversely, $s_l\left[k + \frac{K}{2}\right] > 0$ also indicates $s_1[k] = 0$.

The probability of having $s_l[k] > 0$ is $\frac{1}{2}$, which is a consequence of their independent distribution. Moreover, the event of having $(s_1[k] > 0)$ is independent of the rest of the symbols $(s_1[k'],\ k' \neq k$ or $k + \frac{K}{2})$ in the signal stream. Therefore, Eq. (3.43) can be re-written based on [75]

$$\begin{aligned}\Pr(\text{PAPR}\{\boldsymbol{x}\} \le z) &= \Pr\Big(x[0] \le \sqrt{P_{\text{LACO}} z},\ x\Big[\frac{K}{2}\Big] \le \sqrt{P_{\text{LACO}} z}\Big) \\ &\quad \times \Pr\Big(x[1] \le \sqrt{P_{\text{LACO}} z},\ x\Big[\frac{K}{2} + 1\Big] \le \sqrt{P_{\text{LACO}} z}\Big) \times \dots \\ &\quad \times \Pr\Big(x\Big[\frac{K}{2} - 1\Big] \le \sqrt{P_{\text{LACO}} z},\ x[K-1] \le \sqrt{P_{\text{LACO}} z}\Big) \\ &= \prod_{k=0}^{\frac{K}{2}-1} \Pr\Big(x[k] \le \sqrt{P_{\text{LACO}} z},\ x\Big[\frac{K}{2} + k\Big] \le \sqrt{P_{\text{LACO}} z}\Big) \\ &= \Big\{\Pr\Big(x[0] \le \sqrt{P_{\text{LACO}} z},\ x\Big[\frac{K}{2}\Big] \le \sqrt{P_{\text{LACO}} z}\Big)\Big\}^{\frac{K}{2}}.\end{aligned} \tag{3.45}$$

The law of full probability can assist us in further simplifying Eq. (3.45) by considering the cases, when either $s_1[k]$ or $s_1\left[\frac{K}{2}+k\right]$ is zero, yielding:

$$\begin{aligned}
&\Pr\bigg(x[0] \leq \sqrt{P_{\text{LACO}} z},\ x\left[\frac{K}{2}\right] \leq \sqrt{P_{\text{LACO}} z}\bigg) \\
&= \Pr\bigg(x[0] \leq \sqrt{P_{\text{LACO}} z},\ x\left[\frac{K}{2}\right] \leq \sqrt{P_{\text{LACO}} z},\ s_1[0] > 0\bigg) + \\
&\quad \Pr\bigg(x[0] \leq \sqrt{P_{\text{LACO}} z},\ x\left[\frac{K}{2}\right] \leq \sqrt{P_{\text{LACO}} z},\ s_1\left[\frac{K}{2}\right] > 0\bigg) \\
&= \Pr\Big(x[0] \leq \sqrt{P_{\text{LACO}} z},\ s_1[0] > 0\Big) + \Pr\bigg(x\left[\frac{K}{2}\right] \leq \sqrt{P_{\text{LACO}} z},\ s_1\left[\frac{K}{2}\right] > 0\bigg) \\
&= 2\Pr\Big(x[0] \leq \sqrt{P_{\text{LACO}} z},\ s_1[0] > 0\Big) \\
&= 2\left(F_{\boldsymbol{x}}\Big(\sqrt{P_{\text{LACO}} z}\Big) - \frac{1}{2}\right) = 2F_{\boldsymbol{x}}\Big(\sqrt{P_{\text{LACO}} z}\Big) - 1, \qquad (3.46)
\end{aligned}$$

where $F_{\boldsymbol{x}}(\cdot)$ is the CDF of the signal $\boldsymbol{x}$ according to Eq. (3.23).

Therefore, the CDF of the PAPR can be expressed as

$$\begin{aligned}
\Pr(\text{PAPR}\{\boldsymbol{x}\} \leq z) &= \Big[2F_{\boldsymbol{x}}\Big(\sqrt{P_{\text{LACO}} z}\Big) - 1\Big]^{\frac{K}{2}} \\
&= \left[2\int_{-\infty}^{\sqrt{P_{\text{LACO}} z}} f_{\boldsymbol{x}}(z_L)\, \mathrm{d}z_L - 1\right]^{\frac{K}{2}}.
\end{aligned} \qquad (3.47)$$

Finally, the Complementary CDF (CCDF) of the signal's PAPR can be easily obtained as

$$\Pr(\text{PAPR}\{\boldsymbol{x}\} > z) = 1 - \Pr(\text{PAPR}\{\boldsymbol{x}\} \leq z)\,. \qquad (3.48)$$

3.5.2 Discussion

For LACO-OFDM consisted by more layers, less zeros would be found on the TD signal, due to the superposition of more layers. Meanwhile, the average power of the signal increases faster than the peak power as more layers are utilised.

More specifically, if we are to fix the average signal power of the different layers, we will find that the CDF of the higher layer LACO-OFDM would become more steep, which is formulated as:

$$F_{\boldsymbol{x}_{L_1}}(z) \geq F_{\boldsymbol{x}_{L_2}}(z)\,, \qquad \text{for } L_1 > L_2 \qquad (3.49)$$

where

$$\boldsymbol{x}_{L_1} = \sum_{l=1}^{L_1} \boldsymbol{s}_l \qquad \text{and} \qquad \boldsymbol{x}_{L_2} = \sum_{l=1}^{L_2} \boldsymbol{s}_l, \qquad (3.50)$$

while ensuring the same P_{LACO} for both signals by

$$\mathbb{E}\{\boldsymbol{x}_{L_1}^2\} = \mathbb{E}\{\boldsymbol{x}_{L_2}^2\}\,. \tag{3.51}$$

This yields that the probability $\Pr(\mathrm{PAPR}\{\boldsymbol{x}\} \leq z)$ increases with L. In other words, the higher layer LACO-OFDM signals tend to have a lower PAPR than the lower layer signals. Therefore, it is plausible that LACO-OFDM mitigates the PAPR problem.

3.5.3 Numerical Results

Figure 3.13 provides the CCDF of a 2-layer (*i.e.* $L = 2$) LACO-OFDM signal. Different number of FFT points K are used, which results in different length of the LACO-OFDM signal/symbol. A logarithmic vertical axis is selected for the CCDF axis for a more clear view.

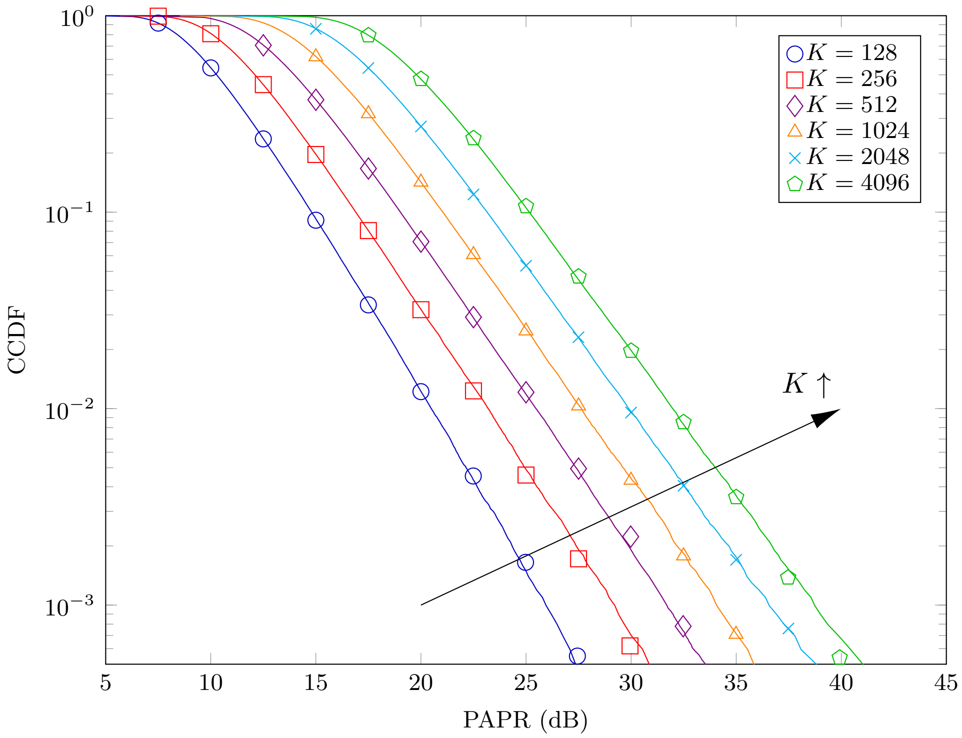

Figure 3.13: CCDF of the 2-Layer LACO-OFDM TD signal's PAPR using different number of subcarriers K. Lines represent the theoretical values of Eq. (3.47) and markers the simulation results. All parameters are summarised in Table 3.1.

According to Fig. 3.13, the PAPR generally increases upon increasing the number of FFT points, which corresponds to the length of each OFDM symbol. This trend is identical to those found in RF-OFDM systems, where increasing the number K of subcarrier increases the chance of having more FD symbols adding up during the IFFT processing, hence resulting in a TD sample of higher amplitude. On the other hand, the hypothetical curves based on the theoretical analysis of Eq. (3.47) closely match the simulation results, which verifies the above derivations.

Figure 3.14 compares the CCDF of several LACO-OFDM time-domain signals' PAPR, where the number of subcarriers K is fixed to 1024. Various number of layers L are used.

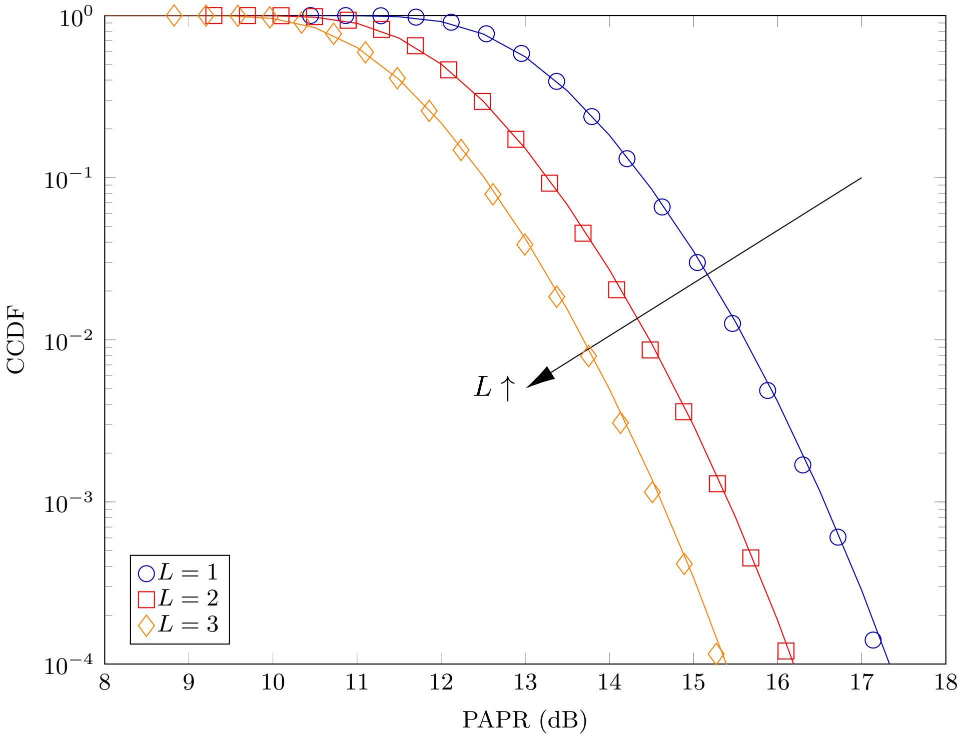

Figure 3.14: CCDF of the PAPR of 1024-subcarrier LACO-OFDM TD signals. Lines represent the theoretical values of Eq. (3.47) and markers the simulation results. All parameters are summarised in Table 3.1.

The trend that LACO-OFDM signal having more layers tends to exhibit lower PAPR can be clearly observed when the total number of subcarriers is fixed. This means that the peak power increases slower than the average power upon combining more layers. This is consistent with the analysis in this section.

3.6 PAPR Reduction

Although increasing the number of layers reduces the PAPR, further improvements may be achieved with the aid of tone injection [74, 76], as demonstrated in this section. We continue with the signal model of the proposed method, followed by the conversion of the PAPR reduction problem into a Mixed Integer Linear Programming (MILP) problem. A further simplification of the optimisation problem using ℓ_1-minimisation is also proposed.

3.6.1 Tone-Injected LACO-OFDM Signal

3.6.1.1 Signal Formulation

For each of the symbols in the original FD signals $\boldsymbol{S}_l$, an additional symbol is added to it, *i.e.*

$$\begin{gathered} Y_l[u] = S_l[u] + T_l[u], \\ l = 1, 2, \ldots, L, \qquad u = 0, 1, \ldots, K_l/4 - 1 \end{gathered} \tag{3.52}$$

where $\boldsymbol{T}_l$ is the injecting signal and $\boldsymbol{Y}_l$ is the resultant signal. The modified symbol will shift the corresponding point in the constellation diagram to one of a few legitimate locations and can be recovered losslessly at the RX by the modulo operation, regardless of which location it was shifted to.

Figure 3.15 shows an example of the constellation pattern of a 16QAM signal, demonstrating the tone-injection method.

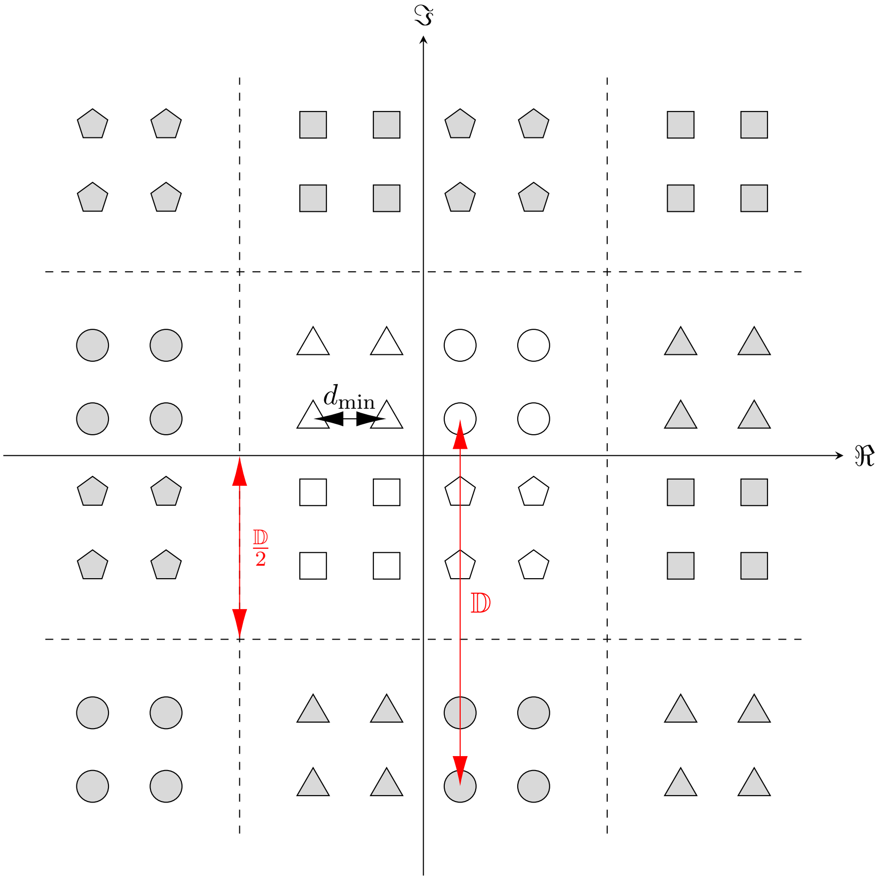

Figure 3.15: Constellation diagram of 16QAM featuring tone-injection technique. Hollow points in the centre are from the original constellation, while the shaded points around are additional after injection. Points of same marker indicate possible shifting locations when modified.

The 16 hollow markers in the centre are the constellation patterns $\mathcal{S}_l$ of the original signal $\boldsymbol{S}$. The real and imaginary parts of the symbol may or may not be shifted by a constant distance $\mathbb{D}$ for mitigating the PAPR. When shifting by $\mathbb{D}$ is invoked, this may shift the related constellation point to other quadrants. The full set of markers shown in Fig. 3.15 represents the legitimate constellation points in $\boldsymbol{Y}_l$, while the shaded ones represent the shifted points, whose original markers are of the same shape but left hollow and located in the centre.

3.6.1.2 Signal Detection

Clearly, a decision threshold of $\frac{\mathbb{D}}{2}$ can be set for both the real and imaginary branches in order to classify the points into two categories, namely those that are shifted and those that remain in their original place. Based on the quadrant symmetry observed in Fig. 3.15, the RX eliminates the shifting of the points by invoking the modulo-$\frac{\mathbb{D}}{2}$ operation to find the corresponding original position, hence recovering the signal losslessly. Explicitly, the detection process, which is step ⑧ of Fig. 2.8 and originally formulated in Eq. (3.28), has to be modified into

$$\hat{\boldsymbol{S}}_l[u] = \arg\min_{X\in\mathcal{S}_l}\left|X - \mathrm{Mod}\left(2R_l[u],\ \frac{\mathbb{D}}{2}\right)\right|, \qquad 0 \le u \le \left(\frac{K_l}{4} - 1\right), \tag{3.53}$$

where the complex modulo function $\mathrm{Mod}(\cdot,\cdot)$ is given by:

$$\mathrm{Mod}(a + bj,\ c) = \mathrm{mod}(a,\ c) + j\mathrm{mod}(b,\ c), \qquad a, b, c \in \mathbb{R}. \tag{3.54}$$

3.6.1.3 Signal Injection for Reducing the PAPR

The injected signal $\boldsymbol{T}_l$ is appropriately selected, so that the resultant signal $\boldsymbol{Y}_l$ exhibits a reduced PAPR, where each subcarrier symbol of it can be decomposed as

$$T_l[u] = -\mathrm{sgn}(\Re\{S_l[u]\})\, p_{l,u}\mathbb{D} - j\mathrm{sgn}(\Im\{S_l[u]\})\, q_{l,u}\mathbb{D}, \tag{3.55}$$

where $\mathrm{sgn}(\Re\{\cdot\})$ and $\mathrm{sgn}(\Im\{\cdot\})$ return the sign of the real and imaginary parts of the symbol, so that only un-shifted symbols will stay within the original quadrant. The sign function is defined as

$$\mathrm{sgn}(x) = \begin{cases} -1, & \text{if } x < 0, \\ 0, & \text{if } x = 0, \\ 1, & \text{if } x > 0, \end{cases} \qquad \text{for } x \in \mathbb{R}. \tag{3.56}$$

The variables $\boldsymbol{p}$ and $\boldsymbol{q}$ in Eq. (3.55) are Booleans used for indicating whether or not the real and imaginary parts will be shifted, respectively, where 1 represents shifting and 0 the absence of it, formulated as

$$\begin{aligned} &p_{l,u} \in \{0,1\}, && q_{l,u} \in \{0,1\}, \\ &\forall l = 1,2,\ldots,L, && \forall u = 0,1,\ldots,\left(\frac{K_l}{4}-1\right). \end{aligned} \tag{3.57}$$

Still referring to Eq. (3.55) and Fig. 3.15, the shifting $\mathbb{D}$ is quantified by

$$\mathbb{D} = \rho d_{\min}\sqrt{M}, \tag{3.58}$$

where $\rho > 1$ is a scaling factor, $d_{\min}$ is the minimum distance for symbols with unitary average power detailed in Tab. 3.2, and M is the number of constellation points in the modulation scheme.

The subcarrier symbols of the resultant signals $\boldsymbol{Y}_l$ are then mapped to their desired subcarriers in the usual manner to form $\overline{\boldsymbol{Y}}_l$ in the FD as in Eq. (2.6), which have a length of K and satisfy the Hermitian symmetry for all layers, as shown in Fig. 3.4 ⑭. Then, the IFFT is performed on $\overline{\boldsymbol{Y}}_l$ and the resultant TD signal $\overline{\boldsymbol{y}}_l$ of layer l can be expressed as

$$\begin{aligned} \overline{y}_l[n] &= \frac{1}{\sqrt{K}}\sum_{k=0}^{K-1}\overline{Y}_l[k]W_K^{kn} \\ &\overset{(2.6)}{=\!=} \frac{1}{\sqrt{K}}\sum_{u=0}^{\frac{K_l}{4}-1}\left[Y_l[u]W_K^{(2^l u+2^{l-1})n} + Y_l^*[u]W_K^{[K-(2^l u+2^{l-1})]n}\right] \\ &\overset{(3.52)}{=\!=} \frac{1}{\sqrt{K}}\sum_{u=0}^{\frac{K_l}{4}-1}\left[(S_l[u]+T_l[u])W_K^{(2^l u+2^{l-1})n} + (S_l^*[u]+T_l^*[u])W_K^{[K-(2^l u+2^{l-1})]n}\right] \\ &\overset{(A.9)}{=\!=} \frac{1}{\sqrt{K}}\sum_{u=0}^{\frac{K_l}{4}-1}\left((S_l[u]+T_l[u])W_K^{(2^l u+2^{l-1})n} + (S_l^*[u]+T_l^*[u])W_K^{-(2^l u+2^{l-1})n}\right) \\ &= \frac{1}{\sqrt{K}}\sum_{u=0}^{\frac{K_l}{4}-1}\left((S_l[u]+T_l[u])W_K^{(2^l u+2^{l-1})n} + \left[(S_l[u]+T_l[u])W_K^{-(2^l u+2^{l-1})n}\right]^*\right) \\ &= 2\cdot\Re\left\{\frac{1}{\sqrt{K}}\sum_{u=0}^{\frac{K_l}{4}-1}(S_l[u]+T_l[u])W_K^{(2^l u+2^{l-1})n}\right\}, \end{aligned} \tag{3.59}$$

which follows a similar method as in Appendix A.1.1. Meanwhile, by splitting the summations of $\boldsymbol{S}_l$ and $\boldsymbol{T}_l$ in Eq. (3.59), the second part becomes

$$\begin{aligned} T_l[u]W_K^{-(2^l u+2^{l-1})n} &= [-\mathrm{sgn}(\Re\{S_l[u]\})\,p_{l,u}\mathbb{D} - j\mathrm{sgn}(\Im\{S_l[u]\})\,q_{l,u}\mathbb{D}] \\ &\quad\times\left[\cos\left(2\pi n\frac{2^l u+2^{l-1}}{K}\right) + j\sin\left(2\pi n\frac{2^l u+2^{l-1}}{K}\right)\right]. \end{aligned} \tag{3.60}$$

The real part of Eq. (3.60) only contains two terms in the product, *i.e.*

$$\begin{aligned}\Re\left\{T_l[u]W_K^{-(2^l u+2^{l-1})n}\right\} = &-\mathrm{sgn}(\Re\left\{S_l[u]\right\})\,p_{l,u}\mathbb{D}\cdot\cos\left(2\pi n\frac{2^l u+2^{l-1}}{K}\right)\\ &+\mathrm{sgn}(\Im\left\{S_l[u]\right\})\,q_{l,u}\mathbb{D}\cdot\sin\left(2\pi n\frac{2^l u+2^{l-1}}{K}\right).\end{aligned} \tag{3.61}$$

Substituting Eq. (3.61) back into Eq. (3.59) gives

$$\begin{aligned}\overline{y}_1[n] &= 2\cdot\Re\left\{\frac{1}{\sqrt{K}}\sum_{u=0}^{\frac{K_l}{4}-1}S_l[u]W_K^{(2^l u+2^{l-1})n}\right\}+2\cdot\Re\left\{\frac{1}{\sqrt{K}}\sum_{u=0}^{\frac{K_l}{4}-1}T_l[u]W_K^{(2^l u+2^{l-1})n}\right\}\\
&\overset{(3.61)}{=\!=}2\cdot\Re\left\{\frac{1}{\sqrt{K}}\sum_{u=0}^{\frac{K_l}{4}-1}S_l[u]W_K^{(2^l u+2^{l-1})n}\right\}+\\
&\qquad\frac{2}{\sqrt{K}}\sum_{u=0}^{\frac{K_l}{4}-1}\left\{-\mathrm{sgn}(\Re\left\{S_l[u]\right\})\,p_{l,u}\mathbb{D}\cdot\cos\left(2\pi n\frac{2^l u+2^{l-1}}{K}\right)\right.\\
&\qquad\qquad\left.+\mathrm{sgn}(\Im\left\{S_l[u]\right\})\,q_{l,u}\mathbb{D}\cdot\sin\left(2\pi n\frac{2^l u+2^{l-1}}{K}\right)\right\}\\
&\overset{(3.63)}{=\!=}2\cdot\Re\left\{\frac{1}{\sqrt{K}}\sum_{u=0}^{\frac{K}{4}-1}S_l[u]W_K^{(2^l u+2^{l-1})n}\right\}+\\
&\qquad\frac{2}{\sqrt{K}}\sum_{u=0}^{\frac{K}{4}-1}\left\{-\mathrm{sgn}(\Re\left\{S_l[u]\right\})\,p_{l,u}\mathbb{D}\cdot\cos\left(2\pi n\frac{2^l u+2^{l-1}}{K}\right)\right.\\
&\qquad\qquad\left.+\mathrm{sgn}(\Im\left\{S_l[u]\right\})\,q_{l,u}\mathbb{D}\cdot\sin\left(2\pi n\frac{2^l u+2^{l-1}}{K}\right)\right\}\end{aligned} \tag{3.62}$$

In the last equality of Eq. (3.62), the mapped symbols $\boldsymbol{S}_l$ belonging to layers $l \geq 2$ are padded with 0, so that they are all of length $K/4$ and properly aligned with layer 1. Explicitly,

$$S_l[u] = 0, \qquad \forall u > \frac{K_l}{4}, \tag{3.63}$$

and consequently,

$$p_{l,u} = q_{l,u} = 0, \qquad \forall u > \frac{K_l}{4}, \tag{3.64}$$

based on the definition of the sign function in Eq. (3.56). This operation allows us to prepare the structure of the signal for the optimisation process.

As shown in Fig. 3.4, these signals $\overline{\boldsymbol{y}}_l$ will be clipped at 0 and superimposed as in

$$\breve{x}[n] = \sum_{l=1}^{L} y_l[n] = \sum_{l=1}^{L} \left\lfloor \overline{y}_l[n] \right\rfloor, \qquad n = 0, 1, \ldots, (K-1), \tag{3.65}$$

where $\overleftarrow{\boldsymbol{x}}$ denotes the composite L-layer LACO-OFDM signal. The PAPR of the resultant LACO-OFDM signal $\overleftarrow{\boldsymbol{x}}$ can then be expressed by substituting Eq. (3.65) into Eq. (3.42).

3.6.2 Problem Formation and Solution

Since the signals $\boldsymbol{T}_l$ are independent from the original signals $\boldsymbol{S}_l$ for all layers, their sum will have a higher average signal power than either of them in isolation according to the law of energy conservation. According to Eq. (3.42), in order to reduce the PAPR, we have to minimise the peak power of the TD signal $\overleftarrow{x}[n]$.

$$\min_{p,q} \max_{0 \le n \le K-1} \left(\overleftarrow{x}[n]\right)^2, \qquad \text{s.t. } Eq.\ (3.57) \text{ and } Eq.\ (3.64). \tag{3.66}$$

Proposition 3.4. *The problem formulated in Eq.* (3.66) *represents minimising the maximum amplitude of the composite LACO-OFDM signal constituted by all the lower layers, which may be expressed as:*

$$\min_{p,q} \max_{\substack{0 \le n \le K-1 \\ 1 \le L' \le L}} \sum_{l=1}^{L'} y_l[n], \qquad s.t.\ Eq.\ (3.57)\ and\ Eq.\ (3.64). \tag{3.67}$$

Proof. Given that the TD signal obeys $\overleftarrow{x}[n] \ge 0$ and Eq. (3.65), the optimisation problem in Eq. (3.66) can be formulated as

$$\min_{p,q} \max_{0 \le n \le K-1} \sum_{l=1}^{L} y_l[n], \qquad \text{s.t. } Eq.\ (3.57) \text{ and } Eq.\ (3.64). \tag{3.68}$$

Let h_1, h_2, $\ldots$, h_w, $\ldots$ represent the random layer indices of the LACO-OFDM signal that are not equal to each other. Since clipping guarantees that $y_l[n] \ge \overline{y}_l[n]$, it can be deduced that at each time slot n, the composite symbol $\overleftarrow{x}[n]$ has a higher power than the sum of any combination of its constituent layers $\overline{y}_{h_1}[n] + \overline{y}_{h_2}[n] + \ldots$, *i.e.* we have:

$$\overleftarrow{x}[n] \ge \sum_{w=1}^{L'} \overline{y}_{h_w}[n], \qquad \begin{array}{l} \forall L' \in \{1, 2, \ldots, L\}, \\ \forall h_w \in \{1, 2, \ldots, L\}, \\ \forall n \in \{0, 1, \ldots, K-1\}. \end{array} \tag{3.69}$$

Assuming that the sample index of the TD peak is n^*, *i.e.* that $\max\{\overleftarrow{\boldsymbol{x}}\} = \overleftarrow{x}[n^*]$, equality applies in Eq. (3.69) for this particular TD sample of n^*, yielding:

$$\overleftarrow{x}[n^*] = \max_{L', h_w} \sum_{w=1}^{L'} \overline{y}_{h_w}[n^*]. \tag{3.70}$$

Given the specific nature of the higher layers detailed in Chapter 2 and Appendix A.3, as well as the Hermitian symmetry, the TD samples of each layer have to satisfy

$$\begin{aligned}
\overline{y}_1[n] &= -\overline{y}_1\left[n+\frac{K}{2}\right], \\
\overline{y}_2[n] &= -\overline{y}_2\left[n+\frac{K}{4}\right] = \overline{y}_2\left[n+\frac{K}{2}\right] = -\overline{y}_2\left[n+\frac{3K}{4}\right], \\
\overline{y}_3[n] &= -\overline{y}_3\left[n+\frac{K}{8}\right] = \overline{y}_3\left[n+\frac{K}{4}\right] = -\overline{y}_3\left[n+\frac{3K}{8}\right] = \overline{y}_3\left[n+\frac{K}{2}\right] \\
&= -\overline{y}_3\left[n+\frac{5K}{8}\right] = \overline{y}_3\left[n+\frac{3K}{4}\right] = -\overline{y}_3\left[n+\frac{7K}{8}\right], \\
&\cdots
\end{aligned} \tag{3.71}$$

Let us now assume that the maximum in Eq. (3.70) is found when $L' = 1$, *i.e.* the maximum sample is located at a time slot, when only the layer with index h_1 (at the moment we do not know the exact layer index) is not clipped, yielding:

$$y_l[n^*] = 0, \qquad \forall l \neq h_1. \tag{3.72}$$

Let us assume furthermore that $h_1 = 2$ and $n^* \leq \frac{K}{2} - 1$, where n^* is the TD sample index of the maximum, when the symbols of all layers other than layer 2 are clipped. This further implies that

$$y_l\left[n^*+\frac{K}{2}\right] \overset{(3.71)}{=\!=} y_l[n^*] \overset{(3.72)}{=\!=} 0, \qquad \forall l > 2. \tag{3.73}$$

Since at $n = n^*$, the layer 1's symbol is clipped, $\overline{y}_1[n^*] < 0$, and obviously

$$\overline{y}_1\left[n^*+\frac{K}{2}\right] \overset{(3.71)}{=\!=} -\overline{y}_1[n^*] > 0, \tag{3.74}$$

as shown in Fig. 3.16.

On the other hand,

$$\begin{aligned}
\overleftarrow{x}\left[n^*+\frac{N}{2}\right] &= y_1\left[n^*+\frac{K}{2}\right] + y_2\left[n^*+\frac{K}{2}\right] + \sum_{l=3}^{L} y_l\left[n^*+\frac{K}{2}\right] \\
&\overset{(3.71),\ (3.73)}{=\!=\!=\!=} y_1\left[n^*+\frac{K}{2}\right] + y_2[n^*] \\
&> y_2[n^*] = 0 + y_2[n^*] + 0 \\
&= y_1[n^*] + y_2[n^*] + \sum_{l=3}^{L} y_l[n^*] = \overleftarrow{x}[n^*],
\end{aligned} \tag{3.75}$$

which contradicts to the assumptions stipulated above, as shown in Fig. 3.16. The same conclusion can be made, when $n^* > \frac{N}{2} - 1$. Therefore, the probability of $\overleftarrow{\boldsymbol{x}}[n^*] = y_2[n^*]$,

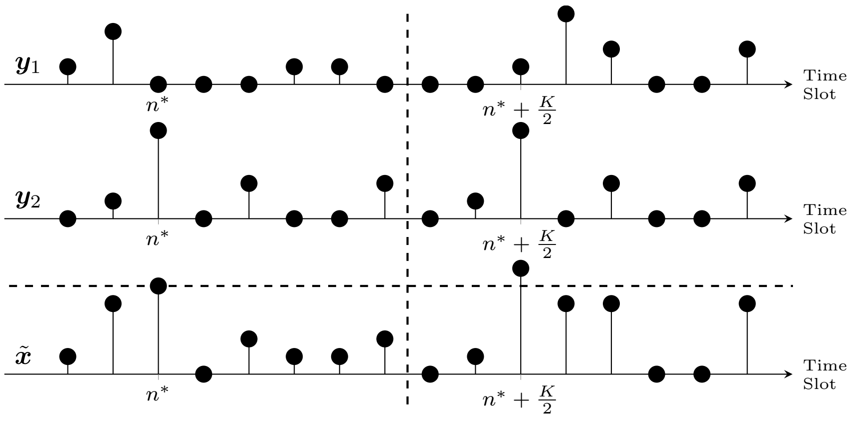

Figure 3.16: Time domain views of a 2-Layer LACO-OFDM signal, where $\boldsymbol{y}_1$, $\boldsymbol{y}_2$ and $\bar{\tilde{\boldsymbol{x}}}$ represent the layer 1, layer 2 and the overall signal, respectively. n^* and $n^* + \frac{N}{2}$ are the time slots of interests. The vertical dashed line separates the first and second half of the time slots.

or equivalently $(L' = 1,\ h_1 = 2)$, is negligible.

This process can also be further expanded to cover all situations, when

$$\forall L' > 1,\ \exists h_w,\ \text{s.t. } h_w > L'. \tag{3.76}$$

The only legitimate combinations of the different layer-symbols left would be

$$\bar{\tilde{x}}[n^*] = \max_{L'} \sum_{l=1}^{L'} \bar{y}_l[n^*]\,. \tag{3.77}$$

By substituting Eq. (3.77) back into Eq. (3.68), the equivalent problem Eq. (3.67) is obtained, which concludes the proof. □

Let us now return to our PAPR optimisation problem. Let t be the target of the optimisation. Then, a linear programme prototype can be formed as

$$\begin{aligned} \min_{\boldsymbol{p},\boldsymbol{q}} \quad & t \\ \text{s.t.} \quad & \sum_{l=1}^{L'} y_l[n] \le t, \quad \forall\, 0 \le n \le K-1, \forall\, 1 \le L' \le L \\ & \text{and } \mathit{Eqs.}\ (3.57),\ (3.64). \end{aligned} \tag{3.78}$$

With the aid of Eq. (3.62), the term $\sum_{l=1}^{L'} y_l[n]$ can be expressed in a linear form by introducing the following vectorial and matrix constants.

Since Eq. (3.62) considers the possibility of all (n, L') combinations, the final linear form has to contain a total of (NL) rows, where each row represents the sum of the first L' layers' nth TD sample from $\bar{y}_1[n]$.

The first term in Eq. (3.62) represents the participation of the original signal $\boldsymbol{S}_l$ in $\boldsymbol{Y}_l$, and it is identical to $\boldsymbol{s}_l[n]$, *i.e.*

$$s_l[n] = 2 \cdot \Re\left\{ \frac{1}{\sqrt{K}} \sum_{u=0}^{\frac{K}{4}-1} S_l[u] W_K^{(2^l u + 2^{l-1})n} \right\}. \tag{3.79}$$

A vector of length (LK) can then be formed, with the $((L'-1)K+1)$th row to the $(L'K)$th row representing the length-K summation of the first L' layers, expressed as

$$\begin{aligned} \varsigma = \Big[& \quad s_1[0], \quad s_1[1], \quad \cdots, \quad s_1[K-1], \\ & \sum_{l=1}^{2} s_l[0], \; \sum_{l=1}^{2} s_l[1], \; \cdots, \; \sum_{l=1}^{2} s_l[K-1], \\ & \quad \vdots \qquad \vdots \qquad \ddots \quad \vdots \\ & \sum_{l=1}^{L} s_l[0], \; \sum_{l=1}^{L} s_l[1], \; \cdots, \; \sum_{l=1}^{L} s_l[K-1] \Big]^{\mathrm{T}}, \end{aligned} \tag{3.80}$$

where $[\cdot]^{\mathrm{T}}$ represents the transpose of a vector or matrix.

For the second summation term in the last equality of Eq. (3.62), the two parts within it can be expresses separately. For the nth time slot sample of the layer l's TD signal, the contribution of the uth mapped symbol in the corresponding FD signal $\boldsymbol{T}_l$ would be

$$c_{l,n,u} = \frac{2}{\sqrt{K}} \operatorname{sgn}(\Re\{S_l[u]\}) \, \mathbb{D} \cdot \cos\left(2\pi n \frac{2^l u + 2^{l-1}}{K}\right), \tag{3.81}$$

$$g_{l,n,u} = \frac{2}{\sqrt{K}} \operatorname{sgn}(\Im\{S_l[u]\}) \, \mathbb{D} \cdot \sin\left(2\pi n \frac{2^l u + 2^{l-1}}{K}\right). \tag{3.82}$$

The terms corresponding to different time slot samples can be grouped into vectors, and the vectors corresponding to different FD symbols of the same layer can be further grouped into vectors, yielding:

$$\boldsymbol{c}_{l,n} = \left[c_{l,n,0}, \; c_{l,n,1}, \; \ldots, \; c_{l,n,K/4-1}\right]^{\mathrm{T}}, \tag{3.83}$$

$$\boldsymbol{C}_l = \left[\boldsymbol{c}_{l,0}, \; \boldsymbol{c}_{l,1}, \; \ldots, \; \boldsymbol{c}_{l,K-1}\right]^{\mathrm{T}}, \tag{3.84}$$

$$\boldsymbol{g}_{l,n} = \left[g_{l,n,0}, \; g_{l,n,1}, \; \ldots, \; g_{l,n,K/4-1}\right]^{\mathrm{T}}, \tag{3.85}$$

$$\boldsymbol{G}_l = \left[\boldsymbol{g}_{l,0}, \; \boldsymbol{g}_{l,1}, \; \ldots, \; \boldsymbol{g}_{l,K-1}\right]^{\mathrm{T}}. \tag{3.86}$$

In this way, a large matrix can be constructed with the lth block row (multiple rows from the same smaller matrix) being used to calculate the summation within Eq. (3.78) when $L' = l$.

$$\boldsymbol{A} = \begin{bmatrix} -\boldsymbol{C}_1 & \boldsymbol{G}_1 & & & & & \\ -\boldsymbol{C}_1 & \boldsymbol{G}_1 & -\boldsymbol{C}_2 & \boldsymbol{G}_2 & & & \\ \vdots & \vdots & \vdots & \vdots & \ddots & & \\ -\boldsymbol{C}_1 & \boldsymbol{G}_1 & -\boldsymbol{C}_2 & \boldsymbol{G}_2 & \cdots & -\boldsymbol{C}_L & \boldsymbol{G}_L \end{bmatrix}, \tag{3.87}$$

where the upper right region of the matrix is left blank, because those are zero-padding areas, as shown in Eq. (3.63). Meanwhile, the minus signs of all $\boldsymbol{C}_l$ elements correspond to the negative sign in the penultimate line of Eq. (3.62).

Likewise, the parameters $\boldsymbol{p}$ and $\boldsymbol{q}$ can also be grouped as vectors, yielding:

$$\boldsymbol{p}_l = \left[p_{l,0},\ p_{l,1},\ \ldots,\ p_{l,K/4-1}\right]^{\mathrm{T}}, \tag{3.88}$$

$$\boldsymbol{q}_l = \left[q_{l,0},\ q_{l,1},\ \ldots,\ q_{l,K/4-1}\right]^{\mathrm{T}}, \tag{3.89}$$

$$\boldsymbol{v} = \left[\boldsymbol{p}_1^{\mathrm{T}},\ \boldsymbol{q}_1^{\mathrm{T}},\ \boldsymbol{p}_2^{\mathrm{T}},\ \boldsymbol{q}_2^{\mathrm{T}},\ \ldots,\ \boldsymbol{p}_L^{\mathrm{T}},\ \boldsymbol{q}_L^{\mathrm{T}}\right]^{\mathrm{T}}. \tag{3.90}$$

Concerning the vectors $\{\boldsymbol{p}_l\}_{u=1}^{K/4-1}$, $\{\boldsymbol{q}_l\}_{u=1}^{K/4-1}$ defined above, note that for all $u \geq K_l/4$, the corresponding vector elements should always be zero, because they are padded for alignment purposes, according to Eq. (3.64). In other words, for the length-$(KL/2)$ vector $\boldsymbol{v}$, the elements having the following indices are always left zero:

$$v_u \equiv 0, \qquad \text{if } \exists\ l,\ \text{s.t. } \mathrm{mod}\left(u, \frac{K}{4}\right) > \frac{K_l}{4}. \tag{3.91}$$

In this way, the original PAPR reduction problem of Eq. (3.66) can be rewritten as

$$\begin{aligned} \min_{\boldsymbol{v}} \quad & t \\ \text{s.t.} \quad & \boldsymbol{\varsigma} + \boldsymbol{A}\boldsymbol{v} \leq t \cdot \boldsymbol{1}_{(NL\times 1)} \\ & p_{l,u}, q_{l,u} \begin{cases} \in \{0,1\}, & u < K_l/4, \\ = 0, & \text{otherwise}, \end{cases} \end{aligned} \tag{3.92}$$

which is now transformed into a mixed integer linear programming (MILP) problem. Hence, off-the-shelf solvers can be applied [80].

3.6.3 Optimisation Simplification

It has been shown in [74, 81] that the majority of the elements in the optimisation variable vector $\boldsymbol{v}$ would be zeros, indicating that with a few subcarrier symbol shifts, the PAPR may be considerably reduced. This result also shows that the vector $\boldsymbol{v}$ is sparse. Hence, based on [74,76,82] we can further simplify the optimisation problem by minimising the ℓ_1-norm $\|\boldsymbol{v}\|_1$ of the desired sparse vector $\boldsymbol{v}$ as

$$\begin{aligned} \min_{\boldsymbol{v}} \quad & \|\boldsymbol{v}\|_1 \\ \text{s.t.} \quad & \boldsymbol{\varsigma} + \boldsymbol{A}\boldsymbol{v} \leq t' \cdot \mathbf{1}_{(NL\times 1)}, \\ & \mathbf{0}_{(NL/2\times 1)} \leq \boldsymbol{v} \leq \mathbf{1}_{(NL/2\times 1)}, \\ & \boldsymbol{\mathcal{W}}\boldsymbol{v} = \mathbf{0}_{(NL/2\times 1)}, \end{aligned} \tag{3.93}$$

where $\boldsymbol{\mathcal{W}}$ is a diagonal matrix employed for ensuring that the subcarriers not controlled by the current layer would not be shifted, the majority of whose elements are 0. This is achieved by setting all illegitimate indices to 1, while forcing their corresponding element in $\boldsymbol{v}$ to 0, which is formulated as:

$$\mathcal{W}_{i,j} = \begin{cases} 1, & i = j \text{ and } Eq. \text{ (3.91)}, \\ 0, & \text{otherwise}. \end{cases} \tag{3.94}$$

Furthermore, t' is a pre-determined peak amplitude reduction target that varies both with the number of layers L and with the number of FFT points K according to [74,76]. In this thesis, empirical values of $t' = 0.7$ is used for 4LACO-OFDM.

It is worth mentioning that Eq. (3.93) relaxes the restriction formulated in Eq. (3.57). Thus, the resultant vector $\boldsymbol{v}^*$ contains floating-point numbers within $[0, 1]$. Then, according to [74], a total of Z candidate vectors containing only 0 and 1 will be generated, each of which has a probability of being 1 given by the corresponding value in $\boldsymbol{v}^*$.

Given the resultant solution vector $\boldsymbol{v}^*$, for the zth of the Z independent and identically distributed (*i.i.d.*) candidate vectors $\{\boldsymbol{p}^{(z)}, \ \boldsymbol{q}^{(z)}\}$, the associated generation process is formulated as:

$$p_{l,u}^{(z)} \sim \mathcal{B}(1, v^*[2u]), \tag{3.95a}$$

$$q_{l,u}^{(z)} \sim \mathcal{B}(1, v^*[2u+1]), \tag{3.95b}$$

where $\mathcal{B}(1, p)$ is the Bernoulli distribution with success probability p.

The PAPRs of each candidate signal are then calculated by applying Eq. (3.52), in order to obtain the injected LACO-OFDM signal $\breve{\boldsymbol{x}}^{(z)}$. The one achieving the minimum PAPR would be selected as the final solution, which is given by:

$$z^* = \arg \min_{0\leq z\leq Z} \text{PAPR}\{\breve{\boldsymbol{x}}^{(z)}\}, \tag{3.96}$$

where z^* is the index of the optimum pair $\boldsymbol{p}^{(z^*)}, \ \boldsymbol{q}^{(z^*)}$, while the PAPR is calculated using Eq. (3.41).

This simplified algorithm has been summarised in Alg. 1, which describes the operation of the ‘PAPR Reduction’ block in Fig. 3.4.

Algorithm 1 The simplified LACO-OFDM PAPR reduction algorithm

```
Input: ${\boldsymbol{s}_1, \boldsymbol{s}_2, \ldots, \boldsymbol{s}_L}$, $K$, $L$, $\mathbb{D}$, $t'$, $Z$
Output: ${\boldsymbol{T}_1, \boldsymbol{T}_2, \ldots, \boldsymbol{T}_L}$
Construct vector $\boldsymbol{\varsigma}$ using Eq. (3.80);
Construct matrix $\boldsymbol{A}$ using Eq. (3.81) $\sim$ Eq. (3.87) and $\boldsymbol{\mathcal{W}}$ using $Eq.$ (3.94);
Solve the MILP problem of Eq. (3.93) and obtain $\boldsymbol{v}^*$;
$z := 0$;
repeat
    $z = z + 1$,
    Generate $\boldsymbol{p}^{(z)}$ and $\boldsymbol{q}^{(z)}$ according to Eq. (3.95a),
    Obtain the injected signal $\boldsymbol{Y}_l^{(z)}$ using Eq. (3.52) and Eq. (3.55),
    Take $\boldsymbol{Y}_l^{(z)}$ through the LACO-OFDM TX processing shown in Fig. 3.4 and get the injected LACO-OFDM signal $\tilde{\breve{\boldsymbol{x}}}^{(z)}$,
    Calculate PAPR${\tilde{\breve{\boldsymbol{x}}}^{(z)}}$ using Eq. (3.41),
until $z = Z$;
Find $z^*$ based on Eq. (3.96);
Find the corresponding $\boldsymbol{p}^{(z^*)}$, $\boldsymbol{q}^{(z^*)}$;
Obtain the final $\boldsymbol{T}_l$ using Eq. (3.55);
return ${\boldsymbol{T}_1, \boldsymbol{T}_2, \ldots, \boldsymbol{T}_L}$.
```

3.6.4 Numerical Results

Figure 3.17 portrays the CCDF of the proposed PAPR reduction method for 3LACO-OFDM 16QAM signals for a total of 64 subcarriers. The number of candidate solution vectors generated Z is treated as a variable and its PAPR improvement is quantified. At the CCDF $= 10^{-3}$ level, our tone-injection technique provides a PAPR reduction of around 5 dB, provided that sufficient candidate vectors are generated. Naturally, a higher PAPR improvement can be observed, when a larger Z is used, albeit at a higher computational complexity. Therefore, we struck a compromise at $Z = 200$ for our further simulation.

On the other hand, the PAPR improvement is a function of the number of layers L. Fig. 3.18 characterises this feature by comparing the PAPR improvement of different LACO-OFDM signals. The improvement of the PAPR at the CCDF $= 10^{-3}$ level is used for our evaluation. It is clear that the PAPR improvement is reduced as the number of layers increases. A plausible reason for this trend based on Fig. 3.14 is that the PAPR decreases as L increases, which in turn makes further improvements even harder to achieve. However, if we compare the PAPR of the injection-aided 4LACO-OFDM signal to the original 2LACO-OFDM, the improvement now appears more dramatic.

The influence of the proposed PAPR reduction method on the BER performance is characterised in Fig. 3.19. The BER versus γ_{b} performance of the 3LACO-OFDM signals under various clipping ratios featuring the proposed PAPR reduction method are depicted by the solid lines, together with their original direct-clipping based counterparts

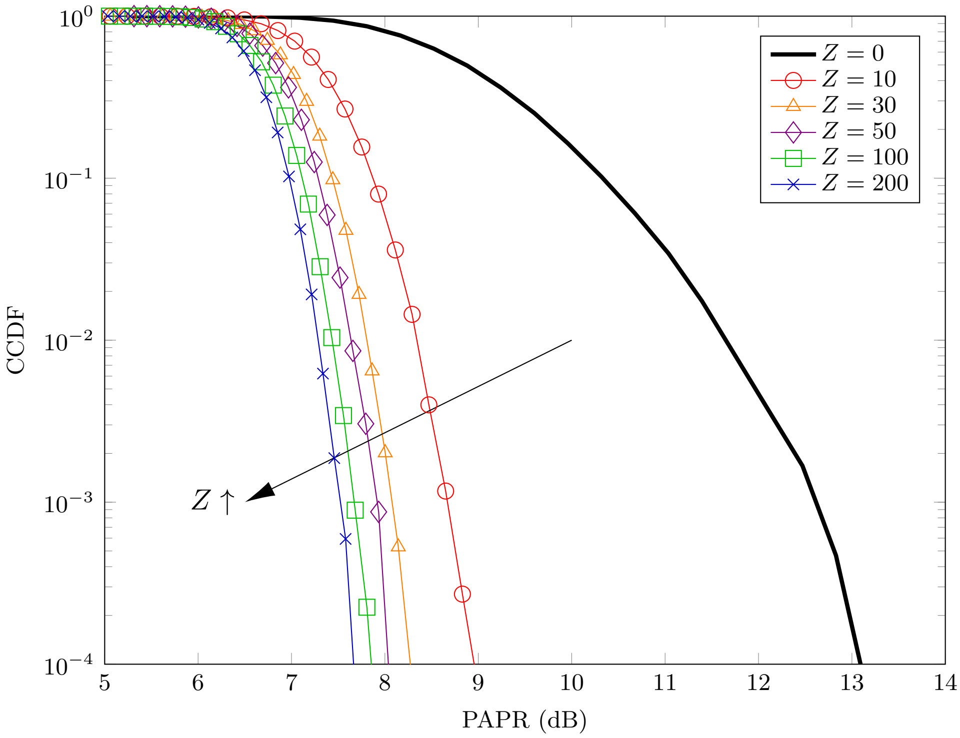

Figure 3.17: CCDF of the PAPR of LACO-OFDM TD signals from our PAPR reduction technique with different number of candidate vectors generated Z. All parameters are summarised in Table 3.1.

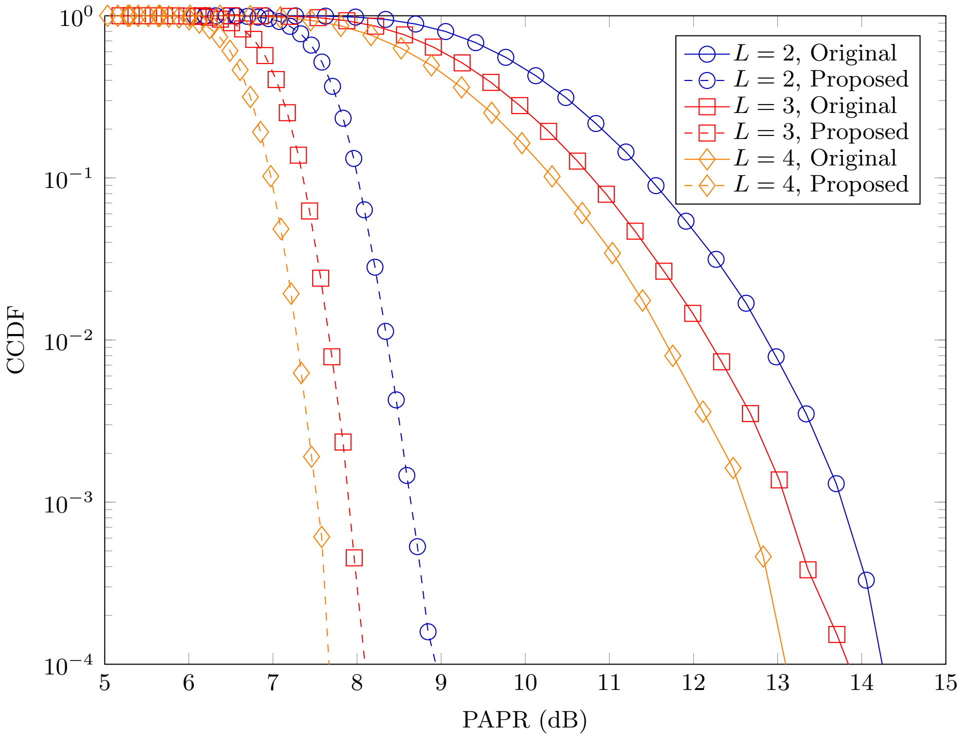

Figure 3.18: CCDF of the PAPR of LACO-OFDM TD signals. Solid lines represent the resultant signal from our PAPR reduction technique and dashed lines their original counterparts. All parameters are summarised in Table 3.1.

represented by the dashed lines. The proposed method expands the size of the constellation pattern by shifting the constellation points to locations farther apart, while keeping the minimum distance between each pair of points the same. In this way the effective γ_b for the resultant signals becomes lower than that of their original signals, which imposes a higher information loss. However, for $\gamma_b > 20$ dB, the proposed PAPR reduction technique starts to outperform its direct-clipping counterparts for both 7 dB and 9 dB clipping ratios. This is an explicit benefit of its reduced clipping distortion.

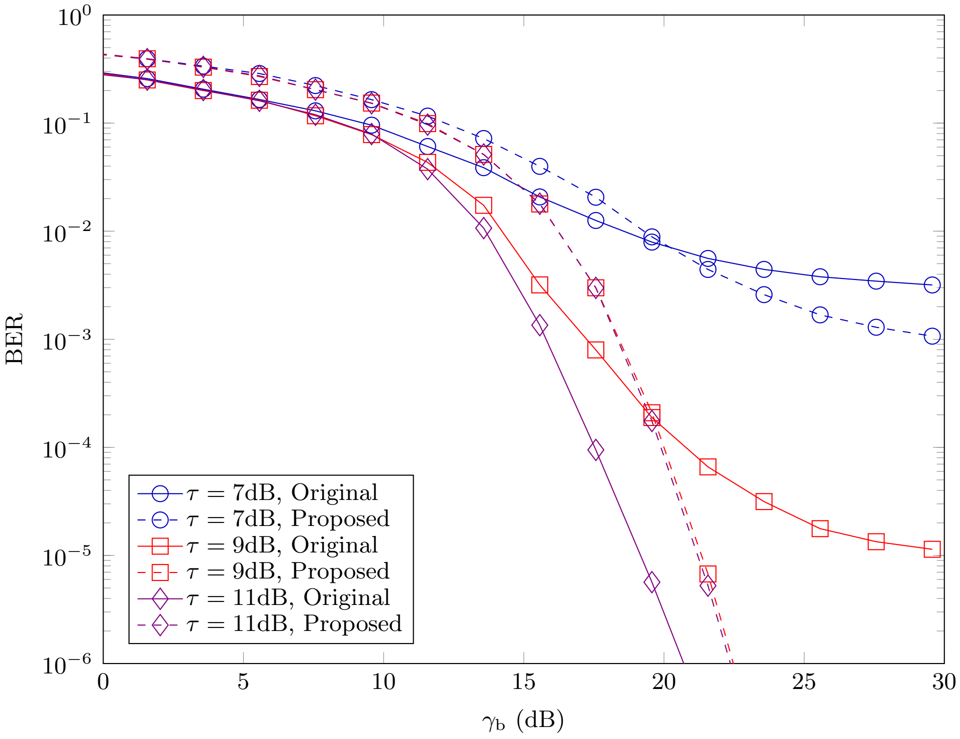

Figure 3.19: Comparison of BER performance over AWGN channel for 16QAM 3LACO-OFDM signals under different UB clipping ratios (τ). Shown in solid lines are signals gone through the proposed PAPR reduction method, while those in dashes lines are the signals without PAPR reduction. All unmentioned parameters are summarised in Table 3.1.

3.7 Chapter Conclusions

In this chapter, new theoretical expressions of its BER and of its PAPR have been derived and verified by simulations for the state-of-the-art of the LACO-OFDM scheme. Explicitly, the BER performance has been analysed in the face of noise, ILI and clipping distortion. The higher layers tend to have worse BER performance due to the interference imposed by the lower layers, while the first layer has the same performance as ACO-OFDM. We demonstrated that the LACO-OFDM PAPR is significantly influenced by that of its first layer. The PAPR expression indicates that adding more layers will result in a TD signal with lower PAPR, hence LACO-OFDM attains PAPR reduction. A novel PAPR reduction method based on tone-injection was also proposed for LACO-OFDM, which is capable of achieving in excess of 5 dB PAPR reduction on top of LACO-OFDM's own reduction capability. The BER simulations also match with our analysis, demonstrating that the signals composed of more layers exhibit a better resistance against clipping, albeit their BER performance becomes much worse when, no clipping is imposed. The proposed PAPR reduction method also helps improve the BER. As a result, our LACO-OFDM solution exhibits excellent spectral and energy efficiency.

3.8 Chapter Summary

3.8.1 Structure of the Chapter

Figure 3.20 provides a detailed schematic diagram of the relationships between each of the sections in this chapter.

In Sec. 3.2, we commenced with the introduction of the UB clipping module of Fig. 3.2, and the introduction of the tone injection module of Fig. 3.4.

Next, the basic statistical characteristics of the LACO-OFDM TD signal was studied in Sec. 3.3. The PDF and moments of each of the layers was considered first.

Then, the BER performance of the LACO-OFDM signal was formulated mathematically in Sec. 3.4. The expression of the BER takes into consideration the UB clipping, ILI and the layer bit rate. We emphasised that the PAPR has played an important role in predetermining the BER performance. Therefore, the PAPR of the LACO-OFDM signal was discussed in Sec. 3.5.

Finally, in Sec. 3.6, we proposed a PAPR reduction algorithm based on tone injection. The linear problem of reducing the PAPR was formulated by minimising the sums of first L' layers, which can be solved by MILP. A further simplification of the algorithm was also proposed. The PAPR reduction also improved the BER performance under clipping, as discussed in Sec. 3.4.

3.8.2 Summary of Simulation Results

In Sec. 3.3.5, the PDF of LACO-OFDM was investigated as a function of the number of layers L, while the total power P_{LACO} of the signals was normalised to 1 W.

The BER performance of LACO-OFDM is evaluated by simulations in Sec. 3.4.5. In Fig. 3.11, the performance of each separate layer is compared, which shows that the

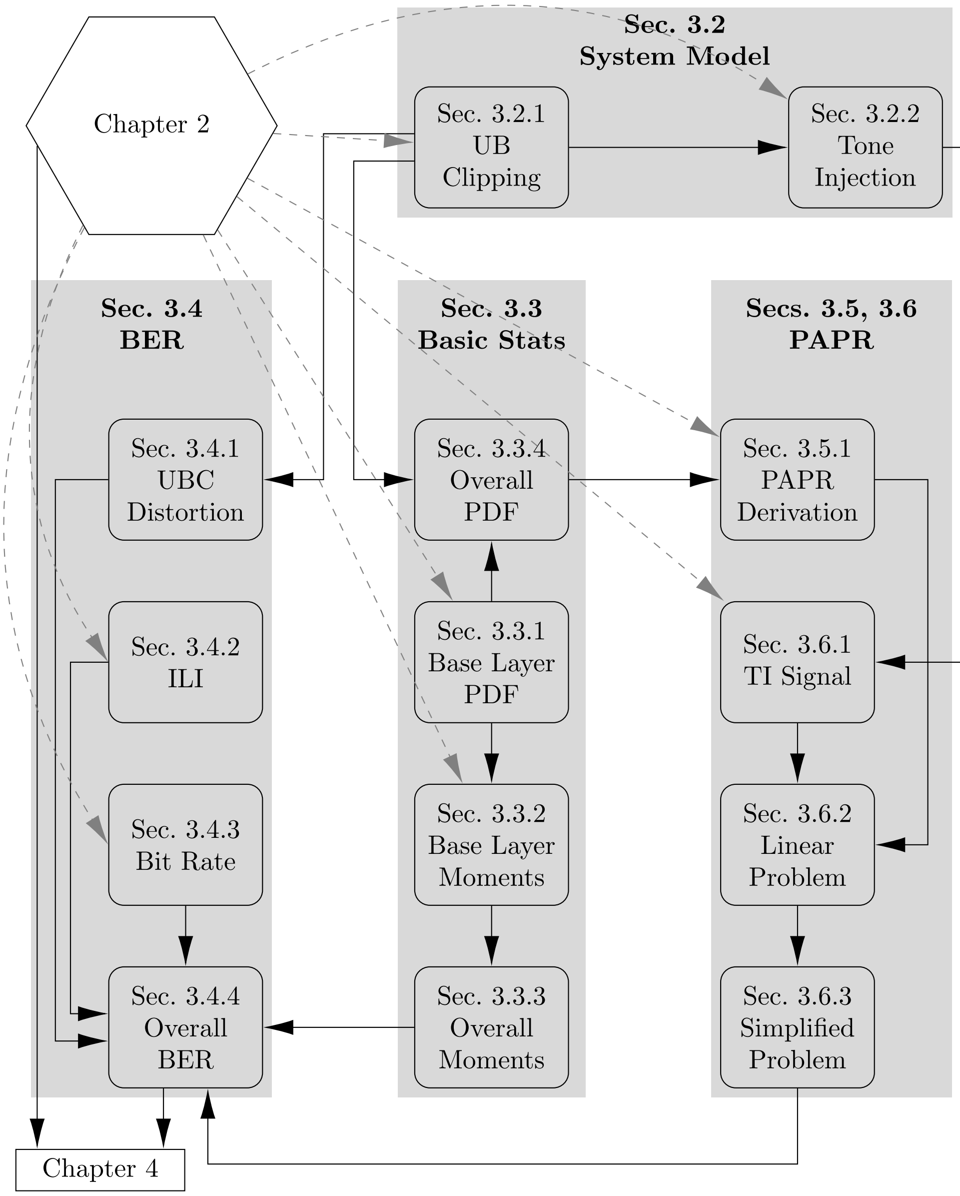

Figure 3.20: Summary of Chapter 3.

higher layers have worse performance, due to their higher ILI contamination by the previous layers. In Fig. 3.12, the BER performance of LACO-OFDM composed of different number of layers is compared. When no UB clipping is considered, the signals having fewer layers have better performance, because the higher layers have worse performance according to Fig. 3.11, hence degrading the average BER. However, when UB clipping is considered, the advantage of having a low PAPR associated with more layers becomes clear, which is reflected by their better BER performance of Fig. 3.19, because they suffer from less UB clipping distortion.

The PAPR related simulations are discussed in Secs. 3.5.3 and 3.6.4, respectively, where the former considers the original PAPR, while the latter the reduced PAPR. Fig. 3.13

shows that the PAPR of LACO-OFDM increases with the number of subcarrier K, while Fig. 3.14 demonstrates that it is reduced upon increasing the number of layers L. Figs. 3.17 and 3.18 quantify the PAPR performance improvement of our Alg. 1. Fig. 3.17 portrays the PAPR reduction against the number of candidate solutions Z, while Fig. 3.18 compares the PAPR reduction for different number of layers L, with Z fixed at 200, which exhibits a maximum of 5 dB PAPR reduction.

Finally, Fig. 3.19 connects the BER and PAPR analyses of this chapter by comparing the UB-clipped signal's BER performance both with and without our PAPR reduction method. The results show that our method beneficially reduces the PAPR and ultimately improves the BER performance by reducing the UB clipping distortion.

Chapter 4

Multi-Class Coded LACO-OFDM

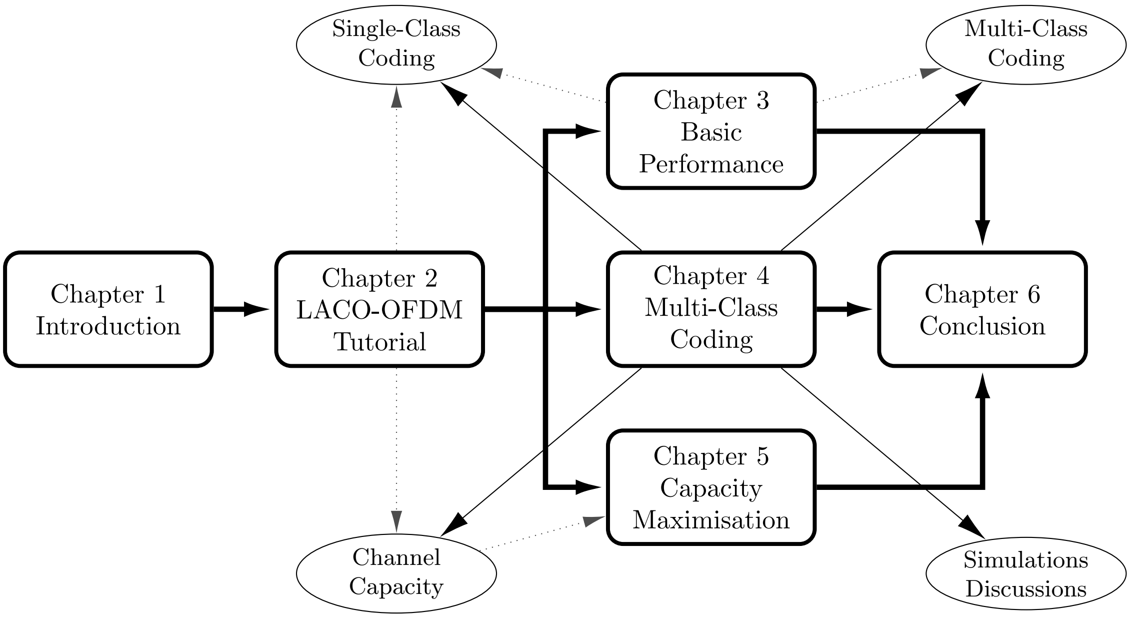

Figure 4.1: Linkage of Chapter 4 within the thesis structure.

4.1 Introduction

In Chapter 3, the BER performance for LACO-OFDM system has been mathematically analysed and evaluated. In this chapter, we focus our attention on improving the performance by employing sophisticated FEC techniques for approaching the channel capacity.

Since the higher layers of a LACO-OFDM frame rely on the lower layers for estimating interference, any residual detection errors in the lower layers propagate through all the successive layers. Consequently, the higher layers exhibit a higher BER than the lowers layers [1]. As a further advance, Q. Wang *et al.* [56] also conceived an improved detection method, which exploits the TD signal for reducing the ILI. Another improved LACO-OFDM receiver relying on soft SIC was proposed by T. Wang *et al.* [58], which exploits the idea of diversity combining for eliminating ILI. Parallel to those developments, Mohammed *et al.* [59] studied both FD and TD diversity combining conceived for LACO-OFDM systems.

Against this background, in this chapter we conceive an integrated multi-class FEC code and LACO-OFDM framework, which invokes carefully harmonised FEC codes for correcting channel errors as well as for eliminating the ILI. Our main contributions in this chapter are:

- We quantify the achievable rate of LACO-OFDM systems relying on different modulation schemes and different number of layers, which is based on both the theoretical mutual information and simulations.
- We conceive a novel FEC coded LACO-OFDM system, which intrinsically amalgamates the classic FEC codes with our LACO-OFDM system. Our results demonstrate that the proposed coded LACO-OFDM system significantly outperforms the benchmark system consisting of a separate FEC and LACO-OFDM scheme in terms of its BER performance as well as the decoding complexity.
- We further analyse the layered BER of the proposed coded system. It is demonstrated that the proposed coded LACO-OFDM system is capable of drastically reducing the ILI. Quantitatively, the coded LACO-OFDM system relying on 4-layer 16QAM LACO-OFDM and turbo coding (8-iteration) completely eliminates the ILI at $E_b/N_0 = 10$ dB, which is 9 dB lower than that of the uncoded system.

The structure of this chapter is as follows. In Sec. 4.2, we define and derive the CCMC and DCMC capacity of our LACO-OFDM system. This is followed by a simple single-class coded LACO-OFDM system in Sec. 4.3. As a further improvement, our multi-class coded LACO-OFDM architecture is presented in Sec. 4.4. Our numerical simulation results, together with our further discussions on the attainable coding performance are given in Sec. 4.5. Finally, our conclusions and chapter summary are offered in Sections 4.6 and 4.7, respectively. Again, the *Equal Power per Bit* power allocation strategy developed in Sec. 2.4 is followed.

4.2 Channel Capacity Analysis

In this section, we study the channel capacity of a LACO-OFDM system. Both the Continuous-input Continuous-output Memoryless Channel (CCMC) capacity and the

Discrete-input Continuous-output Memoryless Channel (DCMC) capacity are quantified [83, 84].

Definition 4.1 (CCMC)**.** In CCMCs, the channel input is a *continuous*-amplitude, discrete-time Gaussian-distributed signal. The CCMC capacity is *only* restricted either by the signalling energy or by the bandwidth. Therefore, the CCMC is also often referred to as the *unrestricted channel.*

Definition 4.2 (DCMC)**.** In DCMCs, the channel input is a *discrete*-amplitude, discrete-time signal. More specifically, the input of the channel contains a groups of symbols belonging to a finite and discrete symbol set $\mathcal{S}$, while the amplitude of channel's output is continuously distributed and may potentially take any value. The DCMC capacity is therefore *additionally* characterised by the finite symbol set $\mathcal{S}$. Hence, the DCMC is often referred to as the *restricted channel.*

We will firstly quantify the capacity of the ACO-OFDM system, followed by that of LACO-OFDM. Explicitly, we will quantify the CCMC capacity for different number of layers, and the DCMC capacity for different modulation schemes. Naturally, the throughput of a LACO-OFDM system increases, as more layers are incorporated and higher-order modulation schemes are used. The channel capacity derived in this section will be subsequently used in Sec. 4.5 for benchmarking the performance of the proposed coded LACO-OFDM system.

For simplifying our analysis, the influence of the OFDM CP on the capacity has been ignored, and an AWGN channel is assumed. More detailed discussion on these topics may be found in [85].

4.2.1 CCMC Capacity

In this subsection, we firstly review the pioneering works of [85, 86] in the derivation of CCMC capacity for RF and ACO-OFDM systems, before presenting the corresponding results for LACO-OFDM systems.

4.2.1.1 CCMC Capacity of RF and ACO-OFDM Systems

The most well-known and generic capacity formula was proposed by Shannon for RF systems, where the capacity for a limited frequency bandwidth of $\mathbb{W}$ Hz is given by:

$$\mathsf{C}_{\mathrm{RF}}^{\mathrm{CCMC}} = \mathbb{W}\log_2\left(1+\frac{E_{\mathrm{s}}}{N_0}\right) \quad \text{(bits/s)}, \tag{4.1}$$

where $\dfrac{E_{\mathrm{s}}}{N_0}$ is the SNR of the received signal.

Recall from Sec. 2.2.1 that ACO-OFDM has distinctive loading strategies for even-indexed ($k = 2u$) and odd-indexed ($k = 2u+1$) subcarriers. The odd-indexed subcarriers have QAM symbols loaded onto them in the same manner as in RF systems, which contributes to the total capacity by an amount of

$$\mathsf{C}^{\text{CCMC}}_{\text{ACO},k} = \mathbb{W}_k \log_2\left(1 + \frac{E_{\text{s},k}}{N_{0,k}}\right) \quad \text{(bits/s)}, \qquad k = 1, 3, \ldots, \frac{K}{2} - 1, \tag{4.2}$$

where $\frac{E_{\text{s},k}}{N_{0,k}}$ is the effective SNR of the kth subcarrier, defined as the energy ratio of the of the symbol on the subcarrier and its corresponding effective noise. Sadly, for the even-indexed blank subcarriers, we have:

$$\mathsf{C}^{\text{CCMC}}_{\text{ACO},k} = 0, \qquad k = 2, 4, \ldots, K - 2. \tag{4.3}$$

Note that for Eq. (4.2)

1. The term $\mathbb{W}_k$
    - The OFDM system employed has a total of K subcarriers, and given the total bandwidth of $\mathbb{W}$, the bandwidth per subcarrier becomes:

$$\mathbb{W}_k = \frac{\mathbb{W}}{K} \quad \text{(Hz)}, \qquad \forall\ 0 \leq k \leq K; \tag{4.4}$$

    - The subcarrier indices k in Eq. (4.2) only occupy the first half of the odd values, because the second half has to have the conjugated symbols transmitted, which do not carry any new information.
2. The term effective SNR $\frac{E_{\text{s},k}}{N_{0,k}}$
    - The SNR expression is identical for all odd-indexed subcarriers, given our the assumption of having (statistically) uniform power spread across the subcarriers, when communicating over an AWGN channel;
    - The LB clipping process averages the energy distribution among the subcarriers, while accommodating all the clipping distortions on the even-indexed subcarriers, which are assumed to have the same energy as those on the odd-indexed subcarriers, yielding:

$$E_{\text{s},2u+1} = E_{\text{s},2u} = E_{\text{s}}, \qquad \forall\ u \in \mathbb{Z}; \tag{4.5}$$

    - Despite the fact that the noise is complex-valued, the receiver drops the imaginary component of the signal, because the intensity-modulated signal is always real-valued, which effectively halves the power of noise, yielding:

$$N_{0,k} = \frac{1}{2} N_0; \tag{4.6}$$

- This leads to the following relationship between $\frac{E_{\mathrm{s}}}{N_0}$ and $\frac{E_{\mathrm{s},k}}{N_{0,k}}$:

$$\frac{E_{\mathrm{s},k}}{N_{0,k}} = \frac{2E_{\mathrm{s}}}{N_0}. \tag{4.7}$$

Therefore, the total CCMC capacity of an ACO-OFDM system having a bandwidth of $\mathbb{W}$ is

$$\begin{aligned}\mathsf{C}_{\mathrm{ACO}}^{\mathrm{CCMC}} &= \sum_{k=0}^{K-1} \mathsf{C}_{\mathrm{ACO},k}^{\mathrm{CCMC}} = \sum_{u=0}^{\frac{K}{4}-1} \mathsf{C}_{\mathrm{ACO},2u+1}^{\mathrm{CCMC}} \\ &= \sum_{u=0}^{\frac{K}{4}-1} \mathbb{W}_k \log_2\left(1+\frac{E_{\mathrm{s},k}}{N_{0,k}}\right) = \frac{1}{4}\mathbb{W}\log_2\left(1+\frac{2E_{\mathrm{s}}}{N_0}\right) \qquad \text{(bits/s)}.\end{aligned} \tag{4.8}$$

4.2.1.2 CCMC Capacity of LACO-OFDM Systems

In LACO-OFDM, the spectral efficiency has been improved by actively exploiting the idle subcarriers left blank in ACO-OFDM. This implies that LACO-OFDM systems achieve a higher CCMC capacity than ACO-OFDM systems within the same bandwidth.

According to Sec. 2.3.1, each of the LACO-OFDM layers constitutes an ACO-OFDM signal, which has the same subcarrier bandwidth $\mathbb{W}_k$ but different number of subcarriers K_l. More specifically, adding the lth layer may "activate" a total of $\frac{1}{2^{l+1}}$ subcarriers, enabling them to carry useful information, and thus increases the total capacity. Therefore, for a LACO-OFDM system having a total of L layers, the capacity contribution of each of the K subcarriers becomes:

$$\mathsf{C}_{\mathrm{LACO},k}^{\mathrm{CCMC}} = \begin{cases} \mathbb{W}_k \log_2\left(1+\frac{E_{\mathrm{s},k}}{N_{0,k}}\right) \quad \text{(bits/s)}, & k \leq \frac{K}{2}-1 \text{ and } \mathrm{mod}\big(k,\ 2^L\big) \neq 0, \\ 0, & \text{otherwise}, \end{cases} \tag{4.9}$$

where the restriction of $\mathrm{mod}\big(k,\ 2^L\big) \neq 0$ ensures that subcarrier k has a symbol on one of the L layers.

However, for LACO-OFDM, the relationship between $E_{\mathrm{s},k}$ and E_{s} is more complicated than the ACO-OFDM's case in Eq. (4.5). According to Fig. 2.9, upon denoting the LB clipped signal of layer l in the FD by $\mathcal{F}\{\boldsymbol{s}_l\}$, the information symbols occupy a total of $\frac{K}{2^l}$ subcarriers, while the clipping distortions of the same layer occupy another $\frac{K}{2^l}$ subcarriers. Therefore, the relationship between the subcarrier energy $E_{\mathrm{s},k}$ and the layer's average power $\mathbb{E}\big\{\boldsymbol{s}_l^2\big\}$ is given by:

$$E_{\mathrm{s},k} = 2^{l-1}\mathbb{E}\big\{\boldsymbol{s}_l^2\big\} \overset{(3.10)}{=\!=} \frac{\sigma_1^2}{2}, \tag{4.10}$$

where σ_1^2 is the variance of the unclipped layer 1 signal $\mathbb{D}\{\bar{\boldsymbol{s}}_1\}$.

On the other hand, according to Sec. 3.3.3, we have:

$$E_{\mathrm{s}} = P_{\mathrm{LACO}} \overset{(3.16)}{=\!=} \frac{\sigma_1^2}{\pi}\left[\frac{\left(1-2^{-L/2}\right)^2}{3-2\sqrt{2}} + (\pi-1)\left(1-\frac{1}{2^L}\right)\right], \tag{4.11}$$

which yields the relationship between $\frac{E_{\mathrm{s}}}{N_0}$ and $\frac{E_{\mathrm{s},k}}{N_{0,k}}$ for an L-layer LACO-OFDM system formulated as

$$\frac{E_{\mathrm{s},k}}{N_{0,k}} = \frac{E_{\mathrm{s}}}{\frac{1}{2}N_0} \times \frac{\pi}{\left[\frac{\left(1-2^{-L/2}\right)^2}{3-2\sqrt{2}} + (\pi-1)\left(1-\frac{1}{2^L}\right)\right]}. \tag{4.12}$$

Therefore, the CCMC capacity of a LACO-OFDM having a total of L layers can be expressed as

$$\begin{aligned}
\mathsf{C}_{\mathrm{LACO}}^{\mathrm{CCMC}} &= \sum_{k=0}^{K-1} \mathsf{C}_{\mathrm{LACO},k}^{\mathrm{CCMC}} = \left(\frac{1}{4}+\frac{1}{8}+\cdots+\frac{1}{2^{l+1}}\right) \times \mathbb{W}_k \log_2\left(1+\frac{E_{\mathrm{s},k}}{N_{0,k}}\right)\\
&= \left(\frac{1}{2}-\frac{1}{2^{l+1}}\right) \times \mathbb{W} \times\\
&\quad \log_2\left(1+\frac{E_{\mathrm{s}}}{N_0}\times\frac{\pi}{\left[\frac{\left(1-2^{-L/2}\right)^2}{3-2\sqrt{2}} + (\pi-1)\left(1-\frac{1}{2^L}\right)\right]}\right) \quad \text{(bits/s)}.
\end{aligned} \tag{4.13}$$

Since LACO-OFDM systems having different number of layers have different throughput, it is unfair to directly compare their capacities at a given $\frac{E_{\mathrm{s}}}{N_0}$. Therefore, we introduce a new metric. For quantifying the CCMC capacity, we define the *information* bit to noise power ratio γ_{ib} as the energy assigned to each successfully received bit. Since the energy of each OFDM symbol is E_{s} and the amount of deliverable information per symbol at a particular SNR is quantified by the CCMC capacity itself, it is straightforward to see that we have:

$$\gamma_{\mathrm{ib}} = \frac{E_{\mathrm{s}}}{N_0} \times \frac{\mathbb{W}}{\mathsf{C}^{\mathrm{CCMC}}}, \tag{4.14}$$

where the term $\frac{\mathsf{C}^{\mathrm{CCMC}}}{\mathbb{W}}$ has a unit of (bits/symbol).

4.2.2 DCMC Capacity of ACO-OFDM Systems

For DCMC capacity, let us first analyse a simple single-layer LACO-OFDM system, which is basically ACO-OFDM. The majority of the notations in this subsection are the same as those in Sec. 2.2, where the system model of ACO-OFDM was defined.

If an FD symbol $S[k]$ is transmitted from TX of Fig. 2.2, the FD symbol received at the RX side can be expressed as

$$R[k] = S[k] + N, \tag{4.15}$$

where N is the halved power-effective AWGN represented in the FD.

Let $d_{1,k,m}$ be the Euclidean distance between the received symbol $R[k]$ and the mth symbol $\mathcal{S}^{\langle m \rangle}$ of the M_1QAM constellation set $\mathcal{S}$ $(m = 0, 1, \ldots, M_1 - 1)$, which is given by:

$$d_{1,k,m} = \left\| R[k] - \mathcal{S}^{\langle m \rangle} \right\|_2 = \left\| S[k] + N - \mathcal{S}^{\langle m \rangle} \right\|_2, \tag{4.16}$$

where $\|\cdot\|_2$ is the ℓ_2-norm operator.

Then, the soft channel information $\Pr\big(R[k] \mid S[k] = \mathcal{S}^{\langle m \rangle}\big)$, which denotes the probability of receiving the symbol $R[k]$ at the kth instant when $S[k] = \mathcal{S}^{\langle m \rangle}$ is transmitted, is computed by the demapper using the distance $d_{1,k,m}$ and the Gaussian-distributed noise N as [87]

$$\Pr\Big(R[k] \mid S[k] = \mathcal{S}^{\langle m \rangle}\Big) = \frac{\exp\left[-\dfrac{d_{1,k,m}^2}{\sigma_n^2/2}\right]}{\pi \cdot \sigma_n^2/2}. \tag{4.17}$$

Here, $\sigma_n^2/2$ is the power of the effective AWGN N of Eq. (4.15), which may be expressed as

$$N \sim \mathcal{CN}\left(0, \frac{\sigma_n^2}{2}\right). \tag{4.18}$$

It is pertinent to mention that if the channel SNR is $\dfrac{E_\mathrm{s}}{N_0}$ for unit symbol energy, then the effective noise power may be estimated by:

$$\frac{E_s}{N_0} = \gamma_\mathrm{b} \cdot \left(\frac{1}{4}\log_2 M\right) = \frac{1}{\sigma_n^2/2}, \tag{4.19}$$

which yields

$$\frac{\sigma_n^2}{2} = \frac{1}{\gamma_\mathrm{b} \cdot \frac{1}{4}\log_2 M} \tag{4.20}$$

for ACO-OFDM.

Using Bayes's Theorem, the *a posteriori* probability of the transmitted symbol $S[k] = \mathcal{S}^{\langle m \rangle}$ given a received symbol $R[k]$ becomes:

$$\Pr\Big(S[k] = \mathcal{S}^{\langle m \rangle} \mid R[k]\Big) = \frac{\Pr\big(R[k] \mid S[k] = \mathcal{S}^{\langle m \rangle}\big) \cdot \Pr\big(S[k] = \mathcal{S}^{\langle m \rangle}\big)}{\Pr(R[k])}. \tag{4.21}$$

Since the transmitted symbols are uniformly distributed over the same constellation pattern, the *a priori* probability for any of the M transmitted symbols is given by

$$\Pr\Big(S[k] = \mathcal{S}^{\langle m \rangle}\Big) = \frac{1}{M} \qquad \forall\, m. \tag{4.22}$$

Furthermore, the probability of received symbols $R[k]$ may be computed using:

$$\Pr(R[k]) = \sum_{m=1}^{M} \left[\Pr\Big(R[k] \mid S[k] = \mathcal{S}^{\langle m \rangle}\Big) \times \Pr\Big(S_1[k] = \mathcal{S}^{\langle m \rangle}\Big)\right]. \tag{4.23}$$

Substituting Eqs. (4.22) and (4.23) into Eq. (4.21) yields:

$$\Pr\Big(S[k] = \mathcal{S}^{\langle m\rangle} \mid R[k]\Big) = \frac{\Pr\big(R[k] \mid S[k] = \mathcal{S}^{\langle m\rangle}\big)}{\sum\limits_{m'=1}^{M} \Pr\big(R[k] \mid S[k] = \mathcal{S}^{\langle m'\rangle}\big)}. \tag{4.24}$$

Hence, Eq. (4.24) implies that $\Pr\big(S[k] = \mathcal{S}^{\langle m\rangle} \mid R[k]\big)$ is equivalent to the *normalised counterpart* of $\Pr\big(R[k] \mid S[k] = \mathcal{S}^{\langle m\rangle}\big)$, when the transmitted symbols $\boldsymbol{S}$ are equiprobable.

According to Shannon's theorem [86], the capacity of a channel is equivalent to the maximum information conveyed, which equals to the entropy of the source minus the average information lost. The DCMC capacity, based on its definition on page 77, is restricted by the specific modulation scheme used, which discretises the input of the channel. Therefore, we express the DCMC capacity as

$$\mathsf{C}_{\text{ACO}}^{M\text{QAM}} = \max I(\mathsf{S},\mathsf{R}) = \max \left[\overset{\text{ACO}}{\mathsf{H}(\mathsf{S})} - \overset{\text{ACO}}{\mathsf{H}(\mathsf{S} \mid \mathsf{R})}\right], \tag{4.25}$$

where $I(\cdot\ ,\ \cdot)$ is the mutual information function and $\mathsf{H}(\cdot)$ is the information entropy function, while S stands for the source/Tx and R the sink/Rx.

Since we have considered equiprobable source symbols, we have [88, 89]

$$\overset{\text{ACO}}{\mathsf{H}(\mathsf{S})} = \frac{K/4}{K}\log_2 M = \frac{1}{4}\log_2 M. \tag{4.26}$$

On the other hand, the conditional entropy $\overset{\text{ACO}}{\mathsf{H}(\mathsf{S} \mid \mathsf{R})}$ relies on the normalised probability of Eq. (4.24), which can be further expressed in Eq. (4.27) on the next page. The term of $\frac{K/4}{K} = \frac{1}{4}$ incorporated in both Eq. (4.26) and Eq. (4.27) indicates the four-fold spectral efficiency reduction of ACO-OFDM, which is reflected in the CCMC capacity analysis. Explicitly, the expectation operator $\mathbb{E}\{\cdot\}$ of Eq. (4.27) computes the average of all TD symbols across all occupied subcarriers. Therefore, a factor of $\frac{K/4}{K}$ has to be incorporated to get the average entropy of a LACO-OFDM frame.

Finally, the DCMC capacity of an ACO-OFDM system can be expressed as

$$\mathsf{C}_{\text{ACO}}^{\text{DCMC}} = \frac{1}{4}\ \log_2 M - \mathsf{H}(\mathsf{S} \mid \mathsf{R}) \quad \text{(bits/symbol)}, \tag{4.29}$$

where the unit of capacity is (bits/s) for CCMC, and it is (bits/symbol) for DCMC capacity.

$$\begin{aligned}
\overset{\text{ACO}}{\mathsf{H}}(\mathsf{S} \mid \mathsf{R}) &= \frac{K/4}{K}\ \mathbb{E}\left\{ -\sum_{m=1}^{M} \left[\Pr\Big(S[k] = \mathcal{S}^{\langle m \rangle},\ R[k]\Big) \times \log_2 \Pr\Big(S[k] = \mathcal{S}^{\langle m \rangle} \mid R[k]\Big) \right] \right\} \\
&= \frac{1}{4}\ \mathbb{E}\left\{ -\sum_{m=1}^{M} \left[\Pr\Big(R[k] \mid S[k] = \mathcal{S}^{\langle m \rangle}\Big) \times \Pr\Big(S[k] = \mathcal{S}^{\langle m \rangle}\Big) \times \log_2 \Pr\Big(S[k] = \mathcal{S}^{\langle m \rangle} \mid R[k]\Big) \right] \right\} \\
&\overset{(4.24)}{=\!=} \frac{1}{4}\ \mathbb{E}\left\{ -\frac{1}{M} \sum_{m=1}^{M} \left[\Pr\Big(R[k] \mid S[k] = \mathcal{S}^{\langle m \rangle}\Big) \times \log_2 \left(\frac{\Pr\big(R[k] \mid S[k] = \mathcal{S}^{\langle m \rangle}\big)}{\sum\limits_{m'=1}^{M} \Pr\big(R[k] \mid S[k] = \mathcal{S}^{\langle m' \rangle}\big)} \right) \right] \right\} \\
&\overset{(4.17)}{=\!=} \frac{1}{4}\ \mathbb{E}\left\{ -\frac{1}{M} \sum_{m=1}^{M} \left[\frac{\exp\left[-\frac{d_{1,k,m}^2}{\sigma_n^2/2}\right]}{\pi \cdot \sigma_n^2/2} \times \log_2 \left(\frac{\frac{\exp\left[-\frac{d_{1,k,m}^2}{\sigma_n^2/2}\right]}{\pi \cdot \sigma_n^2/2}}{\sum\limits_{m'=1}^{M} \frac{\exp\left[-\frac{d_{1,k,m'}^2}{\sigma_n^2/2}\right]}{\pi \cdot \sigma_n^2/2}} \right) \right] \right\} \\
&= \frac{1}{4}\ \mathbb{E}\left\{ -\frac{1}{M} \sum_{m=1}^{M} \left[\frac{\exp\left[-\frac{d_{1,k,m}^2}{\sigma_n^2/2}\right]}{\pi \cdot \sigma_n^2/2} \times \log_2 \left(\frac{\exp\left[-\frac{d_{1,k,m}^2}{\sigma_n^2/2}\right]}{\sum\limits_{m'=1}^{M} \exp\left[-\frac{d_{1,k,m'}^2}{\sigma_n^2/2}\right]} \right) \right] \right\}.
\end{aligned} \tag{4.27}$$

$$\overset{\text{LACO}}{\mathsf{H}}(\mathsf{S}_l \mid \mathsf{R}_l) = \frac{1}{4}\ \mathbb{E}\left\{ -\frac{1}{M_l} \sum_{m=1}^{M_l} \left[\frac{\exp\left[-\frac{d_{l,k,m}^2}{\sigma_n^2/2}\right]}{\pi \cdot \sigma_n^2/2} \times \log_2 \left(\frac{\exp\left[-\frac{d_{l,k,m}^2}{\sigma_n^2/2}\right]}{\sum\limits_{m'=1}^{M_l} \exp\left[-\frac{d_{l,k,m'}^2}{\sigma_n^2/2}\right]} \right) \right] \right\}. \tag{4.28}$$

4.2.3 DCMC Capacity of LACO-OFDM Systems

Next, we extend the aforementioned DCMC capacity analysis to the more complex LACO-OFDM system, which also relies on the classic information theoretic capacity Eq. (4.25), *i.e.*

$$\mathsf{C}_{\text{LACO}}^{\text{DCMC}} = \max\left[\mathsf{H}(\mathsf{S}) - \mathsf{H}(\mathsf{S} \mid \mathsf{R})\right]. \tag{4.30}$$

For an L-layer LACO-OFDM scheme, the overall conveyed information quantified by the channel capacity can be expressed as

$$\mathsf{C}_{\text{LACO}}^{\text{DCMC}} = I(\mathsf{S}_1, \mathsf{S}_2, \ldots, \mathsf{S}_L \ ; \ \mathsf{R}_1, \mathsf{R}_2, \ldots, \mathsf{R}_L), \tag{4.31}$$

where the first half represents the source symbols of each layer, while the second half denotes their corresponding sink symbols.

Recall that each layer of LACO-OFDM is an ACO-OFDM signal and the transmitted symbols of each layer are independent, while the received symbols are correlated due to the presence of ILI. Therefore, Eq. (4.31) can be rearranged as

$$\begin{aligned} \mathsf{C}_{\text{LACO}}^{\text{DCMC}} &= \sum_{l=1}^{L} I(\mathsf{S}_l \ ; \ \mathsf{R}_1, \mathsf{R}_2, \ldots, \mathsf{R}_L) \\ &= I(\mathsf{S}_1 \ ; \ \mathsf{R}_1, \mathsf{R}_2, \ldots, \mathsf{R}_L) + I(\mathsf{S}_2 \ ; \ \mathsf{R}_1, \mathsf{R}_2, \ldots, \mathsf{R}_L) + \cdots \\ &\quad + I(\mathsf{S}_l \ ; \ \mathsf{R}_1, \mathsf{R}_2, \ldots, \mathsf{R}_L) + \cdots + I(\mathsf{S}_L \ ; \ \mathsf{R}_1, \mathsf{R}_2, \ldots, \mathsf{R}_L). \end{aligned} \tag{4.32}$$

For the sake of simplifying this cascaded ILI in the capacity calculation, we exploit the widely used chain rule [90]. Consequently, each of the terms in Eq. (4.32) can be rewritten as

$$\begin{aligned} & I(\mathsf{S}_l \ ; \ \mathsf{R}_1, \mathsf{R}_2, \ldots, \mathsf{R}_l, \ \ \mathsf{R}_{l+1}, \ldots, \mathsf{R}_L) \\ &= I(\mathsf{S}_l ; \mathsf{R}_1, \ldots, \mathsf{R}_l) + I(\mathsf{S}_l ; \mathsf{R}_{l+1}, \ldots, \mathsf{R}_L | \mathsf{R}_1, \ldots, \mathsf{R}_l). \end{aligned} \tag{4.33}$$

Recall that each layer is only affected by the ILI of lower layers. Consequently, the symbols $\boldsymbol{R}_l$ received on layer l are independent of the symbols $\{\boldsymbol{R}_{l+1}, \boldsymbol{R}_{l+2}, \ldots, \boldsymbol{R}_L\}$ received in the upper layers. Hence, the second term in Eq. (4.33) is always zero, while the first term can be further expanded as

$$I(\mathsf{S}_l \ ; \ \mathsf{R}_1, \mathsf{R}_2, \ldots, \mathsf{R}_l) = \mathsf{H}(\mathsf{S}_l) - \mathsf{H}(\mathsf{S}_l \mid \mathsf{R}_1, \ldots, \mathsf{R}_l), \tag{4.34}$$

which is the source entropy of layer l, minus the loss of information caused by layers $1 \sim l$.

As it will be demonstrated in Sec. 4.5, the ILI can be substantially reduced by appropriately incorporating FEC codes. Hence, under the assumption of perfect error correction (or equivalently, perfect detection), the ILI can be completely eliminated. Consequently, it is reasonable to assume that we have:

$$\mathsf{H}(\mathsf{S}_l \mid \mathsf{R}_1, \ldots, \mathsf{R}_l) \approx \mathsf{H}(\mathsf{S}_l \mid \mathsf{R}_l) \qquad \forall\, 1 \leq l \leq L, \tag{4.35}$$

where $\mathsf{H}(\mathsf{S}_l \mid \mathsf{R}_l)$ related to layer l can be computed using Eq. (4.27). This in turn implies that the overall conveyed information can be estimated by adding together the information conveyed by each independent ACO-OFDM layer.

Hence, the DCMC capacity of an L-layer LACO-OFDM system can be expressed in bits/symbol as follows:

$$\mathsf{C}_{\text{LACO}}^{\{Ml\}\text{QAM}} = \sum_{l=1}^{L} 2^{-l-1} \left[\log_2 M_l - \mathsf{H}(\mathsf{S}_l \mid \mathsf{R}_l)\right], \tag{4.36}$$

where the factor 2^{-l-1} denotes the spectrum efficiency of layer l. If all layers invoke the same modulation scheme, i.e. we have $M_l = M$, $\forall\, l$, then Eq. (4.36) can be further simplified as follows:

$$\mathsf{C}_{\text{LACO}}^{M\text{QAM}} \overset{(4.38),(4.39)}{=\!=\!=\!=} \left(\frac{1}{2} - \frac{1}{2^{L+1}}\right) \left[\log_2 M - \mathsf{H}(\mathsf{S}_1 \mid \mathsf{R}_1)\right] \qquad \text{(bits/symbol)}, \tag{4.37}$$

because

$$\mathsf{H}(\mathsf{S}_l \mid \mathsf{R}_l) \equiv \mathsf{H}(\mathsf{S}_1 \mid \mathsf{R}_1), \tag{4.38}$$

and

$$\sum_{l=1}^{L} 2^{-l-1} = \frac{1}{4} + \frac{1}{8} + \cdots + \frac{1}{2^{L+1}} = \left(\frac{1}{2} - \frac{1}{2^{L+1}}\right). \tag{4.39}$$

Moreover, similar to the CCMC capacity, the information bit to noise power ratio γ_{ib} can also be defined based on the DCMC capacity, which represents the amount of deliverable information at a certain SNR *using a certain modulation scheme*, expressed as

$$\gamma_{\text{ib}} = \frac{E_{\text{s}}}{N_0} \times \frac{1}{\mathsf{C}_{\text{LACO}}^{M\text{QAM}}}. \tag{4.40}$$

Again, the capacity $\mathsf{C}_{\text{LACO}}^{M\text{QAM}}$ has the unit of (bits/symbol).

It is also worth mentioning that when calculating $\mathsf{H}(\mathsf{S}_1 \mid \mathsf{R}_1)$ for LACO-OFDM, the noise power should be higher for a given value of $\frac{E_{\text{s}}}{N_0}$, because the total symbol energy increases as more layers are superimposed and more idle subcarriers are filled up. More specifically, if equal symbol energy is assigned to every subcarrier, as in [1,53], the total unnormalised LACO-OFDM symbol power is equivalent to Eq. (3.16). Consequently, Eq. (4.19) should be modified as

$$\frac{E_\mathrm{s}}{N_0} = \gamma_\mathrm{b} \cdot \sum_{l=1}^{L} \left(\frac{1}{2^{l+1}} \cdot \log_2 M_l \right) = \frac{E_\mathrm{s}}{\sigma_n^2/2}, \tag{4.41}$$

which in turn modifies Eq. (4.20) into

$$\frac{\sigma_n^2}{2} = \frac{\frac{2}{\pi}\left[\frac{\left(1-2^{-L/2}\right)^2}{3-2\sqrt{2}} + (\pi - 1)\left(1 - \frac{1}{2^L}\right) \right]}{\gamma_\mathrm{b} \cdot \sum_{l=1}^{L} \left(\frac{1}{2^{l+1}} \cdot \log_2 M_l \right)}. \tag{4.42}$$

for LACO-OFDM.

4.2.4 Numerical Capacity Results

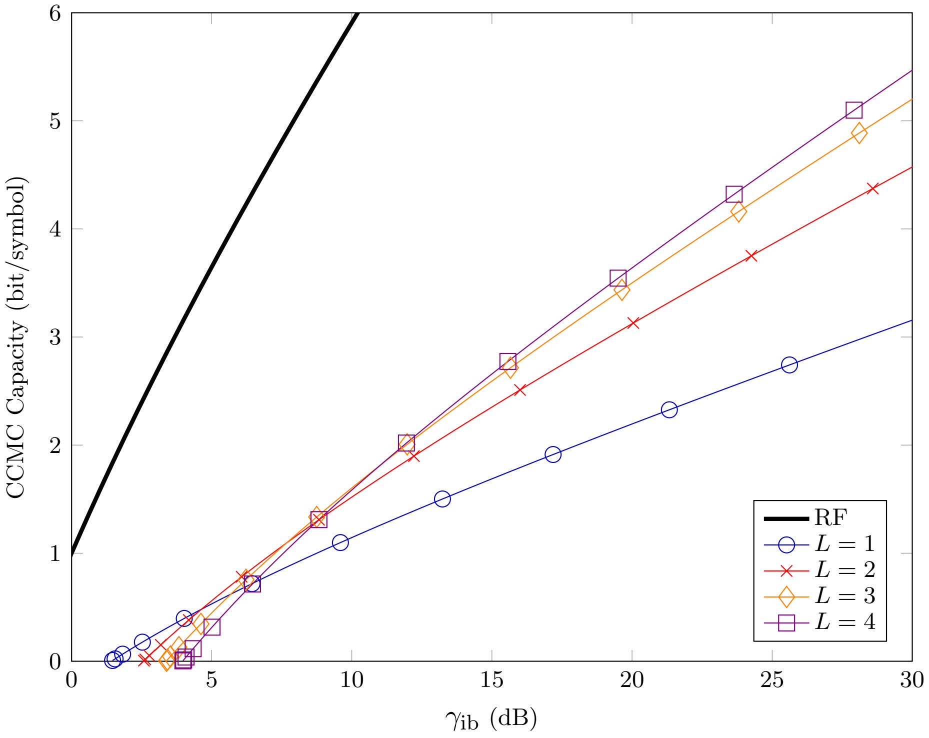

Figure 4.2: CCMC capacity versus information bit to noise power ratio γ_ib of LACO-OFDM systems having different number of layers L. The CCMC capacity of RF systems is also shown for reference.

Figure 4.2 plots the CCMC capacity of LACO-OFDM against the information bit to noise power ratio, based on the analysis of Sec. 4.2.1. LACO-OFDM systems having different number of layers L are compared to each other, as well as to the RF capacity, where the influence of throughput difference has been eliminated by normalisation using γ_ib.

It is firstly clear that all the IM/DD optical schemes have a lower capacity than their the RF counterparts, due to the loss of the imaginary part of the TD signal. Meanwhile, LACO-OFDM schemes with less layers tend to perform better in the low-SNR region. This is mainly due to the overall poor performance under such channel conditions, preventing the lower layers from being correctly detected, which in turn imposes excessive ILI and further degrades the performance. Once sufficient power becomes available, the schemes having more layers start to exhibit more steep capacity improvements. However, at a high SNR, such as for example $\gamma_{\text{ib}} = 20$ dB, it can be observed that the gaps between the capacity curves is reduced as L increases.

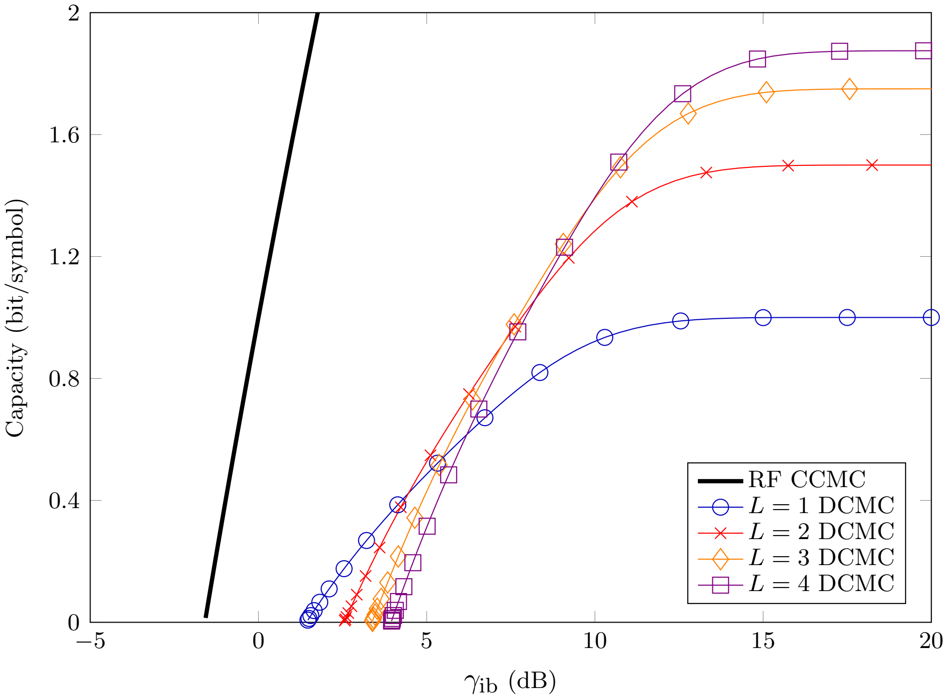

Figure 4.3: DCMC capacity versus the information bit to noise power ratio γ_{ib} of 16QAM LACO-OFDM systems for different number of layers L. The CCMC capacity of an RF system is also plotted for reference.

By contrast, Fig. 4.3 shows the DCMC capacity of LACO-OFDM systems for different number of layers L, when 16QAM is used. The CCMC capacity of RF systems is provided again for reference using γ_{ib} as x-axis. However, bear in mind that the definitions of γ_{ib} are slightly different for the CCMC and DCMC models.

Similar capacity trends can also be observed by comparing Fig. 4.3 to the CCMC models' of Fig. 4.2, where the low-SNR and high-SNR region have performance curves ranked in opposite order, when parameterised by the number of layers L. Meanwhile, since the DCMC capacity is ultimately restricted by the choice of modulation scheme, all the curves converge to a level corresponding to $\frac{1}{4}\left(\frac{1}{2} - \frac{1}{2^{L+1}}\right)\log_2 M$.

Finally, Figs. 4.4 and 4.5 compare the capacities of LACO-OFDM systems by fixing the number of layers L and varying the modulation constellation size M.

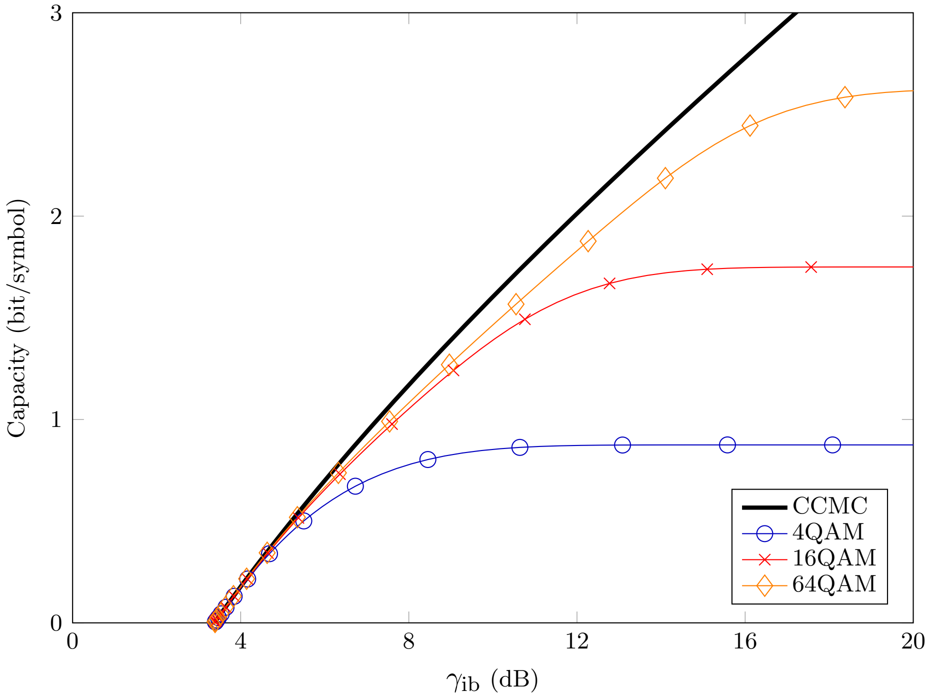

Figure 4.4: DCMC capacity versus the information bit to noise power ratio γ_{ib} of 3-layer LACO-OFDM systems for different QAM constellation sizes M. The CCMC capacity of a 3-layer LACO-OFDM system is also plotted for reference.

In Fig. 4.4, the 3-layer LACO-OFDM systems' DCMC capacities are presented, together with the CCMC capacity of the same system, where all the curves are plotted vs γ_{ib}. By contrast, Fig. 4.5 depicts the 3-layer and 4-layer LACO-OFDM systems' DCMC capacities vs $\frac{E_{\text{s}}}{N_0}$, namely the SNR. It is clear that for all figures, the DCMC capacity is tightly bounded by the CCMC capacity, especially in the low-SNR region. The DCMC capacity curves representing lower modulation orders branch off from the CCMC capacity earlier and converge to a lower capacity level, due to the limitation of the individual modulation schemes. This trend is similar to those of the RF systems [87].

4.3 Single-Class Coding System

One of the most important reasons to study the channel capacity is to numerically evaluate the performance of FEC codes - in other words, how much closer they allow us to approach the capacity limit.

In this section, we firstly conceive a naïve coding system, where the channel coding is simply implemented by cascading the transceiver with the corresponding codec. We refer to this system as a *single-class* coding scheme, as opposed to the *multi-class* coding scheme of the next section.

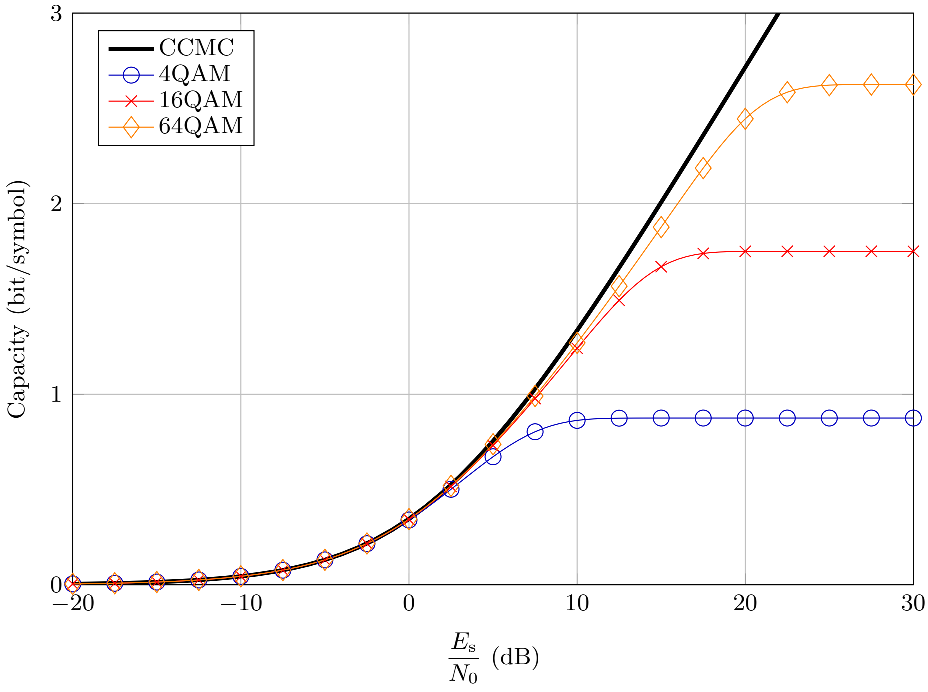

(a) 3-layer

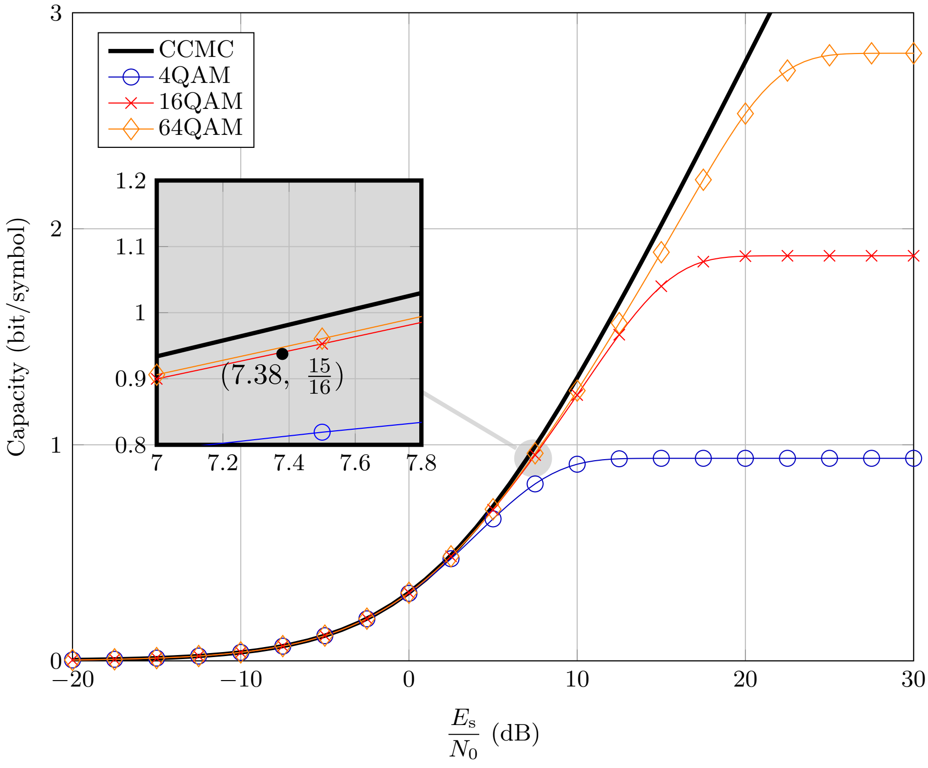

(b) 4-layer

Figure 4.5: DCMC capacity versus the symbol to noise power ratio $\frac{E_s}{N_0}$ of (a) 3-layer and (b) 4-layer LACO-OFDM systems for different QAM constellation sizes M. The CCMC capacity of 3-layer and 4-layer LACO-OFDM systems are also plotted for reference, respectively.

4.3.1 System Model

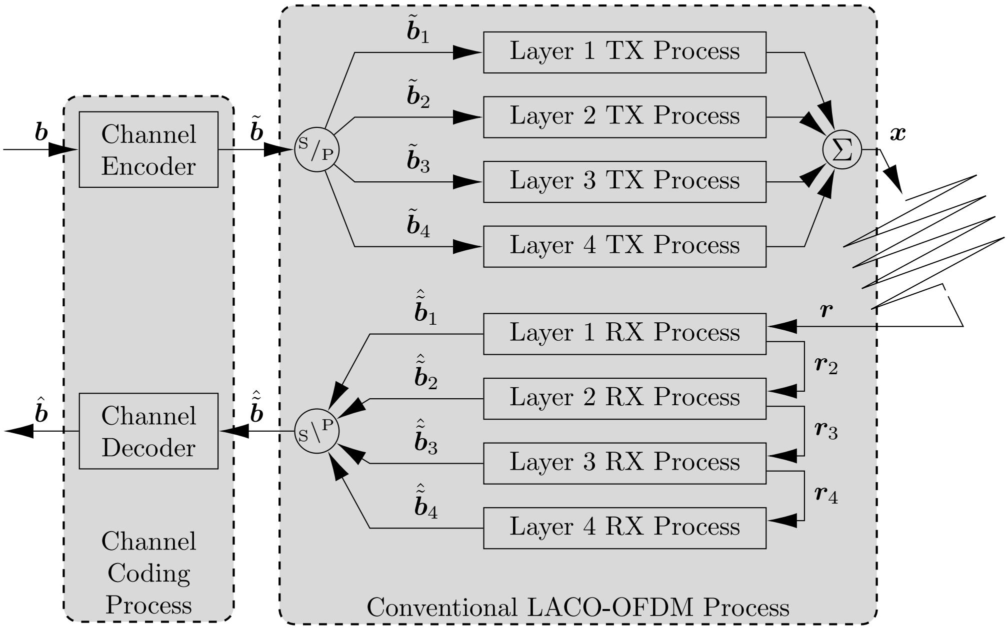

Figure 4.6: Single-Class coded LACO-OFDM transceiver for a 4-layer LACO-OFDM system.

Figure 4.6 depicts the schematic of a single-class LACO-OFDM system. The top half represents the transmitter, where each of the “Layer l TX Process” blocks in the middle uses the ACO-OFDM-style modulation for each layer, similar to those seen in Fig. 2.6. The bit stream $\boldsymbol{s}$ is passed through the channel encoder, which produces the coded sequence $\tilde{\boldsymbol{b}}$. Then, the LACO-OFDM transmitter separates the single stream into several sub-streams $\tilde{\boldsymbol{b}}_l$, each corresponding to a LACO-OFDM layer. The FEC-coded bits are then mapped into symbols and modulated according to Sec. 2.3.1.

The receiver of the system is seen at the bottom of Fig. 4.6, where the received signal $\boldsymbol{r}$ is detected on a layer-by-layer manner as in Sec. 2.3.2, and each of the “Layer l RX Process” stages includes both the layer detection and its clipping distortion cancellation processes, as detailed in Fig. 2.7. The detected bits of each layer $\hat{\tilde{\boldsymbol{b}}}_l$ are combined into a single stream $\hat{\tilde{\boldsymbol{b}}}$ in a chronological order before channel decoding, resulting in $\hat{\boldsymbol{b}}$ of Fig. 4.6.

Again, as shown in Fig. 4.6, in this single-class scheme, the channel coding components receive the hard-decision bit stream from the LACO-OFDM scheme.

In the next subsection, we will conduct Monte-Carlo simulation for characterising this single-class coded scheme for various choice of FEC codes, as well as LACO-OFDM configurations.

4.3.2 Numerical Results

Unless otherwise specified, the following parameters given in Tab. 4.1 apply to all the simulations both within this section for our single-class system and the next section for the multi-class system.

Table 4.1: Parameters Used for Simulation Results in Chapter 4

Symbol	**Definition**	**Value**	**Applicable Figures**
M	Size of the constellation pattern	16	4.7, 4.8, 4.11, 4.12, 4.13, 4.14
L	Number of layers composing the LACO-OFDM signal	4	4.7, 4.11, 4.12, 4.13, 4.14
K	Number of FFT/IFFT points	2048	4.7, 4.8, 4.11, 4.12, 4.13
N/A	Channel	AWGN	4.7, 4.8, 4.11, 4.12, 4.13, 4.14

Figure 4.7 shows the BER performance of a 4-layer 16QAM-modulated LACO-OFDM system employing the above-mentioned single-class scheme, where the choice of FEC codes is varied. A weaker convolutional code with memory $\mathcal{M} = 2$ (Scheme 2) and the octally represented generator polynomial $(7, 5)$ as well as a code-rate of $\mathsf{R} = \frac{1}{2}$ is used. A stronger turbo code relying on a pair of $\mathcal{M} = 3$ Recursive Systematic Convolutional (RSC) codes (Scheme 4) using the generator polynomials $(15, 13)$ and a maximum of $\mathcal{I} = 8$ decoding iterations is also employed for comparison. The coding rate was again $\mathsf{R} = \frac{1}{2}$ after puncturing. The performance is also compared against the uncoded results of Scheme 1 characterised Fig. 3.12 in Chapter 3. Meanwhile, the BER performance of a convolutional code with memory $\mathcal{M} = 7$ (Scheme 3) is also provided, which is of the same complexity as the turbo code Scheme 4.

As shown in Fig. 4.7, utilising the single-class coding system does improve the BER performance of our LACO-OFDM system. Explicitly, employing the $\mathcal{M} = 3$ convolutional code (Scheme 2) starts to produce a lower BER than its uncoded counterpart (Scheme 1) for SNR beyond $\gamma_\mathrm{b} \approx 15.5$ dB, while having a coding gain of around 0.25 dB at $\mathbb{P}_\mathrm{b} = 10^{-3}$. Moreover, the performance can be further improved by the $\mathcal{I} = 8$, $\mathcal{M} = 2$ turbo code (Scheme 4), which outperforms both the convolution code scheme with the same complexity (Scheme 3) and its uncoded counterpart for SNRs in exceeds of $\gamma_\mathrm{b} = 8.5$ dB, giving a 3.9 dB gain at $\mathbb{P}_\mathrm{b} = 10^{-3}$.

Furthermore, we have used $\frac{1}{2}$-rate FEC codes for the three coded Schemes. Hence, the overall throughput (or rate) of the resultant coded LACO-OFDM system can be

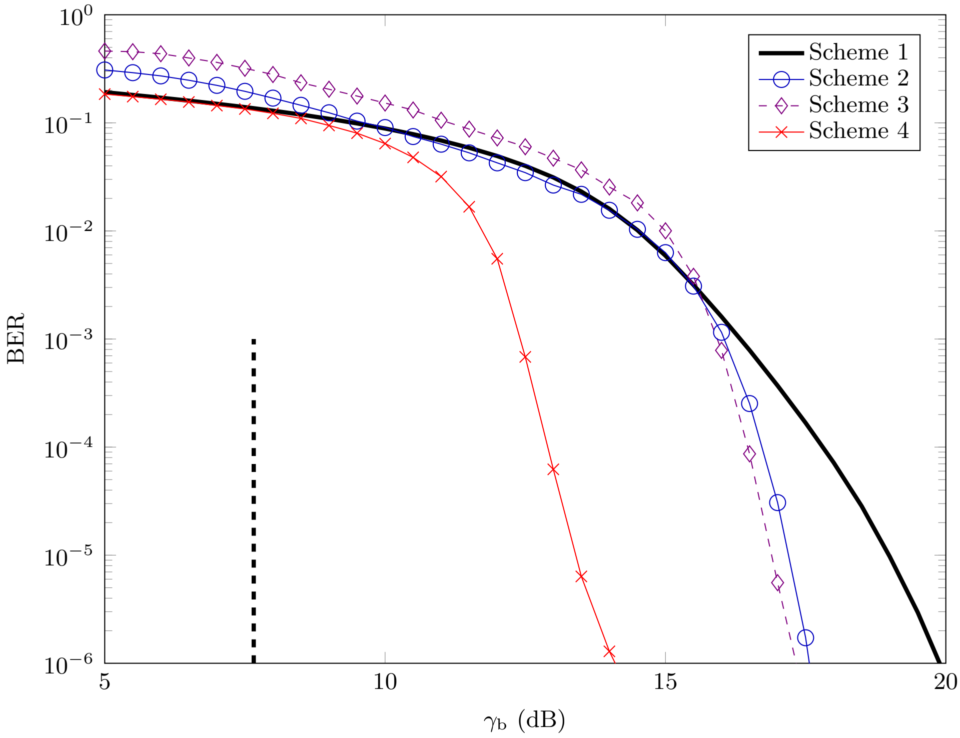

Figure 4.7: BER performance of 4-layer single-class coded LACO-OFDM for 16QAM modulation. All parameters are summarised in Table 4.1. Details about the simulation schemes are also summarised in Table 4.2 on page 98.

formulated as follows:

$$\mathsf{R}_{\text{4LACO}}^{\text{16QAM}}\Big|_{r=1/2} = \frac{1}{2} \times \left(\log_2(16) \times \frac{1}{4} \times \sum_{l=1}^{4} \frac{1}{2^{l-1}} \right) = \frac{15}{16} \text{ bits/symbol.} \tag{4.43}$$

Based on Shannon's information theorem [86], the achievable rate under such throughput would be $\frac{15}{16}$ bits/symbol, which corresponds to a limit SNR $E_s/N_0 = 7.38$ dB (or equivalently $\gamma_b = 7.66$ dB) according to Fig. 4.5(b).

Still referring to Fig. 4.7 at the $\mathbb{P}_b = 10^{-3}$ level, the two convolutional codes (Schemes 2 and 3) are 8.68 dB and 8.26 dB far away from the capacity, respectively. On the other hand, the stronger turbo code (Scheme 4) narrows the gap down to 5 dB.

The above-mentioned coding gains are achieved at the cost of the following decoding complexities. The 8-state convolutional code of Scheme 2 has 8 Add-Compare-Select (ACS) arithmetic operations, while the 128-state convolutional code of Scheme 3 has 128 ACS operations. By contrast, the turbo code has a pair of identical 8-state RCS decoders, which rely on $\mathcal{I} = 8$ iterations. Hence, it has a maximum complexity of $8 \times 2 \times 8 = 128$ ACS operations.

Meanwhile, Fig. 4.8 shows the BER performance of 16QAM-modulated LACO-OFDM systems employing the single-class scheme, where the number of layers is varied. The two convolutional coding schemes (Scheme 2 and Scheme 3) are applied for comparing their error correction abilities.

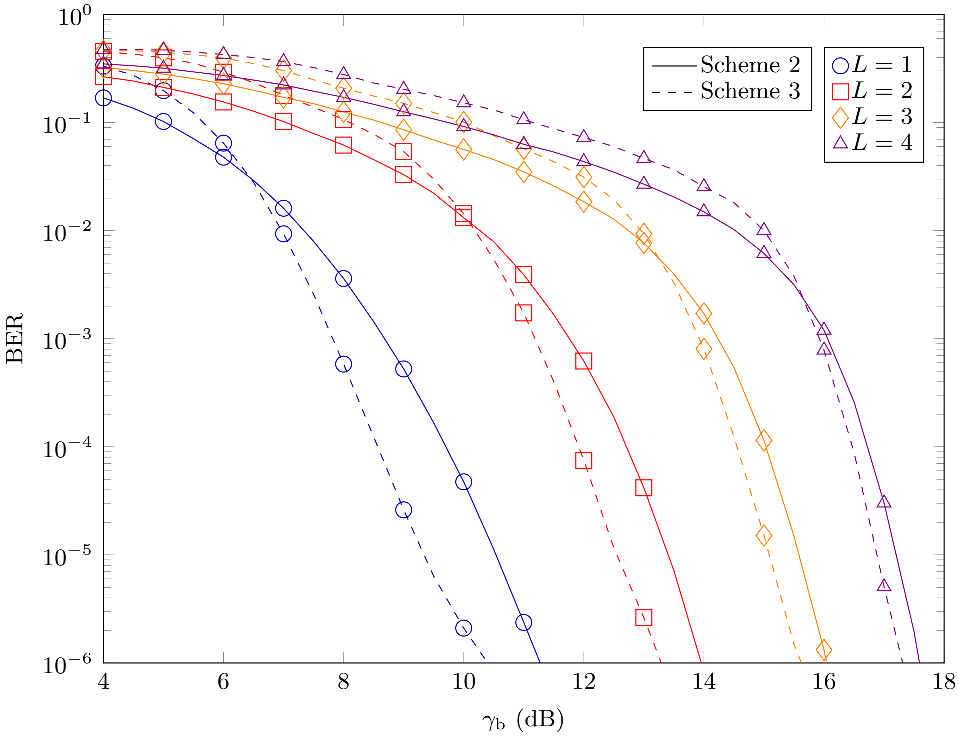

Figure 4.8: BER performance of single-class coded LACO-OFDM for 16QAM modulation having different number of layers and employing convolutional codes with different memory lengths. All parameters are summarised in Table 4.1. Details about the simulation schemes are also summarised in Table 4.2 on page 98.

Observe in Fig. 4.8 that the 32-times more complex 128-state convolutional code of Scheme 3 achieves a modest γ_b gain of about 1.5 dB at $\mathbb{P}_b = 10^{-4}$ for our single-layer scheme. Moreover, its γ_b advantage gradually erodes for the 2-, 3- and 4-layer schemes, owing to the increased ILI. Hence, a better trade-off is struck by the 4-state convolutional code of Scheme 2.

4.3.3 Discussions

Although the single-class coded LACO-OFDM succeeds in slightly improving the BER performance, this structure has several impediments that limit its overall performance. Specifically,

1. The original TX of Fig. 2.5 has a parallel structure. The signal processing of all layers can be carried out simultaneously, before their respective clipped signals are superimposed onto each other. However, in case of the conventional single-class

coded LACO-OFDM system, the encoder operates serially. Hence, the higher layers have to wait for their bits to be encoded. This introduces delay at the TX. It is also worth noting that the delay increases upon increasing the frame length.

2. The conventional coded LACO-OFDM system fails to exploit the full potential of FEC codes. The FEC codes are capable of alleviating the impact of ILI, if invoked in a carefully matched layered manner. As it will be detailed later in this section, ILI in the conventional system is the same as that in the uncoded system.
3. One of the benefits of a LACO-OFDM system is its flexibility [1]. Specifically, the number of layers, the modulation scheme as well as the power allocation invoked for each layer can be adjusted to achieve a desired QoS or throughput requirement. However, since all bits are encoded jointly in a single-class coded system, the same coding rate, and more importantly the same code, must be used for all input bits; hence, the system loses flexibility. This can be particularly disadvantageous in scenarios, where one would like to use stronger codes for particular layers to provide a higher level of protection.

Against this background, we present our new multi-class coded LACO-OFDM system, where the encoding and decoding components are integrated within the original layered structure. In this way, the system avoids the aforementioned problems, since each layer has its own encoding and decoding units.

4.4 Multi-Class Coding System

In this section, we present our multi-class coded LACO-OFDM architecture, where Sec. 4.4.1 introduces the TX design, while the RX is presented in Sec. 4.4.2.

4.4.1 Transmitter Design

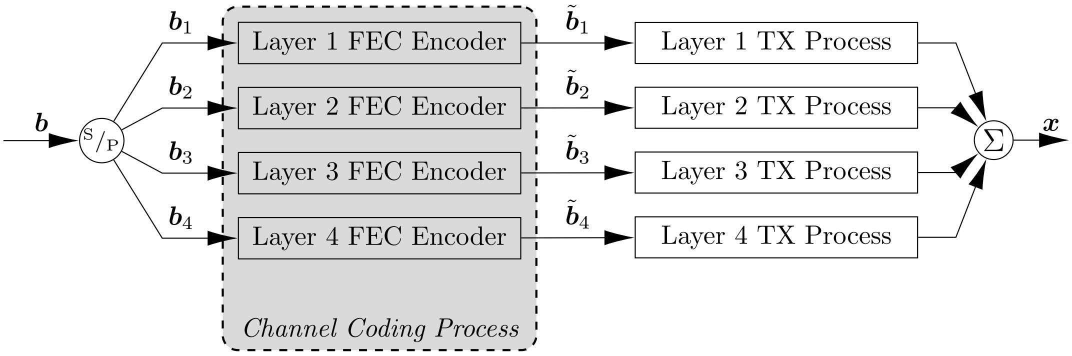

Figure 4.9: A LACO-OFDM transmitter integrated with FEC encoders. The 'LACO TX CORE' block is given in Fig. 2.5.

Figure 4.9 shows the schematic of the proposed multi-class LACO-OFDM transmitter, which intrinsically integrates layer-specific FEC encoders within the layered structure of the LACO-OFDM system. Each layer of the LACO-OFDM system of Fig. 4.9 has its own choice of constellation size M_l, coding rate r_l as well as the type of FEC code. First, the S/P block divides the input bit stream b into L blocks, so that the lth layer has B_l uncoded bits, denoted as b_l. Each layer then independently encodes its input bits b_l using an FEC code having a coding rate of r_l. The resultant encoded bits $\bar{b}_l$ and the desired constellation size M_l are then fed to the 'LACO TX CORE' block of Fig. 2.5 for further processing.

The multi-class FEC encoder of Fig. 4.9 simultaneously processes each layer. Since each layer only has a portion of the original bit stream b, it takes shorter time to complete the entire encoding process. Moreover, this design allows us to individually choose the FEC code type and the coding rate for each layer, hence facilitating adaptive LACO-OFDM FEC coding.

4.4.2 Receiver Design

Figure 4.10 shows the schematic of the proposed LACO-OFDM RX, where the FEC decoders are integrated into the multi-class coded structure of LACO-OFDM, similar to the transmitter of Fig. 4.9. Analogously to the uncoded RX of Fig. 2.7, the RX of Fig. 4.10 operates layer-wise, commencing from the first layer, which is not contaminated by ILI. However, the clipped signal $\lfloor s_l \rfloor$ of the lth layer is now regenerated based on the output of the FEC decoder, rather than relying on the hard-output of the QAM demapper. More specifically, the soft QAM demapper of Fig. 4.10 computes the *a priori* LLRs $\mathcal{L}_{\mathrm{a}}\left(\tilde{\boldsymbol{b}}_l\right)$ of the encoded bits $\tilde{\boldsymbol{b}}_l$ from the bit-based counterparts of the symbol-based likelihood probabilities of Eq. (4.17). The *a priori* LLRs $\mathcal{L}_{\mathrm{a}}\left(\tilde{\boldsymbol{b}}_l\right)$ are then fed to the FEC decoder of Fig. 4.10, which is essentially a Soft-In-Soft-Out (SISO) decoder. This SISO decoder yields the *a posteriori* LLRs $\mathcal{L}_{\mathrm{p}}(\boldsymbol{b}_l)$ of the uncoded bits $\boldsymbol{b}_l$. Finally, hard-decision is applied both to $\mathcal{L}_{\mathrm{p}}\left(\tilde{\boldsymbol{b}}_l\right)$ and to $\mathcal{L}_{\mathrm{p}}(\boldsymbol{b}_l)$, yielding $\hat{\boldsymbol{b}}_l$ and $\hat{\tilde{\boldsymbol{b}}}_l$, respectively. The resultant $\hat{\boldsymbol{b}}_l$ is then fed to the 'ACO TX' block of Fig. 2.2 for estimating the ILI imposed on the $(l+1)$st layer. The rest of the process at RX of Fig. 4.10 is the same as that of the uncoded system. Hence, the proposed RX estimates the ILI based on the output of the FEC decoder. Since the FEC decoder corrects most of the channel errors, the resultant ILI estimations become more accurate. Consequently, the ILI is substantially reduced, provided that the receiver design of Fig. 4.10 is invoked. Therefore, the FEC encoders of Fig. 4.10 substantially mitigate the impact of ILI.

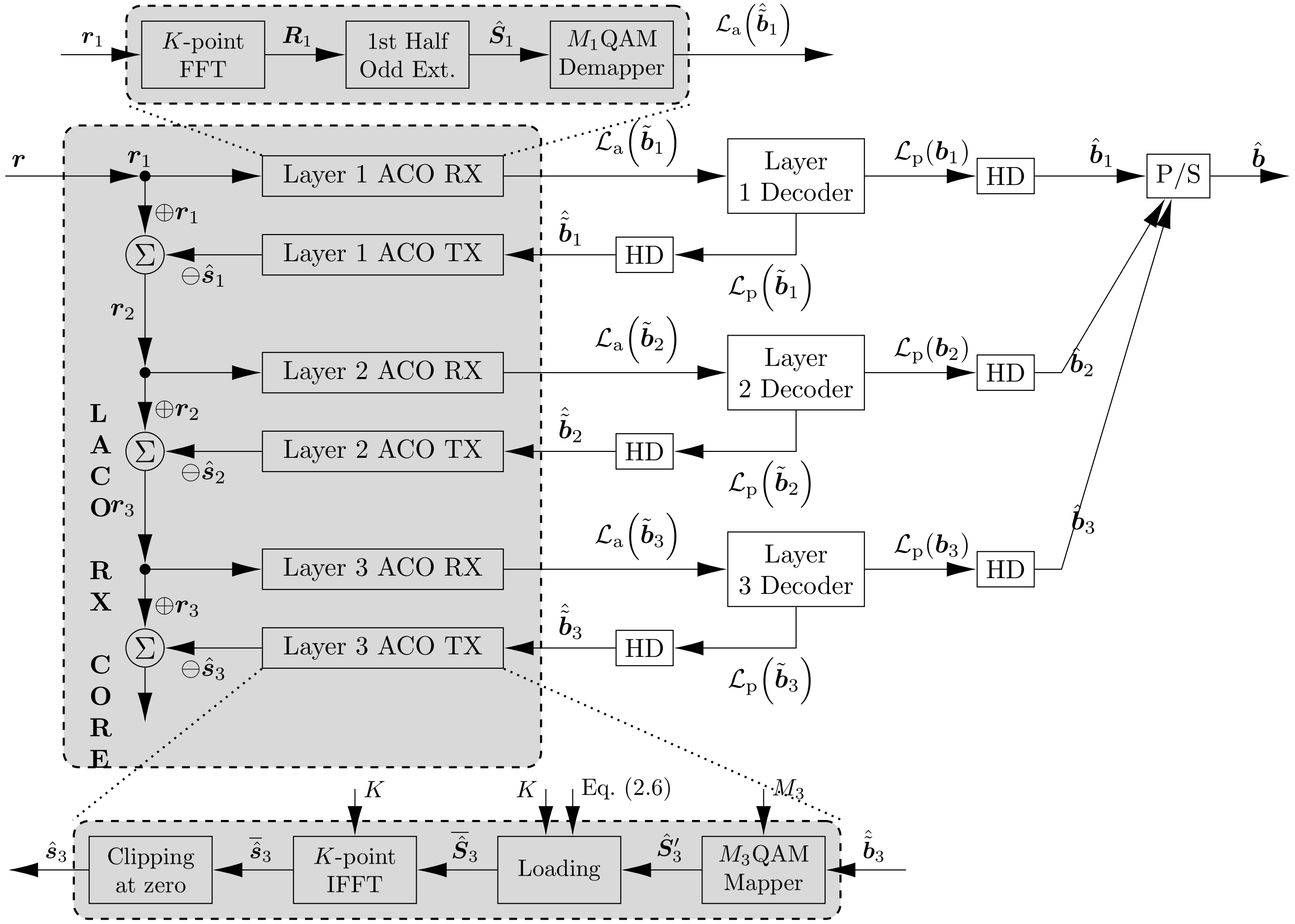

Figure 4.10: Multi-Class Coded LACO-OFDM RX

4.5 Simulations and Discussions

In this section, we evaluate the performance of our proposed multi-class coded system. First we benchmark the BER performance against the single-class coded LACO-OFDM system as well as the achievable rate limit. Then we will analyse the detailed influence of FEC codes on each LACO-OFDM layer. In all simulations we have used a 4-layer LACO-OFDM scheme communicating through an AWGN channel relying on a total of 2048 subcarriers and 16QAM.

Similar to the discussion for the single-class coded system on page 92, the SNR corresponding to the capacity limit of a 4-layer LACO-OFDM system using a half-rate FEC channel code is at $\gamma_{\mathrm{b}} = 7.66$ dB.

4.5.1 Performance of Different FEC Codes

Figure 4.11 shows the BER performance recorded for different coding scenarios listed in Table 4.2. Specifically, we have invoked both convolutional codes having a memory of M and turbo codes relying on I decoding iterations. The performance is benchmarked against the corresponding single-class scenarios as well as the achievable rate limit.

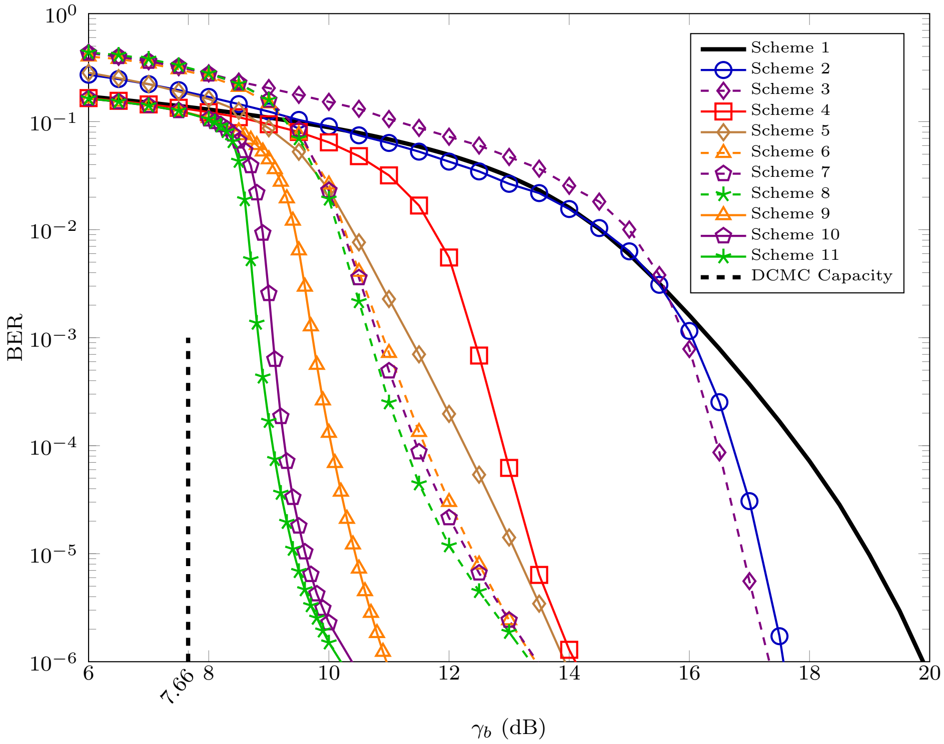

Figure 4.11: BER performance of a 4-layer LACO-OFDM system operating 16QAM on all of its layers communicating in AWGN channels. The channel coding schemes of Table 4.2 are used.

Table 4.2: Channel Coding Schemes Used for Simulations

№	Structure	Code	Parameter	Rate	Polynomials	States
1	Single-Class	N/A	N/A	N/A	N/A	N/A
2		Convolutional	$\mathcal{M} = 2$	$\frac{1}{2}$	$(7, 5)$	4
3			$\mathcal{M} = 7$		$(371, 247)$	128
4		Turbo	$\mathcal{M} = 3$, $\mathcal{I} = 8$		$(15, 13)$	128
5	Multi-Class	Convolutional	$\mathcal{M} = 2$		$(7, 5)$	4
6			$\mathcal{M} = 5$		$(75, 53)$	32
7			$\mathcal{M} = 6$		$(171, 133)$	64
8			$\mathcal{M} = 7$		$(371, 247)$	128
9		Turbo	$\mathcal{M} = 3$, $\mathcal{I} = 2$		$(15, 13)$	32
10			$\mathcal{M} = 3$, $\mathcal{I} = 4$			64
11			$\mathcal{M} = 3$, $\mathcal{I} = 8$			128

We may observe in Fig. 4.11 that the multi-class Scheme 5, Scheme 8 and Scheme 9 significantly outperform their single-class counterparts of Scheme 2, Scheme 3 and Scheme 4, respectively. Quantitatively, the layered turbo coded system Scheme 9 operates within 1.1 dB of the achievable rate at a BER of 10^{-3}, while Scheme 4 of the single-class turbo coded system is 4.7 dB away from the achievable rate. Hence, our layered design offers a 3.6 dB gain at the same encoding and decoding complexity. We may also observe in Fig. 4.11 that even the less sophisticated multi-class convolutional coded Scheme 5 of Table 4.2 outperforms the single-class turbo coded Scheme 4, which has a significantly higher decoding complexity.

More explicitly, the decoding complexity as well as time delay of trellis codes is proportional to the number of trellis states invoked during the decoding process [71]. A memory-2 convolutional code invokes only $2^2 = 4$ trellis states. By contrast, a turbo code relying on two parallel concatenated memory-3 convolutional codes invokes $(2^3 \times 2) = 16$ states in each iteration; hence invoking a total of $(16 \times 8) = 128$ states in 8 iterations. This implies that the layered convolutional-coded system imposes 32 times lower decoding decoding complexity than the single-class turbo-coded system in addition to providing a better BER performance. In Fig. 4.12 we plot the distance to the achievable rate limit versus coding complexity for a 4-layer LACO-OFDM system utilising the proposed multi-class coding architecture. The coding complexities are quantified by the number of states used, and are also summarised in Table 4.2. As shown in Fig. 4.12, a closer match to the achievable rate limit can be obtained upon increasing the coding complexity by increasing the memory of the convolutional codes and the number of turbo iterations.

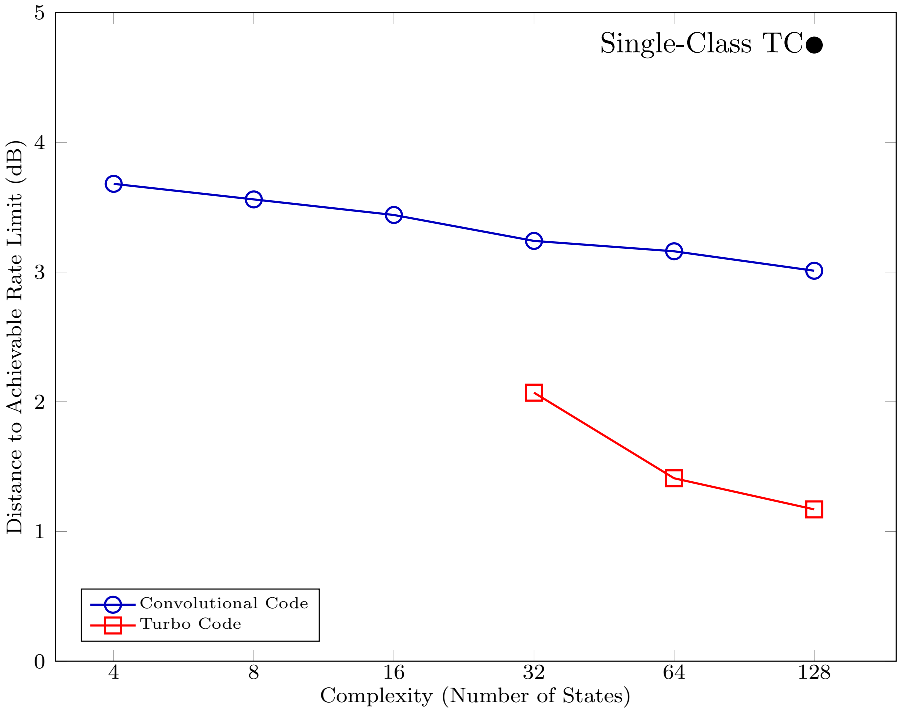

Figure 4.12: Distance to the achievable rate limit for multi-class coded 4-layer LACO-OFDM using different coding schemes. Convolutional code with various memory size and turbo code concatenating two memory-3 convolutional code with various iterations are used.

4.5.2 Performance of Different LACO-OFDM Layers

Next, we embark on a more detailed analysis of the coding of each LACO-OFDM layer. Turbo coding with a maximum $I = 8$ iterations (scheme 10 of Table 4.2) is considered here owing to its best performance.

Figure 4.13(a) records the layer-wise BER performance of the uncoded system, while Fig. 4.13(b) depicts the BER performance of the layered turbo coded system. We may observe a dramatic performance improvement for all layers. However, the BER curves of the layers in the turbo-coded scenario do not converge even for very high SNRs. This is because the turbo interleaver length is reduced, as we move up the layers and the performance of the turbo code degrades upon decreasing the interleaver length. More specifically, the first layer has a turbo interleaver length of 2^{11} bits, while that of the fourth layer is only 2^8. Consequently, the turbo code of the first layer performs better than that of the fourth layer, since it is widely recognised that the performance of the turbo code improves upon increasing the interleaver length.

For the sake of demonstrating that the coded system is capable of completely eliminating the ILI, in the investigation of Fig. 4.14 we use a frame length of 2^8 bits for all layer. Since the first three layers are capable of conveying more bits, their input frames are partitioned into sub-frames of length 2^8, which are encoded (and similarly decoded)

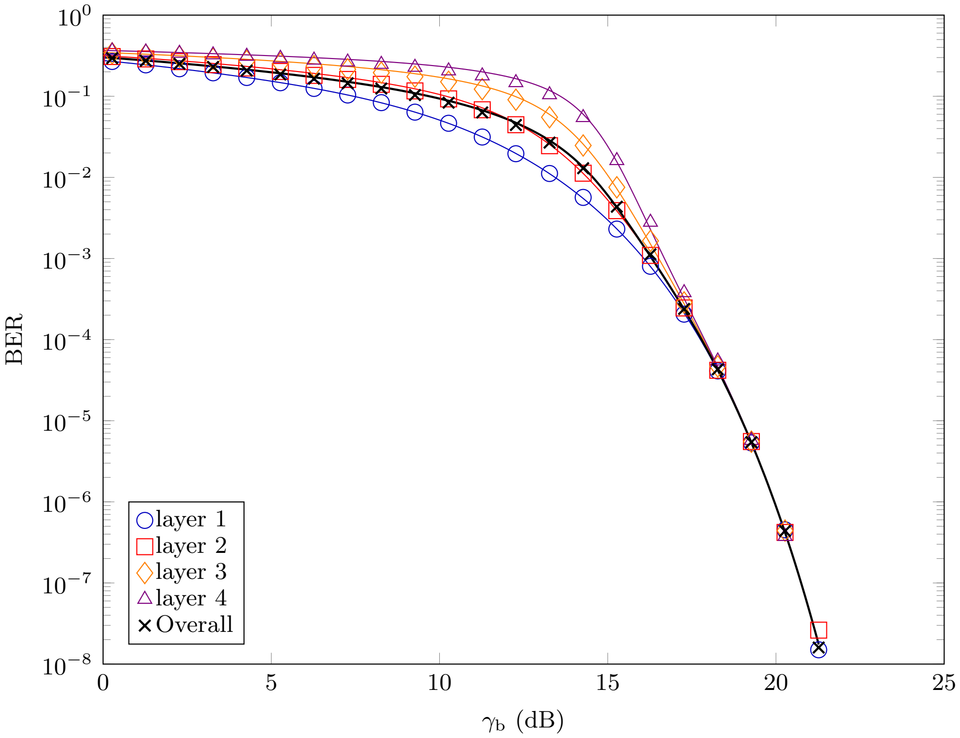

(a) Without FEC (replica of Fig. 3.11 of Chapter 3)

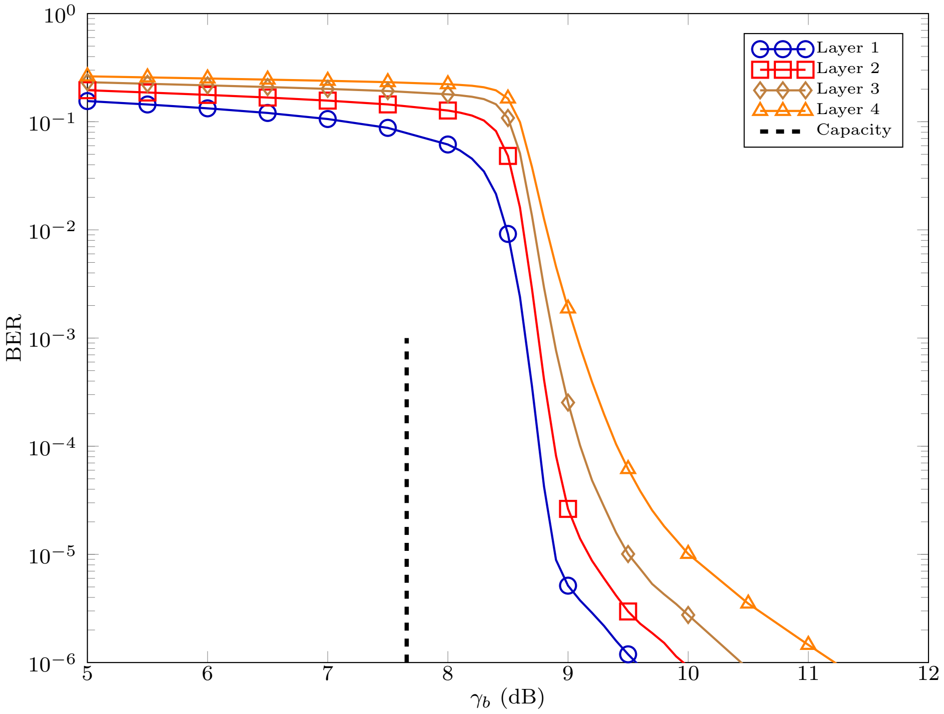

(b) With FEC

Figure 4.13: BER performance on each layer of a 4-layer LACO-OFDM system operating 16QAM on all of its layers communicating in AWGN channels. (a) without FEC. (b) with 8-iteration turbo code, and each layer having its maximum achievable interleaver length.

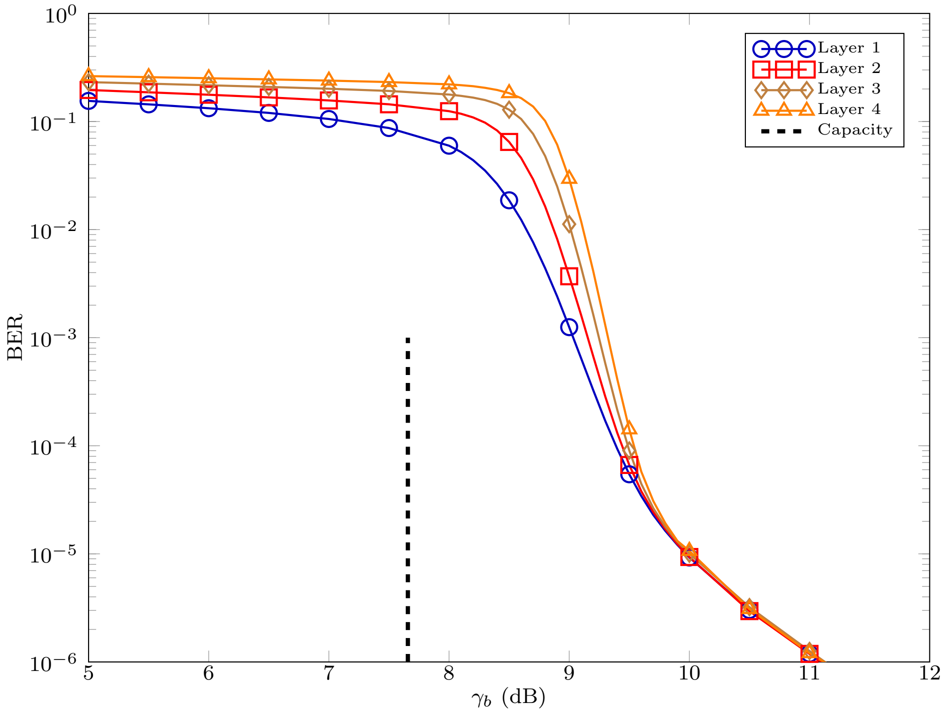

Figure 4.14: BER performance of each layer of a 4-layer LACO-OFDM system invoking 16QAM on all of its layers communicating in AWGN channels with 8-iteration turbo code, and each layer having the same interleaver length.

separately. The resultant BER performance curves are recorded in Fig. 4.14. As shown in Fig. 4.14, all layers now converge around BER $= 10^{-5}$, which echoes the same trend as that in Fig. 4.13(a). This implies that the layered turbo coded system is capable of completely eliminating the ILI around $E_b/N_0 = 10$ dB. By contrast, this was only possible around $E_b/N_0 = 19$ dB in the uncoded regime, as demonstrated in Fig. 4.13(a).

4.6 Chapter Conclusions

In this chapter, a layered channel coding system was proposed for optical IM/DD communications. We first detailed the LACO-OFDM system architecture, and derived the achievable rate with the aid of our mutual information analysis. Next, we discussed the limitations of the single-class system, which was followed by the introduction of our proposed layered LACO-OFDM architecture. Finally, we quantified the benefits of the proposed coded optical communications system by invoking both convolutional and turbo codes. Quantitatively, it was demonstrated that our turbo coded system operated within 1.1 dB of the achievable rate at a BER of 10^{-3}. Furthermore, our convolutional coded system outperformed the single-class turbo coded system despite the 32 times lower decoding complexity of the former. We also demonstrated that the layered coded system is capable of drastically reducing the ILI.

4.7 Chapter Summary

Figure 4.15 portrays relationships between each of the sections in this chapter.

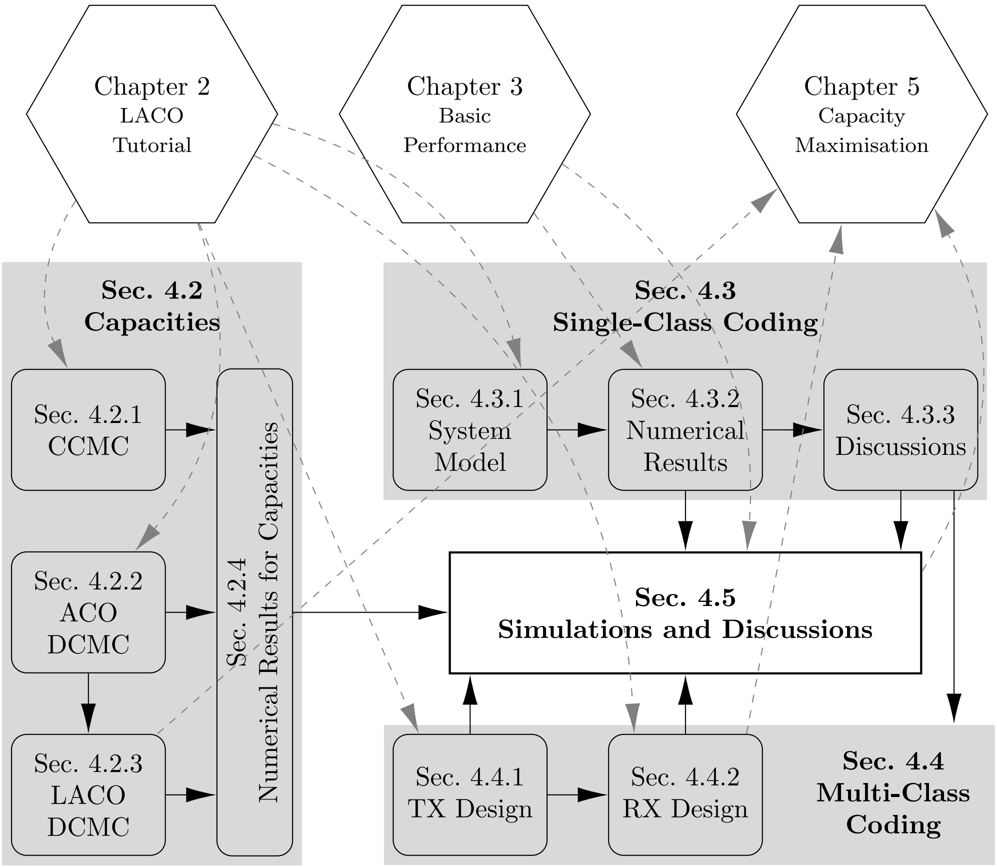

Figure 4.15: Summary of Chapter 4.

As a key technique of improving the BER performance of LACO-OFDM developed in Chapter 3, the multi-class coded LACO-OFDM system has been conceived in this chapter based on the structure introduced in Chapter 2.

Section 4.2 quantified the capacity of LACO-OFDM. Explicitly, in Sec. 4.2.1, the CCMC capacity was analysed, while the DCMC capacity of ACO-OFDM and LACO-OFDM was quantified in Secs. 4.2.2 and 4.2.3, respectively. In both cases, we commenced by analysing the capacity of RF systems, before appropriately modifying our formulae for the optical domain for ACO-OFDM, and finally dealing with the more sophisticated LACO-OFDM system.

In Sec. 4.3, a naïve single-class coding was conceived for LACO-OFDM by simply cascading the layered LACO-OFDM transceiver of Chapter 2 with a hard-decision FEC encoder/decoder, as detailed in Sec. 4.3.1. In Sec. 4.3.2, the performance of the single-class coding system was evaluated and compared to the uncoded results of Chapter 3, while the limitations of this scheme were further discussed in Sec. 4.3.3, ultimately leading to the proposal of our novel multi-class coded system in Sec. 4.4.

Explicitly, in Sec. 4.4, our multi-class coded LACO-OFDM scheme was conceived for improving the FEC performance. The layered encoding and decoding scheme was integrated with the LACO-OFDM structure of Chapter 2 in Secs. 4.4.1 and 4.4.2, respectively. The performance of the proposed scheme was evaluated and compared to that of the single-class system of Sec. 4.3 as well as to the uncoded results of Chapter 3.

Moreover, the LACO-OFDM capacity derived in Sec. 4.2 was used for benchmarking the performance of the different coding schemes. With the aid of the proposed multi-class coding scheme, we have attained a substantial coding gain and approached the to channel capacity within about 1.1 dB.

Chapter 5

Optimum Power Allocation in LACO-OFDM

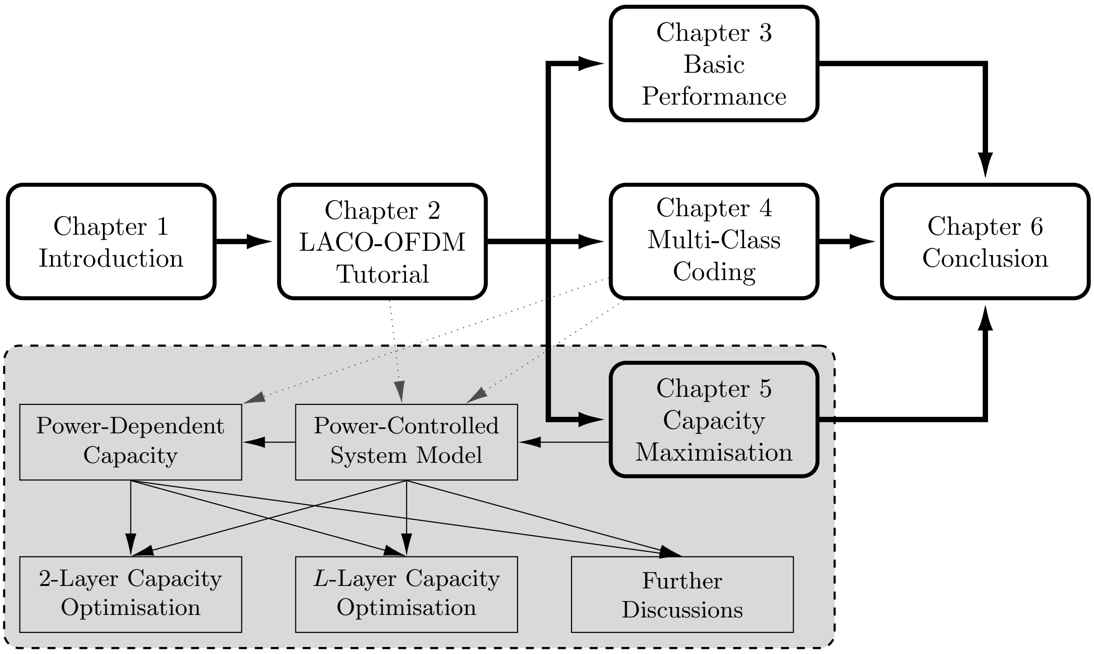

Figure 5.1: Linkage of Chapter 5 within the thesis structure.

5.1 Introduction

In the previous chapter, we derived the channel capacity of LACO-OFDM systems and employed the multi-class coding structure for achieving near-capacity communication. Up to this stage, we have used the *Equal Power per Bit* strategy for sharing the power amongst the layers, in order to be "fair" to all the bits conveyed. However, it has yet to be justified, whether this strategy achieves the best performance.

According to Chapter 4, the channel capacity of LACO-OFDM depends on the SNRs experienced by each of the layers, which in turn is related to the effective power of each layer. As a result, adjusting the power assigned to each layer may potentially result in a higher channel capacity, and the sophisticated coding scheme of Chapter 4 may help further improve the system's throughput. This topic was briefly touched upon in [60]. However, the DCMC capacity, which is the more practical bound and related to the attainable throughput, has never been used. In the spirit of this, we analyse the relationship between the power sharing among the layers and the overall DCMC capacity of the LACO-OFDM system for maximising the throughput. Explicitly, our contributions may be summarised as follows:

- We derive the DCMC capacity of a LACO-OFDM system as a function of the SNR and the number of layers in the system, as well as the power sharing amongst the layers. In this paper, the DCMC capacity is hereafter referred to as "channel capacity" or simply "capacity".
- We provide an algorithm for determining the optimum power allocation strategy for 2-layer LACO-OFDM system at a given SNR, followed by our generalised algorithm.
- Finally, we compare the optimised capacities of LACO-OFDM systems relying on different number of layers, which leads to an adaptive scheme using the optimum number of layers maximising the capacity at a given SNR.

This chapter is organised as follows. In Sec. 5.2, the architecture of the LACO-OFDM transceiver is discussed, followed by our DCMC capacity expression derived in Sec. 5.3. Section 5.4 focuses on the optimisation of a 2-layer LACO-OFDM system's capacity, which is also applied to a system having three or layers in Sec. 5.5. The algorithm proposed is further evaluated in Sec. 5.6. Finally, this chapter is concluded and summarised in Secs. 5.6 and 5.8, respectively.

5.2 System Model

In this section, we briefly review the multi-class coded LACO-OFDM system proposed in Chapter 4, while introducing the power control modules into the scheme.

5.2.1 Power-Controlled Transmitter

Figure 5.2 shows the detailed layer-based schematic of a multi-class coded LACO-OFDM transmitter.

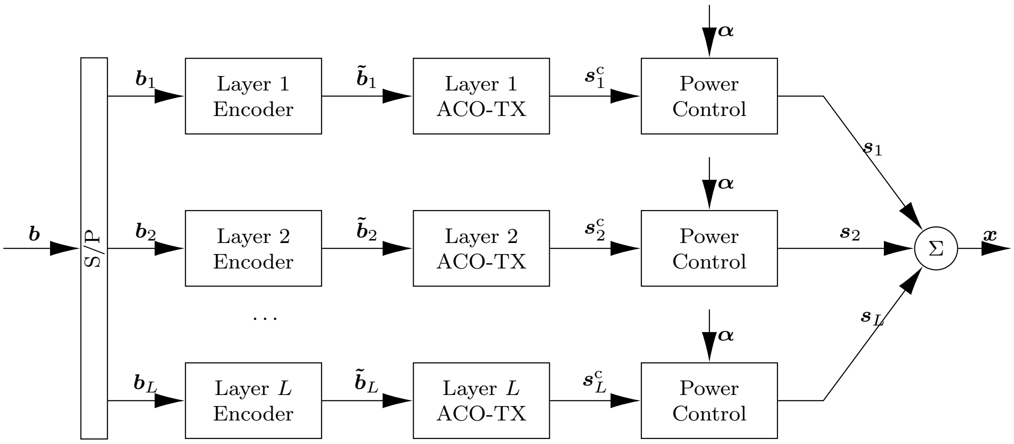

Figure 5.2: Schematic diagram of a multi-class coded LACO-OFDM transmitter with power controllers.

As discussed in Chapters 2 and 4, the information bits of each layer are parallelly FEC-coded (Sec. 4.4.1), QAM-mapped, IFFT-modulated and clipped at zero (Sec. 2.2). In this chapter, these clipped layer signals are denoted by $\boldsymbol{s}_l^{\mathrm{c}}$, where the subscript l is the layer index, while the superscript 'c' stands for clipping. After power control (to be detailed later in this section), each layer's signal $\boldsymbol{x}_l$ is superimposed in order to form the LACO-OFDM TD signal $\boldsymbol{x}$ (Sec. 2.3), which would be forwarded to the electrical/optical front-end for further IM process.

Assuming that all layers use an MQAM constellation for mapping, the average effective energy on all modulated subcarriers would be same. Since the lth layer has $K/2^{l+1}$ modulated subcarriers for conveying its information, the power ratio between each layer would be $P_l = \frac{1}{2^l}P_1$ according to Eq. (2.16). Based on Parseval' theorem [71] and the central limit theorem, which indicate that the clipped TD signal $\boldsymbol{s}_l^{\mathrm{c}}$ retains half the power of the original QAM-mapped FD signal $\overline{\boldsymbol{S}}_l$, the power ratio between $\boldsymbol{s}_l^{\mathrm{c}}$ is still

$$\mathbb{E}\{(\boldsymbol{s}_l^{\mathrm{c}})^2\} = \frac{1}{2^l}\mathbb{E}\{(\boldsymbol{s}_1^{\mathrm{c}})^2\}. \tag{5.1}$$

Observe in Fig. 5.2 that a power control module is employed after clipping for ensuring that each layer has the most appropriate power share. A set of power sharing factors $\boldsymbol{\alpha} = \{\alpha_1, \alpha_2, \dots \alpha_{L-1}\}$ is used by these power controllers for ensuring that the signal $\boldsymbol{s}_l$ has an electric power of P_l:

$$\mathbb{E}\{(\boldsymbol{s}_l)^2\} = P_l \begin{cases} = \frac{1}{2^l}P_1, & \textit{Equal Power per Bit}, \\ \neq \frac{1}{2^l}P_1, & \text{otherwise}, \end{cases} \tag{5.2}$$

where "$\neq$" indicates that the ratio between P_l and P_1 is no longer fixed, which is in contrast to Eq. (5.1). This process will be further discussed in Secs. 5.4 and 5.5.

5.2.2 Power-Controlled Receiver

Let us now present the receiver design of multi-class coded LACO-OFDM, which is shown in Fig. 5.3, where $\boldsymbol{\alpha}$ stands for the power control factors, while the rest of the signals were defined in Sec. 4.4.2.

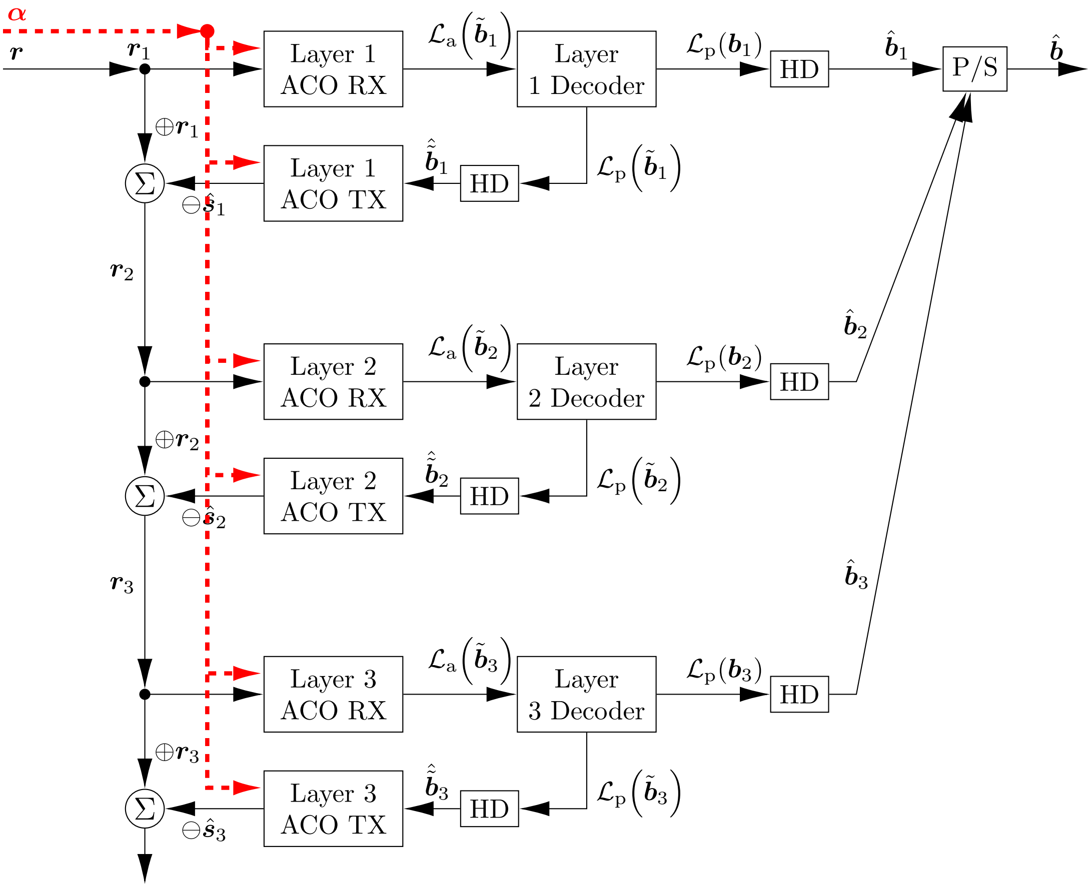

Figure 5.3: Schematic diagram of a multi-class coded LACO-OFDM receiver with power controllers.

The multi-class design of the layer-by-layer receiver follows the philosophy of Figs. 2.7 and 4.10. Explicitly, the general layer detection, clipping distortion regeneration and cancellation were covered in Sec. 2.3.2, while the detailed LLR calculation and decoder design were developed in Sec. 4.4.2.

However, in the absence of the *Equal Power per Bit* restriction Eq. (5.1), the layer detection method introduced in Sec. 2.3.2 has to be modified. Explicitly, in Eq. (2.13) (and more generally in Eq. (3.28)), the factor 2 was employed for normalising the signal to a unitary average power, so that the demapper could compare it to the standard constellation. As a result, $\boldsymbol{\alpha}$ must now be taken into account within the "Layer l ACO RX" blocks, so that suitable compensation can be made for each layer signal. Meanwhile, $\boldsymbol{\alpha}$ is also required when estimating the LLR, because the effective SNR of the different layers will vary. Moreover, the "Layer l ACO TX" blocks also need $\boldsymbol{\alpha}$ for re-generating the clipping distortion, ensuring that the clipping distortion cancellation operates correctly.

5.3 DCMC Capacity for Variable Layer Power

5.3.1 DCMC Capacity of an RF-OFDM System

Let us define the channel SNR Γ as the channel energy per symbol (E_s) to noise power spectral density (N_0) ratio, namely as $\Gamma = E_s/N_0$ for an RF system. Using an approach that is different from that given in Eq. (4.25), we define the channel capacity of an M-QAM scheme as [89, 91]

$$\begin{aligned} \mathsf{C}_{\mathrm{RF}}(\Gamma) &= (\text{Sink Entropy}) - (\text{Noise Entropy}) \\ &= \underbrace{-\int_{-\infty}^{\infty} p(R)\log_2\left[p(R)\right]\,\mathrm{d}R}_{(a)} - \underbrace{\log_2\left(\frac{\pi e}{\Gamma}\right)}_{(b)}, \end{aligned} \tag{5.3}$$

where part (b) in Eq. (5.3) represents the entropy of the noise, which is complex-valued having a variance of N_0. Furthermore, in part (a) of Eq. (5.3), the integration should take place across the entire complex-valued plane, if high order modulation ($M > 2$) is applied, where the probability of received symbols $\Pr(R[n])$ is given by

$$\begin{aligned} \Pr(R[n]) &= \frac{1}{M}\sum_{m=1}^{M}\Pr\Big(R[n]|\mathcal{S}^{\langle m\rangle}\Big) = \frac{1}{M}\sum_{m=1}^{M}\left[\frac{1}{\pi N_0}\cdot\exp\left(\frac{\left|R[n]-\mathcal{S}^{\langle m\rangle}\right|^2}{N_0}\right)\right] \\ &= \frac{1}{M}\sum_{m=1}^{M}\left[\frac{\Gamma}{\pi}\cdot\exp\left(-\Gamma\cdot\left|R[n]-\mathcal{S}^{\langle m\rangle}\right|^2\right)\right] \\ &= \frac{\Gamma}{\pi M}\sum_{m=1}^{M}\exp\left(-\Gamma\cdot\left|R[n]-\mathcal{S}^{\langle m\rangle}\right|^2\right), \end{aligned} \tag{5.4}$$

where $\mathcal{S}^{\langle m\rangle}$ is the mth points in the MQAM constellation $\mathcal{S}$ having a unity average power, and $\Pr\big(r|\mathcal{S}^{\langle m\rangle}\big)$ is the complex-valued Gaussian distribution PDF with a mean of $\mathcal{S}^{\langle m\rangle}$ and variance of $1/\Gamma$. This part cannot be analytically evaluated, due to the summation within the logarithm shown in Eq. (5.4). However, Monte-Carlo method can be used for approximating it by generating a sufficiently high number of the realisations of the received symbols ($\boldsymbol{R} = R[1], R[2], \dots, R[n], \dots$), yielding:

$$(a) = \mathbb{E}\{-\log_2(\Pr(R))\} \approx -\frac{1}{N}\sum_{n=1}^{N}\log_2\left[\Pr(R[n])\right], \tag{5.5}$$

where $\mathbb{E}\{\cdot\}$ is the statistical expectation, and the approximation converges as $N \to \infty$. Hence, Eq. (5.3) can be simplified as:

$$\begin{aligned}\mathsf{C}_{\mathrm{RF}}(\Gamma) &\approx -\log_2\left(\frac{\pi e}{\Gamma}\right) - \frac{1}{N}\sum_{n=1}^{N}\log_2\left[\frac{\Gamma}{\pi M}\sum_{m=1}^{M}\exp\left(-\Gamma\cdot\left|R[n]-\mathcal{S}^{\langle m\rangle}\right|^2\right)\right]\\ &= -\frac{1}{N}\sum_{n=1}^{N}\log_2\left[\frac{e}{M}\sum_{m=1}^{M}\exp\left(-\Gamma\cdot\left|R[n]-\mathcal{S}^{\langle m\rangle}\right|^2\right)\right],\end{aligned} \tag{5.6}$$

where the "≈" sign can be replaced by "=" as $N \to \infty$.

Moreover, the derivative of C_{RF} with respect to Γ indicates the sensitivity of channel capacity to SNR changes, expressed as

$$\frac{\partial \mathsf{C}_{\mathrm{RF}}}{\partial \Gamma} = \frac{\sum\limits_{n=1}^{N}\left[\frac{\sum\limits_{m=1}^{M}\left|R[n]-\mathcal{S}^{\langle m\rangle}\right|^2\exp\left(-\Gamma\cdot\left|R[n]-\mathcal{S}^{\langle m\rangle}\right|^2\right)}{\ln 2\cdot\sum\limits_{m=1}^{M}\exp\left(-\Gamma\cdot\left|R[n]-\mathcal{S}^{\langle m\rangle}\right|^2\right)}\right]}{N}. \tag{5.7}$$

5.3.2 DCMC Capacity of an ACO-OFDM System

Recall from Chapter 2 that in ACO-OFDM only $K/4$ symbols can be conveyed by a total of K subcarriers. Therefore, the channel capacity contribution can be divided into two parts:

- The $3K/4$ subcarriers loaded either with the conjugate of the transmitted symbols or with the FD-product of the TD clipping distortion, whose capacity-contribution is 0 because they provide no new information, and
- The $K/4$ subcarriers loaded with the desired transmitted symbols.

The $K/4$ FD subcarriers in the second part may be viewed as isolated RF carriers, where Eq. (5.3) can be applied. Therefore, the capacity of an ACO-OFDM system is given by

$$\mathsf{C}_{\mathrm{ACO}}(\Gamma) = \frac{K/4}{K}\mathsf{C}_{\mathrm{RF}}(\Gamma) + \frac{3K/4}{K}\cdot 0 = \frac{1}{4}\mathsf{C}_{\mathrm{RF}}(\Gamma), \tag{5.8}$$

where the coefficient 1/4 represents the bandwidth efficiency.

Since the total signal power P_{ACO} is equally spread across the $K/4$ transmitted subcarrier symbols (25%), the $K/4$ conjugate symbols (25%) and the $K/2$ distortion symbols (50%), we have:

$$\Gamma_{\mathrm{ACO}} = \frac{E_s}{\frac{1}{2}N_0} = \frac{\frac{1}{4}P_{\mathrm{ACO}}}{\frac{K/4}{K}\frac{1}{2}N_0} = \frac{P_{\mathrm{ACO}}}{\frac{1}{2}N_0}, \tag{5.9}$$

where the factor $\frac{1}{2}$ in the denominator is because the imaginary part of the complex-valued TD noise has no effect on the performance.

5.3.3 Power Relationships in LACO-OFDM

Recall from Sec. 3.3.2 that the means and variances of each LACO-OFDM layer signal $\boldsymbol{s}_l$ can be represented by the power of the layer P_l:

$$\begin{aligned}\mathbb{E}\{\boldsymbol{s}_l\} &= \frac{\sigma}{\sqrt{2\pi}} = \sqrt{\frac{P_l}{\pi}},\\ \mathbb{D}\{\boldsymbol{s}_l\} &= \frac{\pi-1}{2\pi}\sigma^2 = \left(1-\frac{1}{\pi}\right)P_l,\end{aligned} \tag{5.10}$$

while Sec. 3.3.3 showed that the mean, variance and power of the superimposed signal $\boldsymbol{x}$ of Fig. 5.2 is given by Eqs. (3.13), (3.14) and (3.15)

$$\mathbb{E}\{\boldsymbol{x}\} = \mathbb{E}\left\{\sum_{l=1}^{L}\boldsymbol{s}_l\right\} = \sum_{l=1}^{L}\mathbb{E}\{\boldsymbol{s}_l\} \tag{5.11a}$$

$$\mathbb{D}\{\boldsymbol{x}\} = \mathbb{D}\left\{\sum_{l=1}^{L}\boldsymbol{s}_l\right\} = \sum_{l=1}^{L}\mathbb{D}\{\boldsymbol{s}_l\} \tag{5.11b}$$

$$P_{\text{LACO}} = \mathbb{D}\{\boldsymbol{x}\} + \left(\mathbb{E}\{\boldsymbol{x}\}\right)^2. \tag{5.11c}$$

However, in the absence of the *Equal Power per Bit* strategy, as detailed in Sec. 2.4 and Eq. (2.16), the means and variances Eq. (5.10) are no longer geometrical series. Therefore, the power P_{LACO} could not be simplified and expressed as a function of the number of layers L, as in Eq. (3.16). Instead, the contribution of each layer's power P_l to P_{LACO} should be individually reflected, given as

$$\begin{aligned}P_{\text{LACO}} &= \left(\sum_{l=1}^{L}\mathbb{D}\{\boldsymbol{s}_l\}\right) + \left(\sum_{l=1}^{L}\mathbb{E}\{\boldsymbol{s}_l\}\right)^2 = \left[\sum_{l=1}^{L}\left(1-\frac{1}{\pi}\right)P_l\right] + \left(\sum_{l=1}^{L}\sqrt{\frac{P_l}{\pi}}\right)^2\\ &= \left(1-\frac{1}{\pi}\right)\sum_{l=1}^{L}P_l + \frac{1}{\pi}\left(\sum_{l=1}^{L}\sqrt{P_l}\right)^2\\ &= \left(1-\frac{1}{\pi}\right)\sum_{l=1}^{L}P_l + \frac{1}{\pi}\left(\sum_{i=1}^{L}\sum_{j=1}^{L}\sqrt{P_i}\sqrt{P_j}\right)\\ &= \sum_{l=1}^{L}P_l + \frac{2}{\pi}\sum_{i\neq j}\sqrt{P_iP_j}.\end{aligned} \tag{5.12}$$

5.3.4 DCMC Capacity of a LACO-OFDM System

Table 5.1 shows the composition of each layer of a LACO-OFDM signal. On the lth layer of a LACO-OFDM scheme, only $\frac{K}{2^{l+1}}$ information-earning symbols can be transmitted, complemented by $\frac{K}{2^{l+1}}$ subcarriers for themselves, and another $\frac{K}{2^{l+1}}$ subcarriers for their conjugates, and by $\frac{K}{2^{l}}$ additional subcarriers that are occupied by the FD-products of

Table 5.1: Composition of an LACO-OFDM signal showing the number of subcarriers ($\mathcal{N}$) and average symbol power ($\mathcal{P}$) of the four parts of each layer: Desired Transmitted Symbols (TX), Conjugate Symbols (Conj.), Clipping distortions of the current layer (Dist.) and idle subcarriers after clipping (Idle).

Layer Index	Layer Power	TX or Conj.		Dist.		Idle	
		$\mathcal{N}$	$\mathcal{P}$	$\mathcal{N}$	$\mathcal{P}$	$\mathcal{N}$	$\mathcal{P}$
1	P_1	$K/4$	P_1	$K/2$	P_1	0	0
2	P_2	$K/8$	$2P_2$	$K/4$	$2P_2$	$K/2$	0
3	P_3	$K/16$	$4P_3$	$K/8$	$4P_3$	$3K/4$	0
				$\cdots$			
l	P_l	$K/2^{l+1}$	$2^{l-1}P_l$	$K/2^l$	$2^{l-1}P_l$	$K-K/2^{l-1}$	0
				$\cdots$			

the TD clipping distortion. The power allocated to the lth layer shall be (statistically) equally shared among these $\frac{K}{2^{l-1}}$ subcarriers, which results in $2^{l-1}P_l$ for each subcarrier. The remaining $\left(1-\frac{1}{2^{l-1}}\right)K$ subcarriers are left empty, having zero power.

Given a sufficiently high SNR, the receiver can be expected to fully cancel out the TD-clipping distortions with the help of FEC codes [2]. When detecting the lth layer at the receiver, its SNR Γ_l would be calculated using the power of the subcarriers loaded with the symbols, yielding:

$$\Gamma_l = \frac{2^{l-1}P_l}{N_0/2}. \tag{5.13}$$

For LACO-OFDM, its first layer signal is constituted by an ACO-OFDM signal. As a result, the capacity contribution of LACO-OFDM from its first layer is:

$$\mathsf{C}_1(\Gamma_1) = \mathsf{C}_{\text{ACO}}(\Gamma_1) = \frac{1}{4}\mathsf{C}_{\text{RF}}(\Gamma_1). \tag{5.14}$$

Similarly, for the second and higher layer signals, their transmission rate contribution can be written as

$$\mathsf{C}_l(\Gamma_l) = \frac{1}{2^{l-1}}\mathsf{C}_{\text{ACO}}(\Gamma_l) = \frac{1}{2^{l+1}}\mathsf{C}_{\text{RF}}(\Gamma_l). \tag{5.15}$$

Therefore, the overall capacity of a LACO-OFDM system having a total of L layers can be written as

$$\mathsf{C}_{\text{LACO}} = \sum_{l=1}^{L}\mathsf{C}_l(\Gamma_l) = \frac{1}{2^{l+1}}\mathsf{C}_{\text{RF}}(\Gamma_l). \tag{5.16}$$

Explicitly, C_{LACO} is a function of the individual SNR of each layer $(\Gamma_1, \Gamma_2, \ldots, \Gamma_L)$, which is in turn a function of the power allocated to each layer $(P_1, P_2, \ldots, P_L)$, subject to the constraint

$$\begin{aligned} 0 \le P_l \le P_{\mathrm{LACO}}, \quad \forall\, l, \\ \text{and } Eq.\ (5.12). \end{aligned} \tag{5.17}$$

5.4 2-Layer LACO-OFDM System

In this section, the total power and capacity of a 2-layer LACO-OFDM system, *i.e.* $P_{\mathrm{LACO}}^{(2)}$ and $\mathsf{C}_{\mathrm{LACO}}^{(2)}$, represent P_{LACO} and $\mathsf{C}_{\mathrm{LACO}}$, respectively.

5.4.1 Capacity of 2-layer LACO-OFDM

Let us consider a LACO-OFDM system consisting of 2 layers only and define the power sharing factor α ($0 \le \alpha \le 1$) as the specific fraction of the total power belonging to the first layer. Naturally, the second layer has then $(1-\alpha)$ portion of the power, *i.e.* we have:

$$\frac{P_1}{P_2} = \frac{\alpha}{1-\alpha}. \tag{5.18}$$

Substituting this into Eq. (5.12), we arrive at

$$\begin{aligned} P_{\mathrm{LACO}} &= P_1 + P_2 + \frac{2}{\pi}\sqrt{P_1P_2} = P_1 + \frac{1-\alpha}{\alpha}P_1 + \frac{2}{\pi}\sqrt{P_1 \cdot \frac{1-\alpha}{\alpha}P_1} \\ &= P_1\left(\frac{1}{\alpha} + \frac{2}{\pi}\sqrt{\frac{1-\alpha}{\alpha}}\right). \end{aligned} \tag{5.19}$$

Therefore, P_1 can be represented as

$$P_1 = \frac{\alpha \cdot P_{\mathrm{LACO}}}{1 + \frac{2}{\pi}\sqrt{\alpha(1-\alpha)}}. \tag{5.20}$$

Similarly,

$$P_2 = \frac{(1-\alpha) \cdot P_{\mathrm{LACO}}}{1 + \frac{2}{\pi}\sqrt{\alpha(1-\alpha)}}. \tag{5.21}$$

For a given power constraint P_{LACO} and noise power N_0, the overall channel SNR of LACO-OFDM is defined as $\Gamma_{\mathrm{LACO}} = P_{\mathrm{LACO}}/N_0$. Using Eq. (5.13), the corresponding SNR of each of the two layers becomes

$$\Gamma_1 = \frac{P_1}{N_0/2} = \frac{\alpha \cdot \Gamma_{\mathrm{LACO}}}{1 + \frac{2}{\pi}\sqrt{\alpha(1-\alpha)}}, \tag{5.22a}$$

$$\text{and } \Gamma_2 = \frac{2P_2}{N_0/2} = \frac{2(1-\alpha) \cdot \Gamma_{\mathrm{LACO}}}{1 + \frac{2}{\pi}\sqrt{\alpha(1-\alpha)}}. \tag{5.22b}$$

Note that the layer SNRs defined in Eq. (5.22) can be treated as a function both of the overall SNR Γ_{LACO} and of the power sharing ratio α.

In this way, the overall capacity of this 2-layer LACO-OFDM system can be written according to Eq. (5.16) as

$$\mathsf{C}_{\text{LACO}} = \mathsf{C}_1(\Gamma_1) + \mathsf{C}_2(\Gamma_2) = \frac{\mathsf{C}_{\text{RF}}(\Gamma_1)}{4} + \frac{\mathsf{C}_{\text{RF}}(\Gamma_2)}{8}. \tag{5.23}$$

The chain rule of functions indicates that C_{LACO} shall also be a function of Γ_{LACO} and α. Therefore, the maximum throughput at a given SNR Γ can be determined by solving the following problem:

$$\begin{aligned} \max_{\alpha} \quad & \mathsf{C}_{\text{LACO}}(\Gamma_{\text{LACO}},\ \alpha) \\ \text{s.t.} \quad & 0 \le \alpha \le 1 \\ & \text{and } \mathit{Eq.}\ (5.19). \end{aligned} \tag{5.24}$$

5.4.2 Characteristics of C_{LACO}

5.4.2.1 Existence of Maxima

For a given Γ, C_{LACO} is non-negative by definition, having a lower bound of zero. On the other hand, the DCMC capacity is upper bounded by the general CCMC capacity [87] of

$$0 \le \mathsf{C}_{\text{LACO}}(\Gamma,\ \alpha) \le \log_2(1+\Gamma), \quad \forall\ \alpha. \tag{5.25}$$

Since C_{LACO} is formed of elementary functions, it is also continuous within $\alpha \in [0, 1]$. According to the extreme value theorem [92], at least one maximum must be attained by C_{LACO} for any given Γ within the interval $\alpha \in [0, 1]$.

5.4.2.2 Monotonicity of SNRs

If we take the partial derivative of C_{LACO} in Eq. (5.23) with respect to α, we have:

$$\frac{\partial \mathsf{C}_{\text{LACO}}}{\partial \alpha} = \frac{\partial}{\partial \alpha}\frac{\mathsf{C}_{\text{RF}}(\Gamma_1)}{4} + \frac{\partial}{\partial \alpha}\frac{\mathsf{C}_{\text{RF}}(\Gamma_2)}{8} = \underbrace{\frac{1}{4}\underbrace{\frac{\partial \mathsf{C}_{\text{RF}}}{\partial \Gamma_1}}_{\text{(c1)}}\underbrace{\frac{\partial \Gamma_1}{\partial \alpha}}_{\text{(c2)}}}_{\text{(c)}} + \underbrace{\frac{1}{8}\underbrace{\frac{\partial \mathsf{C}_{\text{RF}}}{\partial \Gamma_2}}_{\text{(d1)}}\underbrace{\frac{\partial \Gamma_2}{\partial \alpha}}_{\text{(d1)}}}_{\text{(d)}}. \tag{5.26}$$

Since the channel capacity is always monotonically non-decreasing vs. the SNR [87], we have:

$$\frac{\partial \mathsf{C}_{\text{RF}}}{\partial \Gamma_1} \ge 0, \qquad \text{and} \qquad \frac{\partial \mathsf{C}_{\text{RF}}}{\partial \Gamma_2} \ge 0. \tag{5.27}$$

Using Eq. (5.22), the partial derivative of Γ_1 with respect to α is

$$\frac{\partial \Gamma_1}{\partial \alpha} = \frac{\partial}{\partial \alpha}\left(\frac{\alpha \cdot \Gamma_{\mathrm{LACO}}}{1 + \frac{2}{\pi}\sqrt{\alpha(1-\alpha)}}\right) = \frac{\pi\left(\alpha + \pi\sqrt{(1-\alpha)\alpha}\right)\Gamma_{\mathrm{LACO}}}{\sqrt{(1-\alpha)\alpha}\left(2\sqrt{(1-\alpha)\alpha} + \pi\right)^2}, \tag{5.28}$$

where $\mathsf{C}_{\mathrm{LACO}}$ is locally treated as a positive constant. Symbolic analysis of Eq. (5.28) in Sec. 5.4.4 shows that $\dfrac{\partial \Gamma_1}{\partial \alpha}$ is always positive within $\alpha \in [0, 1]$, with a minimum of $0.7241 \cdot \Gamma_{\mathrm{LACO}} > 0$ at $\alpha = 0.3074$. Similarly, the partial derivative of Γ_2 with respect to α is

$$\frac{\partial \Gamma_2}{\partial \alpha} = -\frac{2\pi\left(1 - \alpha + \pi\sqrt{(1-\alpha)\alpha}\right)\Gamma_{\mathrm{LACO}}}{\sqrt{(1-\alpha)\alpha}\left(2\sqrt{(1-\alpha)\alpha} + \pi\right)^2}, \tag{5.29}$$

which is always negative within $\alpha \in [0, 1]$ having a maximum of $-1.4483\Gamma_{\mathrm{LACO}} < 0$ at $\alpha = 0.6926$. Therefore, upon referring to Eq. (5.26), we have:

$$(c) = \frac{1}{4}\frac{\partial \mathsf{C}_{\mathrm{RF}}}{\partial \Gamma_1}\frac{\partial \Gamma_1}{\partial \alpha} \geq 0, \tag{5.30a}$$

$$\text{and} \quad (d) = \frac{1}{8}\frac{\partial \mathsf{C}_{\mathrm{RF}}}{\partial \Gamma_2}\frac{\partial \Gamma_2}{\partial \alpha} \leq 0. \tag{5.30b}$$

5.4.2.3 Maximum of $\mathsf{C}_{\mathrm{LACO}}$

As α approaches 0 from the right hand side, *i.e.* for $\alpha \to 0^+$, the majority of the power would be assigned to layer 2 according to Eq. (5.18), resulting in $P_1 \to 0$ and in turn $\Gamma_1 \to 0$ (linear) or $\Gamma_1 \to -\infty$ (dB). Therefore, (c1) in Eq. (5.26) tends to plus infinity according to Sec. 5.3.1, while (c2) is a smaller value based on Γ_{LACO}. In this case, we have:

$$(\mathrm{c}) = \frac{1}{4}(\mathrm{c1}) \cdot (\mathrm{c2}) > -\frac{1}{8}(\mathrm{d1}) \cdot (\mathrm{d2}) = -(\mathrm{d}), \tag{5.31}$$

which yields

$$\left.\frac{\partial \mathsf{C}_{\mathrm{LACO}}}{\partial \alpha}\right|_0 > 0. \tag{5.32}$$

By symmetry, when $\alpha = 1$, part (d) in Eq. (5.26) obeys

$$\left.\frac{\partial \mathsf{C}_{\mathrm{LACO}}}{\partial \alpha}\right|_1 < 0. \tag{5.33}$$

According to Bolzano's theorem [92], due to having opposite sign for $\dfrac{\partial \mathsf{C}_{\mathrm{LACO}}}{\partial \alpha}$ at the two edges, we arrive at

$$\exists\ \alpha^* \in [0, 1], \quad \text{s.t.} \quad \left.\frac{\partial \mathsf{C}_{\mathrm{LACO}}}{\partial \alpha}\right|_{\alpha^*} = 0. \tag{5.34}$$

As it will be shown in the next Section, $\frac{\partial \mathsf{C}_{\text{LACO}}}{\partial \alpha}$ is actually monotonically decreasing throughout the interval $\alpha \in [0, 1]$. Hence, the maximum of C_{LACO} for a particular Γ is obtained at $\alpha = \alpha^*$.

5.4.3 Maximum Search

Here, we propose an algorithm for finding the maximum of C_{LACO} for any given Γ, as well as the corresponding optimum α^*.

Algorithm 2 Power allocation in 2-layer LACO-OFDM

```
Input: $M$, $\Gamma_{\text{LACO}}$, $N$, $\epsilon$
Output: $\alpha^*$, $\mathsf{C}^*_{\text{LACO}}$
$p := 0$, $q := 1$;
repeat
    $\overline{\alpha} := (p + q)/2$,
    Calculate $\Gamma_1(\overline{\alpha})$ and $\Gamma_2(\overline{\alpha})$ using Eq. (5.22),
    Calculate $\left.\frac{\partial \mathsf{C}_{\text{LACO}}}{\partial \Gamma_1}\right|_{\overline{\alpha}}$ and $\left.\frac{\partial \mathsf{C}_{\text{LACO}}}{\partial \Gamma_2}\right|_{\overline{\alpha}}$, by substituting $\Gamma_1(\overline{\alpha})$ and $\Gamma_2(\overline{\alpha})$ into
  Eq. (5.7), respectively,
    Calculate $\left.\frac{\partial \Gamma_1}{\partial \alpha}\right|_{\overline{\alpha}}$ using Eq. (5.28) and $\left.\frac{\partial \Gamma_2}{\partial \alpha}\right|_{\overline{\alpha}}$ using Eq. (5.29),
    Calculate $\left.\frac{\partial \mathsf{C}_{\text{LACO}}}{\partial \alpha}\right|_{\overline{\alpha}}$ at $\alpha$ by substituting the above 4 terms into Eq. (5.26);
    if $\left.\frac{\partial \mathsf{C}_{\text{LACO}}}{\partial \alpha}\right|_{\alpha=\overline{\alpha}} > 0$ then
        $p := \overline{\alpha}$,
    else
        $q := \overline{\alpha}$,
    end if
until $\left|\frac{\partial \mathsf{C}_{\text{LACO}}}{\partial \alpha}\right| < \epsilon$ ;
return $\alpha^* = \overline{\alpha}$ ;
return $\mathsf{C}^*_{\text{LACO}} = \mathsf{C}_{\text{LACO}}(\alpha^*)$ ;
```

As seen in Alg. 2, we commence by entering the modulation order M and the overall channel SNR Γ_{LACO}, as well as the number of Monte-Carlo simulations N used for approximating the capacity and a decision threshold ϵ to determine if the stationary point of C_{LACO} is sufficiently accurate.

A binary search philosophy is adopted to find the optimum α^*. A pair of variables, p and q, are employed as the left and right search boundaries, having initial values of 0 and 1, respectively. The testing point of α is their average $\overline{\alpha} = \frac{p+q}{2}$. As elaborated on before, the optimum value α^* is the stationary point of C_{LACO}. Therefore, a subroutine is provided for calculating the derivative of C_{LACO} at α_0.

The program commences by calculating the SNR $\Gamma_1(\alpha)$ and $\Gamma_2(\alpha)$ of each layer at the initial $\overline{\alpha}$, using their corresponding relationships with α presented in Eq. (5.22).

These two SNR values are subsequently substituted into the partial derivatives of the capacity expression with respect to the layer SNR formula, which is provided in Eq. (5.7) by differentiating Eq. (5.6). This leads to the value of (c1) and (d1) in Eq. (5.26). Meanwhile, $\overline{\alpha}$ is also substituted into Eqs. (5.28) and (5.29) for obtaining (c2) and (d2) of Eq. (5.26), respectively. Having all components of Eq. (5.26) available, the algorithm becomes capable of providing $\frac{\partial \mathsf{C}_{\text{LACO}}}{\partial \alpha}$ for the current $\overline{\alpha}$.

With the process of calculating $\left.\frac{\partial \mathsf{C}_{\text{LACO}}}{\partial \alpha}\right|_{\overline{\alpha}}$ completed (corresponding to states 4-7 of Alg. 2), the problem can be simplified to finding the root of an equation. We have shown in Sec. 5.4.2 that there is only a single root α^* and that $\frac{\partial \mathsf{C}_{\text{LACO}}}{\partial \alpha}$ is monotonically decreasing from a positive value down to a negative value as a function of α. Therefore, by checking the sign of $\left.\frac{\partial \mathsf{C}_{\text{LACO}}}{\partial \alpha}\right|_{\overline{\alpha}}$ at both ends of the search region of $[0, 1]$ and gradually shrinking the searching window, the root can be eventually obtained within an accuracy of ϵ.

5.4.4 Numerical Results

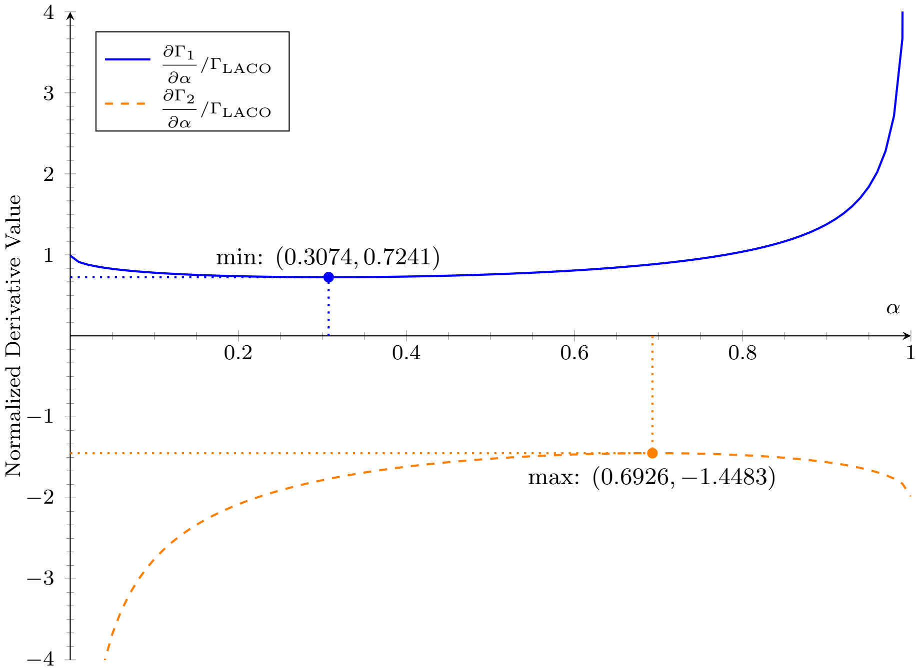

Figure 5.4: The normalised derivatives of Γ_1 and Γ_2 in Eqs. (5.28) and (5.29) vs. α.

Figure 5.4 plots the partial derivatives of Γ_1 and Γ_2 with respect to α based on Eqs. (5.28) and (5.29), whose derivatives have been normalised by Γ_{LACO}. It is clearly shown that $\frac{\partial \Gamma_1}{\partial \alpha}$ is always positive, while $\frac{\partial \Gamma_2}{\partial \alpha}$ is always negative, in line with Eqs. (5.32) and (5.33).

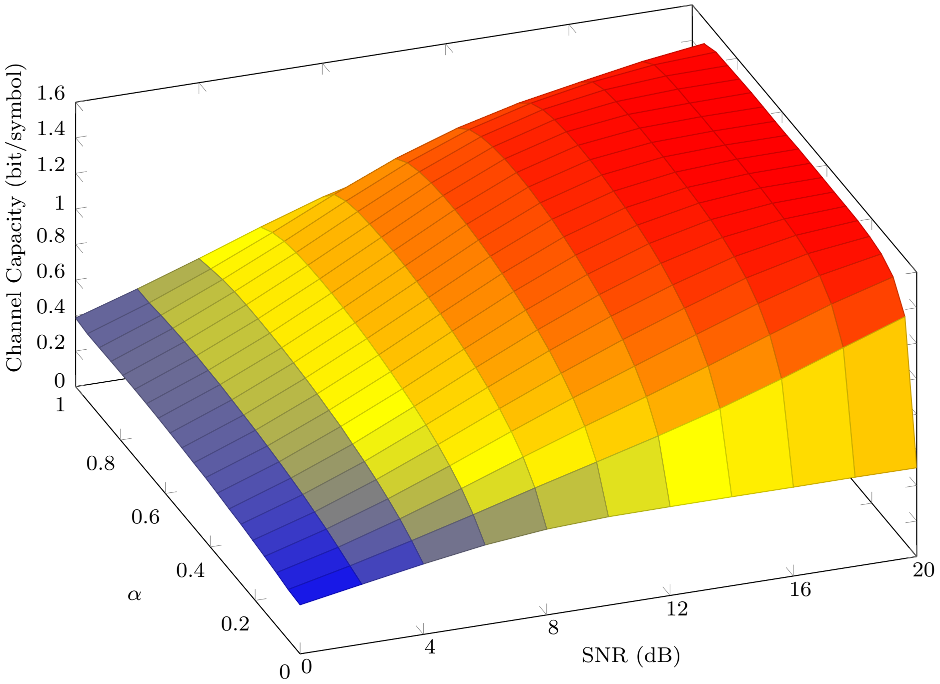

Figure 5.5: α and SNR versus channel capacity of a 2-layer LACO-OFDM using 16QAM.

Figure 5.5 shows the channel capacity of 2-layer LACO-OFDM using 16QAM both vs. the overall SNR and vs. the power sharing factor α. Focusing our attention on the SNR axis, it is clear that the channel capacity converges to 1.5 bits/symbol upon increasing the SNR. This agrees with Eq. (5.23), because we have $\lim_{\Gamma\to\infty} C_{\mathrm{RF}(\Gamma)} = 4$ for 16QAM. Similar trends can be found for all SNR values, namely that as α is increased from 0 to 1, the corresponding capacity first significantly increases and then decreases, albeit its maximum is not very pronounced.

A more clear view is provided in Fig. 5.6, where both the capacity as well as its derivative are plotted against α at SNR $= 12$ dB. The channel capacity increases up to the power sharing factor of $\alpha = 0.6841$, reaching a maximum of 1.3498 bits/symbol, before falling again. The corresponding derivative is monotonically decreasing and has a zero-crossing at $\alpha = 0.6841$, which verifies Alg. 2.

Meanwhile, Fig. 5.6 also indicates that the conventional power allocation strategy of $P_1 : P_2 = 1 : 2$ corresponding to $\alpha = \frac{2}{3} \approx 0.6666$, yields a lower capacity. Up to this point, the derivative still remains positive, hence the capacity still increases with α. This trend will be further discussed in Sec. 5.6.

Moreover, the optimum channel capacity versus SNR for 2-layer LACO-OFDM associated with different modulation schemes is summarised in Fig. 5.7.

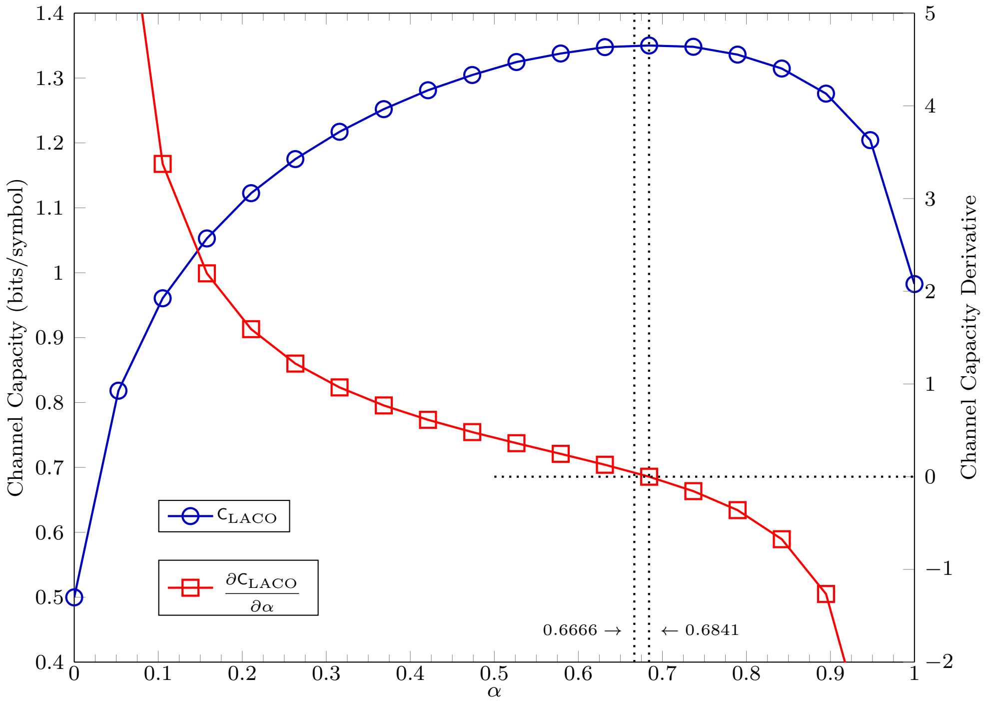

Figure 5.6: Channel capacity and its derivative for 2-layer LACO-OFDM using 16QAM at SNR = 12 dB vs. the power sharing factor α.

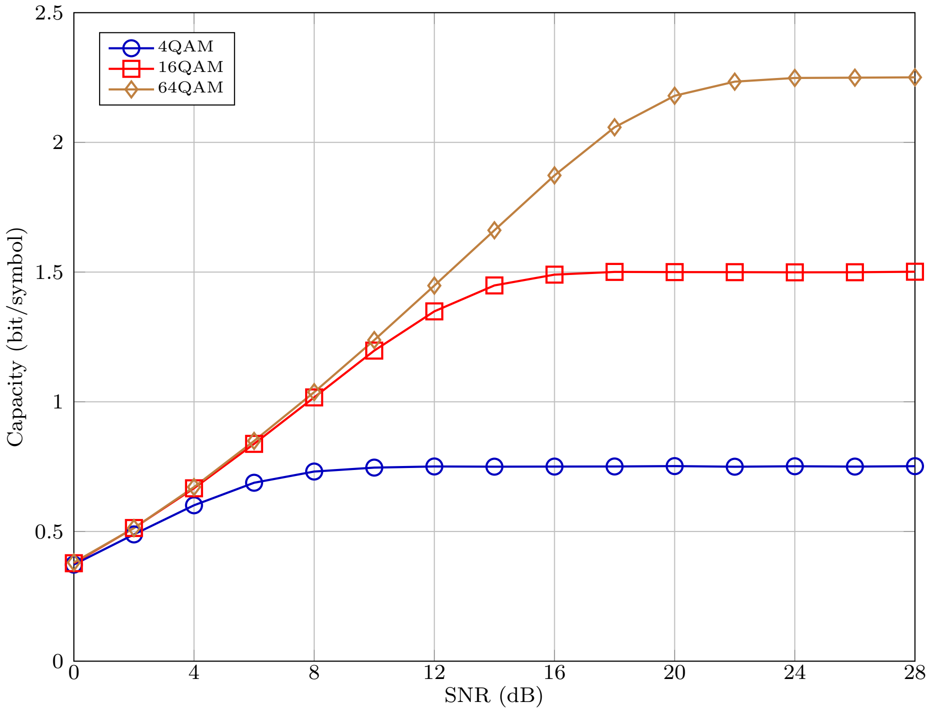

Figure 5.7: Optimised capacity of 2-layer LACO-OFDM using Alg. 2 vs. the SNR.

5.5 3- and Higher-Layer LACO-OFDM System

In this section, we explore the capacity maximisation problem of 3-layer LACO-OFDM systems, before generalising it to multi-layer LACO-OFDM systems. In subsections 5.5.1 to 5.5.3, the variables P_{LACO}, Γ_{LACO} and C_{LACO} represent the corresponding metrics of a 3-layer LACO-OFDM system, while in subsection 5.5.4, they are for L-layer LACO-OFDM systems.

5.5.1 Capacity of 3-Layer LACO-OFDM

For 3-layer LACO-OFDM systems, the relationships between the power of the three base layers can be reflected by introducing a pair of power sharing factors: α_1 and α_2:

$$\frac{P_1}{P_2} = \frac{\alpha_1}{1-\alpha_1} \quad \text{and} \quad \frac{P_1}{P_3} = \frac{\alpha_2}{1-\alpha_2}, \tag{5.35}$$

where $0 \leq \alpha_1 \leq 1$ and $0 \leq \alpha_2 \leq 1$.

Based on Eq. (5.12), the overall power for the 3-layer LACO-OFDM system can now be expressed in terms of P_1 only as in Eq. (5.36). Therefore, with the additional help of Eq. (5.35), the SNR of each layer can be expressed as

$$\Gamma_1 = \frac{P_1}{N_0/2} = \frac{\alpha_1\alpha_2 \cdot \Gamma_{\text{LACO}}}{\mathrm{P}^{\star}}, \tag{5.38a}$$

$$\Gamma_2 = \frac{2P_2}{N_0/2} = \frac{2(1-\alpha_1)\alpha_2 \cdot \Gamma_{\text{LACO}}}{\mathrm{P}^{\star}}, \tag{5.38b}$$

$$\Gamma_3 = \frac{4P_3}{N_0/2} = \frac{4\alpha_1(1-\alpha_2) \cdot \Gamma_{\text{LACO}}}{\mathrm{P}^{\star}}, \tag{5.38c}$$

where $\mathrm{P}^{\star}$ was defined in Eq. (5.36), which is a function of both α_1 and α_2. The overall DCMC capacity of a 3-layer LACO-OFDM can then be expressed as the sum of the 3 layers' capacities:

$$\mathsf{C}_{\text{LACO}} = \mathsf{C}_1(\Gamma_1) + \mathsf{C}_2(\Gamma_2) + \mathsf{C}_3(\Gamma_3) = \frac{\mathsf{C}_{\text{RF}}(\Gamma_1)}{4} + \frac{\mathsf{C}_{\text{RF}}(\Gamma_2)}{8} + \frac{\mathsf{C}_{\text{RF}}(\Gamma_3)}{16}. \tag{5.39}$$

Apparently, for any given total SNR (Γ_{LACO}), C_{LACO} depends[1] on both α_1 and α_2. Bearing this in mind, let us now study the associated capacity maximisation problem.

5.5.2 Maximisation of 3-Layer LACO-OFDM Capacity

The extreme values of the dual-variable function C_{LACO} will only occur at points, where its gradient equals zero. Therefore, the partial derivatives of C_{LACO} with respect to α_1

---

[1] At the moment, all other variables, such as M and N, are treated as constants.

$$
\begin{aligned}
P_{\mathrm{LACO}} &= P_1 + P_2 + P_3 + \frac{2}{\pi}\left(\sqrt{P_1P_2} + \sqrt{P_1P_3} + \sqrt{P_2P_3}\right) \\
&= P_1 + \frac{1-\alpha_1}{\alpha_1}P_1 + \frac{1-\alpha_2}{\alpha_2}P_1 + \frac{2}{\pi}\left(\sqrt{P_1\cdot\frac{1-\alpha_1}{\alpha_1}P_1} + \sqrt{P_1\cdot\frac{1-\alpha_2}{\alpha_2}P_1} + \sqrt{\frac{1-\alpha_1}{\alpha_1}P_1\cdot\frac{1-\alpha_2}{\alpha_2}P_1}\right) \\
&= P_1\left[1 + \frac{1-\alpha_1}{\alpha_1} + \frac{1-\alpha_2}{\alpha_2} + \frac{2}{\pi}\left(\sqrt{\frac{1-\alpha_1}{\alpha_1}} + \sqrt{\frac{1-\alpha_2}{\alpha_2}} + \sqrt{\frac{(1-\alpha_1)(1-\alpha_2)}{\alpha_1\alpha_2}}\right)\right] \\
&= \frac{P_1}{\alpha_1\alpha_2}\cdot\underbrace{\left[\alpha_1 + \alpha_2 - \alpha_1\alpha_2 + \frac{2}{\pi}\left(\alpha_2\sqrt{\alpha_1(1-\alpha_1)} + \alpha_1\sqrt{\alpha_2(1-\alpha_2)} + \sqrt{\alpha_1\alpha_2(1-\alpha_1)(1-\alpha_2)}\right)\right]}_{\mathrm{P}^\star}.
\end{aligned}
\tag{5.36}
$$

$$\frac{\partial\Gamma_1}{\partial\alpha_1} = \frac{\Gamma_{\mathrm{LACO}}}{(\mathrm{P}^\star)^2}\left(\alpha_2\mathrm{P}^\star - \alpha_1\alpha_2\frac{\partial\mathrm{P}^\star}{\partial\alpha_1}\right), \tag{5.37a}$$

$$\frac{\partial\Gamma_2}{\partial\alpha_1} = \frac{\Gamma_{\mathrm{LACO}}}{(\mathrm{P}^\star)^2}\left(-2\alpha_2\mathrm{P}^\star - \alpha_1\alpha_2\frac{\partial\mathrm{P}^\star}{\partial\alpha_1}\right), \tag{5.37b}$$

$$\frac{\partial\Gamma_3}{\partial\alpha_1} = \frac{\Gamma_{\mathrm{LACO}}}{(\mathrm{P}^\star)^2}\left(4(1-\alpha_2)\mathrm{P}^\star - \alpha_1\alpha_2\frac{\partial\mathrm{P}^\star}{\partial\alpha_1}\right), \tag{5.37c}$$

where

$$\frac{\partial\mathrm{P}^\star}{\partial\alpha_1} = 1 - \alpha_2 + \frac{2}{\pi}\sqrt{\alpha_2(1-\alpha_2)} + \frac{(1-2\alpha_1)\left(\alpha_2 + \sqrt{\alpha_2(1-\alpha_2)}\right)}{\pi\sqrt{\alpha_2(1-\alpha_2)}}; \tag{5.37d}$$

and

$$\frac{\partial\Gamma_1}{\partial\alpha_2} = \frac{\Gamma_{\mathrm{LACO}}}{(\mathrm{P}^\star)^2}\left(\alpha_1\mathrm{P}^\star - \alpha_1\alpha_2\frac{\partial\mathrm{P}^\star}{\partial\alpha_2}\right), \tag{5.37e}$$

$$\frac{\partial\Gamma_2}{\partial\alpha_2} = \frac{\Gamma_{\mathrm{LACO}}}{(\mathrm{P}^\star)^2}\left(2(1-\alpha_1)\mathrm{P}^\star - \alpha_1\alpha_2\frac{\partial\mathrm{P}^\star}{\partial\alpha_2}\right), \tag{5.37f}$$

$$\frac{\partial\Gamma_3}{\partial\alpha_2} = \frac{\Gamma_{\mathrm{LACO}}}{(\mathrm{P}^\star)^2}\left(-4\alpha_1\mathrm{P}^\star - \alpha_1\alpha_2\frac{\partial\mathrm{P}^\star}{\partial\alpha_2}\right), \tag{5.37g}$$

where

$$\frac{\partial\mathrm{P}^\star}{\partial\alpha_2} = 1 - \alpha_1 + \frac{2}{\pi}\sqrt{\alpha_1(1-\alpha_1)} + \frac{(1-2\alpha_2)\left(\alpha_1 + \sqrt{\alpha_1(1-\alpha_1)}\right)}{\pi\sqrt{\alpha_2(1-\alpha_2)}}. \tag{5.37h}$$

and α_2 are expressed as:

$$\frac{\partial \mathsf{C}_{\text{LACO}}}{\partial \alpha_1} = \frac{1}{4}\frac{\partial \mathsf{C}_{\text{RF}}}{\partial \Gamma_1}\frac{\partial \Gamma_1}{\partial \alpha_1} + \frac{1}{8}\frac{\partial \mathsf{C}_{\text{RF}}}{\partial \Gamma_2}\frac{\partial \Gamma_2}{\partial \alpha_1} + \frac{1}{16}\frac{\partial \mathsf{C}_{\text{RF}}}{\partial \Gamma_3}\frac{\partial \Gamma_3}{\partial \alpha_1} \tag{5.40a}$$

$$\frac{\partial \mathsf{C}_{\text{LACO}}}{\partial \alpha_2} = \frac{1}{4}\frac{\partial \mathsf{C}_{\text{RF}}}{\partial \Gamma_1}\frac{\partial \Gamma_1}{\partial \alpha_2} + \frac{1}{8}\frac{\partial \mathsf{C}_{\text{RF}}}{\partial \Gamma_2}\frac{\partial \Gamma_2}{\partial \alpha_2} + \frac{1}{16}\frac{\partial \mathsf{C}_{\text{RF}}}{\partial \Gamma_3}\frac{\partial \Gamma_3}{\partial \alpha_2}. \tag{5.40b}$$

The characteristics of C_{LACO} are similar to those of its 2-layer counterpart shown in Sec. 5.4.2, which is monotonically increasing and then decreasing within $[0,1]$ for both α_1 and α_2. The optimum point (α_1^*, α_2^*) can be found by solving

$$\text{diag}\{\nabla \mathsf{C}_{\text{LACO}}(\alpha_1, \alpha_2)\} = \mathbf{0}. \tag{5.41}$$

To proceed, we provide the expressions for each of the components in Eq. (5.40), shown at the bottom of page 121. Since α_1 appears in the expressions of (5.37e-5.37h) and α_2 in (5.37a-5.37d), a nested algorithm is required for solving Eq. (5.41).

Algorithm 3 Power allocation in 3-layer LACO-OFDM

```
Input: $M$, $\Gamma_{\text{LACO}}$, $N$, $\epsilon$
Output: $\alpha_1^*$, $\alpha_2^*$, $\mathsf{C}_{\text{LACO}}^*$
$p_1 := 0$, $q_1 := 1$
repeat
    $\overline{\alpha}_1 := (p_1 + q_1)/2$,
    Find $\overline{\alpha}_2$ under current $\overline{\alpha}_1$ using Alg. 4;
    Calculate $\Gamma_l(\overline{\alpha}_1, \overline{\alpha}_2)$ for $l = 1,2,3$ using Eq. (5.38),
    Calculate $\left.\frac{\partial \mathsf{C}_{\text{LACO}}}{\partial \Gamma_l}\right|_{(\overline{\alpha}_1,\overline{\alpha}_2)}$ for $l = 1,2,3$ using Eq. (5.29),
    Calculate $\left.\frac{\partial \Gamma_l}{\partial \alpha_1}\right|_{(\overline{\alpha}_1,\overline{\alpha}_2)}$ for $l = 1,2,3$ using Eq. (5.37),
    Calculate $\left.\frac{\partial \mathsf{C}_{\text{LACO}}}{\partial \alpha_1}\right|_{(\overline{\alpha}_1,\overline{\alpha}_2)}$ by substituting the above 6 terms into Eq. (5.40a);
    if $\left.\frac{\partial \mathsf{C}_{\text{LACO}}}{\partial \alpha_1}\right|_{(\overline{\alpha}_1,\overline{\alpha}_2)} > 0$ then
        $p_1 := \overline{\alpha}_1$,
    else
        $q_1 := \overline{\alpha}_1$,
    end if
until $\left|\frac{\partial \mathsf{C}_{\text{LACO}}}{\partial \alpha_1}\right|_{(\overline{\alpha}_1,\overline{\alpha}_2)} < \epsilon$ at $(\alpha_1, \alpha_2)$;
return $\alpha_1^* = \overline{\alpha}_1$, $\alpha_2^* = \overline{\alpha}_2$ ;
return $\mathsf{C}_{\text{LACO}}^* = \mathsf{C}_{\text{LACO}}(\alpha_1^*, \alpha_2^*)$ ;
```

As shown in Alg. 3, the search is conducted in the twinned directions: of α_1 and α_2, respectively. The inner loop is detailed in Alg. 4, which takes a given value of $\overline{\alpha}_1$ and substitutes it into Eq. (5.40b), followed by finding the corresponding α_2 coordinate where the zero-crossing occurs using similar methods to those in Alg. 2. The outer loop

Algorithm 4 Zero Crossing Finder for Eq. (5.40b)

```
Input: $M$, $\Gamma_{\text{LACO}}$, $N$, $\epsilon$, $\overline{\alpha}_1$
Output: $\overline{\alpha}_2$
$p_2 := 0$, $q_2 := 1$;
repeat
    $\bar{\bar{\alpha}}_2 := (p_2 + q_2)/2$,
    Calculate $\Gamma_l(\overline{\alpha}_1, \bar{\bar{\alpha}}_2)$ for $l = 1, 2, 3$ using Eq. (5.38),
    Calculate $\frac{\partial \mathsf{C}_{\text{LACO}}}{\partial \Gamma_l}$ at $\Gamma_l(\overline{\alpha}_1, \bar{\bar{\alpha}}_2)$ for $l = 1, 2, 3$ using Eq. (5.29),
    Calculate $\left.\frac{\partial \Gamma_l}{\partial \alpha_2}\right|_{(\overline{\alpha}_1, \bar{\bar{\alpha}}_2)}$ for $l = 1, 2, 3$ using Eq. (5.37),
    Calculate $\left.\frac{\partial \mathsf{C}_{\text{LACO}}}{\partial \alpha_2}\right|_{(\overline{\alpha}_1, \bar{\bar{\alpha}}_2)}$ by substituting the above 6 terms into Eq. (5.40b);
    if $\left.\frac{\partial \mathsf{C}_{\text{LACO}}}{\partial \alpha_2}\right|_{(\overline{\alpha}_1, \bar{\bar{\alpha}}_2)} > 0$ then
        $p_2 := \bar{\bar{\alpha}}_2$,
    else
        $q_2 := \bar{\bar{\alpha}}_2$,
    end if
until $\left.\frac{\partial \mathsf{C}_{\text{LACO}}}{\partial \alpha_2}\right|_{(\overline{\alpha}_1, \bar{\bar{\alpha}}_2)} < \epsilon$ ;
return $\overline{\alpha}_2 = \bar{\bar{\alpha}}_2$ ;
```

of Alg. 3 then takes the returned value $\overline{\alpha}_2$ to determine whether a zero-crossing has also be found for Eq. (5.40a). If not, $\overline{\alpha}_1$ will be updated in a binary-search manner and forwarded to Alg. 4 for the corresponding new $\overline{\alpha}_2$. The process continues by checking and updating $\overline{\alpha}_1$ and $\overline{\alpha}_2$, until a zero-crossing occurs in both directions, thus reaching the stationary point.

5.5.3 Numerical Results

In Fig. 5.8, we portray the channel capacity of a 3-layer LACO-OFDM system vs. its power sharing factors α_1 and α_2, using 16QAM modulation at an SNR of 12 dB. Observe that the capacity first increases and then decreases with respect to both α_1 and α_2, resulting in a global peak in the middle.

To elaborate a little further, in Fig. 5.9 we provide sectional views of the capacity by slicing the 3D surface of Fig. 5.8 along α_1 and α_2, respectively. The derivatives with respect to the corresponding variables are also depicted in the same figure. In Fig. 5.9(a), the capacity peak can be found at the zero crossing of its derivative, namely at $\alpha_1 = 0.701$. Fig. 5.9(b) is then sliced by the vertical plane at $\alpha_1 = 0.701$, leading to same capacity peak at $\alpha_2 = 0.6841$, which in turn decides where to slice for Fig. 5.9(a). Since the capacity derivatives are zero in both directions at $(\alpha_1,\ \alpha_2) = (0.701, 0.6841)$, the peak can be recognised as a global capacity maximum.

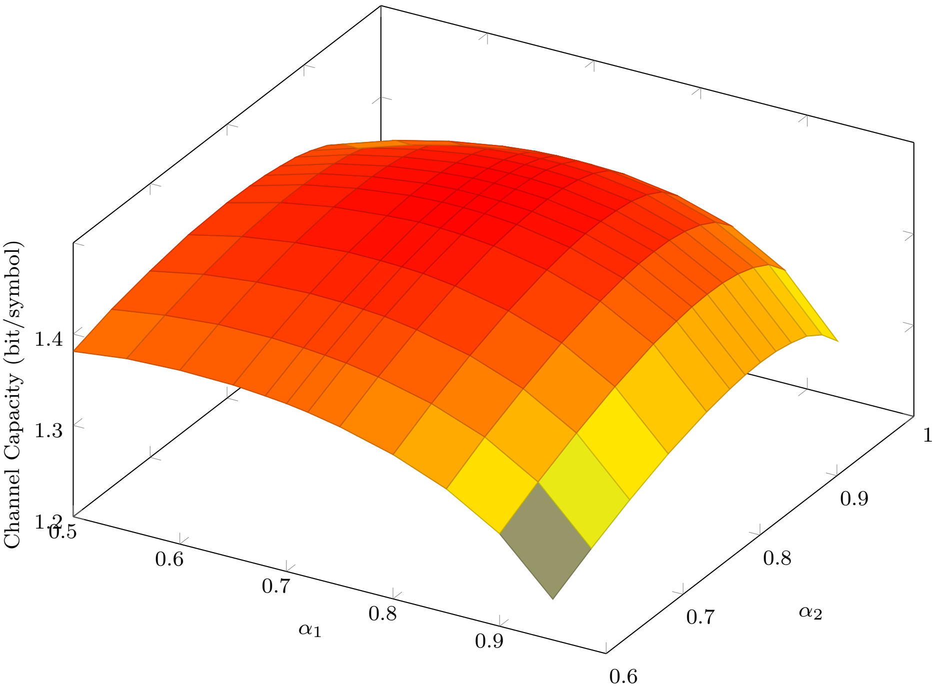

Figure 5.8: Channel capacity of 3-Layer LACO-OFDM using 16QAM at SNR = 12 dB vs. α_1 and α_2.

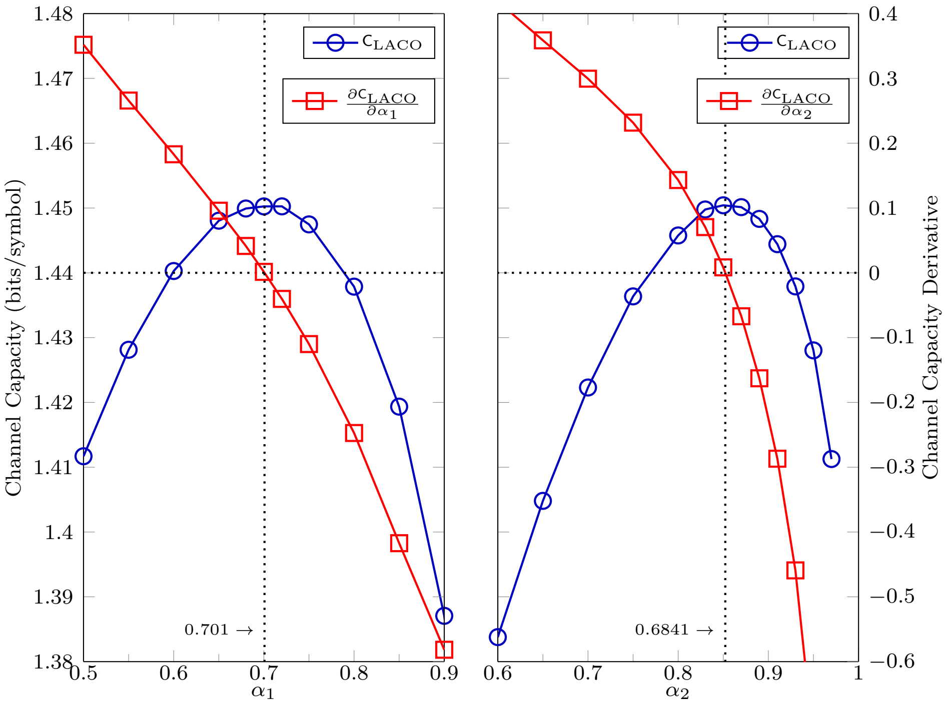

(a) Sliced by $\alpha_2 = 0.6841$

(b) Sliced by $\alpha_1 = 0.7010$

Figure 5.9: Channel capacity of 3-layer LACO-OFDM extracted from Fig. 5.8 and its derivatives.

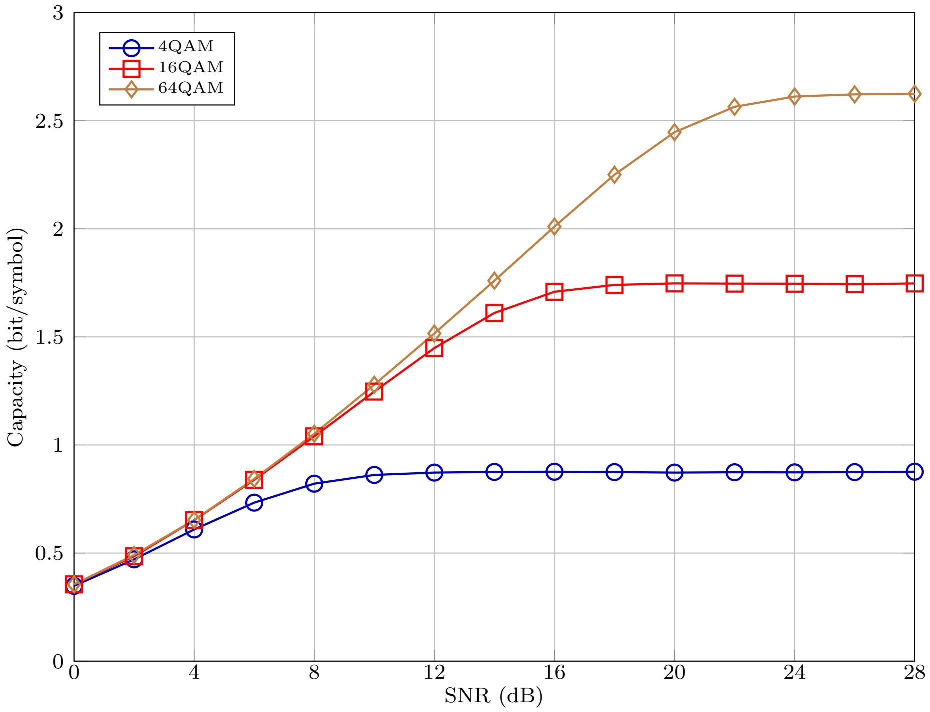

Figure 5.10: Optimised DCMC capacity of 3-Layer LACO-OFDM vs. SNR using the proposed algorithm.

To provide further insights, Fig. 5.10 depicts the optimum channel capacity versus SNR for 3-layer LACO-OFDM in conjunction with different modulation schemes.

5.5.4 Generalisation of the Algorithm

Let us now continue by summarising the optimum power allocation of 3-layer LACO-OFDM systems and by generalising it for L-layer LACO-OFDM.

1. Let us establish the power sharing factors using $\boldsymbol{\alpha} = [\alpha_1, \ldots, \alpha_l, \ldots, \alpha_{L-1}]$, and
$$\frac{P_1}{P_l} = \frac{\alpha_{l-1}}{1-\alpha_{l-1}}, \quad 0 \leq \alpha_{l-1} \leq 1. \tag{5.42}$$
2. Let us then express the SNRs of each layer Γ_l in terms of the total SNR Γ_{LACO} and $\boldsymbol{\alpha}$, using Eqs. (5.12) and (5.13).
3. Obtain the total capacity formula C_{LACO} using Eq. (5.16), and differentiate it with respect to every element of $\boldsymbol{\alpha}$.
4. Using an $(L-1)$-stage nested loop, in the power-sharing algorithm to find the maximum of C_{LACO}:
    (a) Fix the values of $\alpha_1, ...\alpha_{L-2}$ and substitute them into $\dfrac{\partial \mathsf{C}_{\text{LACO}}}{\partial \alpha_{L-1}} = 0$. Find the root α_{L-1} using binary search within $[0, 1]$ and return to its upper loop.

(b) Sweep the value of α_{L-2} across its legitimate range and calculate the corresponding α_{L-1} each time, until $\frac{\partial \mathsf{C}_{\mathrm{LACO}}}{\partial \alpha_{L-2}} = 0$ is reached. Forward α_{L-1} and α_{L-2} to the upper loop.

(c) Repeat this procedure until the top stage of the loop is reached and find the values of all elements in $\boldsymbol{\alpha}$ so that we have $\mathrm{diag}\{\nabla \mathsf{C}_{\mathrm{LACO}}\} = \mathbf{0}$.

5.6 Discussions

5.6.1 Comparison to Conventional Power Allocation Strategy

In previous contributions on LACO-OFDM [1, 3, 53], the *Equal Power per Bit* strategy has been employed, where the same amount of power is assigned to all information bits in the system, regardless of their location in the layers. Explicitly, if the same modulation order is applied for all layers, each layer should have twice the energy of its directly-following layer, because the former transmits twice the amount of information bits than the latter. This leads to a fixed $\boldsymbol{\alpha} = \{\alpha_1, \alpha_2, \dots \alpha_{L-1}\}$ vector, regardless of the channel SNR. According to Eq. (5.42), we have:

$$\alpha_l = \frac{P_1}{P_1 + P_{l+1}} = \frac{2^l P_{l+1}}{2^l P_{l+1} + P_{l+1}} = 1 - \frac{1}{2^{l+1}}. \tag{5.43}$$

In Fig. 5.11, we compare the capacity improvement attained by using the Algorithm proposed. Observe that the *Equal Power per Bit* strategy is outperformed by the proposed one.

Specifically, at SNR = 12 dB, a beneficial capacity improvement of about 0.18 bits/symbol can be attained by 3-layer LACO-OFDM using 16QAM. From a different prospective, this can also be equivalently expressed as a 1.8 dB SNR gain, because the conventional strategy reaches the same capacity at a 1.8 dB higher SNR. By contrast, the difference for a 2-layer system remains negligible.

5.6.2 Adapting the Number of Layers

It may also be observed from Fig. 5.11 that the capacity curves do cross each other, before saturating for SNR $\geq$ 20 dB. LACO-OFDM schemes having more layers have lower capacity in the low-SNR region before crossing all other curves. In the spirit of achieving the maximum capacity, we propose to adapt the number of layers based on the overall SNR.

In Fig. 5.12, an example is provided for 16QAM LACO-OFDM, where the number of layers ranges from 1 to 4, with 1 representing ACO-OFDM instead of LACO-OFDM.

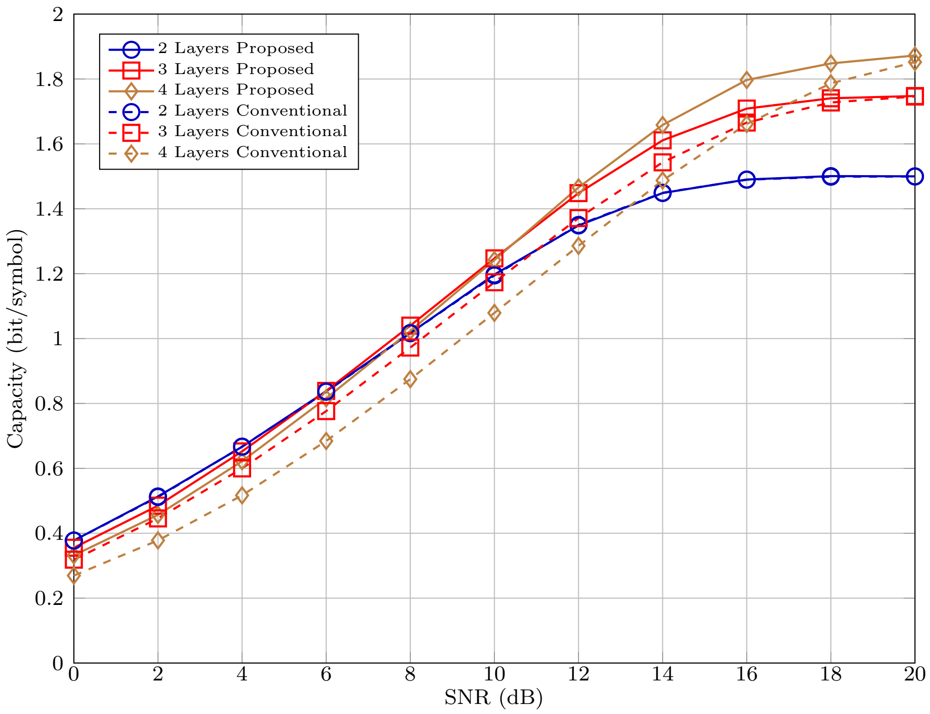

Figure 5.11: Capacity comparison for LACO-OFDM schemes using conventional and proposed power allocation algorithms. 16QAM modulation is used for all simulations.

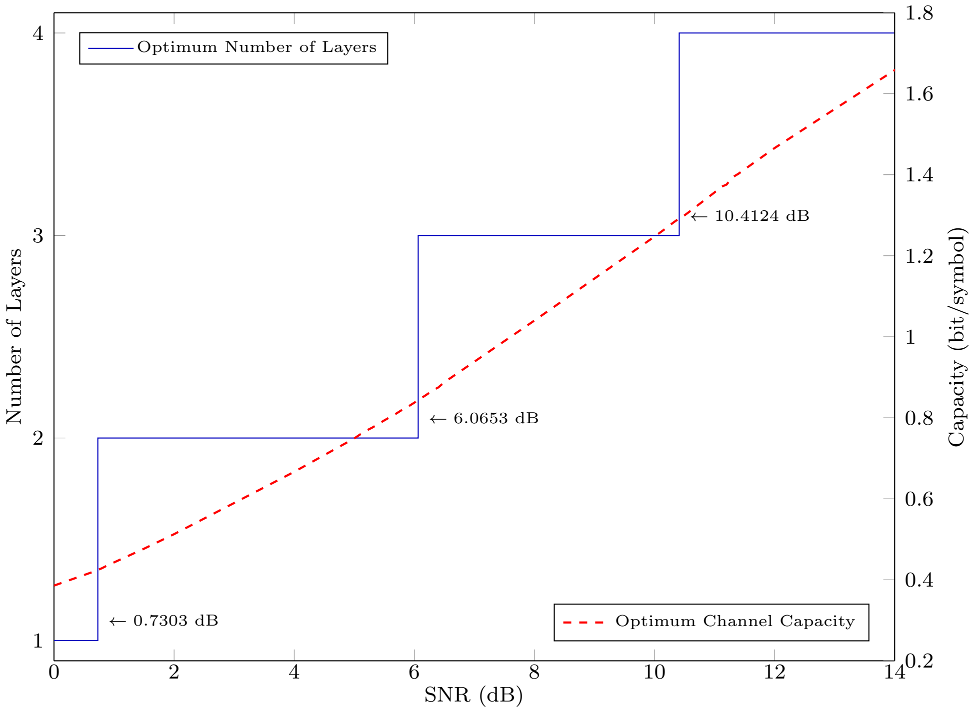

Figure 5.12: Adaptive layer number selection for maximum capacity in LACO-OFDM based on the SNR.

In this case, when SNR is lower than 0.7303 dB, using the second layer is detrimental, because the power has to be shared between two layers. After that, utilising a LACO-OFDM shows to be more profitable capacity-wise. The handover between 2- and 3-layer LACO-OFDM occurs that SNR = 6.0653 dB, where they have equal capacity, and for 3- and 4-layer it is at SNR = 10.4124 dB.

The transmitter would require the channel SNR to be fed back from the receiver side and determine the number of layers to use, based on which interval the SNR lies in Fig. 5.12. It will then find the optimum power allocation strategy using our proposed algorithm, which can be made as a look-up table. These decisions made send to the relevant part in Fig. 5.2 to generate the transmitting signal, which has the maximised capacity under the current SNR.

5.7 Chapter Conclusions

In this chapter, we derived the DCMC capacity of LACO-OFDM for a given number of layers and their power allocation strategy. The formula is used as object function to maximise the capacity by tuning the power allocation factors and later the number of layers as well. Specific algorithms have been proposed for the optimisation problem with the help of partial derivative analyses. Recursive algorithms are designed for systems with more than 2 layers. Numerical results shows an up to 0.18 bits/symbol increase of capacity after adopting the proposed power allocation strategy instead of the conventional one for 4-layer LACO-OFDM. An adaptive layer number selection scheme further maximising the capacity is also proposed based on the DCMC capacity for LACO-OFDM with different number of layers.

5.8 Chapter Summary

Figure 5.13 provides a detailed schematic diagram of the relationships amongst the sections in this chapter.

The chapter commenced with a discussion in Sec. 5.1 about the factors influencing the capacity of LACO-OFDM, which leads to the requirement of an optimum layer power allocation solution. In Sec. 5.3, a review of the multi-class coded LACO-OFDM system proposed in Chapter 4 and the *Equal Power per Bit* strategy given in Chapter 2 was provided, while our new power control modules used in both the TX and RX designs were introduced.

Sec. 5.3 analysed the DCMC capacity of the LACO-OFDM system, in preparation for the power optimisation discussed in the ensuing sections. The analysis started with reviewing the capacity of an RF system in Sec. 5.3.1, before moving to the ACO-OFDM

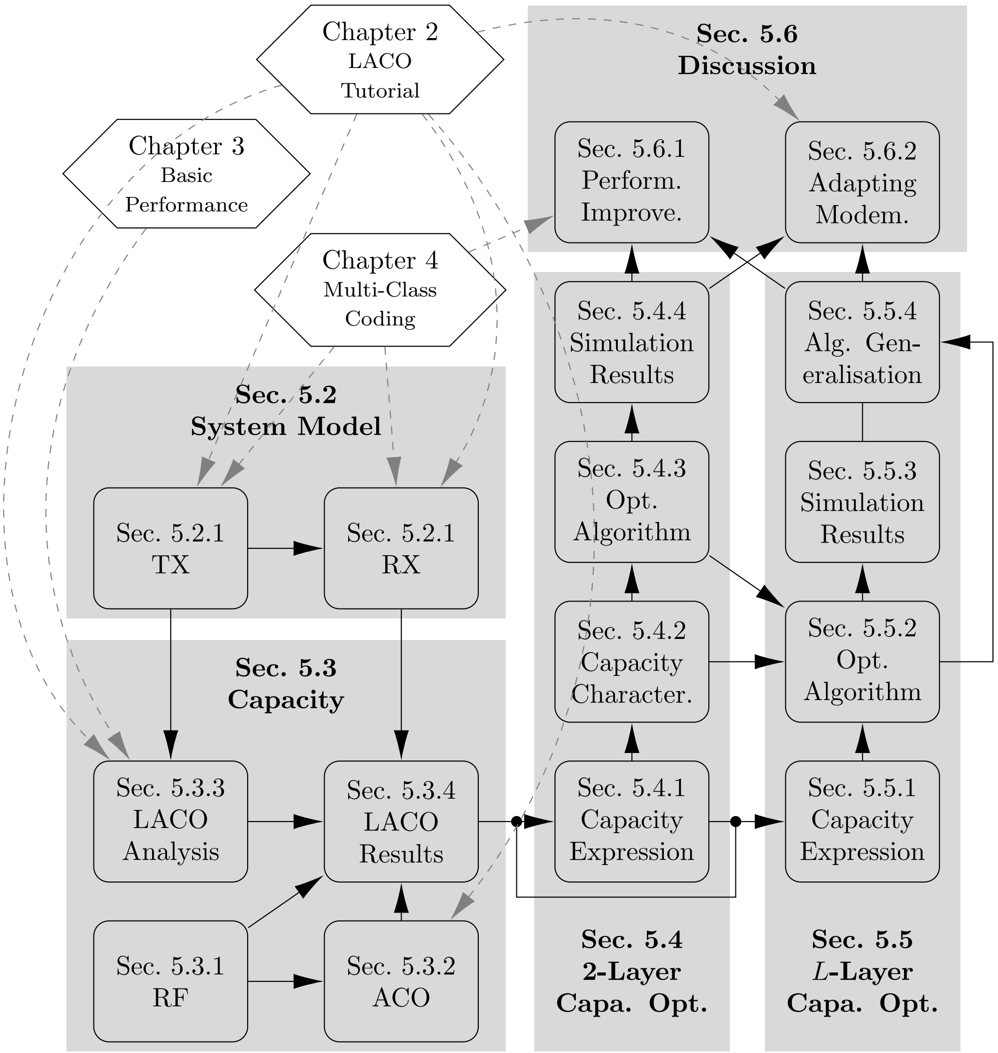

Figure 5.13: Summary of Chapter 5.

system in Sec. 5.3.2. Sec. 5.3.3 detailed the power and information composition of LACO-OFDM, assisted by the statistical analysis results of Chapter 3, which ultimately led to the DCMC capacity expression of LACO-OFDM in Sec. 5.3.4. Explicitly, the derivation used in this section differs from the one given in Chapter 4 in the following ways, as summarised in Tab. 5.2.

Table 5.2: Comparison of the DCMC analysis in Chapters 4 and 5

Topic	Chapter 4	Chapter 5
Purpose	Benchmarking the coded BER performance	Optimising the overall throughput
Formula	Entropy of the Sink minus that of the noise Eq. (4.25)	Entropy of the Source less the average information lost Eq. (5.3)
Commencement	ACO-OFDM (Sec. 4.2.2)	RF (Sec. 5.3.1)
Parameters	L, M, Γ	L, M, Γ, $\boldsymbol{\alpha}$

In particular, for the parameter comparison in Tab. 5.2, the capacity expression derived in this chapter contains the SNR of each individual layer, so that the influence of different power allocation strategies can also be reflected, while the results of Chapter 4 relied on the *Equal Power per Bit* strategy.

With the general capacity expression in hand, Sec. 5.4 optimised a 2-layer LACO-OFDM system. The channel capacity was expressed in Sec. 5.4.1 as a function of the SNRs of the two constituent layers, which are in turn the function of the power allocation factor. The characteristics of this function were studied in Sec. 5.4.2, which showed the existence of an optimum power allocation factor that corresponds to the maximum DCMC capacity. Then, an algorithm was proposed in Sec. 5.4.3 for finding the optimum point. The corresponding numerical results followed in Sec. 5.4.4.

Sec. 5.5 followed the path of Sec. 5.4 and extended the analysis to 3-layer system. Explicitly, Sec. 5.5.1 defined the capacity as a function of the three layer-SNRs, which are in turn functions of their pairwise power allocation factors. An optimisation algorithm was proposed in Sec. 5.5.2 for a 3-layer system by nesting the work of Sec. 5.4.3. The corresponding numerical results are given in Sec. 5.5.3. A more generalised algorithm applicable to systems having more layers was proposed in Sec. 5.5.4.

Finally, Sec. 5.6.1 showcased the capacity improvement attained by the proposed algorithm by comparing to the *Equal Power per Bit* results obtained in Chapter 4, which showed that improved capacity can be attained without increasing the system complexity. Finally, an adaptive system was proposed in Sec. 5.6.2 for maximising the capacity by determining the number of layers and the power allocation based on the overall SNR
.

Chapter 6

Conclusions and Future Research

In this chapter, we summarise the findings of this thesis, and provide a bird's-eye perspective of our work in Sec. 6.1, followed by Sec. 6.2 providing a selection of potential future research directions.

6.1 Thesis Summary and Conclusions

Recall from Sec. 1.4.1 that we commence on discussions with the structure of this thesis in Fig. 1.2. Chapter 2 introduced the basic system model, followed by the three substantial chapters dedicated to the performance analysis and improvement of LACO-OFDM. In Fig. 6.1, we depict the *main* topics discussed at each stage and elaborate on their connections.

6.1.1 Design Guidelines

As discussed in Sec. 1.2, the inspiration of LACO-OFDM is to strike a trade-off between the power and spectral efficiencies of ACO-OFDM and DCO-OFDM. While ACO-OFDM avoids the requirement of a substantial DC offset and hence achieves power-efficient transmission, this is at the cost of reducing the spectral efficiency by a factor of two, again, striking a trade-off between the power and spectral efficiency. The relationship of various techniques discussed throughout this thesis are summarised in Fig. 6.2.

The rest of this subsection discusses the three trade-off pairs depicted in Fig. 6.2 with reference to the topics mentioned in Chapters 1 and 2.

- The amount of information that may be conveyed at a given power efficiency (PE) is directly related to the amount of spectral efficiency (SE).

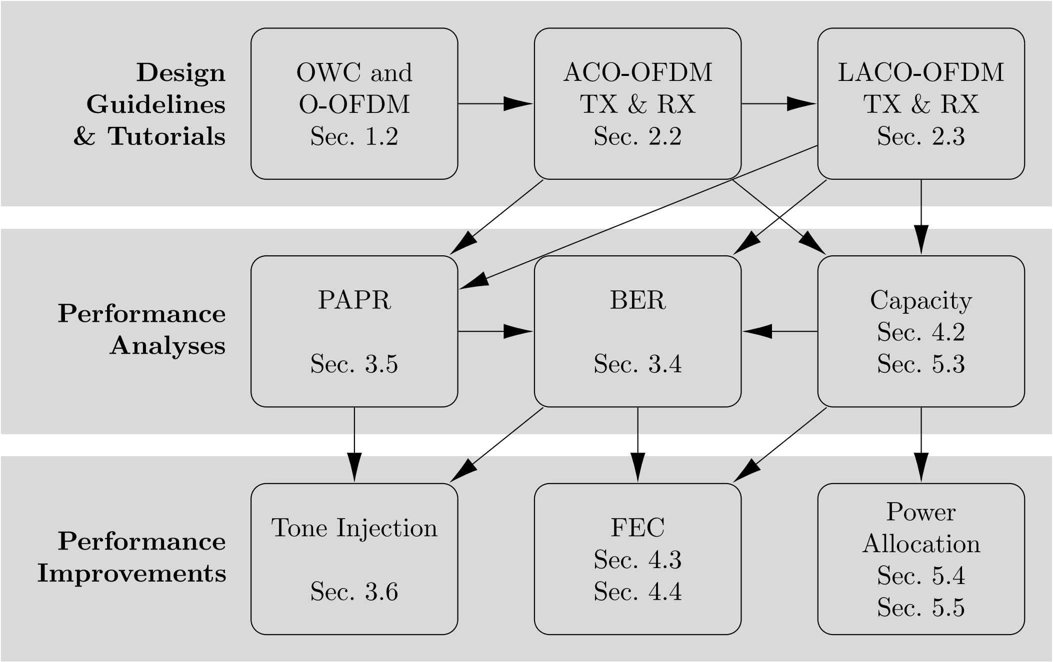

Figure 6.1: Summary of main topics and important findings of this thesis.

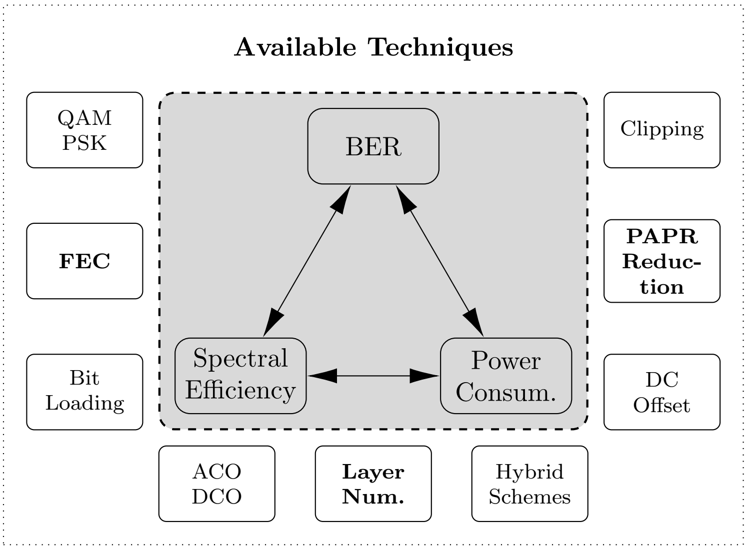

Figure 6.2: Relationship of the proposed techniques, resulting the different design trade-offs.

  - Recall from Fig. 1.1 that ACO-OFDM and DCO-OFDM may be deemed to have a high SE and PE, respectively. Therefore, the simplest way to improve PE is to switch from DCO-OFDM to using ACO-OFDM, while reconfiguration the other way around improves the SE.
  - According to Tab. 1.3, hybrid O-OFDM schemes, such as ADO-OFDM [47], HACO-OFDM [49] *etc.*, strike a compromise in terms of the SE and PE, compared to ACO-OFDM and DCO-OFDM, because they are designed to amalgamate the advantages of the basic O-OFDM schemes by relying on a pair of schemes simultaneously.
  - As one of the most advanced solutions in terms of the SE-PE trade-off, LACO-OFDM provides even higher flexibility, since the number of layers L can be readily adapted in response to different operational requirements. In the example of Fig. 1.1, the dotted lines represent LACO-OFDM schemes having different number of layers L. By increasing L, the SE curves gradually move from the low-efficiency ACO-OFDM scheme to the high-efficiency DCO-OFDM arrangement. By contrast, the PE curves would move in the opposite direction, as we increase the SE by using more layers at the cost of more power.

- Naturally, in LACO-OFDM, the relationship between the BER and PE also has to obey a trade-off, where generally reduced BER can be achieved at increased power consumption.
  - The relationship between the BER performance and the channel conditions (*i.e.* SNR, SINR) have been characterised in Eq. (3.40) and Fig. 3.11.
  - On the other hand, due to the limitation of the linear range in optical front-end components (such as the LEDs), the signal at high power inevitably suffers from non-linear distortions. Hence, UB clipping (UBC) must be used, but this increases the BER.
  - A problem closely related to the UBC is the PAPR of the signal, where the UBC distortion can be reduced when the signal has a lower PAPR, leading to a better BER performance. As proposed in Fig. 3.4 and Alg. 1, the tone-injection-based solution is capable of reducing the PAPR. However, the BER is also related to the minimum Euclidean distance ($d_{\min}$) between the modulated constellation points, which may be improved by using more power for increasing the minimum distance, hence reducing the PE.

- Finally, we discuss the trade-off between the SE and BER.
  - The most obvious relationship between the SE and BER is related to the specific choice of the QAM constellation utilised for each subcarrier. According to Tab. 3.2, given the total power and the number of layers L, by reducing

the number of information bits conveyed, upon reducing the modulation order and the SE, $d_{\min}$ is increased, which in turn increases the BER.

- Another popular performance improvement technique is constituted by FEC. As covered in Secs. 4.3 and 4.4, a powerful FEC is capable of drastically reducing the BER, provided that the SNR is high enough. However, the transmitter has to send additional redundant bits for error correction, which reduces the SE, since the portion of information bits is reduced and so is the energy per bit.

6.1.2 Performance Analyses

As shown in Fig. 6.1, the PAPR, BER and capacity of LACO-OFDM constitute the salient parameters analysed in this thesis. The main contributions to analysing the performance of LACO-OFDM in this thesis are summarised in Tab. 6.1.

1. The study of LACO-OFDM performance commenced with the basic statistical characteristics of its TD signal in Sec. 3.3. The PDF of each layer was shown in Fig. 3.9, which helped us derive the expression of the superimposed signal by exploiting to the statistical independence of each layer, as detailed in Appendix B. The UB clipping module is considered in Sec. 3.3.4 when deriving the PDF. Table 6.2 summaries the simulation results related to this topic.

2. We then proceed in Sec. 3.3 to derive the means and variances of each layer of LACO-OFDM using the PDF. The statistical moments of the composite LACO-OFDM signal were formulated by summing the metrics characterising the individual layers. Table 6.3 summaries the simulation results related to this topic.

3. One of the more important statistics is the (electric) power of the LACO-OFDM signals, because it is directly related to the SNR. By exploiting the relationship amongst the statistical parameters, the *Equal Power per Bit* strategy was conceived in Sec. 3.3.3. On the other hand, in the absence of the *Equal Power per Bit* restriction, Sec. 5.3.3 provided an expression for quantifying showing the independent contribution of each layer to the overall power.

4. We observed that the PAPR has played an important role in the BER performance. Therefore, a further analysis of the LACO-OFDM signal PAPR was provided Sec. 3.5.

5. Then, the BER and SER performance of LACO-OFDM signal was mathematically formulated in Sec. 3.4. The BER and SER expressions take into consideration the UB clipping, ILI and the layers' bit rate. Table 6.4 summaries the simulation results related to this topic.

Table 6.1: Summary of LACO-OFDM Performance Analysis Contributions in this Thesis

№	Symbol(s)	Section	Contribution
1	$f_{\boldsymbol{s}}(z)$, $f_{\boldsymbol{x}}(z)$, $F_{\boldsymbol{s}}(z)$, $F_{\boldsymbol{x}}(z)$	3.3	PDF, CDF of ACO-OFDM and LACO-OFDM signals
2	$\mathbb{E}\{\boldsymbol{s}\}$, $\mathbb{E}\{\boldsymbol{x}\}$, $\mathbb{D}\{\boldsymbol{s}\}$, $\mathbb{D}\{\boldsymbol{x}\}$	3.3	Mean and various of ACO-OFDM and LACO-OFDM signals
3	P_{LACO}	3.3, 5.3	Power of LACO-OFDM signals
4	$\text{PAPR}\{x\}$	3.5	PAPR of LACO-OFDM signals
5	$\mathbb{P}_{\text{b}}$, $\mathbb{P}_{\text{s}}$	3.4	BER and SER of LACO-OFDM signals
6	$\mathsf{C}_{\text{ACO}}^{\text{CCMC}}$, $\mathsf{C}_{\text{LACO}}^{\text{CCMC}}$, $\mathsf{C}_{\text{ACO}}^{\text{DCMC}}$, $\mathsf{C}_{\text{LACO}}^{\text{DCMC}}$	4.2	CCMC and DCMC capacity of ACO-OFDM and LACO-OFDM signals
7	$\mathsf{C}_l(\Gamma_l)$, $\mathsf{C}_{\text{LACO}}(\Gamma, \alpha)$	5.3	Power-allocation-dependent DCMC capacity of LACO-OFDM

Table 6.2: Summary of Simulation Results for PDF and CDF Performance Analysis

Item to Compare	Notation	Fig.	Number of Layers L			
			1	2	3	4
Lower Tail Amplitude	$f_{\boldsymbol{x}}(1.0)$	3.6	2.20_{-1}	3.63_{-1}	4.35_{-1}	4.85_{-1}
Upper Tail Amplitude	$f_{\boldsymbol{x}}(4.0)$	3.8	5.15_{-3}	1.83_{-3}	7.65_{-4}	3.75_{-4}
Coefficient of the impulse at LB	$\frac{f_{\boldsymbol{x}}(0)}{\delta(0)}$	3.9	5.00_{-1}	2.50_{-1}	1.25_{-1}	6.25_{-2}
Coefficient of the impulse at UB τ=9dB	$\frac{f_{\boldsymbol{x}}(2.818)}{\delta(0)}$	3.9	2.29_{-2}	1.23_{-2}	7.75_{-3}	5.38_{-3}

Table 6.3: Summary of Simulation Results for Statistical Moments Performance Analysis

Item to Compare	Notation	Fig.	Number of Layers L			
			1	2	3	4
Mean	$\mathbb{E}\{\boldsymbol{x}\}$	3.7	5.64_{-1}	6.90_{-1}	7.52_{-1}	7.88_{-1}
Variance	$\mathbb{D}\{\boldsymbol{x}\}$	3.7	6.02_{-1}	5.24_{-1}	4.35_{-1}	3.80_{-1}

Table 6.4: Summary of BER Simulation Result

Item to Compare	Notation	Fig.	Number of Layers L			
			1	2	3	4
E_b/N_0 (dB) when $\mathbb{P}_{\rm b} = 10^{-3}$ w/o UBC	$\gamma_{\rm b}^{-1}(10^{-3})$	3.12	13.63	14.87	15.84	16.55
E_b/N_0 (dB) when $\mathbb{P}_{\rm b} = 10^{-3}$ w/ UBC	$\gamma_{\rm b}^{-1}(10^{-3})$	3.12	16.9	17.08	17.08	17.26
E_b/N_0 (dB) when $\mathbb{P}_{\rm b} = 10^{-5}$ w/o UBC	$\gamma_{\rm b}^{-1}(10^{-5})$	3.12	16.55	17.7	18.5	19.12
E_b/N_0 (dB) when $\mathbb{P}_{\rm b} = 10^{-5}$ w/ UBC	$\gamma_{\rm b}^{-1}(10^{-5})$	3.12	20.71	21.15	23.1	28.94

6. To benchmark the BER performance, in Sec. 4.2, we derived the CCMC and DCMC capacities of LACO-OFDM. Table 6.5 summaries the simulation results related to this topic.
7. When our *No Equal Power per Bit* strategy is applied, in Sec. 5.3, we also provide the expression of DCMC capacity as a function of the SNR for each individual layer.

6.1.3 Performance Improvements

Recall from Fig. 6.1 that the PAPR, BER and capacity of LACO-OFDM have been the salient performance metrics in this thesis. The main contributions on improving the

Table 6.5: Summary of Simulation Results for Our Capacity Analysis

Item to Compare	Notation	Fig.	Number of Layers L	
			3	4
4QAM ultimate capacity	$\mathsf{C}(\infty)$	4.5	0.875	0.938
4QAM half-rate limit capacity	$\frac{1}{2}\mathsf{C}(\infty)$	4.5	0.438	0.469
4QAM half-rate limit E_s/N_0 (dB)	$\mathsf{C}^{-1}[(\frac{1}{2}\mathsf{C}(\infty)]$	4.5	1.85	2.037
16QAM ultimate capacity	$\mathsf{C}(\infty)$	4.5	1.75	1.875
16QAM half-rate limit capacity	$\frac{1}{2}\mathsf{C}(\infty)$	4.5	0.875	0.938
16QAM half-rate limit E_s/N_0 (dB)	$\mathsf{C}^{-1}[(\frac{1}{2}\mathsf{C}(\infty)]$	4.5	6.3	7.38
64QAM ultimate capacity	$\mathsf{C}(\infty)$	4.5	2.625	2.815
64QAM half-rate limit capacity	$\frac{1}{2}\mathsf{C}(\infty)$	4.5	1.313	1.408
64QAM half-rate limit E_s/N_0 (dB)	$\mathsf{C}^{-1}[(\frac{1}{2}\mathsf{C}(\infty)]$	4.5	10.93	10

performance of LACO-OFDM in this thesis are summarised in Tab. 6.6.

Table 6.6: Summary of LACO-OFDM Performance Improvement Contributions in this Thesis

№	Symbol(s)	Section	Contribution
1	PAPR$\{x\}$	3.6	A PAPR reduction method based on tone injection
2	$\mathbb{P}_\mathrm{b}$, $\mathbb{P}_\mathrm{s}$	4.4	A multi-class channel coding system for reducing the BER
3	$\mathsf{C}_\mathrm{LACO}(\Gamma, \alpha)$	5.5	An optimum power allocation algorithm for maximising the capacity

1. In Sec. 3.6, we proposed a PAPR reduction technique based on tone injection, which relied on the module introduced back in Sec. 3.2 and on the LACO-OFDM TX architecture of Fig. 2.8. An optimisation problem aiming for reducing the PAPR by minimising the sum of the first L' layers was formulated, which was then resolved by MILP. A further simplification of the algorithm was also proposed. The results of the PAPR reduction also helped improve the BER performance under clipping, as discussed in Sec. 3.4 and demonstrated in Fig. 3.19. Table 6.7 summaries the simulation results related to this topic.

2. A layered channel coding system was proposed for LACO-OFDM in Chapter 4. We discussed the limitations of the single-class system in Sec. 4.3, which was followed by the introduction of our proposed layered LACO-OFDM architecture in Sec. 4.4. The benefits of the proposed coded optical communications system were

Table 6.7: Summary of Simulation Results for PAPR Reduction

Item to Compare	Notation	Fig.	Number of Layers L		
			2	3	4
PAPR (dB) at CCDF= 10^{-3} w/o reduction method	$\mathrm{PAPR}^{-1}(10^{-3})$	3.18	7.5	7.902	8.661
PAPR (dB) at CCDF= 10^{-3} w/ reduction method	$\mathrm{PAPR}^{-1}(10^{-3})$	3.18	12.589	13.125	13.75
Improvement (dB)		3.18	5.089	5.223	5.089

quantified by invoking both convolutional and turbo codes. Quantitatively, it was demonstrated that our turbo coded system operated within 1.1 dB of the achievable rate at a BER of 10^{-3}, as seen in Fig. 4.11. Furthermore, our convolutional coded system outperformed the single-class turbo coded system despite the 32 times lower decoding complexity of the former. We also demonstrated that the layered coded system is capable of drastically reducing the ILI. Table 6.8 summaries the simulation results related to this topic.

3. Finally, we expressed the DCMC capacity of LACO-OFDM as a function of the number of layers and their power allocation strategy. This formula was used as our object function for maximising the capacity by tuning both the power allocation factors and the number of layers as well. Our optimisation algorithms relied on the partial derivative of Eqs. (5.26) and (5.40) followed by a binary search in Algs. 2 and 4. Table 6.9 summaries the simulation results related to this topic.

6.2 Future Research

Downlink/Uplink Decoupling

Although both downlink and uplink VLC transmissions have been investigated literature [93–95] and efforts have also been dedicated to bidirectional VLC transmissions [96, 97], much of the research has been focused on the downlink. This is partially due to the difficulties of uplink VLC implementations. Hence, RF WiFi solutions have been adopted as the uplink counterpart of a VLC downlink [98], which decouples the transmission links and creates heterogeneous networks (HetNets). Apart from its simpler implementation and lower deployment costs [99], RF uplink solutions have been shown to have lower TX power requirements and/or better SNR [100], resulting in higher data rates [101]. Therefore, further research should be devoted to the design of a decoupled HetNet RF/VLC system relying on LACO-OFDM, where further cooperation and scheduling challenges have to be tackled.

Table 6.8: Summary of Simulation Results for Multi-Class Coding

Scheme	Structure	Code	Parameter	States	γ_{b} at $\mathbb{P}_{\mathrm{b}} = 10^{-3}$	Coding Gain	Distance to Limit
1	Single Class	uncoded	N/A	N/A	16.3335	0	8.6735
2		CC	$\mathcal{M} = 2$	4	16.0471	0.2864	8.3871
3			$\mathcal{M} = 7$	128	15.9234	0.4101	8.2634
4		TC	$\mathcal{M} = 3, \mathcal{I} = 8$	128	12.4089	3.9246	4.7489
5	Multi Class	CC	$\mathcal{M} = 2$	4	11.3496	4.9839	3.6896
6			$\mathcal{M} = 5$	32	10.9059	5.4276	3.2459
7			$\mathcal{M} = 6$	64	10.8214	5.5121	3.1614
8			$\mathcal{M} = 7$	128	10.679	5.6545	3.019
9		TC	$\mathcal{M} = 3, \mathcal{I} = 2$	32	9.7295	6.604	2.0695
10			$\mathcal{M} = 3, \mathcal{I} = 4$	64	9.067	7.2665	1.407
11			$\mathcal{M} = 3, \mathcal{I} = 8$	128	8.8273	7.5062	1.1673

Table 6.9: Summary of Simulation Results for Capacity Optimisation

Item to Compare	Number of Layers L		
	2	3	4
Ultimate capacity	1.5	1.75	1.813
Half-rate limit capacity	0.75	0.875	0.906
half-rate limit E_s/N_0 (dB) w/o Optimisation	4.975	6.361	6.87
half-rate limit E_s/N_0 (dB) w/ Optimisation	4.981	7.006	8.308
Improvement (dB)	0.006	0.645	1.438

Power Line Backhaul

Apart from the uplink issues discussed above, the backhaul also plays an important role in VLC networks, which should ideally be provided by Power Line Communications (PLC) [102] instead of laying an extra Ethernet link. However, typical PLC transmissions are susceptible to the impulse noise and the multipath reflections, which are commonly found in this hostile medium [103, 104], creating a unique type of system, which requires dedicated tools for equalising the channel effects and mitigating the errors. As a result, despite the huge throughput potential of VLC, the PLC-based backhaul requires much more research attention. Therefore, a joint system design must be conceived, considering both what the end user requires and what the PLC backhaul can offer. Fortunately, the flexibility of LACO-OFDM provides us with increased design freedom, thanks to its flexible SE and PE trade-off.

Fibre Optics Communications

A more reliable but more costly wired communications technique of connecting the LED transmitters is over the optical fibres, which have a higher than PLC throughput. Experiments have been conducted using LACO-OFDM signals over short-haul ($\sim$ 20 km) fibre-optic links with data rates ranging from 4.375 Gb/s [61,105] up to 9.375 Gb/s [106]. These experiments have demonstrated notable improvements in spectral efficiency over conventional optic-fibre links based mainly on DCO-OFDM. However, similarly to PLC, optic-fibre channels also have their unique impairments, hence requiring further research.

Multiuser LACO-OFDM

Original conceived way back in the 1960s [107], Multiple-Input Multiple-Output (MIMO) systems have been widely studied in the RF field [108–110] for supporting simultaneous communications for multiple users within the same spectral resources. More recently, adopting MultiUser MIMO (MU-MIMO) techniques for VLC systems has also attracted much attention [111,112] for further improving the system's performance. However, due to the unique structure of LACO-OFDM and its requirement of layer-by-layer detection at the receiver, conventional Orthogonal Multiple Access (OMA) techniques cannot be readily applied, since each user requires the knowledge of all users' information for cancelling the clipping distortion in each layer. As a remedy, NOMA may be harnessed [113] for supporting multiple users with the aid of LACO-OFDM, where other users' information can either be cancelled out or regarded as noise [68]. However, scheduling and power allocation still remain us challenging upon issues, when applying NOMA techniques in MU-MIMO LACO-OFDM systems, which requires further investigations.

Outdoor VLC

At the time of writing, the vast majority research on VLC have been dedicated to indoor scenarios, given the vulnerability of optical signals to the shot noise induced by the filtered sunlight [114]. However, given the recent development of sophisticated techniques and the better understanding of the outdoor channel characteristics [115], powerful adaptive bandwidth based counter-measurements have been proposed to improve the performance and mitigate the shot noise [116]. More recently, the performance of the basic ACO-OFDM and DCO-OFDM schemes operating in outdoor scenario have also been characterised [117], calling for more sophisticated, robust and power-efficient schemes relying on strong FEC techniques, such as our multi-class coded LACO-OFDM scheme.

Appendix A

Mathematical Proof of Asymmetry in ACO- and LACO-OFDM Signals

A.1 Asymmetry in ACO-OFDM

In this section, we provide mathematical proof of the asymmetry in ACO-OFDM TD signals' amplitude formulated in Theorem A.1.

Theorem A.1 (Asymmetry in ACO-OFDM). *If the FD subcarriers of a signal* $\overline{\boldsymbol{S}}$ *are loaded in the following way:*

- (Hermitian Symmetry) *The second half of the subcarriers have to satisfy the conjugate complex property formulated as:*

$$\overline{S}[k] = \overline{S}^{*}[K-k], \quad 1 \leq k \leq \left(\frac{K}{2} - 1\right), \tag{A.1a}$$

$$\overline{S}[0] = \overline{S}\left[\frac{K}{2}\right] = 0, \tag{A.1b}$$

  where K *is the total number of subcarriers, bearing in mind that the subcarriers* $\overline{S}[0]$ *and* $\overline{S}[\frac{K}{2}]$ *are left blank for the DC components.* Furthermore:

- *All even-indexed subcarriers are left blank, i.e.*

$$\overline{S}[2k] = 0, \quad 0 \leq k \leq (K-1), \tag{A.2}$$

Then, the TD signal $\overline{\boldsymbol{s}}$ *satisfies the Hermitian symmetry, i.e.*

- *it is all real-valued,* and

- *the second half of the samples is the negative counterpart of the first half, which is expressed as:*

$$-\,\overline{s}\,[n] = \overline{s}\left[\frac{K}{2}+n\right], \quad 0 \le n < \frac{K}{2}. \tag{A.3}$$

A.1.1 The TD Modulated Signal Is Read-Valued

Proof. Using the definition of the Inverse Discrete Fourier Transform (IDFT), the TD signal can be written as

$$\overline{s}[n] = \frac{1}{\sqrt{K}}\sum_{k=0}^{K-1}\overline{S}[k]W_K^{kn} = \frac{1}{\sqrt{K}}\sum_{k=0}^{\frac{K}{2}-1}\overline{S}[k]W_K^{kn} + \frac{1}{\sqrt{K}}\sum_{k=\frac{K}{2}}^{K-1}\overline{S}[k]W_K^{kn}, \tag{A.4}$$

where $W_K = e^{j\frac{2\pi}{K}}$ is the Kth root of unity, *e.g.* $W_K^{kn} = e^{j\frac{2\pi}{K}kn}$. Using $(K-k)$ to replace k in the last term yields

$$\frac{1}{\sqrt{K}}\sum_{k=\frac{K}{2}}^{K-1}\overline{S}[k]W_K^{kn} \overset{Eq.\ \text{(A.1b)}}{=\!=\!=\!=} \frac{1}{\sqrt{K}}\sum_{K=\frac{K}{2}+1}^{K-1}\overline{S}[k]W_K^{kn} \tag{A.5}$$

$$\overset{k\to(K-k)}{=\!=\!=\!=\!=} \frac{1}{\sqrt{K}}\sum_{K=1}^{\frac{K}{2}-1}\overline{S}[K-k]W_K^{(K-k)n} \overset{\text{(A.1b)}}{=\!=\!=} \frac{1}{\sqrt{K}}\sum_{k=0}^{\frac{K}{2}-1}\overline{S}[K-k]W_K^{(K-k)n} \tag{A.6}$$

$$\overset{\text{(A.1a)}}{=\!=\!=} \frac{1}{\sqrt{K}}\sum_{k=0}^{\frac{K}{2}-1}\overline{S}^*[k]W_K^{(K-k)n} \overset{\text{(A.9)}}{=\!=\!=} \frac{1}{\sqrt{K}}\sum_{k=0}^{\frac{K}{2}-1}\overline{S}^*[k]\left(W_K^{kn}\right)^* \tag{A.7}$$

$$= \frac{1}{\sqrt{K}}\sum_{k=0}^{\frac{K}{2}-1}\left(\overline{S}[k]e^{j\frac{2\pi n}{K}k}\right)^* = \left(\frac{1}{\sqrt{K}}\sum_{k=0}^{\frac{K}{2}-1}\overline{S}[k]W_K^{kn}\right)^*, \tag{A.8}$$

where the second equalities in Eqs. (A.5) and (A.6) are add/remove the blank subcarriers reserved for the DC counterpart, which do not affect the summation process. The first equality of Eq. (A.7) is based on Eq. (A.1), while the second equality is valid because

$$W_K^{(K-k)n} = W_K^{Kn}W_K^{-kn} = W_1^{n}W_K^{-kn} = W_K^{-kn} = \left(W_K^{kn}\right)^*, \ \forall n \in \mathbb{Z}. \tag{A.9}$$

Given that Eq. (A.8) proves that the two terms of Eq. (A.4) are conjugate pairs, Eq. (A.4) can be simplified as

$$\begin{aligned} \overline{s}[n] &= \frac{1}{\sqrt{K}}\sum_{k=0}^{\frac{K}{2}-1}\overline{S}[k]W_K^{kn} + \left(\frac{1}{\sqrt{K}}\sum_{k=0}^{\frac{K}{2}-1}\overline{S}[k]W_K^{kn}\right)^* \\ &= 2\cdot\Re\left\{\frac{1}{\sqrt{K}}\sum_{k=0}^{\frac{K}{2}-1}\overline{S}[k]W_K^{kn}\right\} \in \mathbb{R}, \end{aligned} \tag{A.10}$$

because adding its conjugate cancels out the imaginary part of a complex number. □

A.1.2 Asymmetry of the Signal Amplitude

Proof. The $\left(\frac{K}{2}+n\right)$th ($0 \le n \le \frac{K}{2}$) sample in $\overline{\boldsymbol{s}}$ can be expressed as

$$\overline{s}\left[\frac{K}{2}+n\right] = \frac{1}{\sqrt{K}}\sum_{k=0}^{K-1}\overline{S}[k]W_K^{k\left(\frac{K}{2}+n\right)} = \frac{1}{\sqrt{K}}\sum_{k=0}^{K-1}\overline{S}[k]e^{j\pi k}W_K^{kn}. \tag{A.11}$$

Meanwhile,

- when k is an odd number, $e^{j\pi k} = -1$, we have:

$$\overline{S}[k]e^{j\pi k} = -\overline{S}[k],\ k = 2u+1,\ u \in \mathbb{Z}; \tag{A.12}$$

- when k is an even number, $e^{j\pi k} = 1$. However, now the rule of Eq. (A.2) should apply, and the value below is zero:

$$\overline{S}[k]e^{j\pi k} = \overline{S}[k] \overset{\text{(A.2)}}{=\!=\!=} 0 = -\overline{S}[k],\ k = 2u,\ u \in \mathbb{Z}. \tag{A.13}$$

Since Eqs. (A.12) and (A.13) unify the expression of $\overline{S}[k]e^{j\pi k}$ as $-\overline{S}[k]$, Eq. (A.11) can be simplified to

$$\overline{s}\left[\frac{K}{2}+n\right] = \frac{1}{\sqrt{K}}\sum_{k=0}^{K-1}\left(-\overline{S}[k]\right)W_K^{kn} = -\frac{1}{\sqrt{K}}\sum_{k=0}^{K-1}\left(-\overline{S}[k]\right)W_K^{kn} = -\overline{s}[n], \tag{A.14}$$

which concludes the proof. □

A.2 The Two LACO-OFDM TX Models of Section 2.3.1 Are Equivalent

In this section, we prove that the pair of LACO-OFDM TX models introduced in Secs. 2.3.1.1 and 2.3.1.2, respectively, are equivalent. In other words,

Theorem A.2. *For a FD symbol stream* $\boldsymbol{S}_l$ *of length* $\frac{K}{2^{l+1}}$ *on layer* l ($1 \le l \le L$)*, the following two methods provide identical TD (clipped) layer signal* $\boldsymbol{s}_l$*.*

1. *TX Implementation Model 1 of Sec. 2.3.1.1*
    (a) *Load the symbols on each layer according to Eq.* (2.6) *to construct* $\overline{\boldsymbol{S}}_l$ *of Fig. 2.5,*

   (b) *Apply the K-point IFFT to $\overline{\boldsymbol{S}}_l$, resulting in $\overline{\boldsymbol{s}}_l$ of Fig. 2.5,*
   (c) *Clip all negative samples in $\overline{\boldsymbol{s}}_l$ to obtain $\boldsymbol{s}_l$ of Fig. 2.5;*

2. *TX Implementation Model 2 of Sec. 2.3.1.2*
   (a) *Load the symbols on each layer in the ACO-OFDM way according to Eq.* (2.9) *to construct $\overline{\overline{\boldsymbol{S}}}_l$ of Fig. 2.6,*
   (b) *Apply the K_l-point IFFT to $\overline{\overline{\boldsymbol{S}}}_l$, resulting in $\overline{\overline{\boldsymbol{s}}}_l$ of Fig. 2.6,*
   (c) *Clip all negative samples in $\overline{\overline{\boldsymbol{s}}}_l$ to obtain $\lfloor\overline{\overline{\boldsymbol{s}}}\rfloor_l$ of Fig. 2.6,*
   (d) *Repeat $\lfloor\overline{\overline{\boldsymbol{s}}}\rfloor_l$ for $(2^{l-1}-1)$ times, attenuate its output by a factor of $2^{(l-1)/2}$ for energy conservation, to construct the length-K $\boldsymbol{s}_l$ of Fig. 2.6.*

Proof. When using model 1, the unclipped signal $\overline{\boldsymbol{s}}_l$ produced for layer l can be represented using the original symbols $\boldsymbol{S}$ as

$$\begin{aligned}\overline{s}_l[n] &= \frac{1}{\sqrt{K}}\sum_{k=0}^{K-1}\overline{S}_l[k]W_K^{kn}\\ &\overset{(2.6)}{=\!=} \frac{1}{\sqrt{K}}\sum_{u=0}^{\frac{K_l}{4}-1}\left(S_l[u]W_K^{(2^l u+2^{l-1})n}+S_l^*[u]W_K^{[K-(2^l u+2^{l-1})]n}\right)\\ &\overset{(A.9)}{=\!=} \frac{1}{\sqrt{K}}\sum_{u=0}^{\frac{K_l}{4}-1}\left(S_l[u]W_K^{2^{l-1}(2u+1)n}+S_l^*[u]W_K^{-2^{l-1}(2u+1)n}\right).\end{aligned} \tag{A.15}$$

The clipping process used for obtaining $\boldsymbol{s}^{(1)}$ (the superscript is employed to distinguish it from the signal generated using model 2) can be modelled as follows:

$$s^{(1)}[n] = \overline{s}_l[n]\cdot \mathsf{u}(\overline{s}_l[n])\,, \tag{A.16}$$

where $\mathsf{u}(\cdot)$ is the Heaviside step function defined in Eq. (3.6).

On the other hand, the intermediate length-K_l TD signal $\overline{\overline{\boldsymbol{s}}}_l$ generated using model 2 can be represented as

$$\begin{aligned}\overline{\overline{s}}_l[n'] &= \frac{1}{\sqrt{K_l}}\sum_{k=0}^{K_l-1}\overline{\overline{S}}_l[k]W_{K_l}^{kn'}\\ &\overset{(2.6)}{=\!=} \frac{1}{\sqrt{K_l}}\sum_{u=0}^{\frac{K_l}{4}-1}\left(S_l[u]W_{K_l}^{(2u+1)n'}+S_l^*[u]W_{K_l}^{[K_l-(2u+1)]n'}\right)\\ &\overset{(A.9)}{=\!=} \frac{1}{\sqrt{K_l}}\sum_{u=0}^{\frac{K_l}{4}-1}\left(S_l[u]W_{K_l}^{(2u+1)n'}+S_l^*[u]W_{K_l}^{-(2u+1)n'}\right),\end{aligned} \tag{A.17}$$

where the second equality is used for replacing $\overline{\overline{\boldsymbol{S}}}_l$ by the original symbol stream $\boldsymbol{S}_l$ of Fig. 2.6 using the loading rule of Eq. (2.9), while the last equality exploited the property of W_{K_l} similar to that of Eq. (A.9). The clipping process of $\boldsymbol{\bar{\bar{s}}}_l$ can be similarly modelled as

$$\left\lfloor \bar{\bar{s}} \right\rfloor_l [n'] = \bar{\bar{s}}_l[n'] \cdot \mathsf{u}\big(\bar{\bar{s}}_l[n']\big) \, . \tag{A.18}$$

In model 2, the final output signal $\boldsymbol{s}_l^{(2)}$ is obtained by repeating the length-K_l signal $\left\lfloor \boldsymbol{\bar{\bar{s}}} \right\rfloor_l$ up to a length of K, while attenuating (dividing) each sample's amplitude by $\sqrt{K/K_l}$ for energy conservation. Therefore, we have:

$$\begin{aligned} s_l^{(2)}[n] &= \frac{\sqrt{K_l}}{\sqrt{K}} \cdot \left\lfloor \bar{\bar{s}} \right\rfloor_l [\mathrm{mod}(n,\ K_l)] = \frac{\sqrt{K_l}}{\sqrt{K}} \cdot \left\lfloor \bar{\bar{s}} \right\rfloor_l [n - aK_l] \\ &= \frac{\sqrt{K_l}}{\sqrt{K}} \cdot \bar{\bar{s}}_l[n - aK_l] \cdot \mathsf{u}\big(\bar{\bar{s}}_l[n - aK_l]\big) \\ &= \frac{\sqrt{K_l}}{\sqrt{K}} \cdot \bar{\bar{s}}_l[n - aK_l] \cdot \mathsf{u}\left(\frac{\sqrt{K_l}}{\sqrt{K}} \cdot \bar{\bar{s}}_l[n - aK_l]\right) , \end{aligned} \tag{A.19}$$

where $\mathrm{mod}(n,\ K_l)$ is the modulo-K_l operator for n, and $a \in \mathbb{N}$ is the integer quotient of the Euclidean division $(n \div K_l)$, such that $0 \leq (n - aK_l) < K_l$, while the last equality is valid because multiplication by a positive number (in this case $1/\sqrt{K/K_l}$) does not change the sign of $\bar{\bar{s}}_l[n']$. Therefore, it does not change the value of the Heaviside function.

Meanwhile, we have:

$$\begin{aligned} & \frac{\sqrt{K_l}}{\sqrt{K}} \cdot \bar{\bar{s}}_l[n - aK_l] \\ &= \frac{\sqrt{K_l}}{\sqrt{K}} \cdot \frac{1}{\sqrt{K_l}} \sum_{u=0}^{\frac{K_l}{4}-1} \left(S_l[u] W_{K_l}^{(2u+1)(n-aK_l)} + S_l^*[u] W_{K_l}^{-(2u+1)(n-aK_l)} \right) \\ &= \frac{1}{\sqrt{K}} \sum_{u=0}^{\frac{K_l}{4}-1} \left(S_l[u] W_{K_l}^{(2u+1)n} W_1^{(2u+1)a} + S_l^*[u] W_{K_l}^{-(2u+1)n} W_1^{(2u+1)a} \right) \\ &= \frac{1}{\sqrt{K}} \sum_{u=0}^{\frac{K_l}{4}-1} \left(S_l[u] W_{K_l}^{(2u+1)n} + S_l^*[u] W_{K_l}^{-(2u+1)n} \right) \\ &\overset{\text{(A.21)}}{=\!=} \frac{1}{\sqrt{K}} \sum_{u=0}^{\frac{K_l}{4}-1} \left(S_l[u] W_K^{2^{l-1}(2u+1)n} + S_l^*[u] W_K^{-2^{l-1}(2u+1)n} \right) \\ &\overset{\text{(A.15)}}{=\!=} \bar{s}[n], \end{aligned} \tag{A.20}$$

In the penultimate equality, the denominator K_l in W_{K_l} is replaced by K according to (2.5), *i.e.*

$$W_{K_l} = e^{j\frac{2\pi}{K_l}} = e^{j\frac{2\pi}{K/2^{l-1}}} = e^{j\frac{2\pi}{K}2^{l-1}} = W_K^{2^{l-1}} . \tag{A.21}$$

Therefore,

$$s_l^{(2)}[n] = \bar{s}_l[n] \cdot \mathsf{u}(\bar{s}_l[n]) = s^{(1)}[n], \tag{A.22}$$

which concludes the proof. □

A.3 Lossless Clipping in LACO-OFDM

In this section, we provide the mathematical proof of the facts that in LACO-OFDM, the clipping distortion of each layer falls only on the null subcarriers *controlled* by the same layer. The kth subcarrier is *controlled* by layer l, if and only if we have:

$$\operatorname{mod}(k,\ 2^{l-1}) = 0. \tag{A.23}$$

It is worth mentioning that LACO-OFDM inherited these characteristics from ACO-OFDM. Therefore, these conclusions also apply to ACO-OFDM by letting $l = 1$.

Theorem A.3 (Lossless Clipping in LACO-OFDM)**.** *The clipping distortion of layer l in LACO-OFDM only falls onto the subcarriers indexed by*

$$k = u \cdot 2^l,\ 0 \le u \le \frac{K}{2^l} - 1. \tag{A.24}$$

Proof. The theorem mentioned above states the fact that no clipping distortion can be found on the rest of the subcarriers controlled by layer l, where

$$k' = u \cdot 2^l + 2^{l-1},\ 0 \le u \le \frac{K}{2^l} - 1. \tag{A.25}$$

The corresponding symbols on these subcarriers after clipping can be expressed as

$$\mathcal{F}\{\boldsymbol{s}_l\}\,[k'] = \frac{1}{\sqrt{K}} \sum_{n=0}^{K-1} s_l[n] W_K^{-k'n}. \tag{A.26}$$

If we segment the summation of Eq. (A.26) into $\frac{K}{K_l} = 2^{l-1}$ parts, each of which adds up K_l subcarriers, then we have:

$$\begin{aligned}\mathcal{F}\{\boldsymbol{s}_l\}\,[k'] = \frac{1}{\sqrt{K}} \Bigg(& \sum_{n=0}^{K_l-1} s_l[n] W_K^{-k'n} + \sum_{n=K_l}^{2K_l-1} s_l[n] W_K^{-k'n} + \dots \\ & + \sum_{n=bK_l}^{(b+1)K_l-1} s_l[n] W_K^{-k'n} + \dots + \sum_{n=K-K_l}^{K-1} s_l[n] W_K^{-k'n} \Bigg).\end{aligned} \tag{A.27}$$

Replacing n by $(n + bK_l)$ in the $(b + 1)$st summation yields

$$\begin{aligned}\mathcal{F}\{\boldsymbol{s}_l\}\,[k'] &= \sum_{b=0}^{2^{l-1}-1} \left[\frac{1}{\sqrt{K}} \sum_{n=0}^{K_l-1} \left(s_l[n + bK_l] W_K^{-k'(n+bK_l)} \right) \right] \\ &\overset{\text{(A.30)}}{=\!=} \frac{1}{\sqrt{K}} \sum_{n=0}^{K_l-1} \left[s_l[n] W_K^{-k'n} \left(\sum_{b=0}^{2^{l-1}-1} W_K^{-bk'K_l} \right) \right] \\ &\overset{\text{(A.29)}}{=\!=} \frac{B_{l,k'}}{\sqrt{K}} \sum_{n=0}^{K_l-1} s_l[n] W_K^{-k'n},\end{aligned} \tag{A.28}$$

where

$$B_{l,k'} = \sum_{b=0}^{2^{l-1}-1} W_K^{-bk'K_l} = \sum_{b=0}^{2^{l-1}-1} \exp\left[\frac{-bk'K_l}{K} \right] = \sum_{b=0}^{2^{l-1}-1} \exp\left[\frac{-bk'}{2^{l-1}} \right] \tag{A.29}$$

is a constant only dependent on l and k', thus can be taken outside. The second equality in Eq. (A.28) takes advantage of the repetition in the layer signal formulated as:

$$s_l[n] = s_l[n + K_l] = s_l[n + 2K_l] = \dots \tag{A.30}$$

The final summation in Eq. (A.28) can be further split into two parts as

$$\begin{aligned}\mathcal{F}\{\boldsymbol{s}_l\}\,[k'] &= \frac{B_{l,k'}}{\sqrt{K}} \left(\sum_{n=0}^{\frac{K_l}{2}-1} s_l[n] W_K^{-k'n} + \sum_{n=\frac{K_l}{2}}^{K_l-1} s_l[n] W_K^{-k'n} \right) \\ &= \frac{B_{l,k'}}{\sqrt{K}} \left(\sum_{n=0}^{\frac{K_l}{2}-1} s_l[n] W_K^{-k'n} + \sum_{n=0}^{\frac{K_l}{2}-1} s_l\left[\frac{K_l}{2} + n \right] W_K^{-k'\left(\frac{K_l}{2}+n\right)} \right) \\ &= \frac{B_{l,k'}}{\sqrt{K}} \left(\sum_{n=0}^{\frac{K_l}{2}-1} s_l[n] W_K^{-k'n} + \sum_{n=0}^{\frac{K_l}{2}-1} s_l\left[\frac{K_l}{2} + n \right] W_K^{-k'n} W_K^{-\frac{k'K_l}{2}} \right),\end{aligned} \tag{A.31}$$

where

$$\begin{aligned}W_K^{-\frac{k'K_l}{2}} &= \exp\left[-j\frac{2\pi}{K}\frac{k'K_l}{2} \right] \overset{\text{(A.25)}}{=\!=} \exp\left[-j\frac{2\pi}{K}\frac{(2^l u + 2^{l-1})(K/2^{l-1})}{2} \right] \\ &= \exp[-j\pi(2u+1)] \equiv -1,\ \forall u \in \mathbb{Z}.\end{aligned} \tag{A.32}$$

Bearing in mind that the this equality only holds when $(2u+1)$ is an odd number, namely that this only happens to fall on subcarriers loaded with the current layer's symbols or their conjugates, we have:

$$\mathcal{F}\{\boldsymbol{s}_l\}\,[k'] = \frac{B_{l,k'}}{\sqrt{K}} \sum_{n=0}^{\frac{K_l}{2}-1} \left(s_l[n] - s_l\left[\frac{K_l}{2} + n \right] \right) W_K^{-k'n}. \tag{A.33}$$

Given the asymmetry of ACO-OFDM signal specified in Sec. A.1, for each element in the summation of Eq. (A.33), either $s_l[n]$ or $s_l\left[\frac{K_l}{2}+n\right]$ should be zero.

- If we have $s_l\left[\frac{K_l}{2}+n\right]=0$, then $\overline{s}_l\left[\frac{K_l}{2}+n\right]$ in the unclipped signal $\overline{\boldsymbol{s}}_l$ must be negative and must have been clipped. Therefore, based on Eq. (A.3), $\overline{s}_l[n]$ should be positive and retained after clipping, yielding:

  $$s[n]=\overline{s}_l[n]=-\overline{s}_l\left[\frac{K_l}{2}+n\right]=\overline{s}_l\left[\frac{K_l}{2}+n\right]W_K^{-\frac{k'K_l}{2}}. \tag{A.34}$$

  Substituting this back to Eq. (A.33) gives

  $$\begin{aligned}
\mathcal{F}\{\boldsymbol{s}_l\}[k'] &= \frac{B_{l,k'}}{\sqrt{K}}\sum_{n=0}^{\frac{K_l}{2}-1} s_l[n]W_K^{-k'n} = \frac{B_{l,k'}}{2\sqrt{K}}\sum_{n=0}^{\frac{K_l}{2}-1}\left(s_l[n]+s_l[n]\right)W_K^{-k'n}\\
&= \frac{B_{l,k'}}{2\sqrt{K}}\sum_{n=0}^{\frac{K_l}{2}-1}\left(\overline{s}_l[n]+\overline{s}_l\left[\frac{K_l}{2}+n\right]W_K^{-\frac{k'K_l}{2}}\right)W_K^{-k'n}\\
&= \frac{B_{l,k'}}{2\sqrt{K}}\left(\sum_{n=0}^{\frac{K_l}{2}-1}\overline{s}_l[n]W_K^{-k'n}+\sum_{n=0}^{\frac{K_l}{2}-1}\overline{s}_l\left[\frac{K_l}{2}+n\right]W_K^{-k'\left(\frac{K_l}{2}+n\right)}\right)\\
&= \frac{B_{l,k'}}{2\sqrt{K}}\left(\sum_{n=0}^{\frac{K_l}{2}-1}\overline{s}_l[n]W_K^{-k'n}+\sum_{n=\frac{K_l}{2}}^{K_l-1}\overline{s}_l[n]W_K^{-k'n}\right)\\
&= \frac{B_{l,k'}}{2\sqrt{K}}\sum_{n=0}^{\frac{K_l}{2}-1}\overline{s}_l[n]W_K^{-k'n},
\end{aligned} \tag{A.35}$$

  where the equality on the 2nd line of Eq. (A.35) replaces the two $s_l[n]$s by $\overline{\boldsymbol{s}}_l$ and $\overline{s}_l\left[\frac{K_l}{2}+n\right]W_K^{-\frac{k'K_l}{2}}$, respectively, according to Eq. (A.34), while the equality on the 4th line of Eq. (A.35) substitutes n in the second summation by $\left(n-\frac{K_l}{2}\right)$. Substituting $B_{l,k'}$ back into the summation can expand the summation range back up to $(K-1)$:

  $$\begin{aligned}
\mathcal{F}\{\boldsymbol{s}_l\}[k'] &= \frac{1}{2}\frac{1}{\sqrt{K_l}}\sum_{n=0}^{\frac{K_l}{2}-1}\overline{s}_l[n]W_K^{-k'n}B_{l,k'}\\
&= \frac{1}{2}\frac{1}{\sqrt{K_l}}\sum_{n=0}^{\frac{K_l}{2}-1}\left(\overline{s}_l[n]W_K^{-k'n}\sum_{b=0}^{2^{l-1}-1}W_K^{-bk'K_l}\right)\\
&= \frac{1}{2}\frac{1}{\sqrt{K_l}}\sum_{b=0}^{2^{l-1}-1}\sum_{n=0}^{\frac{K_l}{2}-1}\overline{s}_l[n+bK_l]W_K^{-k'(n+bK_l)}\\
&= \frac{1}{2}\frac{1}{\sqrt{K}}\sum_{n=0}^{K-1}\overline{s}_l[n]W_K^{-k'n}=\frac{1}{2}\overline{\boldsymbol{S}}_l[k'].
\end{aligned} \tag{A.36}$$

- If $s_l[n] = 0$, we can arrive at

$$-\, s_l\left[\frac{K_l}{2}+n\right] = -\overline{\boldsymbol{s}}_l\left[\frac{K_l}{2}+n\right] = \overline{\boldsymbol{s}}_l\left[\frac{K_l}{2}+n\right] W_K^{-\frac{k'K_l}{2}} = \overline{\boldsymbol{s}}_l[n]. \tag{A.37}$$

Substituting this back into Eq. (A.33) leads to

$$\begin{aligned}\mathcal{F}\{\boldsymbol{s}_l\}\left[k'\right] &= \frac{B_{l,k'}}{\sqrt{K}} \sum_{n=0}^{\frac{K_l}{2}-1} \left(-s_l\left[\frac{K_l}{2}+n\right]\right) W_K^{-k'n} \\ &= \frac{B_{l,k'}}{2\sqrt{K}} \sum_{n=0}^{\frac{K_l}{2}-1} \left(\overline{s}_l[n] + \overline{s}_l\left[\frac{K_l}{2}+n\right] W_K^{-\frac{k'K_l}{2}}\right) W_K^{-k'n},\end{aligned} \tag{A.38}$$

which takes the track of the maths back to that of Eq. (A.35) in the previous case, because the result is the same as the second line of Eq. (A.35). Naturally, the same conclusion as Eq. (A.36) can be given.

It has now been shown that only the subcarriers with indices k' satisfying Eq. (A.25) have their energy halved after the clipping process, with no information loss observed. Therefore, the clipping distortion can only fall onto other subcarriers controlled by the layer, which follows the rule of Eq. (A.24). □

Appendix B

Probability Distribution of LACO-OFDM Signals

B.1 Probability Distribution of the Sum of Independent Signals

In this section, we review the derivation of the PDF of the signal $\boldsymbol{x}_L$, which is the sum of L independent signals $\{\boldsymbol{s}_1, \boldsymbol{s}_2, \ldots, \boldsymbol{s}_l, \ldots, \boldsymbol{s}_L\}$. The variables $x_L[k]$ and $s_l[k]$ represent general symbols within the signals $\boldsymbol{x}_L$ and $\boldsymbol{s}_l$, obeying their own probability distributions denoted by $f_{\boldsymbol{x}_L}(z)$ and $f_{\boldsymbol{s}_l}(z)$, respectively. Meanwhile, the cumulative distribution function (CDF) of the signal $\boldsymbol{x}_L$ is expressed as

$$F_{\boldsymbol{x}_L}(z) = \Pr(x[k] \leq z) = \int_{-\infty}^{z} f_{\boldsymbol{x}_L}(z')\,\mathrm{d}z'. \tag{B.1}$$

We start from the simplest situation, where only two signals are added up, before extending the analysis in multi-variable scenarios.

B.1.1 Sum of Two Signals

When $L = 2$, the elements in the sum signal are

$$x_2[k] = s_1[k] + s_2[k]. \tag{B.2}$$

Due to their mutual independency, the joint probability density function obeys

$$f_{\boldsymbol{s}_1,\boldsymbol{s}_2}(z_1, z_2) = f_{\boldsymbol{s_1}}(z_1) \cdot f_{\boldsymbol{s_2}}(z_2)\,. \tag{B.3}$$

Therefore, the CDF of $\boldsymbol{x}_2$ is formulated as:

$$\begin{aligned}
F_{\boldsymbol{x}_2}(z) &= \Pr(x_2[k] \leq z) = \Pr(s_1[k] + s_2[k] \leq z) \\
&= \iint\limits_{s_1[k]+s_2[k]\leq z} f_{\boldsymbol{s}_1,\boldsymbol{s}_2}(z_1, z_2)\,\mathrm{d}z_1\mathrm{d}z_2 \\
&= \int_{z_1=-\infty}^{z_1=\infty} \left(f_{\boldsymbol{s_1} z_1}(z) \int_{z_2=-\infty}^{z_2=z-z_1} f_{\boldsymbol{s_2}}(z)\,\mathrm{d}z_2 \right) \mathrm{d}z_1 .
\end{aligned} \tag{B.4}$$

Therefore, the PDF of $\boldsymbol{x}_2$ is

$$\begin{aligned}
f_{\boldsymbol{x}_2}(z) = \frac{\mathrm{d}F_{\boldsymbol{x}_2}(z)}{\mathrm{d}z} &= \frac{\mathrm{d}}{\mathrm{d}z} \int_{z_1=-\infty}^{z_1=\infty} \left(f_{\boldsymbol{s_1}}(z_1) \int_{z_2=-\infty}^{z_2=z-z_1} f_{\boldsymbol{s_2}}(z)\,\mathrm{d}z_2 \right) \mathrm{d}z_1 \\
&= \int_{z_1=-\infty}^{z_1=\infty} \left(f_{\boldsymbol{s_1}}(z_1) \frac{\mathrm{d}}{\mathrm{d}z} \int_{z_2=-\infty}^{z_2=z-z_1} f_{\boldsymbol{s_2}}(z)\,\mathrm{d}z_2 \right) \mathrm{d}z_1 \\
&= \int_{-\infty}^{\infty} f_{\boldsymbol{s}_1}(z_1) \cdot f_{\boldsymbol{s}_2}(z - z_1)\,\mathrm{d}z_1 \\
&= f_{\boldsymbol{s}_1}(z) \otimes f_{\boldsymbol{s}_2}(z)\,,
\end{aligned} \tag{B.5}$$

where $\otimes$ represents the convolution.

This indicates that the PDF of the sum of two independent signals is given by the convolution of their own PDFs.

B.1.2 Sum of Three or More Signals

For $L \geq 3$, we have to consolidate the sum of the first $L-1$ signals as $\boldsymbol{x}_{L-1}$, *i.e.*

$$x_L[k] = (s_1[k] + \ldots s_{L-1}[k]) + s_L[k] = x_{L-1}[k] + s_L[k], \tag{B.6}$$

which leads to the PDF expression of

$$f_{\boldsymbol{x}_L}(z) = \Pr(x_{L-1}[k] + s_L[k] = z) = f_{\boldsymbol{x}_{L-1}}(z) \otimes f_{\boldsymbol{s}_L}(z)\,, \tag{B.7}$$

while

$$f_{\boldsymbol{x}_{L-1}}(z) = \Pr(x_{L-2}[k] + s_{L-1}[k] = z) = f_{\boldsymbol{x}_{L-2}}(z) \otimes f_{\boldsymbol{s}_{L-1}}(z)\,. \tag{B.8}$$

Recursively, we have:

$$\begin{aligned}
f_{\boldsymbol{x}_L}(z) &= f_{\boldsymbol{x}_{L-1}}(z) \otimes f_{\boldsymbol{s}_L}(z) \\
&= f_{\boldsymbol{x}_{L-2}}(z) \otimes f_{\boldsymbol{s}_{L-1}}(z) \otimes f_{\boldsymbol{s}_L}(z) \\
&= \cdots \\
&= f_{\boldsymbol{s}_1}(z) \otimes \cdots \otimes f_{\boldsymbol{s}_{L-1}}(z) \otimes f_{\boldsymbol{s}_L}(z)\,.
\end{aligned} \tag{B.9}$$

This indicates that the PDF of the sum of multiple independent signals is the convolution of all of their own PDFs.

B.2 PDF of 2-layer LACO-OFDM Signal

In this section, we provide the mathematical PDF derivation for a LACO-OFDM signal composed of 2 layers, denoted as $\boldsymbol{x}_2$.

$$\begin{aligned}
f_{\boldsymbol{x}_2}(z) &= \int_{-\infty}^{+\infty} f_{\boldsymbol{s}_1}(z_1)\, f_{\boldsymbol{s}_2}(z-z_1)\,\mathrm{d}z_1 \\
&= \int_{-\infty}^{+\infty} \left[\frac{\delta(z_1)}{2} + \phi\big(z_1;\sigma_1^2\big)\,\mathsf{u}(z_1)\right] \left[\frac{\delta(z-z_1)}{2} + \phi\left(z-z_1;\frac{\sigma_1^2}{2}\right)\mathsf{u}(z-z_1)\right]\mathrm{d}z_1 \\
&= \int_{-\infty}^{+\infty} \left[\frac{\delta(z_1)\delta(z-z_1)}{4} + \frac{\delta(z_1)}{2}\phi\left(z-z_1;\frac{\sigma_1^2}{2}\right)\mathsf{u}(z-z_1) + \right. \\
&\qquad \left. \frac{\delta(z-z_1)}{2}\phi\big(z_1;\sigma_1^2\big)\,\mathsf{u}(z_1) + \phi\big(z_1;\sigma_1^2\big)\,\mathsf{u}(z_1)\phi\left(z-z_1;\frac{\sigma_1^2}{2}\right)\mathsf{u}(z-z_1)\right]\mathrm{d}z_1 \\
&= \frac{\delta(z)}{4} + \frac{1}{2}\phi\big(z;\sigma_1^2\big)\,\mathsf{u}(z) + \frac{1}{2}\phi\left(z;\frac{\sigma_1^2}{2}\right)\mathsf{u}(z) + \int_0^z \phi\big(z_1;\sigma_1^2\big)\,\phi\left(z-z_1;\frac{\sigma_1^2}{2}\right)\mathrm{d}z_1 \\
&= \frac{\delta(z)}{4} + \frac{1}{2}\phi\big(z;\sigma_1^2\big)\,\mathsf{u}(z) + \frac{1}{2}\phi\left(z;\frac{\sigma_1^2}{2}\right)\mathsf{u}(z) + \\
&\qquad \phi\left(z;\frac{3\sigma_1^2}{2}\right)\left[\Phi\left(\frac{z}{\sqrt{3}\sigma_1}\right) + \Phi\left(\frac{z}{\sqrt{3}\sigma_1/2}\right) - 1\right]\mathsf{u}(z),
\end{aligned} \tag{B.10}$$

where

$$\Phi(x) = \frac{1}{\sqrt{2\pi}}\int_{-\infty}^{x} e^{-t^2/2}\,\mathrm{d}t \tag{B.11}$$

is the CDF of the standard Gaussian distribution.

With a clipping threshold B_u ($B_\mathrm{u} > 0$), the additional pulse $\mathcal{D}_2\delta(z - B_\mathrm{u})$ in the PDF of the UB-clipped signal $\lceil \boldsymbol{x} \rceil_2$ will be

$$\begin{aligned}
\mathcal{D}_2 &= \int_{B_\mathrm{u}}^{+\infty} f_{\boldsymbol{x}_2}(z)\,\mathrm{d}z \\
&= \int_{B_\mathrm{u}}^{+\infty} \left\{\frac{\delta(z)}{4} + \frac{1}{2}\phi\big(z;\sigma_1^2\big)\,\mathsf{u}(z) + \frac{1}{2}\phi\left(z;\frac{\sigma_1^2}{2}\right)\mathsf{u}(z)\right\}\mathrm{d}z + \\
&\qquad \int_{B_\mathrm{u}}^{+\infty} \left\{\phi\left(z;\frac{3\sigma_1^2}{2}\right)\left[\Phi\left(\frac{z}{\sqrt{3}\sigma_1}\right) + \Phi\left(\frac{z}{\sqrt{3}\sigma_1/2}\right) - 1\right]\mathsf{u}(z)\right\}\mathrm{d}z \\
&= 1 - \frac{1}{2}\Phi\left(\frac{B_\mathrm{u}}{\sigma_1}\right) - \frac{1}{2}\Phi\left(\frac{B_\mathrm{u}}{\sigma_1/\sqrt{2}}\right) - \Phi\left(\frac{B_\mathrm{u}}{\sigma_1/\sqrt{2/3}}\right) + \\
&\qquad \int_{B_\mathrm{u}}^{+\infty} \left[\phi\left(z;\frac{3\sigma_1^2}{2}\right)\Phi\left(\frac{z}{\sqrt{3}\sigma_1}\right) + \phi\left(z;\frac{3\sigma_1^2}{2}\right)\Phi\left(\frac{z}{\sqrt{3}\sigma_1/2}\right)\right]\mathrm{d}z.
\end{aligned} \tag{B.12}$$

Due to the involvement of the term on the last line of (3.19), it is unfortunately impossible to obtain the closed form of $\mathcal{D}_2$.

List of Acronyms

AWGN	Additive White Gaussian Noise
BER	Bit Error Ratio
CC	Convolutional Code
CCDF	Complementary Cumulative Distribution Function
CCMC	Continuous-input Continuous-output Memoryless Channel
CDF	Cumulative Distribution Function
CMA	Complex Multiplications and Additions
CP	Cyclic Prefix
CS	Compressed Sensing
DC	Direct Current
DCMC	Continuous-input Discrete-output Memoryless Channel
DD	Direct Detection
DHT	Discrete Hartley Transform
EVM	Error Vector Magnitude
FD	Frequency Domain
FEC	Forward Error Correction
FFT	Fast Fourier Transform
FSO	Free-Space Optical communication
HD	Hard Decision
HetNet	Heterogeneous Networks
IDFT	Inverse Discrete Fourier Transform
IFFT	Inverse FFT
ILI	Inter-Layer Interference
IM	Intensity Modulation
LB	Lower Bound
LBC	LB Clipping
LLR	Log-Likelihood Ratio
MILP	Mixed Integer Linear Programming
MIMO	Multiple-Input Multiple-Output

MMSE	Minimum Mean Square Estimation
MU-MIMO	MultiUser MIMO
NOMA	Non-Orthogonal Multiple Access
OFDM	Orthogonal Frequency Division Multiplexing
O-OFDM	Optical OFDM
ACO-OFDM	Asymmetrically Clipped O-OFDM
DCO-OFDM	DC-Biased O-OFDM
LACO-OFDM	Layered ACO-OFDM
ADO-OFDM	Asymmetrically clipped DC biased O-OFDM
HACO-OFDM	Hybrid ACO-OFDM
ASCO-OFDM	Asymmetrically and Symmetrically Clipped O-OFDM
AVO-OFDM	Absolute Value O-OFDM
AAO-OFDM	Asymmetrically clipped AVO-OFDM
EACO-OFDM	Enhanced ACO-OFDM
SEE-OFDM	Spectral and Energy Efficient OFDM
OMA	Orthogonal Multiple Access
OWC	Optical Wireless Communications
PAM-DMT	Pulse-Amplitude-Modulated Discrete MultiTone modulation
PD	PhotoDiode
PE	Power Efficiency
PLC	Power Line Communications
QAM	Quadratic Amplitude Modulation
QoS	Quality of Service
RSC	Recursive Systematic Convolutional (code)
RX	Receiver/Receiving
SCFDM	Single-Carrier FD Multiplexing
SE	Spectrum Efficiency
SIC	Serial Interference Cancellation
SINR	Signal-to-Interference-and-Noise power Ratio
SISO	Soft-In Soft-Out
SNR	Signal-to-Noise power Ratio
TC	Turbo Code
TD	Time Domain
TI	Tone Injection
TX	Transmitter/Transmitting
UB	Upper Bound
UBC	UB Clipping
VLC	Visible Light Communications

Bibliography

[1] X. Zhang, Q. Wang, R. Zhang, S. Chen, and L. Hanzo, “Performance analysis of layered ACO-OFDM,” *IEEE Access*, vol. 5, pp. 18 366–18 381, 2017.

[2] X. Zhang, Z. Babar, S. Chen, and L. Hanzo, “Multi-class coded layered asymmetrically clipped optical OFDM,” *IEEE Trans. Commun.*, vol. 67, no. 1, pp. 578–589, Jan. 2019.

[3] Z. Babar, X. Zhang, P. Botsinis, D. Alanis, D. Chandra, S. X. Ng, and L. Hanzo, “Near-capacity multilayered code design for LACO-OFDM-aided optical wireless systems,” *IEEE Trans. Veh. Technol.*, vol. 68, no. 4, pp. 4051–4054, Apr. 2019.

[4] L. Hanzo, H. Haas, S. Imre, D. O’Brien, M. Rupp, and L. Gyongyosi, “Wireless myths, realities, and futures: From 3G/4G to optical and quantum wireless,” *Proc. IEEE*, vol. 100, no. Special Centennial Issue, pp. 1853–1888, May 2012.

[5] S. Dimitrov and H. Haas, *Principles of LED light communications: towards networked Li-Fi.* Cambridge, UK: Cambridge University Press, 2015.

[6] H. Elgala, R. Mesleh, and H. Haas, “Indoor optical wireless communication: Potential and state-of-the-art,” *IEEE Commun. Mag.*, vol. 49, no. 9, pp. 56–62, Sep. 2011.

[7] Z. Wang, Q. Wang, W. Huang, and Z. Xu, *Visible light communications: Modulation and signal processing.* Hoboken, New Jersey: Wiley-IEEE Press, 2018.

[8] P. H. Pathak, X. Feng, P. Hu, and P. Mohapatra, “Visible light communication, networking, and sensing: A survey, potential and challenges,” *IEEE Commun. Surv. Tuts.*, vol. 17, no. 4, pp. 2047–2077, 4th Quart. 2015.

[9] F. Jin, R. Zhang, and L. Hanzo, “Resource allocation under delay-guarantee constraints for heterogeneous visible-light and RF femtocell,” *IEEE Trans. Wireless Commun.*, vol. 14, no. 2, pp. 1020–1034, 2014.

[10] X. Li, R. Zhang, and L. Hanzo, "Cooperative load balancing in hybrid visible light communications and WiFi," *IEEE Trans. Commun.*, vol. 63, no. 4, pp. 1319–1329, Apr. 2015.

[11] X. Li, R. Zhang, J. Wang, and L. Hanzo, "Cell-centric and user-centric multi-user scheduling in visible light communication aided networks," in *Proc. 2015 IEEE Int. Conf. Commun. (ICC)*, London, UK, Jun. 2015, pp. 5120–5125.

[12] X. Li, F. Jin, R. Zhang, J. Wang, Z. Xu, and L. Hanzo, "Users first: User-centric cluster formation for interference-mitigation in visible-light networks," *IEEE Trans. Wireless Commun.*, vol. 15, no. 1, pp. 39–53, Jan. 2015.

[13] F. Jin, X. Li, R. Zhang, C. Dong, and L. Hanzo, "Resource allocation under delay-guarantee constraints for visible-light communication," *IEEE Access*, vol. 4, pp. 7301–7312, 2016.

[14] X. Li, F. Jin, R. Zhang, and L. Hanzo, "Joint cluster formation and user association under delay guarantees in visible-light networks," in *2016 IEEE Global Commun. Conf. (GLOBECOM)*, Washington, DC, USA, Dec. 2016, pp. 1–6.

[15] X. Li, Y. Huo, R. Zhang, and L. Hanzo, "User-centric visible light communications for energy-efficient scalable video streaming," *IEEE Trans. Green Commun. Netw.*, vol. 1, no. 1, pp. 59–73, Mar. 2017.

[16] X. Li, R. Zhang, and L. Hanzo, "Optimization of visible-light optical wireless systems: Network-centric versus user-centric designs," *IEEE Commun. Surv. Tuts.*, vol. 20, no. 3, pp. 1878–1904, 3rd Quart. 2018.

[17] R. W. Chang, "Orthogonal frequency multiplex data transmission system," Jan. 1970, uS Patent 3,488,445.

[18] J. Salz and S. Weinstein, "Fourier transform communication system," in *Proc. 1st ACM Symp. Problems Optim. Data Commun. Syst.* Pine Mountain, GA: ACM, Oct. 1969, pp. 99–128.

[19] A. Peled and A. Ruiz, "Frequency domain data transmission using reduced computational complexity algorithms," in *Proc. '80 ICASSP*, vol. 5, Denver, CO, 1980, pp. 964–967.

[20] L. Cimini, "Analysis and simulation of a digital mobile channel using orthogonal frequency division multiplexing," *IEEE Trans. Commun.*, vol. 33, no. 7, pp. 665–675, Jul. 1985.

[21] R. Lassalle and M. Alard, "Principles of modulation and channel coding for digital broadcasting for mobile receivers," *EBU Tech. Rev*, vol. 224, no. 1, pp. 68–190, 1987.

[22] J. Armstrong, "OFDM for optical communications," *J. Lightw. Technol.*, vol. 27, no. 3, pp. 189–204, Feb. 2009.

[23] S. Feng, X. Li, R. Zhang, M. Jiang, and L. Hanzo, "Hybrid positioning aided amorphous-cell assisted user-centric visible light downlink techniques," *IEEE Access*, vol. 4, pp. 2705–2713, 2016.

[24] S. Feng, R. Zhang, X. Li, Q. Wang, and L. Hanzo, "Dynamic throughput maximization for the user-centric visible light downlink in the face of practical considerations," *IEEE Trans. Wireless Commun.*, vol. 17, no. 8, pp. 5001–5015, Aug. 2018.

[25] J. M. Kahn and J. R. Barry, "Wireless infrared communications," *Proc. IEEE*, vol. 85, no. 2, pp. 265–198, Feb. 1997.

[26] J. Zhou, Y. Yan, Z. Cai, Y. Qiao, and Y. Ji, "A cost-effective and efficient scheme for optical OFDM in short-range IM/DD systems," *IEEE Photon. Technol. Lett.*, vol. 26, no. 13, pp. 1372–1374, Jul. 2014.

[27] J. B. Carruthers and J. M. Kahn, "Multiple-subcarrier modulation for nondirected wireless infrared communication," *IEEE J. Sel. Areas Commun.*, vol. 14, no. 3, pp. 538–546, Apr. 1996.

[28] O. Gonzalez, R. Perez-Jimenez, S. Rodriguez, J. Rabadan, and A. Ayala, "OFDM over indoor wireless optical channel," *IEE Proc. - Optoelectronics*, vol. 152, no. 4, pp. 199–204, Aug. 2005.

[29] J. Armstrong and A. J. Lowery, "Power efficient optical OFDM," *Electron. Lett.*, vol. 42, no. 6, 2006.

[30] J. Armstrong and B. J. C. Schmidt, "Comparison of asymmetrically clipped optical OFDM and DC-biased optical OFDM in AWGN," *IEEE Commun. Lett.*, vol. 12, no. 5, pp. 343–345, May 2008.

[31] N. Cvijetic, D. Qian, and T. Wang, "10Gb/s Free-Space Optical Transmission using OFDM," in *Proc. 2008 OFC/NFOEC Conf. Opt. Fiber Commun./Nat. Fiber Opt. Eng. Conf.*, San Diego, CA, Feb 2008, pp. 1–3.

[32] Z. Lu, P. Liu, and S. Liu, "Experiment of beneficial clipping dco-ofdm based visible light communication," in *Proc. 2017 IEEE 9th Int. Conf. Commun. Softw. Netw. (ICCSN)*, Guangzhou, China, May 2017, pp. 615–618.

[33] T. Jiang, M. Tang, R. Lin, Z. Feng, X. Chen, L. Deng, S. Fu, X. Li, W. Liu, and D. Liu, "Investigation of DC-biased optical OFDM With precoding matrix for visible light communications: Theory, simulations, and experiments," *IEEE Photon. J.*, vol. 10, no. 5, pp. 1–16, Oct. 2018.

[34] J. M. Tang, P. M. Lane, and K. A. Shore, "Transmission performance of adaptively modulated optical OFDM signals in multimode fiber links," *IEEE Photon. Technol. Lett.*, vol. 18, no. 1, pp. 205–207, Jan. 2006.

[35] B. Song, B. Corcoran, Q. Wang, and A. J. Lowery, "Field-trial of layered/enhanced ACO-OFDM," in *Proc. 2017 Eur. Conf. Opt. Commun. (ECOC)*, Gothenburg, Sweden, Sep. 2017, pp. 1–3.

[36] J. Armstrong, B. J. C. Schmidt, D. Kalra, H. A. Suraweera, and A. J. Lowery, "Performance of asymmetrically clipped optical OFDM in AWGN for an intensity modulated direct detection system," in *Proc. IEEE Glob. Commun. Conf.*, San Francisco, CA, USA, Nov. 2006, pp. 1–5.

[37] S. Dimitrov, S. Sinanovic, and H. Haas, "Clipping Noise in OFDM-Based Optical Wireless Communication Systems," *IEEE Trans. Commun.*, vol. 60, no. 4, pp. 1072–1081, Apr. 2012.

[38] A. H. Azhar and D. O'Brien, "Experimental comparisons of optical OFDM approaches in visible light communications," in *Proc. 2013 IEEE GLOBECOM Workshops (GC Wkshps)*, Atlanta, GA, USA, Dec. 2013, pp. 1076–1080.

[39] Y. Wang, Y. Wang, and N. Chi, "Experimental verification of performance improvement for a gigabit wavelength division multiplexing visible light communication system utilizing asymmetrically clipped optical orthogonal frequency division multiplexing," *Photon. Res.*, vol. 2, no. 5, pp. 138–142, Oct. 2014.

[40] M. Tahar, T. Q. Wang, M. F. G. Medina, O. Gonzalez, and J. Armstrong, "Experimental demonstration of diversity combining for asymmetrically clipped optical OFDM," *IEEE Commun. Lett.*, vol. 20, no. 5, pp. 906–909, May 2016.

[41] S. Lee, S. Randel, F. Breyer, and A. Koonen, "PAM-DMT for intensity-modulated and direct-detection optical communication systems," *IEEE Photon. Technol. Lett.*, vol. 21, no. 23, pp. 1749–1751, Dec. 2009.

[42] D. J. Barros, S. K. Wilson, and J. M. Kahn, "Comparison of orthogonal frequency-division multiplexing and pulse-amplitude modulation in indoor optical wireless links," *IEEE Trans. Commun.*, vol. 60, no. 1, pp. 153–163, Jan. 2011.

[43] N. Fernando, Y. Hong, and E. Viterbo, "Flip-OFDM for unipolar communication systems," *IEEE Trans. Commun.*, vol. 60, no. 12, pp. 3726–3733, Dec. 2012.

[44] D. Tsonev, S. Sinanovic, and H. Haas, "Novel unipolar orthogonal frequency division multiplexing (U-OFDM) for optical wireless," in *Proc. IEEE 75th Veh. Technol. Conf. (VTC Spring)*, Yokohama, Japan, May 2012, pp. 1–5.

[45] S. Lu, I. A. Hemadeh, M. El-Hajjar, and L. Hanzo, "Compressed-sensing-aided space-time frequency index modulation," *IEEE Trans. Veh. Technol.*, vol. 67, no. 7, pp. 6259–6271, Jul. 2018.

[46] S. Lu, M. El-Hajjar, and L. Hanzo, "Two-dimensional index modulation for the large-scale multi-user MIMO uplink," *IEEE Trans. Veh. Technol.*, vol. 68, no. 8, pp. 7904–7918, Aug. 2019.

[47] S. D. Dissanayake, K. Panta, and J. Armstrong, "A novel technique to simultaneously transmit ACO-OFDM and DCO-OFDM in IM/DD systems," in *Proc. 2011 IEEE Glob. Commun. Conf. Workshop*, Houston, TX, USA, Dec. 2011, pp. 782–786.

[48] S. D. Dissanayake and J. Armstrong, "Comparison of ACO-OFDM, DCO-OFDM and ADO-OFDM in IM/DD systems," *J. Lightw. Technol.*, vol. 31, no. 7, pp. 1063–1072, Apr. 2013.

[49] B. Ranjha and M. Kavehrad, "Hybrid asymmetrically clipped OFDM-based IM/DD optical wireless system," *J. Opt. Commun. Netw.*, vol. 6, no. 4, pp. 387–396, Apr. 2014.

[50] Q. Wang, Z. Wang, and L. Dai, "Asymmetrical hybrid optical ofdm for visible light communications with dimming control," *IEEE Photon. Technol. Lett.*, vol. 27, no. 9, pp. 974–977, May 2015.

[51] N. Wu and Y. Bar-Ness, "A novel power-efficient scheme asymmetrically and symmetrically clipping optical (ASCO)-OFDM for IM/DD optical systems," *EURASIP J. Adv. Signal Process.*, vol. 2015, no. 3, pp. 1–10, Jan. 2015.

[52] R. Bai, Q. Wang, and Z. Wang, "Asymmetrically clipped absolute value optical OFDM for intensity-modulated direct-detection systems," *J. Lightw. Technol.*, vol. 35, no. 17, pp. 3680–3691, Sep. 2017.

[53] Q. Wang, C. Qian, X. Guo, Z. Wang, D. G. Cunningham, and I. H. White, "Layered ACO-OFDM for intensity-modulated direct-detection optical wireless transmission," *Opt. Express*, vol. 23, no. 9, pp. 12 382–12 393, May 2015.

[54] H. Elgala and T. D. C. Little, "SEE-OFDM: Spectral and energy efficient OFDM for optical IM/DD systems," in *Proc. 2014 IEEE 25th Annu. Int. Symp. Pers. Indoor Mobile Radio Commun. (PIMRC)*, Washington, DC, USA, 2014, pp. 851–855.

[55] M. S. Islim, D. Tsonev, and H. Haas, "On the superposition modulation for OFDM-based optical wireless communication," in *Proc. 2015 IEEE Global Conf. Signal Inf. Process. (GlobalSIP)*, Orlando, FL, USA, 2015, pp. 1022–1026.

[56] Q. Wang, Z. Wang, X. Guo, and L. Dai, "Improved receiver design for layered ACO-OFDM in optical wireless communications," *IEEE Photon. Technol. Lett.*, vol. 28, no. 3, pp. 319–322, Feb. 2016.

[57] A. J. Lowery, “Enhanced asymmetrically clipped optical ODFM for high spectral efficiency and sensitivity,” in *Proc. 2016 Opt. Fiber Commun. Conf. Exhib. (OFC)*, Anaheim, CA, USA, 2016, pp. 1–3.

[58] T. Q. Wang, H. Li, and X. Huang, “Diversity combining for layered asymmetrically clipped optical OFDM using soft successive interference cancellation,” *IEEE Commun. Lett.*, vol. 21, no. 6, pp. 1309–1312, Jun. 2017.

[59] M. A. Mohammed, C. He, and J. Armstrong, “Diversity combining in layered asymmetrically clipped optical OFDM,” *J. Lightw. Technol.*, vol. 35, no. 11, pp. 2078–2085, Jun. 2017.

[60] Y. Sun, F. Yang, and J. Gao, “Comparison of hybrid optical modulation schemes for visible light communication,” *IEEE Photon. J.*, vol. 9, no. 3, pp. 1–13, Jun. 2017.

[61] B. Song, B. Corcoran, Q. Wang, L. Zhuang, and A. J. Lowery, “Subcarrier pairwise coding for short-haul L/E-ACO-OFDM,” *IEEE Photon. Technol. Lett.*, vol. 29, no. 18, pp. 1584–1587, 2017.

[62] F. Yang, Y. Sun, and J. Gao, “Adaptive LACO-OFDM with variable layer for visible light communication,” *IEEE Photon. J.*, vol. 9, no. 6, pp. 1–8, 2017.

[63] J. Zhou, Q. Wang, Q. Cheng, M. Guo, Y. Lu, A. Yang, and Y. Qiao, “Low-PAPR layered/enhanced ACO-SCFDM for optical-wireless communications,” *IEEE Photon. Technol. Lett.*, vol. 30, no. 2, pp. 165–168, 2018.

[64] J. Zhou and W. Zhang, “A comparative study of unipolar OFDM schemes in Gaussian optical intensity channel,” *IEEE Trans. Commun.*, vol. 66, no. 4, pp. 1549–1564, 2018.

[65] T. Q. Wang, H. Li, and X. Huang, “Interference cancellation for layered asymmetrically clipped optical OFDM with application to optical receiver design,” *J. Lightw. Technol.*, vol. 36, no. 11, pp. 2100–2113, 2018.

[66] Y. Sun, F. Yang, and L. Cheng, “An overview of OFDM-based visible light communication systems from the perspective of energy efficiency versus spectral efficiency,” *IEEE Access*, vol. 6, pp. 60 824–60 833, 2018.

[67] T. Q. Wang, H. Li, and X. Huang, “Analysis and mitigation of clipping noise in layered ACO-OFDM based visible light communication systems,” *IEEE Trans. Commun.*, vol. 67, no. 1, pp. 564–577, 2019.

[68] S. Feng, R. Zhang, W. Xu, and L. Hanzo, “Multiple access design for ultra-dense VLC networks: orthogonal vs non-orthogonal,” *IEEE Trans. Commun.*, vol. 67, no. 3, pp. 2218–2232, 2019.

[69] H. Li, Z. Huang, Y. Xiao, S. Zhan, and Y. Ji, “A power and spectrum efficient NOMA scheme for VLC network based on hierarchical rre-distorted LACO-OFDM,” *IEEE Access*, vol. 7, pp. 48 565–48 571, 2019.

[70] M. S. Islim, D. Tsonev, and H. Haas, “Spectrally enhanced PAM-DMT for IM/DD optical wireless communications,” in *Proc. 2015 IEEE 26th Annu. Int. Symp. Pers. Indoor Mobile Radio Commun. (PIMRC).* Hong Kong, China: IEEE, 30 Aug.–2 Sep. 2015, pp. 877–882.

[71] A. Goldsmith, *Wireless Communications*, 1st ed. New York: Cambridge University Press, 2005.

[72] H. Ochiai and H. Imai, “On the distribution of the peak-to-average power ratio in OFDM signals,” *IEEE Trans. Commun.*, vol. 49, no. 2, pp. 282–289, Feb. 2001.

[73] S. H. Han and J. H. Lee, “An overview of peak-to-average power ratio reduction techniques for multicarrier transmission,” *IEEE Wireless Commun.*, vol. 12, no. 2, pp. 56–65, Apr. 2005.

[74] N. Jacklin and Z. Ding, “A linear programming based tone injection algorithm for PAPR reduction of OFDM and linearly precoded systems,” *IEEE Trans. Circuits Syst. I Regul. Pap.*, vol. 60, no. 7, pp. 1937–1945, Jul. 2013.

[75] J. Wang, Y. Xu, X. Ling, R. Zhang, Z. Ding, and C. Zhao, “PAPR anlaysis for OFDM visible light communication,” *Opt. Express*, vol. 24, no. 24, pp. 27 457–27 474, Nov. 2016.

[76] B. Li, W. Xu, H. Zhang, C. Zhao, and L. Hanzo, “PAPR reduction for hybrid ACO-OFDM aided IM/DD optical wireless vehicular communications,” *IEEE Trans. Veh. Technol.*, vol. 66, no. 10, pp. 9561–9566, Oct. 2017.

[77] V. J. Francis, “On the distribution of the sum of n sample values drawn from a truncated normal population,” *Suppl. to J. R. Stat. Soc.*, vol. 8, no. 2, pp. 223–232, 1946.

[78] N. C. Beaulieu, “An infinite series for the computation of the complementary probability distribution function of a sum of independent random variables and its application to the sum of rayleigh random variables,” *IEEE Trans. Commun.*, vol. 38, no. 9, pp. 1463–1474, Sep. 1990.

[79] R. Mesleh, H. Elgala, and H. Haas, “Performance analysis of indoor OFDM optical wireless communication systems,” in *Proc. 2012 IEEE Wireless Commun. Netw. Conf.*, Paris, France, Apr. 2012, pp. 1005–1010.

[80] A. Schrijver, *Theory of linear and integer programming.* Chichester: Johan Wiley & Sons, 1998.

[81] H. Zhang, Y. Yuan, and W. Xu, “PAPR reduction for DCO-OFDM visible light communications via semidefinite relaxation,” *IEEE Photon. Technol. Lett.*, vol. 26, no. 17, pp. 1718–1721, Sep. 2014.

[82] D. L. Donoho, “Compressed sensing,” *IEEE Trans. Inf. Theory*, vol. 52, no. 4, pp. 1289–1306, Apr. 2006.

[83] J. G. Proakis, *Digital Communications*, 3rd ed. New York: McGraw-Hill, 1995.

[84] S. X. Ng and L. Hanzo, “On the MIMO channel capacity of multidimensional signal sets,” *IEEE Trans. Veh. Technol.*, vol. 55, no. 2, pp. 528–536, Mar. 2006.

[85] X. Li, J. Vucic, V. Jungnickel, and J. Armstrong, “On the capacity of intensity-modulated direct-detection systems and the information rate of ACO-OFDM for indoor optical wireless applications,” *IEEE Trans. Commun.*, vol. 60, no. 3, pp. 799–809, Mar. 2012.

[86] C. E. Shannon, “A mathematical theory of communication,” *Bell Syst. Tech. J.*, vol. 27, no. 3, pp. 379–423, Jul. 1948.

[87] L. Hanzo, T. H. Liew, B. L. Yeap, R. Y. S. Tee, and S. X. Ng, *Turbo coding, turbo equalisation and space-time coding: EXIT-chart-aided near-capacity designs for wireless channels.* Chichester: Wiley-IEEE Press, 2011.

[88] J. Kliewer, S. X. Ng, and L. Hanzo, “Efficient computation of EXIT functions for nonbinary iterative decoding,” *IEEE Trans. Commun.*, vol. 54, no. 12, pp. 2133–2136, Dec. 2006.

[89] Z. Babar, S. X. Ng, and L. Hanzo, “Near-capacity code design for entanglement-assisted classical communication over quantum depolarizing channels,” *IEEE Trans. Commun.*, vol. 61, no. 12, pp. 4801–4807, Dec. 2013.

[90] T. M. Cover and J. A. Thomas, *Elements of information theory*, 2nd ed. Hoboken, New Jersey: John Wiley & Sons, 2012.

[91] W. Ryan and S. Lin, *Channel codes: Classical and modern.* New York, USA: Cambridge University Press, 2009.

[92] R. A. Adams and C. Essex, *Calculus: A complete course*, 7th ed. Toronto, Ontario, Canada: Pearson, 2010.

[93] B. Lin, X. Tang, H. Yang, Z. Ghassemlooy, S. Zhang, Y. Li, and C. Lin, “Experimental demonstration of IFDMA for uplink visible light communication,” *IEEE Photon. Technol. Lett.*, vol. 28, no. 20, pp. 2218–2220, Oct. 2016.

[94] Y. F. Liu, C. H. Yeh, C. W. Chow, Y. Liu, Y. L. Liu, and H. K. Tsang, “Demonstration of bi-directional LED visible light communication using TDD traffic with mitigation of reflection interference,” *Opt. Express*, vol. 20, no. 21, pp. 23 019–23 024, Oct. 2012.

[95] Y. Yang, Z. Zeng, J. Cheng, C. Guo, and C. Feng, “A relay-assisted OFDM system for VLC uplink transmission,” *IEEE Trans. Commun.*, vol. 67, no. 9, pp. 6268–6281, Sep. 2019.

[96] M. D. Soltani, X. Wu, M. Safari, and H. Haas, “Bidirectional user throughput maximization based on feedback reduction in LiFi networks,” *IEEE Trans. Commun.*, vol. 66, no. 7, pp. 3172–3186, Jul. 2018.

[97] M. D. Soltani, M. A. Arfaoui, I. Tavakkolnia, A. Ghrayeb, M. Safari, C. M. Assi, M. O. Hasna, and H. Haas, “Bidirectional Optical Spatial Modulation for Mobile Users: Toward a Practical Design for LiFi Systems,” *IEEE J. Sel. Areas Commun.*, vol. 37, no. 9, pp. 2069–2086, Sep. 2019.

[98] L. Feng, R. Q. Hu, J. Wang, P. Xu, and Y. Qian, “Applying VLC in 5G networks: Architectures and key technologies,” *IEEE Netw.*, vol. 30, no. 6, pp. 77–83, Nov./Dec. 2016.

[99] F. Boccardi, J. Andrews, H. Elshaer, M. Dohler, S. Parkvall, P. Popovski, and S. Singh, “Why to decouple the uplink and downlink in cellular networks and how to do it,” *IEEE Commun. Mag.*, vol. 54, no. 3, pp. 110–117, Mar. 2016.

[100] K. Smiljkovikj, P. Popovski, and L. Gavrilovska, “Analysis of the decoupled access for downlink and uplink in wireless heterogeneous networks,” *IEEE Wireless Commun. Lett.*, vol. 4, no. 2, pp. 173–176, Jan. 2015.

[101] S. Singh, X. Zhang, and J. G. Andrews, “Joint rate and SINR coverage analysis for decoupled uplink-downlink biased cell associations in HetNets,” *IEEE Trans. Wireless Commun.*, vol. 14, no. 10, pp. 5360–5373, Oct. 2015.

[102] S. Feng, T. Bai, and L. Hanzo, “Joint Power Allocation for the Multi-User NOMA-Downlink in a Power-Line-Fed VLC Network,” *IEEE Trans. Veh. Technol.*, vol. 68, no. 5, pp. 5185–5190, May 2019.

[103] N. Taherinejad, L. Lampe, and S. Mirabbasi, “An adaptive impedance-matching system for vehicular power line communication,” *IEEE Trans. Veh. Technol.*, vol. 66, no. 2, pp. 927–940, Feb. 2017.

[104] M. Zimmermann and K. Dostert, “A multipath model for the powerline channel,” *IEEE Trans. Commun.*, vol. 50, no. 4, pp. 553–559, Apr. 2002.

[105] B. Song, C. Zhu, B. Corcoran, Q. Wang, L. Zhuang, and A. J. Lowery, “Experimental layered/enhanced ACO-OFDM short-haul optical fiber link,” *IEEE Photon. Technol. Lett.*, vol. 28, no. 24, pp. 2815–2818, Dec. 2016.

[106] Q. Wang, B. Song, B. Corcoran, D. Boland, C. Zhu, L. Zhuang, and A. J. Lowery, “Hardware-efficient signal generation of layered/enhanced ACO-OFDM for short-haul fiber-optic links,” *Opt. Express*, vol. 25, no. 12, pp. 13 359–13 371, Jun. 2017.

[107] D. Shnidman, “A generalized nyquist criterion and an optimum linear receiver for a pulse modulation system,” *Bell Syst. Tech. J.*, vol. 46, no. 9, pp. 2163–277, Nov. 1967.

[108] S. Yang and L. Hanzo, “Fifty years of MIMO detection: The road to large-scale MIMOs,” *IEEE Commun. Surv. Tuts.*, vol. 17, no. 4, pp. 1941–1988, 4th Quart. 2015.

[109] S. Lu, I. A. Hemadeh, M. El-Hajjar, and L. Hanzo, “Compressed sensing-aided multi-dimensional index modulation,” *IEEE Trans. Commun.*, vol. 67, no. 6, pp. 4074–4087, Jun. 2019.

[110] ——, “An adaptive multi-user mimo scheme for the millimeter-wave downlink,” in *Proc. 2018 IEEE 29th Annu. Int. Symp. Pers. Indoor Mobile Radio Commun. (PIMRC).* Bologna, Italy: IEEE, 2018, pp. 1–5.

[111] Q. Wang, Z. Wang, and L. Dai, “Multiuser MIMO-OFDM for visible light communications,” *IEEE Photon. J.*, vol. 7, no. 6, pp. 1–11, Jun. 2015.

[112] F. Wang, C. Liu, Q. Wang, J. Zhang, R. Zhang, L.-L. Yang, and L. Hanzo, “Optical jamming enhances the secrecy performance of the generalized space-shift-keying-aided visible-light downlink,” *IEEE Trans. Commun.*, vol. 66, no. 9, pp. 4087–4102, Sep. 2018.

[113] Y. Liu, Z. Qin, M. Elkashlan, Z. Ding, A. Nallanathan, and L. Hanzo, “Nonorthogonal multiple access for 5G and beyond,” *Proc. IEEE*, vol. 105, no. 12, pp. 2347–2381, Dec. 2017.

[114] A.-M. Căilean and M. Dimian, “Current challenges for visible light communications usage in vehicle applications: A survey,” *IEEE Commun. Surv. Tuts.*, vol. 19, no. 4, pp. 2681–2703, 3rd Quart. 2017.

[115] M. S. Islim, S. Videv, M. Safari, E. Xie, J. J. McKendry, E. Gu, M. D. Dawson, and H. Haas, “The impact of solar irradiance on visible light communications,” *J. Lightw. Technol.*, vol. 36, no. 12, pp. 2376–2386, Jun. 2018.

[116] Y. H. Chung and S.-b. Oh, “Efficient optical filtering for outdoor visible light communications in the presence of sunlight or articifical light,” in *Proc. 2013 Int. Symp. Intell. Signal Process. Commun. Syst. (ISPACS).* Naha, Japan: IEEE, Nov. 2013, pp. 749–752.

[117] B. G. Guzmán, V. P. G. Jiménez, M. C. Aguayo-Torres, H. Haas, and L. Hanzo, “Downlink performance of optical ofdm in outdoor visible light communication,” *IEEE Access*, vol. 6, pp. 76 854–76 866, 2018.

Author Index